PLASMA ENHANCED CHEMICAL VAPOR DEPOSITION

ON LIVING SUBSTRATES:

DEVELOPMENT, CHARACTERIZATION, AND BIOLOGICAL APPLICATIONS

A Dissertation

by

TSUNG-CHAN TSAI

Submitted to the Office of Graduate Studies of
Texas A&M University
in partial fulfillment of the requirements for the degree of

DOCTOR OF PHILOSOPHY

Approved by:

Chair of Committee,	David Staack
Committee Members,	Young-Ki Jo
	Eric L. Peterson
	Melissa A. Grunlan
Head of Department,	Jerald A. Caton

December 2012

Major Subject: Mechanical Engineering

ABSTRACT

This dissertation proposed the idea of "plasma-enhanced chemical vapor deposition on living substrates (PECVD on living substrates)" to bridge the gap between the thin film deposition technology and the biological and living substrates. This study focuses on the establishment of the knowledge and techniques necessary to perform "PECVD on living substrates" and contains three main aspects: development, characterization, and biological applications.

First, a PECVD tool which can operate in ambient air and at low temperature was developed using a helium dielectric barrier discharge jet (DBD jet). It was demonstrated that various materials, such as polymeric, metallic, and composite films, can be readily synthesized through this technique. Second, the PMMA and copper films deposited using DBD jets were characterized. High-rate (22 nm/s), low-temperature (39 ºC) PMMA deposition was achieved and the film surface morphology can be tailored by altering the discharge power. Conductive copper films with an electrical resistivity lower than 1×10^{-7} ohm-m were obtained through hydrogen reduction. Both PMMA and copper films can be grown on temperature-sensitive substrates, such as plastics, pork skin, and even fingernail. The electrical, optical, and imaging characterization of the DBD jets was also conducted and several new findings were reported. Multiple short-duration current pulses instead of only one broad pulse per half voltage cycle were observed when a dielectric substrate was employed. Each short-duration current pulse is induced by a leading ionization wave followed by the formation of a plasma channel. Precursor

addition further changed the temporal sequence of the pulses. An increase in the power led to a mode change from a diffuse DBD jet to a concentrated one. This mode change showed significant dependence on the precursor type, tube size, and electrode configuration. These findings regarding the discharge characteristics can thus facilitate the development of DBD-jet operation strategies to improve the deposition efficacy. Finally, this technique was used to grow PMMA films onto agar to demonstrate one of its potential biological applications: sterile bandage deposition. The DBD jet with the film depositing ability enabled the surface to be not only efficiently sanitized but also protected by a coating from being reached by bacteria.

DEDICATION

To my parents and my wife

ACKNOWLEDGEMENTS

I would like to convey my sincerest gratitude to my advisor, Dr. Staack, who provides great help, guidance and support on this research. I also would like to thank Dr. Jo, Dr. Peterson, and Dr. Grunlan for serving on my committee members and giving valuable comments on my research works and dissertation.

Thanks also go to the department faculty and staffs at Texas A&M University for their help. I also want to extend my gratitude to Dr. Zacharia for providing use of the stylus profilometer and FTIR, and to TAMU Materials Characterization Facility for the use of SEM, AFM, and XPS.

Especially, I am very grateful to all my former and current colleagues, Robert, William, Aditya, Sreekar, Rei, Sagar, Michael, Wayne, Matt, Dani, Jeff, Stephen, Katy, Patricia, and Ghislain, in Plasma Engineering and Diagnostics Lab (PEDL) for their help during my graduate years.

Finally, I would like to express my deepest appreciation to my mother, father, and brother for their support and encouragement and to my wife Li-Ting for her patience and love.

TABLE OF CONTENTS

Page

LIST OF FIGURES

Page

LIST OF TABLES

Page

1. INTRODUCTION

1.1 Background

The main purpose of this dissertation is to initiate our research into "plasma-enhanced chemical vapor deposition on living substrates (PECVD on living substrates)" by developing a thin film deposition technique which can operate at low temperature and in open air conditions. The dielectric barrier discharge jet (DBD jet), which is an atmospheric pressure non-thermal plasma source, was used as the depositing tool to achieve the film deposition on biological and living substrates. Before the detailed motivation of this research is given this subsection introduces a brief background of plasmas, several types of atmospheric pressure non-thermal plasmas, and the techniques used for thin film deposition. These contents are important for better understanding what non-thermal plasmas are, what a DBD jet is, why the PECVD was selected rather than other film deposition techniques.

1.1.1 Introduction to Plasmas

Plasma, first named by Langmuir [1], is a partially or fully ionized gas containing a collection of randomly moving charged particles (e.g., electrons, negative ions and positive ions) and neutral gas atoms (or molecules), as illustrated in Figure 1. Plasma is thus electrically conductive and responds to electric and magnetic fields. The overall gas can be considered to be electrically neutral as typically the electrons and ions are in about equal numbers. Plasma is also called *the fourth state of matter* due to its unique physical

and chemical properties, compared to those in the basic three states of matter — solid, liquid, and gas. In addition to the charged particles existing in the plasma, other chemically reactive media, including free radicals, excited atoms or molecules (metastables) and photons, can be produced in the plasma. These diverse chemically reactive species are normally unavailable in other three basic states of matter. The gas temperature of plasma can either be much higher than those generated by conventional chemical technologies or remain as low as room temperature based on the requirements of specific applications. Due to these unique properties, plasma has received great attention in numerous applications to optics, chemistry, material processing, and even medical treatment.

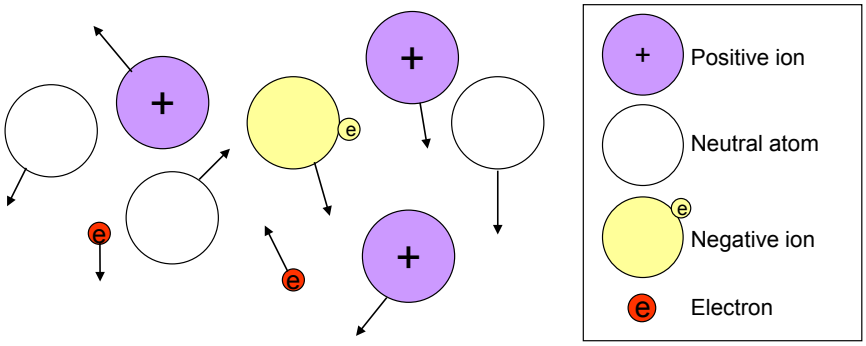

Figure 1. Schematic illustration of plasma composition.

Plasma can occur in the natural environment (> 99% of the universe is comprised of plasma) and can also be generated in the laboratory and industry by the addition of energy to a gas. Examples of plasmas in the nature include lightening, aurora borealis, solar corona, and solar wind. Artificial plasma sources can be produced over a wide

range of pressures (from a millionth of an atmosphere to atmospheric pressure or higher). They can be generated by simply heating up a gas to ionize it or by other methods, such as X-rays [2], electron beams [3], and, the most commonly, electric field (usually several kV or greater is required) [4]. The plasmas induced by electric field are typically called electrical discharges.

The temperatures of the components in a plasma discharge are used to describe the type of plasma. Simply speaking, these temperatures include the electron temperature (T_e), the ion temperature (T_i) and the neutral temperature (or so-called gas temperature T_g). Typically the ions and the neutrals have similar temperatures (i.e., $T_i \approx T_g$). The temperature difference between T_e and T_g divides the plasmas into two categories—thermal plasmas and non-thermal plasmas. Thermal plasmas are typically in a local thermodynamic equilibrium (LTE) sate, which means $T_e \approx T_i \approx T_g$ at each point in the plasma but the single temperature (> 10,000 K) can differ from point to point in space and time. Non-thermal plasmas (or so-called "cold plasmas"), which are in a thermodynamic and chemical non-equilibrium, have the electron temperature greater than 10,000 K but the gas temperature as low as room temperature (i.e., $T_e >> T_i \approx T_g$).

Different properties between thermal and non-thermal plasmas lead to various applications. Thermal plasmas, such as plasma torches and arcs, can produce a high flux of heat (high power delivery), but less selectivity. They are mainly employed in material processing (welding or cutting) which requires high temperature treatment or used in chemical and waste destruction [5]. Non-thermal plasmas offer high energetic electrons without significantly heating up the gas stream. For this reason, thermal damage to the

treated surfaces or electrodes can be avoided using non-thermal plasmas. The energetic electrons lead to the generation of abundant active species, further initiating chemical reactions with treated objects. These plasma sources typically provide low-temperature and high-selectivity treatment [6]. They thus open up a wide range of applications, such as lighting, processing and surface modification of polymers, fuel reforming, pollution control, and even medical treatment (e.g., sterilization). Typical examples of the non-thermal plasma are glow discharges, corona discharges, atmospheric-pressure plasma jets (APPJs), micro-hollow cathode discharges (MHCDs), and dielectric barrier discharges (DBDs) [5-9].

1.1.2 Atmospheric Pressure Non-Thermal Plasmas

Traditional techniques to generate stable and uniform non-thermal plasmas (e.g., glow discharge) require low-pressure environment, especially in the material processing applications. In a low-pressure environment the applied electric field maintains a high T_e, but gas collisions with chamber walls maintain a low T_g. However, vacuum-based plasma reactors have several disadvantages: expensive vacuum equipment, sample size limitation, and vacuum incompatibility of certain substrates. Producing non-thermal plasmas at atmospheric pressure can solve these problems. It can achieve cost savings since less energy and no vacuum pumps are required. The atmospheric pressure non-thermal plasmas are also free from the constraints of vacuum chambers, enabling large area processing, reduced processing steps and increased throughput. Moreover, non-vacuum compatible substrates, such as biological and living substrates, can be treated

using such plasma sources. Nevertheless, the increased interparticle collisions (relative to surface collisions) at atmospheric pressure make maintaining a low T_g more difficult. This typically results in a transition from non-thermal discharges to thermal discharges (i.e., glow-to-arc transition). In other words, atmospheric pressure plasmas are unstable and tend to be "hot". Thus several methods to prevent the "cold-to-hot transition" are employed in the development of the atmospheric pressure non-thermal plasma systems. Typical examples of these plasmas include corona discharges, DBDs, APPJs, and microplasmas. Here only the descriptions of DBDs and APPJ are given in the following subsections since a combination of these two methods was employed to develop our depositing tools. Moreover these two atmospheric pressure plasma sources are able to generate diffuse, stable discharges, which are especially amenable to uniform film deposition. Detailed descriptions of other atmospheric pressure non-thermal plasma sources can be found in many textbooks.

1.1.2.1 Dielectric Barrier Discharges

Dielectric barrier discharges (DBDs) typically contain at least one dielectric layer in the discharge gap between two electrodes to limit the current density of the discharge, as shown in Figure 2 [10]. They are also usually called barrier discharges or silent discharges. Non-thermal plasma conditions are achieved by the dielectric barriers as the dielectric barriers, located in the current path, severely limit current and avoid spark (thermal plasma) formation. The typical discharge gap distance varies from 0.1 mm to several centimeters (usually small gap distances are required for stable plasma

generation). Due to the presence of dielectric layers, a DC power supply is not suitable to operate the DBDs. Instead, they are driven between line frequency (60 Hz) and about 10 MHz (usually in the several tens of kHz range) [7]. Various gases, including helium, neon, oxygen, and air, can be employed as the plasma working gases with low power consumption. These features in DBD devices result in numerous applications, such as ozone generation, UV sources, polymer treatment, and air-pollution control [7, 8, 11, 12]. In addition, DBDs have shown several promising results in biomedical treatment, such as sterilization, blood coagulation, initiation of skin cancer cell apoptosis, and skin disease treatment [13].

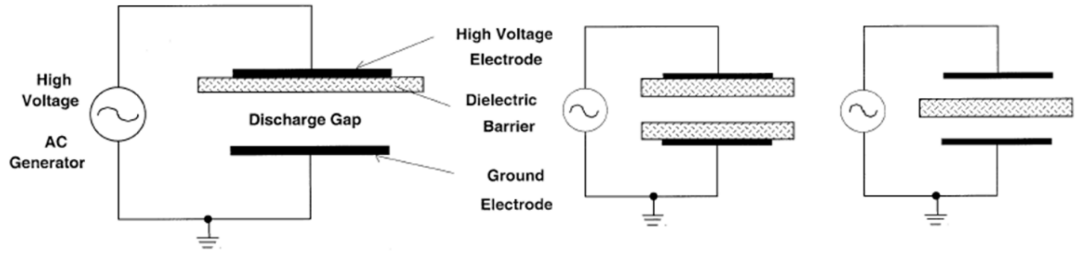

Figure 2. Cross-sectional illustrations of typical DBD configurations [10] (© 2002, IEEE).

When a sufficiently high electric field (~kV) is applied to the electrodes, breakdown occurs in the discharge gap. DBDs can exhibit either a filamentary mode or a diffuse mode based on the working gas, dielectric properties, and the operation conditions. In most gases the filamentary DBDs, in which a large number of short-lived microdischarges are generated, are observed, as shown in Figure 3(a) [13]. As can be seen in this image, such plasma sources can be used to treat living surfaces due to their low

gas temperature properties. Most of the industrial applications, such as ozone generation and volatile organic compound (VOC) destruction, employ the DBDs operating in this mode. However, the filamentary DBDs are spatially non-uniform discharges, which cause inhomogeneous treatment when they are used for material processing. Diffuse DBDs can be achieved by feeding noble gas (e.g., helium or neon) as the major working gas [14], by using mesh electrodes [15, 16], or by selecting the proper discharge gap spacing, operation frequency and applied voltage [17-19]. Such plasma methods provide spatially homogeneous discharge distribution, as shown in Figure 3(b) [20]. Recently they thus have been utilized to achieve uniform surface treatment, such as surface modification [21] and thin film deposition [22]. However, a small gap distance between the parallel-plate electrodes, which is typically required for stable plasma generation, lead to spatial confinement of plasmas, further limiting their ability to treat 3-D free-form substrates.

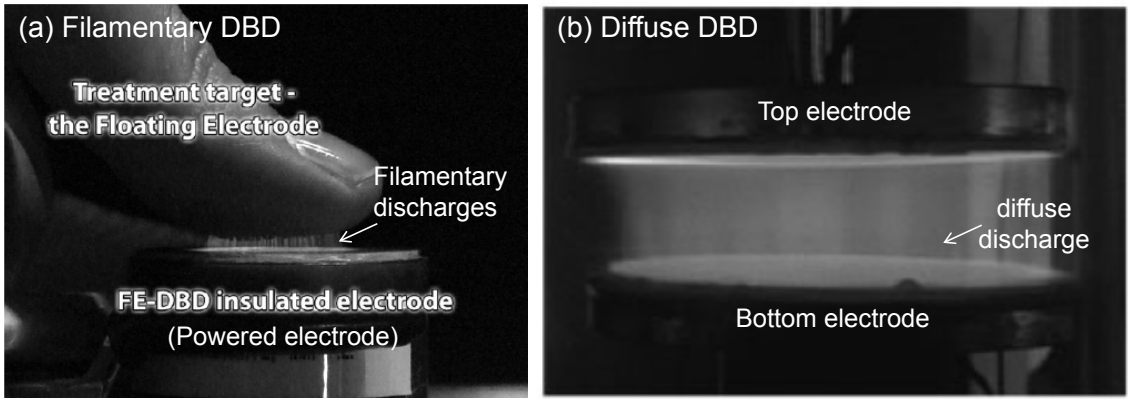

Figure 3. Examples of (a) filamentary DBD [13] (© 2008, WILEY-VCH Verlag GmbH & Co. KGaA, Weinheim) and (b) diffuse DBD [20] (© 2005, WILEY-VCH Verlag GmbH & Co. KGaA, Weinheim).

1.1.2.2 Atmospheric Pressure Plasma Jets

The atmospheric pressure plasma jets (APPJs) have attract more and more attention in recent years due to the fact that the APPJs can not only operate in ambient air and at low temperature but also offer the plasma without being spatially confined by electrodes [9]. Since APPJs can locally generate plasma and offer a longer working distance, they create a more flexible way for treatment of various types of surfaces, compared to the parallel-plate DBDs mentioned earlier. Selected examples of the APPJs can be seen in Figure 4 [23-25]. Typically a noble gas (e.g., helium or argon) is used as the working gas flowing through a plasma reactor to achieve stable non-thermal plasma generation. The gas ionized in an upstream electrode unit by a sufficiently high electric field is blown outside of the reactor along the gas stream. It further forms a jet-like plasma configuration downstream of the reactor. This is the reason this type of plasma is commonly called “plasma jet”. With this unique configuration, any substrates placed in downstream of the APPJs can be directly treated. Their simple setup and easy operation result in the recent development of several different types of APPJs. The features of APPJs enable fast, 3D, large-area processing in many applications, such as surface modification [26], film deposition [27], as well as biomedical treatment [28]. An excellent review of various jet configurations can be seen in the paper by Laroussi and Akan [9].

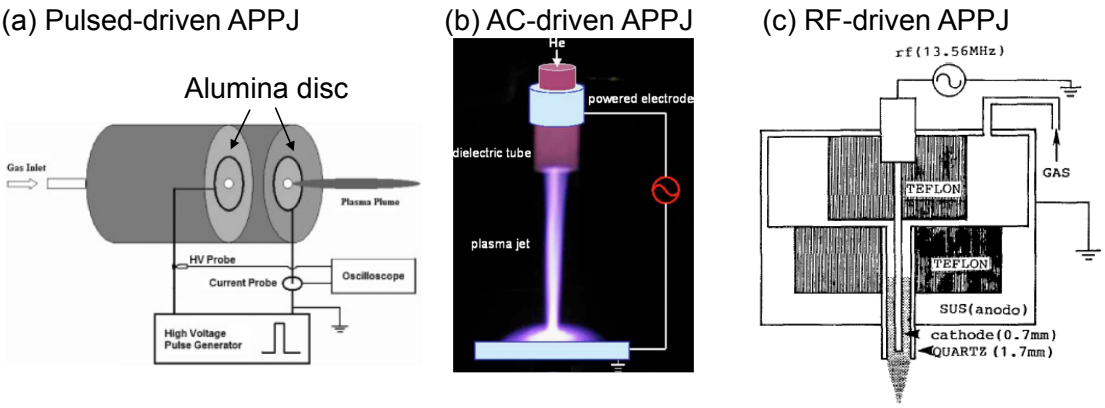

Figure 4. APPJs with different operation frequencies: (a) pulsed DC-driven plasma jet ("plasma pencil") (reprinted with permission from [24]. Copyright © 2006, American Institute of Physics), (b) AC-driven plasma jet (reprinted with permission from [25]. Copyright © 2006, American Institute of Physics), and (c) RF-driven plasma jet (reprinted with permission from [23]. Copyright © 1992, American Institute of Physics).

The APPJs can be classified according to their operation frequency (from pulsed DC to microwave) and electrode geometries. The plasma jets in Figure 4(a), (b), and (c) are selected here as they have different electrode configurations and various driving frequencies. Figure 4(a) shows the so-called "plasma pencil" which is a handheld device developed by Lu and Laroussi [24]. The "plasma pencil" employed two thin copper rings, which are attached to the surfaces of two perforated alumina discs, as the electrodes and a pulsed DC voltage was used to ionize the helium operating gas. The APPJ shown in Figure 4(b) is based on one of the DBD configurations [25]. It consists of a dielectric tube with one tubular electrode (powered) mounted on it. The substrate is the second electrode (grounded). In this case helium was also adopted but the device was driven by an AC sinusoidal high voltage (~kV) in the kHz frequency range (a pulsed DC power source was also employed in the literature for comparison). It should be mentioned that the DBD jet with two tubular electrodes (one is powered and another is

grounded) is also a common configuration. Figure 4(c) illustrates an early example of an RF (13.56 MHz) non-thermal helium plasma jet with a needle-cylinder electrode configuration [23]. The needle electrode inside a quartz tube was used as the powered electrode while the cylindrical electrode covering around the quart tube was grounded. It should be mentioned that impedance matching between the power supply and the plasma is required in RF-driven APPJs. Glow-to-arc transition and device heating after long-term operation are also the possible drawbacks using RF power [29]. Pulsed DC-excited APPJs have been demonstrated to have superior performance to the plasmas driven by AC sinusoidal voltage in the same jet configurations. Compared to the AC-excited plasma jets, using pulsed DC power can achieve the generation of more species, lower energy consumption, stronger optical emission, higher propagation speed of ionization waves, and higher efficacy of sterilization [25, 30, 31]. Nevertheless, such pulsed power supplies are significantly more expensive than AC systems.

Based on the electrode geometries, the APPJs can also be divided into two types—direct plasma and indirect plasma. A direct plasma method basically contains only one electrode which is connected to the high-voltage (HV) power source and the treated substrate is used as the second electrode (grounded or at a floating potential), as shown in Figure 5(a). Examples using the direct plasma methods can be seen in Figure 3(a) and Figure 4(b), and they are usually referred as "floating-electrode" plasmas [12, 13, 32]. In the direct plasma, both excited and charged species (electrons and ions) can be transferred to the substrate surface. In contrast, plasma in an indirect method is always generated between two electrodes (powered electrode and grounded electrode)

and extended outside of the reactor along the gas stream to the treated substrates placed further downstream of the plasma (afterglow), as illustrated in Figure 5(b). In this case with two electrodes and a substrate, charged species usually flow to the second electrode instead of the substrate surface. The plasma jets shown in Figure 4(a) and Figure 4(c) are such indirect plasma kinds. In general floating-electrode or so-called direct plasma methods generate more radicals and active species in the vicinity of the substrate than indirect or afterglow plasma [11, 33]. This feature leads to faster sterilization using the direct plasma sources than those indirect ones [11].

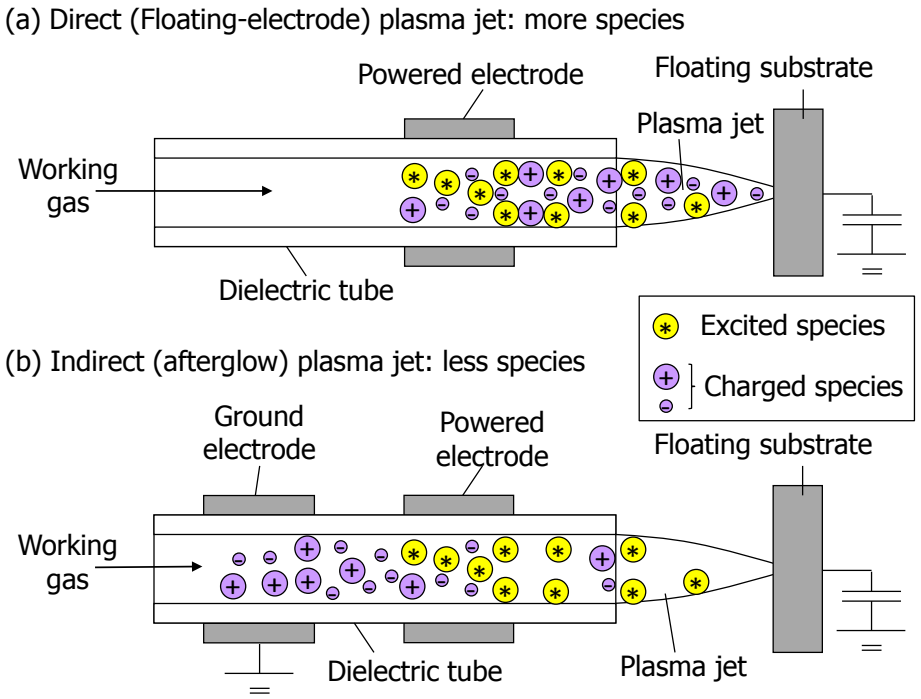

Figure 5. Schematic illustrations of (a) direct and (b) indirect plasma jets.

1.1.3 Thin Film Deposition

Thin film deposition techniques have been developed for decades and widely used in industry and scientific research. Many related products, including semiconductor devices, flat panel displays, and magnetic storage media, played a key role in changing human life in recent years [34, 35]. Based on the deposition mechanism, the thin film deposition techniques generally can be classified into physical vapor deposition (PVD) and chemical vapor deposition (CVD).

PVD is a deposition method employing physical processes rather than chemical reactions to achieve the film coating onto various substrate surfaces. Typically either "evaporation" or "sputtering" is involved in the PVD technology while they both operate in vacuum. In the evaporation processes, the source material (solid or liquid source) is evaporated (or sublimated) by heating up, and the evaporated particles travel toward and condense on the substrate which is placed a distance away. Thermal evaporator, electron beam PVD, and molecular beam epitaxy are examples using evaporation techniques. Sputtering usually employs plasma to achieve ion (e.g., Ar+) bombardment on source surfaces (target). Atoms are thus ejected from target and further deposit onto the substrate. Sputtering methods include DC sputtering, AC sputtering, reactive sputtering and magnetron sputtering. The PVD techniques are typically utilized for deposition of metallic coatings.

In contrast, CVD allows for deposition of diverse types of films, such as non-metallic films, dielectric films, single-crystal semiconductor films, and composite films. Besides, it provides a deposited film with better step coverage than that by PVD. Instead

of solid (or molten) materials in PVD processes, CVD uses gas phase precursors (e.g., SiH_4 for silicon film deposition), volatile liquid or solid precursors as it material sources. The precursor transport and film formation mechanism can be schematically illustrated by Figure 6. The precursor arrives at the reaction region through forced convection [label (a)] and diffusion [label (b)], followed by the adsorption of the gas phase reactants on the substrate surface. Chemical reactions in the precursor [label (b')] may also occur before they diffuse to the surface [label (b")]. And then the precursor reactant diffuses or migrates to the attachment site, allowing for film formation [label (c)] through surface chemical reactions, such as pyrolysis, reduction, oxidation, and compound formation [35]. After chemical reactions, the generated by-products (usually volatile) desorb from the substrate surface, further being transferred away from the reaction zone by diffusion [label (d)] and forced convection [label (e)]. Variants of CVD processing techniques have been developed for decades. Typical examples include atmospheric pressure CVD (APCVD), low pressure CVD (LPCVD), and plasma-enhanced CVD (PECVD).

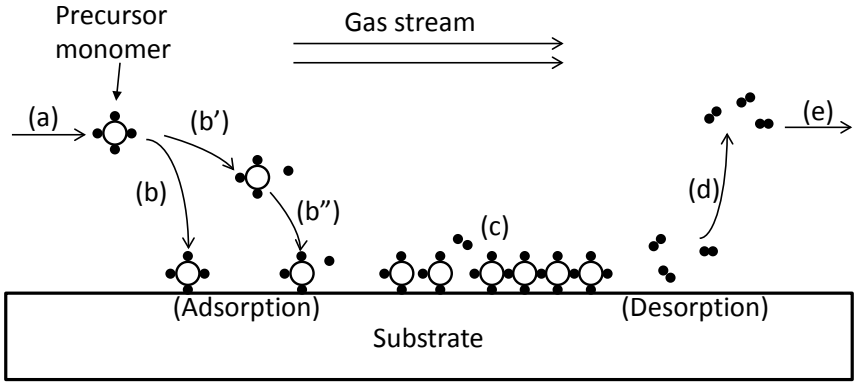

Figure 6. Sequence of precursor transport and adsorption, chemical, and desorption processes in CVD for film growth.

Conventional thermal CVD processes, such as APCVD and LPCVD, employ heat energy to activate the surface chemical reactions. Typically the substrate requires to be heated up to 1000–1300 ºC and 300–900 ºC for APCVD and LPCVD, respectively. The high-temperature operation thus limits their use in the film growth on temperature-sensitive (< 50 ºC) substrates. To achieve low temperature deposition, a non-thermal plasma source is employed in PECVD to provide addition energy to decompose the gas reactants into a variety of component species and to facilitate chemical deposition. Thus a deposition temperature of 200–350 ºC or lower can be achieved using this technique. Using PECVD can achieve ultra-thin, pinhole-free deposited films [36]. The plasma polymerized films are also found to be firmly adhesive to various substrate surfaces, and their physical or chemical features are controllable by adjusting the discharge parameters. These features enable the deposition of various films, such as inorganic compounds and organic polymers, onto temperature-sensitive substrates (e.g., polymers). Typically PECVD systems used for most industrial applications operate at low pressure (10 mTorr to 10 Torr) due to the fact that a self-sustained, diffuse, non-thermal glow discharge is easier to maintain at such pressures [37].

1.2 Motivation

As introduced above, thin film deposition has become a mature technique and it facilitates the development and success of a variety of applications, including semiconductors, optics, energy, aerospace, communications and so on. Although currently being used in such applications thin film deposition appears to be beneficial to

biomedical treatment if it can be applied to biological and living substrates. This technique would allow for in-situ and in-vivo manufacturing of materials. Several potential applications include antibacterial coating on plant seeds, functional coating for promoting cell growth, repair of artificial implants, deposition of sterile bandage on wound or adhesive sutures, wound coatings, and scaffolds for the relief of wound mechanical stresses and decreased scaring, or even manufacture of electronic circuits on skins or organs for physiological measurement and monitor.

Regarding applying artificial films to biological or living substrates, photopolymerization has been utilized to form hydrogel materials directly on tissue surfaces to locally deliver drugs and to serve as barriers [38, 39]. Recently Kim *et al.* integrated electronic systems on a thin, soft, water-soluble polymer substrate, and successfully transferred the device onto human epidermis via van der Waals forces for physiological measurement [40]. However, no studies regarding direct thin film deposition on biological and living surfaces have been reported since almost all thin film deposition methods occur in vacuum (e.g., PVD, LPCVD, and PECVD) or require high working temperature (e.g., evaporation, LPCVD, and APCVD). It is not practicable to place living organisms in controlled environments (e.g., vacuum and chambers). Additionally, vacuum equipment is typically expensive and its sample size is limited. Thus these challenges can only be solved if a film depositing tool which is able to operate in open air and at low temperature can be developed.

Performing PECVD at atmospheric pressure (AP-PECVD) provides considerable opportunities to achieve film deposition on biological and living substrates. The development of AP-PECVD techniques is gaining more and more attention and interests in recent years as no expensive vacuum pumps are required and the deposited films using AP-PECVD can still retain the properties of those films obtained by conventional low pressure PECVD (LP-PECVD). Also, it has been shown that using AP-PECVD has potential for large-area treatment, cost savings, process step reduction, equipment simplification, and increased throughput [41]. Typically non-thermal atmospheric pressure plasma methods, such as DBDs and APPJs, are utilized to construct AP-PECVD systems. In most of these systems, the use of helium or argon (usually helium) mixed with a small trace of precursor gas is required for diffuse, stable plasma generation for uniform film growth. Many AP-PECVD films have been obtained using DBDs with parallel-plate electrodes recently [22, 42-44]. However, the spatial confinement of plasma and the requirement of chambers in the conventional parallel-plate DBDs limit their ability to deposit films onto biological and living substrates. In contrast, the APPJs, which offer cold plasma in chamberless operation environments, are one of the most promising sources for achieving PECVD on biological and living substrates.

1.3 Dissertation Statement

The goal of this dissertation is to establish the knowledge and techniques necessary to perform “PECVD on living substrates”. This study will state “1), the

chemistry in LP-PECVD can be achieved using the DBD-jet-based AP-PECVD with similar operation temperature (low-temperature), but the film quality and deposition rate depend on the plasma operating condition; 2) the discharge characteristics in the DBD jet are determined by the input electrical energy, precursor type and concentration, reactor geometry, and substrate; 3) the helium DBD jet can be used in thin film deposition on temperature-sensitive (< 50 ºC) biological substrates in open air for sterilization and bacterial growth inhibition."

To accomplish this goal, the atmospheric pressure helium dielectric barrier discharge jet (DBD jet) with the floating-electrode configuration, which is similar to that presented in Figure 4(b) [25], is employed in this research, as shown in Figure 7. AC sinusoidal high voltage at 28.5 kHz is used to drive the DBD jet. It is a simple and handheld device, particularly suitable for 3-D and local treatment of temperature-sensitive substrates due to its advantages of non-thermal stable plasma, efficient reaction chemistry, and low power consumption. Film deposition can be readily achieved by feeding helium with gaseous precursors through the plasma reactor. It further leads to film growth on the surface of the substrate placed downstream of the DBD jet. As mentioned earlier, the floating-electrode DBD jet is a "direct" plasma method. More radicals and active species are produced in the vicinity of the substrate than those generated in indirect or afterglow plasma. It is expected that in material deposition applications such direct plasma methods may result in higher deposition rate than indirect methods due to the higher concentrations of active species and charged species near the substrate. Besides, it should be reiterated that the direct plasma method can

achieve more efficient sterilization than those indirect or afterglow ones [11]. With these features in material processing and biomedical treatment, the floating-electrode DBD jet is thus expected to be an amenable tool for PECVD on living substrates.

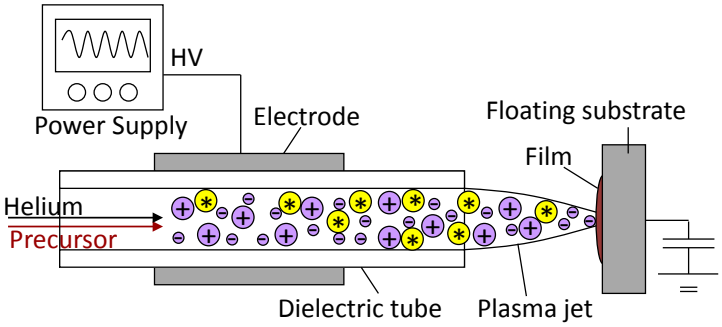

Figure 7. Schematic cross-section of the DBD jet used in this study.

As the inception of the "PECVD on living substrates" project, this study can be divided into three parts: development, characterization, and biological applications. The first is to use the floating-electrode DBD jet for the development of a thin film deposition technique which can operate in ambient conditions. Different ambient environments, applied powers, and precursor concentrations were applied to the deposition experiments. Also, performing deposition on various temperature-sensitive substrates will be presented in order to evaluate the feasibility of this technique. Our particular goal is deposition of polymeric films and metallic films onto temperature-sensitive substrates as prior art focused on inorganic oxide deposition, instead of polymer and metal, onto relative high temperature silicon, metal or glass substrates (detailed in the literature review subsection).

The second part of this study is the characterization of the as-deposited films and the fundamental studies of the floating-electrode DBD jet. Several deposition characteristics were investigated through extensive experiments, such as the deposition rate, deposition temperature, film surface morphology, and film composition. For the DBD jet fundamental studies, we especially focused on the characterization of the plasma physics, including the operation modes and multiple breakdowns. The helium DBD jet used in this study exhibits two operation modes – a diffuse mode and a concentrated mode. And these modes significantly influence the properties of deposited films. Thus the investigation of operation modes is necessary to further control the film properties. When the DBD jet is used as a depositing tool, a small amount of precursors (typically < 1%) are fed with helium working gas for plasma generation. The "impurity" in the helium was found to cause multiple current pulses during each half cycle of the applied voltage. This phenomenon is important as it changes the energy deposition, radical generation, and temperature on the substrate. To understand and optimize the chemical reactions in the film deposition and fabrication processes the study of the physics behind the reactive species generation using the DBD jet is required.

The final portion is to apply this technique to biological applications. As mentioned in the previous subsection, "PECVD on living substrates" has the following potential applications: antibacterial coating on plant seeds, functional coating for promoting cell growth, repair of artificial implants, deposition of sterile bandage on wound, deposition of adhesive sutures, or even manufacture of electronic circuits on skins or organs for physiological measurement and monitor. In this dissertation, the

application “sterile bandage deposition” is specifically our main focus. The idea, which is based upon the combined capabilities of sterilization and film deposition using our DBD jet, can be illustrated in Figure 8. Considering that the film deposited by the DBD jet functions as a bandage, on infected wounds not only can the surface be sterilized but also protected from the future infection. Preliminary experiments used agar as a simplified, temperature-sensitive, moist, nutrient rich surrogate for an actual wound.

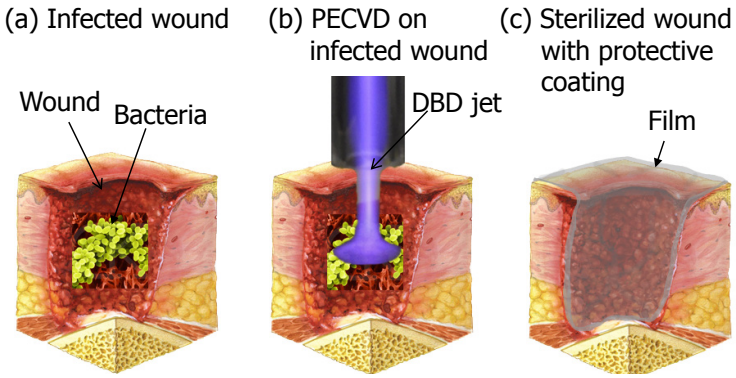

Figure 8. Deposition of “bandage” along with sterilization using the DBD jet (The figures were drawn by Dr. Staack).

1.4 Dissertation Overview

This dissertation contains 9 sections. Section 1 introduces the background and motivation of this dissertation, followed by the research objective and overview. In addition to literature reviews, Section 2 gives the information required for better understanding of the contents of this dissertation. Section 3 presents the system apparatus developed based on the DBD jet to achieve deposition or synthesis of different materials in ambient air conditions. Sections 4 and 5 focus on the material

characterization of the PMMA and copper films, respectively, deposited by using the DBD-jet-based depositing tools. Extensive fundamental studies of the DBD jets are also reported and several unknown phenomena are revealed (Sections 6 and 7). Section 6 studies the effects of the precursor addition on the operation modes, discharge current pulses, and the excited species generation. The discharge uniformity influenced by several parameters, such as precursor types, tube sizes, and electrode configurations, in the DBD jets is investigated and presented in Section 7. Section 8 employs the DBD jet to achieve "sterile bandage deposition" on agar to show the potential of this technique in biomedical applications. It should be mentioned that three papers were published on the subjects corresponding to Section 4 [45] (T.-C. Tsai and D. Staack, "Low-temperature Polymer Deposition in Ambient Air Using a Floating-electrode Dielectric Barrier Discharge Jet," *Plasma Processes and Polymers,* vol. 8, pp. 523-534, 2011.), Section 6 [46] (T.-C. Tsai and D. Staack, "Characteristics of Precursor-Dependent Breakdown in Helium Dielectric Barrier Discharge Jet," *Plasma Science, IEEE Transactions on,* vol. 40, pp. 2931-2945, 2012.) and Section 8 [47] (T.-C. Tsai, J. Cho, K. McIntyre, Y. K. Jo, and D. Staack, "Polymer film deposition on agar using a dielectric barrier discharge jet and its bacterial growth inhibition," *Applied Physics Letters,* vol. 101, pp. 074107-4, 2012). Other two papers are in preparation based on the results in Sections 5 and 7. Finally conclusions and future works are described in Section 9.

2. PREREQUISITE KNOWLEDGE AND LITERATURE REVIEWS

2.1 Prerequisite Knowledge

To better understand the contents presented in this dissertation, prerequisite knowledge regarding several different aspects of plasma and material technology is required and provided in this subsection.

2.1.1 Energy Transfer in Non-Thermal Plasmas

Understanding the energy transfer in plasmas is important to understand why plasmas can be non-thermal. A diagram of the energy flows in electrical discharge can be seen in Figure 9 [48]. Artificial non-thermal discharge is typically sustained by an electric field. The electric field only couples with the charged particles (e.g., electrons and ions) through the Lorentz Force in the plasma, whereas essentially causes no influence on the neutral atoms and molecules. Since the mass of an electron is much lighter than that of an ion, the electron can be significantly accelerated by the external electrical field. In other words, the major part of the energy from the electric field flows to the electrons. The energized electrons then collide with those neutral atoms and molecules in a gas, further leading to various types of collisions. For molecular gases, these collisions include elastic momentum transfer (electron energy to heavy particle translational energy, e-T), rotational excitation (electron energy to rotational energy, e-R), vibrational excitation (electron energy to vibrational energy, e-V), electronic excitation (electron energy to electronic excitation energy, e-E), ionization (electron

energy to ionization energy, e-I), dissociation (electron energy to ionization energy, e-I), and attachment (electron energy to attachment energy, e-A). For monatomic gases, they typically only have momentum transfer (e-T), electronic excitation (e-E), and ionization (e-I) during the collisions due to the lack of internal degrees of freedom (e.g., rotational and vibrational motion) in atoms.

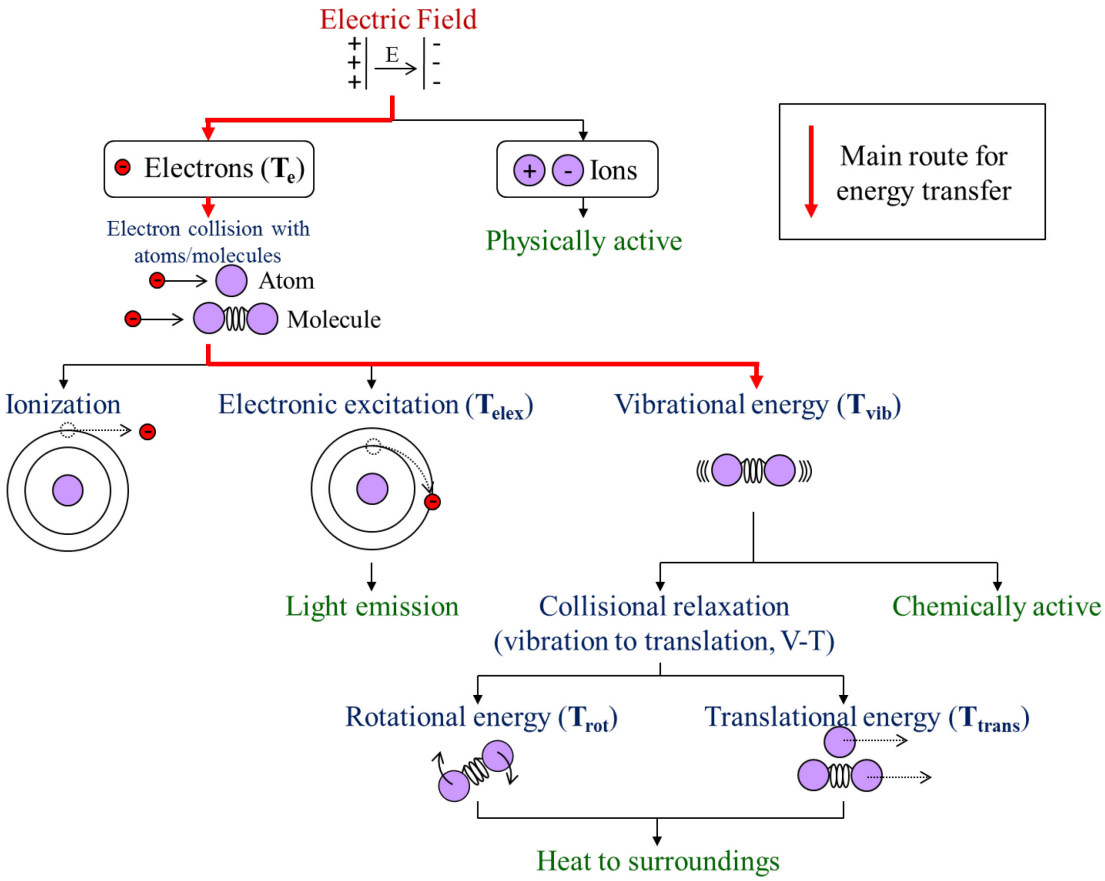

Figure 9. Energy flow diagram for non-thermal plasmas.

In these energy transfer paths, e-T is very inefficient since very little energy can be transferred from the electron to heavy neutral particle due to the significant difference

between the masses of the electron and the heavy particle. Light emission generated from the plasma can be attributed to the e-E energy transfer (electronic excitation). However, this is not a significant route for energy transfer since typically in most gases only few electrons have sufficiently high energy (> 10 eV) to electronically excite the atoms or molecules. A small portion of energy transfer is through the path e-I (Ionization) as, again, there are only a small number electrons with sufficient energy to induce ionization though this is an important process in a plasma source. Similarly (i.e., few electrons have the specific energy), rotational excitation (e-R), dissociation (e-D), and attachment (e-A) are not the main routes for energy transfer. The main energy transfer (80 %) from the electron to the heavy neutral particle is through the vibrational excitation (e-V) in molecular gases because the characteristic energy to induce the vibrational modes of a molecule is about 0.2 – 0.5 eV, which is close to the energy (~ 1 eV) most electrons have. As shown in Figure 9, the vibrational energy can then be used to activate chemical reaction processes. Or the vibrational modes relax after the molecules collide with other neutral atoms or molecules, further leading to rotational modes and/or translational modes of heavy particles through the vibration-translation (V-T) energy transfer. Since the average speed of the rotational and translational motions of the heavy particles represents the gas temperature in a plasma source, the energy transfer to these two modes indicates that the gas temperature in the plasma is increased. Finally the relaxation of these two modes occurs when the atoms or molecules collide with the walls of the plasma system (i.e., gas is cooled by system walls).

Compared to the molecular gases, in monatomic gases (e.g., noble gases) there are no routes for energy transfer to vibrational modes. This is one of the reasons that it is relatively easier to achieve non-thermal plasmas using noble gases, compared to the molecular gases. A good example is the use of helium to achieve non-thermal plasmas. In addition to the absence of vibrational modes, only a small amount of energy transfer happens through e-I and e-E as helium has high ionization energy and electronic excitation energy. The main path for energy transfer from electrons to heavy particles in helium is thus through the elastic momentum transfer (e-T), which is very inefficient as mentioned earlier. Additionally, helium has high thermal conductivity to transfer heat to system walls efficiently. Therefore, helium is especially commonly used to generate stable non-thermal plasmas at atmospheric pressure.

2.1.2 Material Diagnostic Techniques

Several portions of this dissertation cover the material characterization of the deposited films using DBD jets. These include the film thickness, film surface morphology, film surface roughness, elemental compositions at film surface, and functional groups in the film. To obtain these internal/external structures and properties in the film, various diagnostic techniques are usually required. Here we briefly introduce those techniques used to characterize the plasma polymerized films in this dissertation.

2.1.2.1 Profilometer

The film thickness can be measured by a stylus profilometer, which employs a stylus to scan the sample surface to obtain its surface profile. The profilometer used in this study is KLA-Tencor P-6 profiler with a standard 2 μm radius stylus [49]. In this profiling system the vertical displacement of the stylus is obtained by capacitance position sensing. By moving the stylus in x- and y- directions, the surface profile (vertical height) of the measured sample can thus be portrayed. The maximum scan length in the horizontal direction is 60 mm and the maximum vertical range is 327 μm. The vertical resolution is lower than 0.01 Å, and the lateral resolutions in x- and y-directions are 0.2 μm and 2 μm, respectively. The stylus force ranges from 0.5 to 50 mg.

2.1.2.2 Scanning Electron Microscopy (SEM)

The micro-/nano-scale surface images of the deposited films can be acquired by scanning electron microscopy (SEM). The SEM utilizes a focused high-energy electron beam to scan the sample surface. A variety of signals, typically including secondary electrons, back-scattered electrons, and photons, are produced when the energetic electrons interact with the measured sample [50]. Furthermore, these signals are collected and used to construct a two-dimensional image containing the information about the material morphology and topography. An ultra-high resolution field emission SEM (JEOL JSM-7500), located at Materials Characterization Facility (MCF) in Texas A&M University, was utilized to inspect the external structures of our films [51]. The resolution is 1.0 nm at an electron beam accelerating voltage of 15 kV. The

magnification ranges are from 25× to 19000× in the Low Magnification (LM) mode and from 100× – 650000× in the SEM mode.

2.1.2.3 Atomic Force Microscopy (AFM)

The atomic force microscopy (AFM) is also a surface profiling technique which is similar to the stylus profilometer. However, AFM is especially suitable for surface roughness measurement since it can achieve atomic-scale resolution due to several system refinements [52, 53]. AFM employs a cantilever with a microfabricated tip with nanometer-scale radius of curvature to scan the sample surface and obtain the surface topography. Piezoelectric elements are usually utilized to achieve very accurate and precise scanning of the sample in x- and y- directions. To reduce the sample damage caused by the tip and prevent the tip from sticking to the surface during sample scanning, a "tapping mode", in which the cantilever is oscillated near its resonance frequency, is often used to solve these problems. When the oscillated tip is placed very close to the sample surface, the forces (on an atomic scale) between the tip and the sample cause a change in the oscillation amplitude of the cantilever. The measurement of the oscillation amplitude is performed by a laser beam deflection system. The sample is further moved in the z-direction by an additional piezoelectric device to keep the oscillation amplitude constant through a feedback circuit. Using the data in x-, y-, and z-directions, a three-dimensional surface profile with nano-scale resolution can be generated. The AFM used in this study is a Digital Instruments Nanoscope AFM/STM [54], which is also provided by MCF. The scan sizes at x- and y- directions range from

few nanometers to tens of microns. We employed it to measure the surface roughness of the films deposited by DBD jets.

2.1.2.4 X-Ray Photoelectron Spectroscopy (XPS)

Different from those techniques mentioned above, X-ray photoelectron spectroscopy (XPS) is a technique to detect the surface chemistry (e.g., elemental compositions and oxidation states) of a material [55]. To achieve XPS measurement, ultra-high vacuum (~10^{-9} Torr) systems are required. A focused X-ray beam with energy about 1.5 keV is typically employed as the photon source to irradiate the sample. Due to the photoelectric effect induced by the high-energy X-ray, the photo-emitted electrons escape from the surface of the material (usually at the top 1 to 10 nm). The system contains an electron energy analyzer and an electron detector to measure the kinetic energy of the electrons and count the electrons, respectively. The detected energy of electrons and the number of electrons can then be used to construct an XPS spectrum, which is a plot of electron counts (y-axis) versus the binding energy of the electrons (x-axis). Since every element has its own characteristic binding energy values, we can readily identify the elements present in a sample by those peaks shown in the XPS spectrum. By calculating the areas under the XPS peaks, the atomic concentrations of a measured sample can be also obtained. Additionally, the shape and position of an XPS peak provide information about possible chemical bonds/functional groups on the sample surface. The concentrations of these chemical bonds can be further estimated by deconvolution of the peak in the XPS spectrum.

The XPS used to analyze our films in this study is a Kratos Axis Ultra Imaging X-ray photoelectron spectrometer [56], which is also located at MCF in Texas A&M University. In this system, monochromatic aluminum X-rays with a photon energy of 1486 eV are used as the X-ray source. Figure 10 shows an example of an experimental XPS spectrum (dotted line) ranging between 291.4 and 283.0 eV, in which a C 1s (carbon) peak is present. Note that "1s" represents the corresponding atomic orbital of the carbon atom. Typically if there are only hydrocarbon functional groups (e.g., C–C and C–H) in a sample, only one peak at 285.0 eV will be observed in the C 1s peak. However, in this case the C 1s peak appears to be a broad band covering a relatively wide energy range. Simply speaking, the peak is broadened usually due to the fact that the carbon atoms bond with different elements or functional groups or the number of bonding electrons participating in the chemical bonds is different. For this reason, the broadened peak is actually composed of several peaks at different binding energies. In other words, the broadened peak can be deconvolved into several peaks. In the case shown in Figure 10 five peaks (C1–C5) are required to construct a spectrum which fits the experimental spectrum. These five peaks respectively represent five different functional groups present in the sample, as indicated in the figure. The deconvolution of the XPS peaks in this dissertation was performed by using XPSPEAK 4.1, which is a free XPS peak fitting program and is readily available on-line [57]. XPSPEAK4.1 allows users to create peaks at any binding energies, set their full widths at half maximum (FWHMs), and adjust the peak heights. It also provides a peak optimization function which can generate the minimum sum of squared errors. It should be mentioned that the

FWHM is a very important parameter in peak fitting processes. The FWHM is influenced by several factors, such as the lifetime of the core holes, the electron energy analyzer, and the X-ray source. In this study the FWHMs of all the deconvolved peaks were set to be 1.2 eV since it results in the best fitting results.

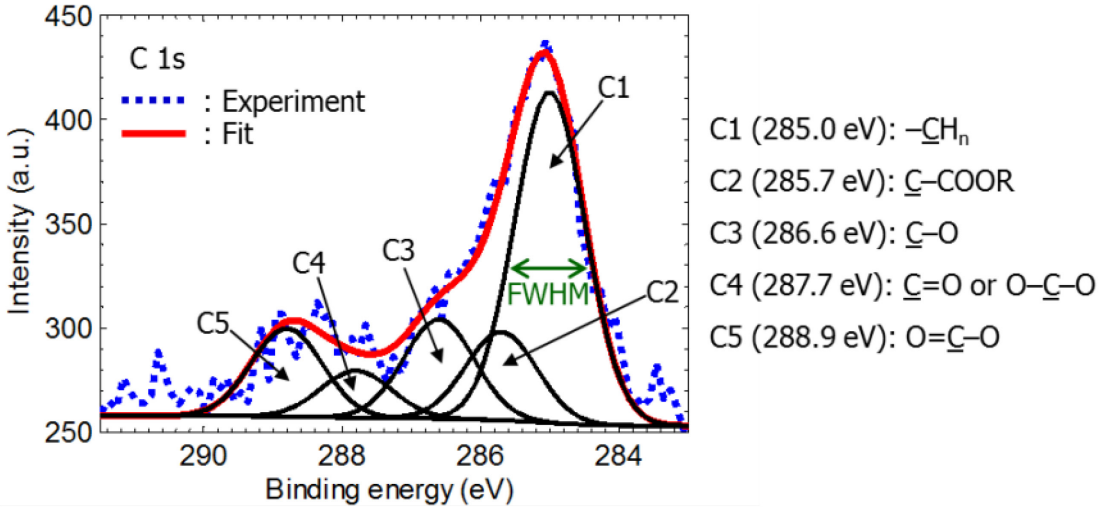

Figure 10. Example of the experimental XPS spectrum (C 1s) and the corresponding fit spectrum consisting of five deconvolved spectra.

2.1.2.5 Fourier Transform Infrared Spectroscopy (FTIR)

The other method to identify and quantify the functional groups in a sample is through Fourier Transform Infrared Spectroscopy (FTIR) [58]. In this technique, a beam of infrared (IR) light enters an interferometer, which creates a new beam (so-called an interferogram) containing all different IR frequencies. And then this interferogram is used to pass through the sample which is analyzed. The sample absorbs some of the IR radiation with specific frequencies. The transmitted light is further collected by an interferogram signal detector. Finally the collected interferogram signal is sent to a

computer and Fourier transformation is performed to convert the interferogram signal into a frequency spectrum, which is a plot of IR intensity (y-axis) versus frequency (x-axis). The specific frequencies of light are absorbed by the specific molecular structures in the sample. In other words, different molecular structures would not result in the same IR spectrum. Thus from the resulting IR spectrum we can know the presence of the specific types of molecular structures in the sample. Additionally, the amplitude of a specific peak can be used to estimate the amount of the corresponding functional group. In this study, a Bruker Optics ALPHA FTIR spectrometer is utilized [59]. This system provides not only the transmission sampling method, but also the attenuated total reflection (ATR) module.

2.1.3 Plasma Diagnostic Techniques

Light emission is one of the most interesting properties in plasma since it contains considerable valuable information about the discharge. The light emission facilitates the observation of the temporal and spatial variations in discharges (plasma dynamics). For example, how an electrical breakdown occurs and how a streamer propagates can be readily observed through the light emission. The color and intensity of the light emitted from the plasma also provide the information about the types and densities of excited species as well as the temperatures in different excitation modes (e.g., electronic excitation, vibrational, and rotational temperature). In this subsection, the diagnostic techniques used in this study for acquisition of the light emission from the plasma are given.

2.1.3.1 High-Speed Intensified Charge-Coupled Device (ICCD) Camera

An intensified charge-coupled device (ICCD) camera is a device which acquires an image in a two-dimensional array of pixels. Each pixel collects the incoming photons and converts the photons into the electrical charges. The number of charges at each pixel is counted and then used to reconstruct the image. In this dissertation, we employed a high-speed ICCD camera (Stanford 4Picos ICCD) [60], in which the minimum exposure time is 200 ps, to acquire plasma images. The high-speed property of this camera enables the fast plasma variations to be temporally and spatially resolved. Note that in helium DBD jet the propagation of the ionization wave, which will be introduced in detail in Section 2.2.2, was observed to be about 10^4–10^5 m/s [61]. And the dimension of the wave front is around 10^{-4}–10^{-3} m. For this reason, a nanosecond-scale exposure time is usually required to capture the propagation. This high shutter speed typically is unable to be achieved by a regular digital camera, in which the shortest exposure time is 1 ms. To obtain the detailed evolution of the DBD jet, the high-speed ICCD is thus required for plasma image acquisition.

2.1.3.2 Photomultiplier Tube (PMT)

A photomultiplier tube (PMT, Hamamatsu R928) serves as the other photon detector in our experiments for plasma diagnostics [62, 63]. The PMT mainly consists of a photocathode, 9 stages of dynodes (placed in-between the photocathode and the anode), and an anode at low pressure conditions (high vacuum). The photocathode, which is made of multialkali (Na-K-Sb-Cs) in this case, collects the incoming light and

produces electrons due to the photoelectric effect. The electrons emitted from the photocathode are then allowed to travel to the first dynode by applied electric field. When the electron arrives at the dynode surface, the secondary electron emission occurs, leading to multiplication of electrons in the system. These electrons are directed toward the second dynode, on which more electrons are produced. These processes repeat from dynode to dynode, which serves as an electron multiplier. Finally, these multiplied electrons are collected at the anode and an electrical current is generated. The output current amplitude can thus be used as an indication of the intensity of the light illuminating the PMT. The PMT used in our study has a rise time of 2.2 ns and a wavelength range between 185 and 900 nm (UV/Vis). It is quite suitable for temporally resolving the light emission sequence during each half voltage cycle in the DBD jet.

2.1.3.3 Optical Emission Spectroscopy (OES)

Optical emission spectroscopy (OES) is an important tool to study the types and densities of the excited species generated from a plasma source. It should be mentioned that light emission (i.e., photon generation) is the consequence of the transition of an electron in an atom/molecule from a higher excited energy state to a lower state. Since each element has its own set of characteristic emission light (photons) with specific wavelengths (or frequencies), we are able to identify the elements present in a plasma source by observing the wavelengths of the emitted light. The OES is a commonly used technique to separate the light into its constituent wavelengths through a diffraction grating and further generate a spectrum, which is plot of light intensity (y-axis) versus

wavelength (x-axis). Thus from the peaks in the OES spectrum not only the types of species in the plasma can be determined from the corresponding wavelengths but also the densities of the species can be estimated from the peak heights. Additionally, the OES spectrum contains information about the electronic structures of an atom or a molecule. Therefore, the temperatures in different excitation modes (e.g., electronic excitation, vibrational, and rotational temperature) can be further estimated by analyzing the emission bands of the spectrum [64, 65]. In this dissertation, a UV/Vis thermoelectric cooled USB spectrometer (Edmund Optics 64813) was employed [66]. It contains a 700 grooves/mm ruled grating and its emission spectrum is in the range of 200–800 nm with a resolution of 1.5 nm.

2.2 Literature Reviews

The first part of this subsection presents prior art on thin film deposition systems developed using various types of non-thermal atmospheric pressure plasma jets (APPJs). These deposition systems are sorted according to their driving frequencies. The working gas, gas temperature, substrate materials and deposited materials are also included. The second part reviews the fundamental physics studies of APPJs in the literature. The physics subsection will particularly focus on those plasma jets operating in the pulsed DC and kHz frequency range, and will cover plasma propagation, operation modes and current pulses. The last part gives the introduction of the recently emerging field – plasma medicine, in which non-thermal plasmas have been shown to have several promising biomedical applications. This part will briefly review why non-thermal

plasmas exhibit sterilization effects and what the possible species are participating in bacterial inactivation.

2.2.1 Thin Film Deposition Using APPJs

Pioneer work on the development of thin film deposition using plasma jets was first made by Koinuma and co-workers in 1992 [23]. They developed a RF (13.56 MHz) capacitively coupled plasma (CCP) non-thermal plasma jet, which was named "microbeam plasma generator", for various applications in material processing (etching, ashing, and deposition), as illustrated in Figure 4(c). Fullerenes (C_{60}), SiO_2, and TiO_2 were successfully deposited in open air on several different substrates, mainly silicon wafer or glass [67-69]. Helium or argon was used as the working gas and the gas temperature (without the addition of precursors) ranges from 255 to 455 ºC. The deposition rate, which depends on gas flow rate, addition of other gases, as well as substrate temperature, is around 10 nm/s for films with high quality. Treating biological tissues has also been mentioned as a potential application using their plasma jet generator [23].

Since the development of "microbeam plasma generator" numerous thin film deposition techniques using RF-driven plasma jets have been proposed through the years. Babayan *et al.* reported an RF (13.56 MHz) helium plasma jet with a water cooling jacket for SiO_2 film deposition on silicon substrates in 1998 [33]. The highest deposition rate it can achieve was 5 nm/s and the plasma gas temperature varies from 100 to 150 ºC (with the cooling system). Modular RF capillary plasma jets at 27 MHz

were used to deposit SiO_x-like films by Weltmann and co-workers [26, 70]. Argon was employed as the working gas and a substrate (bipolar oriented polypropylene) temperature between 35 ºC and 95 ºC during the plasma treatment was measured. A dynamic deposition rate of up to 150 nm/s/cm^2 can be obtained while no detailed static deposition rate was presented. Later the same group employed a similar RF plasma jet with a modified gas delivery configuration, which avoids the film growth inside the tube, to accomplish SiO_x film deposition [27, 71]. Different organosilicon precursors or various operation modes were investigated with or without the addition of oxygen. The best deposition rate recorded using this modified plasma jet was 23 nm/s. Keudell and co-workers achieved deposition of hydrogenated amorphous carbon (a-C:H) and SiO_2 films on silicon substrates using an argon RF (13.56 MHz) microplasma jet [72-75]. The gas temperature of the argon plasma jet with C_2H_2 precursor was shown to be less than 77 ºC regardless of the applied power [76]. The deposition rate of up to 7 nm/s was reported. Deposition of SiO_x films for super-hydrophobic applications using a double-pipe plasma jet driven by 13.56 MHz RF voltage has also been presented [77, 78]. The gas temperature of the double-pipe plasma jet ranges from 40 ºC to 80 ºC when argon (without precursors) was used. No deposition rates were presented in the studies. An argon plasma jet, which was called atmospheric pressure glow discharge torch (APGD-t), was utilized by Leduc *et al.* to deposit patterned polymer film (C:H) on Pyrex Petri dishes for cell culture applications [79]. A gas temperature of about 112 ºC was measured while no deposition rates were reported.

Other than RF plasma jets, several plasma jet sources driven by other frequency ranges (e.g., ultra-high frequency 450 MHz, AC sinusoidal kHz, and pulsed DC) have also been developed. Shimizu *et al.* employed a ultra-high frequency (UHF) inductively coupled plasma (ICP) microplasma jet to grow spherical carbon on metallic substrates [80]. The growth rate was about 33 nm/s but the deposition temperature was not measured. A similar UHF ICP plasma source was used to achieve high rate (up to 1 μm/s) deposition of ZnO films by Stauss and co-workers [81]. The gas temperature was estimated to be 1800 K though the high deposition rate can be achieved. Several plasma jets based on DBD configurations driven by either AC sinusoidal kHz or pulsed DC have also been proposed for thin film deposition. An earlier version of the DBD jet used was reported by Nutsch *et al.* in 1999 [82]. Polymeric films using C_2H_2 precursor gas with a deposition rate of about 3 nm/s was obtained but no detailed results regarding the film compositions and deposition temperature were presented. SiO_2-like or SiO_2 thin films can also be deposited using DBD jets with various electrode configurations [83, 84]. Chen *et al.* utilized a 26 kHz AC-driven argon DBD jet to achieve high-quality SiO_2-like film deposition with the substrate temperature rising up to 130 ºC (deposition rate was not available) [83]. Ito and co-workers tested a coaxial type and two crossed type helium DBD jets for SiO_2 deposition using a bipolar impulse power supply [84]. It was found that using the crossed DBD jet leads to the highest deposition rate (up to 280 nm/s) though no deposition temperature was given. Liu *et al.* showed that the helium DBD jet fed with C_2H_2 can also be used to grow diamond-like carbon (DLC) films with

a deposition rate of 1.21 nm/s and the substrate temperature was heated up to about 72 ºC [85].

In addition to the atmospheric pressure RF-CCP, UHF-ICP, and DBD plasma jets mentioned above, DC hollow cathode microjets, an argon plasma torch, a cold oxygen arc, and an arc-like air plasma jet, have been employed as depositing tools in recent years [86-89]. Hollow cathode plasma microjets were adopted for diamond deposition by Sankaran and Giapis [86]. H_2/CH_4 mixture (no helium or argon was required) was fed to the microjets to achieve deposition with the Mo substrates heated up to 800 ºC. The deposition needed to be performed at subatmospheric pressure (100~500 Torr) though noble working gas was not used. The deposition rate and gas temperature were not presented in this study. The 68 kHz AC-driven argon plasma torch, which had no direct dielectric barrier between the plasma and the powered electrode, was used to conduct poly(methyl methacrylate) (PMMA) film deposition on silicon wafer in a chamber instead of open air [87]. No deposition rate and gas temperature were recorded though the film composition analysis showed that the resulting PMMA films exhibit similar chemical compositions to those in the conventional PMMA. Han *et al.* developed a cold arc plasma jet using oxygen as the working gas to achieve SiO_2 film deposition on the silicon substrate [88]. The deposition rate of 1–5 nm/s was measured but heating the substrate up to 150 ºC was required. Besides, no gas temperature measurement was presented though the plasma source was called “a cold arc plasma jet”. An arc-like plasma jet was reported by Lommatzsch and Ihde for the use of deposition of a plasma polymerized HMDSO film at a very high deposition rate (750 nm/s) [89]. The jet was

operated using dry air with a kHz operation frequency. Although no gas temperature measurement was performed, it was mentioned that the plasma temperature may be higher than most other plasma sources so that the very high deposition rate can be achieved.

It can be seen that most of these studies focused on inorganic film (SiO_2, SiO_x, TiO_2, or diamond) deposition with high power density source (e.g., UHF-ICP, RF-CCP and arc plasma jets) [26, 27, 33, 67-71, 74, 75, 77, 78, 80, 81, 88]. Typically these plasma sources have relatively high plasma density and/or electron temperature [30, 90]. Only a few of these studies used the plasma jets for polymerlike (high temperature C:H film) or polymer film deposition [72, 79, 82, 87] and none of them performed metal film deposition. Besides, there are no reports on the use of the floating-electrode DBD jet for film deposition. All these plasma sources mentioned above except for the DC hollow cathode microjets [86] were indirect (afterglow) plasma methods, which consists of two electrodes and one substrate placed downstream. Only a few of these studies presented the substrate temperature measurement during deposition (plasma gas temperature may be increased while the precursor was fed with the plasma working gas) [83, 85]. There are several gaps in the literature as to substrate temperature and precursor used. Therefore, many studies are required for the development of the thin film deposition technique using the floating-electrode DBD jet.

2.2.2 Fundamental Studies of Plasma Jets

As mentioned earlier, the DBD jet used in this study is driven by 28.5 kHz AC sinusoidal high voltage. Thus here we mainly focus on the review of those non-thermal APPJs operate using kHz AC voltage and pulsed DC with kHz repetition rates. Typically higher driven frequencies (e.g., RF) lead to a continuous plasma flow in the plasma jet [90-92]. However, as observed by Engemann and co-workers the plasma jet excited at several tens of kHz frequency in an indirect-type DBD jet is not a continuous discharge column, but rather a train of ionization waves, or so-called plasma bullets (Figure 11) [61]. Also, the plasma bullet has a donut-shaped structure. The plasma bullet was found to propagate at a velocity of ~10^4 m/s, which is much higher than the gas velocity (several tens of m/s).

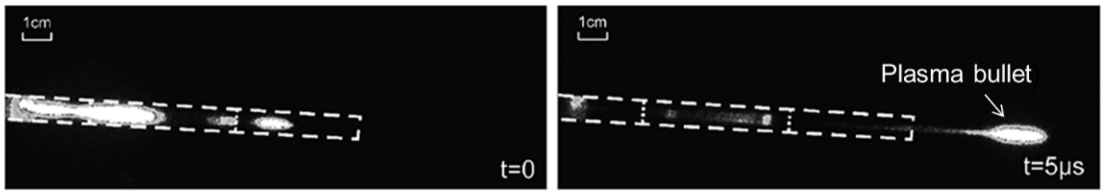

Figure 11. High-speed photographs of the propagation of a plasma bullet [61] (© 2005, IEEE).

Several reports regarding the characterization of the APPJs with various electrode configurations, jet dimensions, and driving frequencies have been presented [24, 25, 29-31, 61, 90-111]. Most of these studies employed helium as the operating gas. The propagation dynamics of the ionization waves, excited species and plasma temperature in the APPJs were frequently studied. The study of the ionization waves,

such as their speed, formation, and structure, especially attracted wide attention. To investigate the plasma propagation behavior a high-speed intensified charge coupled device (ICCD) camera was usually utilized to capture the temporal and spatial evolutions of the APPJs. The excited species and plasma temperature in the plasma can be obtained using optical emission spectroscopy (OES). Typically the gas temperature was measured to be around room temperature, and the most common species observed from OES include OH, N_2, N_2^+, O, and He if helium was employed.

After Engemann's research group revealed the interesting observation on the plasma bullet propagation, the characterization of various types of indirect (afterglow) plasma jets was performed successively. Laroussi and co-workers also observed the propagation of the ionization wave in their "plasma pencil", as given in Figure 4(a) in the previous subsection [24, 102, 107]. The propagation mechanism was explained by a photoionization model. They reported a higher speed (~10^5 m/s) of the bullet propagation compared to that observed by Engemann *et al.* The velocity profile along the propagation path was presented. Different applied voltage and flow rate were employed for the study. In addition to the use of ICCD for the estimation of wave propagation speed, time-resolved OES was also used. The DBD jets with similar electrode configurations (two tubular electrodes) to that presented by Engemann's group were also investigated and the speed of the ionization wave in the range of 10^4 m/s was measured by using ICCD and laser spectroscopic technology [105, 112]. Similar propagation speed (~10^4 m/s) was observed in an APPJ with a needle-cylinder electrode configuration [92].

Beside, APPJs using the direct plasma method were widely studied by various research groups. The DBD jet with a single tubular electrode as given in Figure 4(b) was characterized by Kong and co-workers [25, 91, 97, 108]. It should be noted that the DBD jet used in Kong's studies is similar to the plasma source used in our study but consists of a smaller dielectric tube. It was observed that the plasma pullet travels at a speed ranging from 7×10^4 to 43×10^4 m/s [97]. In addition, the change of the operation mode was reported in this type of APPJs with an increasing applied power [108]. The other direct plasma method, which consists of a single copper wire electrode, was developed by Lu *et al.* and its wave propagation speed was estimated to be in the range of 10^4 –10^5 m/s [31, 96, 101, 109]. The research group showed that the ionization wave can induce a new ionization wave in a tube placed downstream of the plasma jet [101]. Various methods besides ICCD were also employed to measure the speed of the plasma bullet [109]. Shashurin *et al.* [104] and Kim *et al.* [30] characterized a cold plasma jet using a pair of powered electrodes and a plasma jet with a sharpened pin electrode covered with a cone-shaped Teflon tube, respectively. Their ionization waves both propagate at a speed of ~10^4 m/s. It should be mentioned that except for Kong *et al.* and Shashurin *et al.* other research groups conducted the investigation while the substrate (ground electrode) was absent. Thus, from the above results one can conclude that typically the plasma bullet moves at a speed in a range of 10^4–10^5 m/s.

When the APPJs are used for practical applications, such as material processing and medical treatment, a substrate is required to be placed downstream the jets. Taking the treated substrate into consideration is important owing to the fact that electrical field

is stronger than that in the case without the substrate [112]. The presence of a treated substrate also leads to a change in the peak densities of excited species and in the density and ionization mechanism of entrained air molecules near the substrate. However, only few studies using helium DBD jets have included the presence of a substrate, and all of them showed only one discharge current pulse at each half cycle of applied voltage (only one ionization wave propagation per positive half cycle) [25, 95, 97, 98, 108, 110, 112]. In these papers, Walsh *et al.* observed three different operation modes with rising power in their helium DBD jet, but there is always one current pulse in each half cycle when a larger voltage is introduced [108]. Although the self-organized discharge patterns, reported by Nie *et al.* and Feng *et al.*, showed mode changes and similar "concentrated" discharges (multiple plasma channels) in the plasma, only one current pulse was seen per half cycle [95, 110]. There were no reports showing the phenomenon of multiple current pulses in the helium DBD jets.

Similar observation of multiple current pulses has been published when a helium DBD reactor with parallel-plate electrodes was used. Mangolini *et al.* observed that several current pulses per half cycle occur due to the generation of the consecutive glow discharges with different spatial structures [113]. The presence of multiple pulses was explained as the occurrence of the Townsend discharge by Golubovskii *et al.* in their homogeneous helium DBD model [114]. Studies by Radu *et al.* indicated that the multiple current pulses correspond to several successive uniform glow discharges (pseudoglow discharges) generated between the electrodes at each half cycle [17-19]. The number of current pulses per half cycle was found to depend on the applied power,

operation frequency, and the concentration of impurity gas admixtures (e.g., argon, nitrogen, hydrogen or oxygen). Parallel-plate helium DBD fed with a small amount of methane precursor for studying methane decomposition processes was also a case showing multiple current pulses in the discharge current trace [115]. The discharge during film deposition in a helium-ethylene-fed parallel-plate DBD reactor also showed more than one current pulses per half cycle when a higher voltage was applied [116]. Nevertheless, the multiple current pulses in the helium DBD jets observed in this study may be induced by other mechanisms since the different electrode configuration is used and the different breakdown mechanisms (i.e., ionization wave) have been proposed. Thus further characterization needs to be done for better understanding the physics behind the phenomena of the mode change and the multiple current pulses in the plasma jets used in this study.

The relevance of the discharge physics to the thin film deposition processers include the facts that 1) radicals involved in the deposition processes are generated during each ionization wave and 2) energy transfer from the ionization waves to the substrate determine the surface temperature of the substrate. Typically more energy input and higher precursor concentration can lead to higher deposition rate and more active species generation, but can also induce significant substrate heating. Thus the investigation of the discharge physics is important for optimizing the deposition rate and the active species generation without excessive temperature on substrate.

2.2.3 Plasma Medicine

In the past, "heat" generated from atmospheric-pressure thermal plasmas was mainly employed in medicine. A technique called argon plasma coagulation (APC) is one such example [117]. APC, which is a non-contact electrosurgical technique, utilizes the plasma thermal effect to achieve tissue removal and blood staunching. However, the extremely high temperature from thermal plasma may cause tissue damage and desiccation [32]. Recently plasma medicine became an emerging field since the use of atmospheric-pressure non-thermal plasmas in medical research have shown several interesting and promising results. These applications include sterilization [11, 13, 20, 28], genetic transfection [118, 119], protein destruction [120], cell inactivation [121], cell detachment [122-124], cell apoptosis [125-127], and wound healing [13, 32, 128]. In addition, one of the most important properties of the non-thermal plasma treatment is its selectivity. Non-thermal plasma is able to inactivate bacteria in a few seconds, while causes little damage on the surrounding tissue (e.g., skin) by adjusting the plasma doses [13, 129].

Using non-thermal plasmas to inactivate bacteria especially attracts significant attention as the plasma method has potential to replace those traditional sterilization methods, including thermal treatment, chemical solutions (e.g., H_2O_2), or radiation (e.g., X-ray and γ-ray) [130]. Compared to most of the traditional methods, non-thermal plasmas offer a relatively safe and efficient method to inactivate bacteria. Potential agents produced by plasma to cause sterilization include heat, UV radiation, charged species, and chemically reactive species. The gas temperature of the non-thermal plasma

is typically controlled to be around room temperature. Thus the heat effect is not a key factor on the bacteria inactivation. UV radiation may cause lethal damage on bacteria if its wavelength is in the range from 200 to 300 nm with doses of several mJ/cm^2 [20]. However, non-thermal plasmas at intermediate powers usually emit no significant UV radiation in this range. Charged species have been shown to significantly improve the bacterial inactivation efficiency using a direct plasma method (floating-electrode air DBD) instead of an afterglow (indirect plasma) method [11, 129]. It has been reported that not all charged species participate in the inactivation process, but O_2^- appears to play an important role [130]. Atmospheric pressure non-thermal plasma sources, which operate in open air conditions, usually generate abundant chemically reactive species due to the presence of oxygen, nitrogen, and water. These species can be divided into two groups: reactive oxygen species (ROS) and reactive nitrogen species (RNS) [130, 131]. The ROS typically include O, $^1O_2$, O_3, and OH. In RNS, NO and NO_2 are common reactive species produced by the plasmas. Most of these species are strong oxidizing agents. It has been shown that ROS and RNS play key roles in the sterilization effect [20, 130, 131]. Additionally, it was suggested that the reactive species are involved in cancer, wound healing, and cardiovascular therapies. They are also known to participate in many significant oxidation-reduction (redox) reactions in biology, further inducing numerous important biological processes, such as signaling and metabolism in cells and immune mechanisms in animals and plants [131]. The presence of the water and the amount of it in the treated objects also influence the sterilization efficacy [129]. More

detailed information about plasma medicine can be found in several recent reviews [13, 20, 132, 133].

APPJs are widely employed as the atmospheric pressure non-thermal plasma sources for biomedical applications due to their abilities in providing 3-D and local treatment of temperature-sensitive substrates. In addition to bacterial inactivation [134-136], several different types of APPJs have been used to achieve spore inactivation [137, 138], fungus inactivation [139], protein destruction [120], cell detachment [121], cancer cell apoptosis [127, 140], cell migration rate reduction [121, 141], plasmid DNA damage [142], and wound healing [143]. To improve the therapeutic efficacy, most of the studies used noble gas (helium or argon) fed with a small amount of oxygen, instead of just pure noble gas, as the working gas to produce more reactive oxygen species [120, 127, 134, 138, 139, 141, 142]. The addition of H_2O_2 vapor to the APPJ has also been demonstrated to not only increase the bacterial inactivation rate but also reduce the formation of toxic ozone [136]. Due to the low-temperature property and so many cases in biomedical applications using the APPJs, we may open up more promising applications, as mentioned in Section 1, if the APPJs can be modified to achieve PECVD on biological or living substrates. However, no studies have shown to provide medical treatments by adding organic precursors to the APPJs to synthesize materials on top of biological or living substrates.

3. AP-PECVD DEVELOPMENT USING DBD JET

3.1 Introduction to AP-PECVD Development Using DBD Jet

In this section, the development of AP-PECVD systems using the floating-electrode helium DBD jet is presented. The AP-PECVD system was implemented in a chamber initially and then was modified to operate in ambient air. The commonly-used microscope slide and silicon wafer were used as the substrates in the deposition. In addition, different types of precursors, as listed in Table 1, were used to grow various polymeric films and metallic films. Several selected images of the as-deposited films obtained by these systems are given in this section to show that the helium DBD jet is an ideal candidate for open-air thin film deposition. Detailed characterization of the as-deposited films and plasma will be given in the following sections.

3.2 Preliminary Experimental Setup with a Chamber

Before the development of an AP-PECVD system which is able to operate in ambient air, a chamber was utilized in the preliminary experimental setup due to the concern about combustion of the precursors during the plasma chemical reactions in thin film deposition (many precursors have low flash points). Section 3.2.1 illustrates the AP-PECVD experimental setup with the presence of a chamber and presents some images of the as-deposited films using this system. Section 3.2.2 shows the attempt we made to achieve nanoparticle and carbon nanotube (CNT) synthesis using a similar DBD system with slight configuration modifications.

Table 1. Precursors used for thin film deposition in this study.

Precursor Name	Form	Chemical Formula	Chemical Structure	Expected Deposited Film	Supplier
Methyl methacrylate (abbrev: MMA)	Liquid	$CH_2=C(CH_3)COOCH_3$	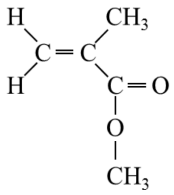	Poly(methyl methacrylate) (abbrev: PMMA)	Sigma-Aldrich
Ethylene	Gas	$H_2C=CH_2$	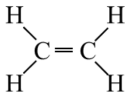	Polyethylene or hydrocarbon film	Acetylene Oxygen Co (AOC)
Copper(II) acetylacetonate (abbrev: Cu(acac)2)	Solid	$Cu(C_5H_7O_2)_2$	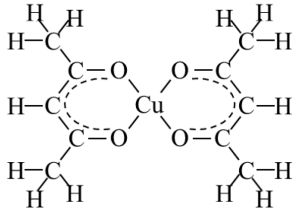	Copper	Sigma-Aldrich
Ferrocene	Solid	$Fe(C_5H_5)_2$	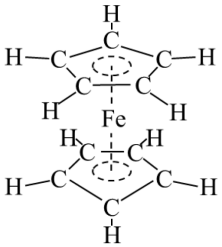	Iron	Sigma-Aldrich

3.2.1 Polymer Film Deposition

Figure 12(a) schematically shows the experimental setup when a chamber was used. It consists of a gas feed system used to deliver helium and precursor gas and a stainless steel reaction chamber which allows the mixture of helium and gaseous precursor to flow into a floating-electrode DBD jet via a borosilicate glass tube. Industrial grade helium (He, Acetylene Oxygen Co, 99.995 %) was employed as the working gas for plasma generation and its flow rate was controlled by an electronic mass flow controller in the range of 2–3 slm (standard liters per minute). The MMA monomer (Sigma-Aldrich, 99%, with stabilizer), which was used as the organic precursor in this system, was vaporized by feeding helium through a glass bubbler containing the liquid monomer at room temperature. The helium carrier flow fed to the bubbler was also controlled by a mass flow controller, and the flow rate in the range of 0.05–0.2 slm was adopted to adjust the concentration of MMA in the feed gas. Theoretically, the actual flow rate of MMA can be calculated by

$$Q_{precursor} = Q_{carrier\_gas} \times \frac{P_{precursor}}{P_{system} + P_{precursor}} \quad \textbf{(Equation 1)}$$

where $Q_{precursor}$ and $Q_{carrier\_gas}$ are the flow rates of the precursor and carrier gas, respectively. $P_{precursor}$ and P_{system} are the precursor vapor pressure and the system pressure (i.e., bubbler pressure in this case), respectively. However, the actual precursor vapor pressure is difficult to determine as it depends on the temperature and the freshness of the precursor though its value provided by the supplier is 29 Torr at 20 ºC. To be more accurate, we measured the consumed quantity of the liquid MMA after 30-min operation

for the calculation of the precursor flow rate. The estimated flow rate of the MMA precursor is thus in the range of 0.002–0.011 slm.

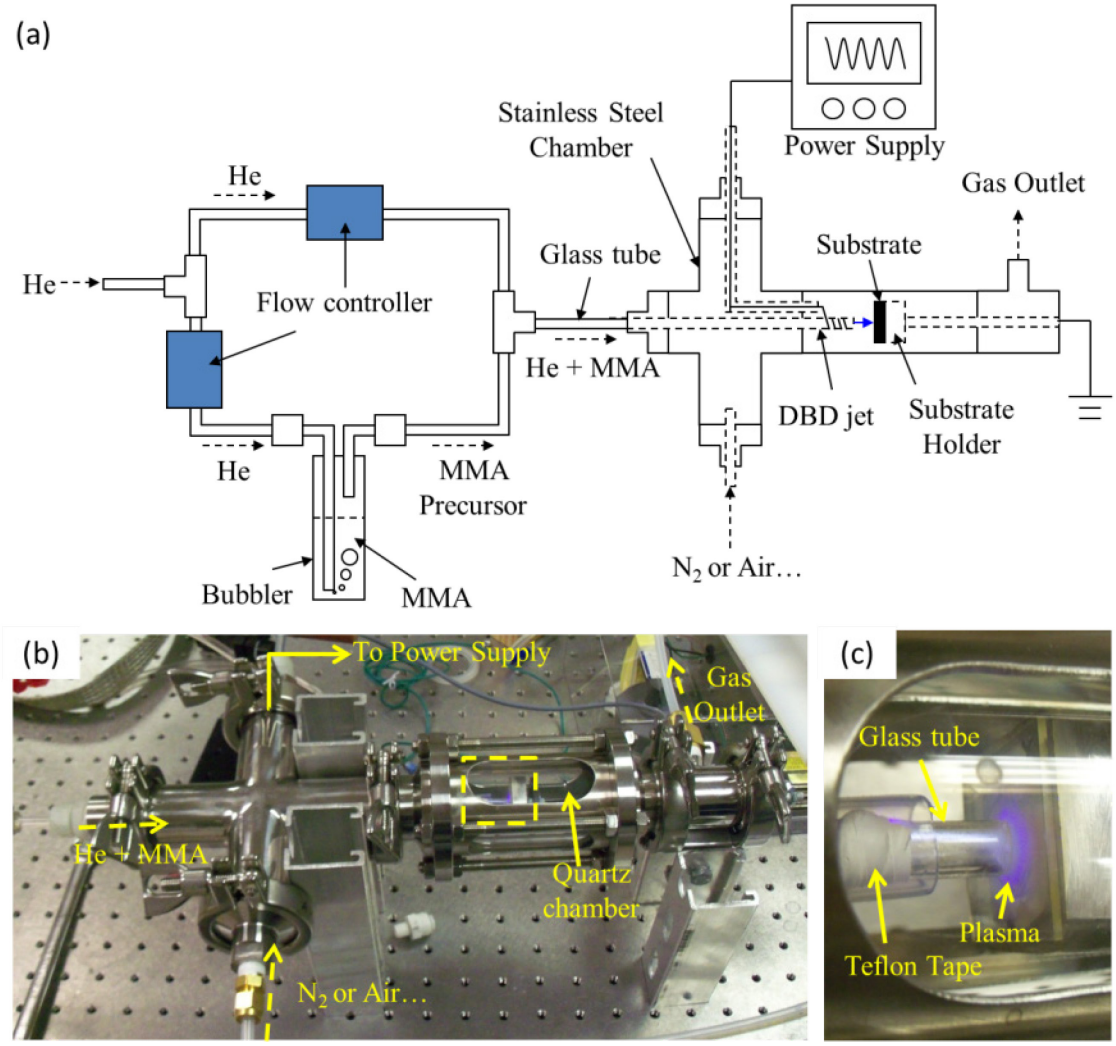

Figure 12. (a) Schematic diagram of the AP-PECVD system constructed using the DBD jet in a chamber; (b) photograph of the actual experimental setup; (c) image of the DBD jet during operation.

The stainless steel reaction chamber contains several feedthroughs for electrical connection and gas transport. The DBD jet was driven by an AC high voltage power

supply (driving frequency: 20–50 kHz) through a wire wrapped around the glass tube. The glass tube is 304.8 mm (12”) in length, 6.35 mm (0.25”) in the outer diameter, and 4 mm (0.16”) in the inner diameter. Nitrogen (N_2, Acetylene Oxygen Co, 99.995 %) or air was fed into the chamber to create a background gas for deposition. Initially nitrogen was used as the background gas. In using air, which contains oxygen, the additional concern is combustion and oxidation of the precursor which may affect the conditions of both the deposition and plasma. The substrate used for PMMA film growth was attached to an electrically-grounded substrate holder and was placed directly downstream of the DBD jet. The distance between the tube end and the substrate surface was set to be around 3 mm. The reaction chamber also contains a transparent quartz cylinder which allows for the visual observation of the plasma, as shown in the actual system photograph in Figure 12(b). Figure 12(c), which is a magnified picture of the dashed box in Figure 12(b), shows the plasma image during operation. The substrate used for thin film deposition was a piece of the microscope slide with a thickness of 1 mm in this case. Teflon tape was employed to cover around the powered wire to serve as an insulation layer.

It should be mentioned that the bubbler-based precursor supply system presented in Figure 12 is just an example when a liquid precursor is used. The precursor delivery method depends on the type of the precursor (i.e., solid, liquid, or gas) utilized in the deposition. For example, in using solid precursor the way to supply precursor is changed wherein the vapor enters the flow through sublimation (typically sublimation is achieved by heating). However, many of these techniques are similar to those used in LP-PECVD.

It was demonstrated that our preliminary DBD-jet-based AP-PECVD system with a chamber successfully deposited PMMA films on the glass substrates. Using air as the background gas showed similar results (i.e., deposited films and plasma appearance) to those using nitrogen. No combustion of the precursor was observed when the air background gas was present around the plasma. The deposited PMMA films with two different types of appearance were observed when a different power was applied, as shown in Figure 13. Figure 13(a) shows a transparent circle-shaped PMMA film obtained using 2 slm helium working gas and 0.1 slm carrier flow with 40-min deposition time. This plasma-polymerized PMMA film appears similar to a common PMMA, which is naturally transparent and colorless. When a relatively high applied voltage was used for deposition, a white opaque film was obtained after 40-min deposition, as displayed in Figure 13(b). The flow rate of the helium working gas was 3 slm, and that of the carrier gas was 0.1 slm. No further measurement of the discharge powers and the film properties was performed as this preliminary system was used to demonstrate the feasibility of employing the DBD jet as our depositing tool. Section 3.3 will show that these two types of PMMA films can be also deposited with no chamber in ambient air. Detailed characterization of the as-deposited films, including the surface morphology and the chemical composition, will be presented in the following section. The experimental results observed using this preliminary system suggest that the helium DBD jet with the addition of precursors is still capable of operating in ambient air and serving as a depositing tool without the use of a chamber.

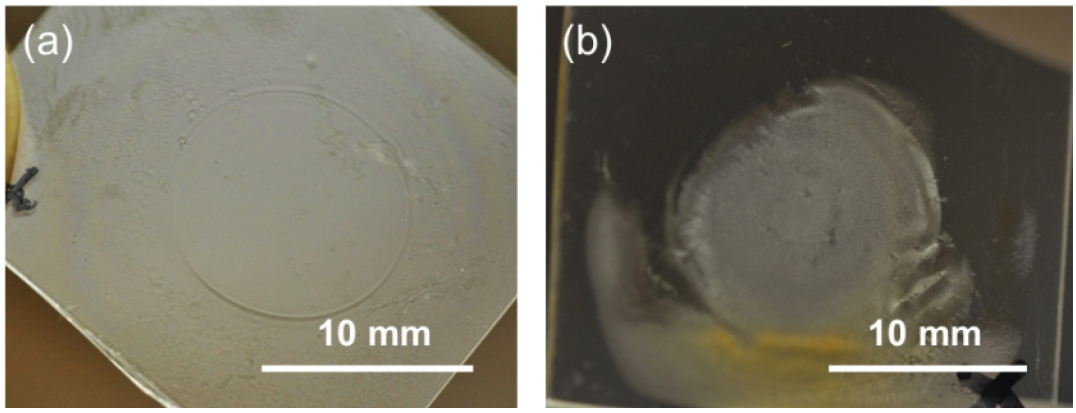

Figure 13. As-deposited (a) transparent and (b) opaque PMMA films obtained by the preliminary AP-PECVD system with the chamber presence.

3.2.2 Nanoparticle and Carbon Nanotube Synthesis

Nanoparticles and carbon nanotubes (CNTs) can be also synthesized when the system in Figure 12 is slightly modified, as illustrated in Figure 14(a). In this experimental setup, only one flow controller at a flow rate of 3 slm was employed to supply the helium working as well as the precursor gas when the precursor used is in the solid form. Typically solid precursors have much lower vapor pressure than the liquid precursors, and they thus require a higher carrier gas flow rate to achieve the same precursor flow rate, as shown in the relationship in Equation 1. In this case, ferrocene [$Fe(C_5H_5)_2$, Sigma-Aldrich, 98 %], which is an organometallic compound in the form of a yellowish powder, was employed as the source material for nanoparticle and CNT synthesis. It has been shown that the iron (Fe) and the carbon (C) atoms in the ferrocene can serve as the catalyst and the carbon source, respectively, for the growth of single-walled CNTs (SWCNTs) [144]. The vapor pressure of ferrocene is about 7.5×10^{-3} Torr at room temperature, which is volatile enough to sufficiently supply vapor phase

ferrocene without the use of any heat source. The ferrocene was placed in a precursor container, in which glass wool (fiberglass insulation) was utilized as a filter to ensure that only the sublimated ferrocene vapor flows out of the precursor container along with the helium stream, as shown in Figure 14(b). Instead of the jet-type DBD directly reaching the treated substrate the DBD plasma in this case was created upstream and was spatially confined by two additional tubular metallic electrodes which fit tightly around the glass tube and were electrically grounded. The distance between the powered electrode and the grounded electrode can be adjusted to change the plasma coverage area in the glass tube, further controlling the plasma-precursor reaction time. When the gas-phase ferrocene passes through the plasma region, the plasma breaks the bonds of the precursor and leads to molecular dissociation, further generating abundant species (atoms, molecules) which are reactive, unstable and tend to react with each other or surrounding surfaces. These species and reaction products then leave the plasma region and flow into a transparent quartz chamber along the glass tube. In the quartz chamber a substrate was placed downstream of the tube to collect the synthesized nanoparticles and CNTs, which likely form in the helium stream and/or on the substrate surface.

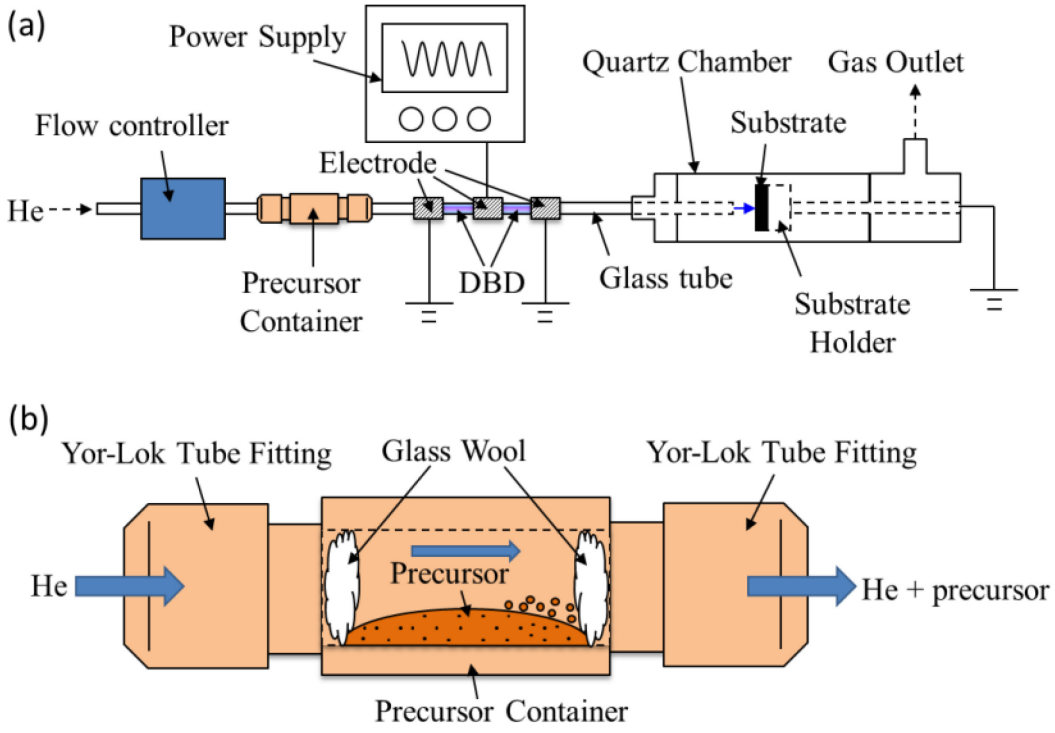

Figure 14. (a) Schematic configuration of the experimental setup for nanoparticle synthesis and (b) cross-section of the precursor container in which glass wool serves as the filter when a solid, powdered precursor is used.

Figure 15 shows the deposition results on a silicon substrate. Two concentric circle patterns with radii of 2 and 5 mm, respectively, were observed, as displayed in Figure 15(a). For visualization of the film surface morphology, scanning electron microscopy (SEM, JEOL JSM-7500F) was employed to acquire the detailed surface images at the film center and the edge, as indicated in Figure 15(a). It was observed in Figure 15(b) that the film center exhibits many web-like clusters. The magnified SEM image of one of the clusters can be seen in Figure 15(c) and it shows the cluster consists of abundant filamentary structures, which are similar to the results presented by [144]. This may imply that these web-like clusters observed here are CNT films. Nanoparticles

(likely iron or iron oxide) were also found at the edge of the film [Figure 15(d)]. However, only the preliminary results are given here in order to show the potential for CNT and nanoparticle synthesis using the helium DBD-based material processing system. Further studies are required to identify the composition and crystallinity of the CNTs and nanoparticles.

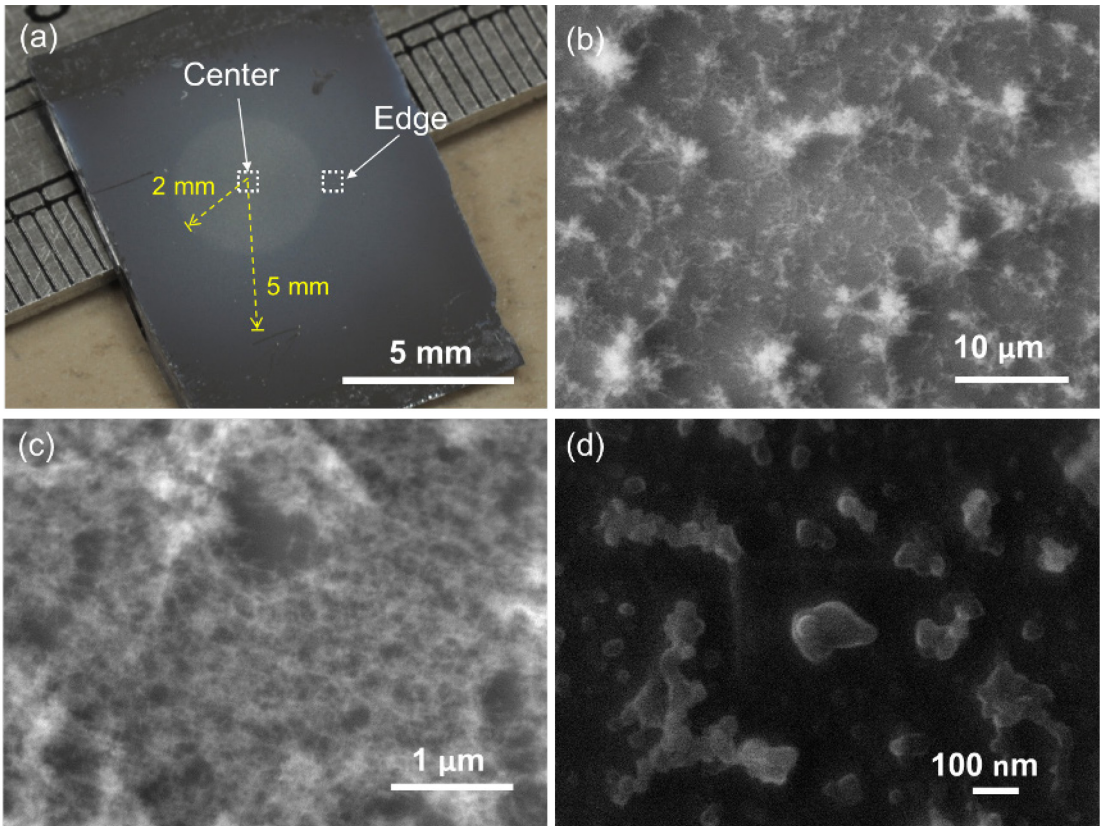

Figure 15. (a) Image of as-deposited nanoparticle and CNT results on the silicon substrate; SEM images of (b) web-like films acquired at the film center with low magnification, (c) filamentary structures at the film center with relatively high magnification, and (d) nanoparticles at the film edge.

3.3 Experimental Setup in Ambient Air

The results presented in prior subsections showed that thin film deposition can be achieved using the helium DBD jet without the adoption of a chamber. In this subsection the deposition system is thus modified to operate in ambient air to meet the requirements of our goal in this study – PECVD on living substrates. As mentioned earlier, we mainly focus on the development of polymer film deposition and metal film deposition in this study. Poly(methyl methacrylate) (PMMA) films and copper films, fabricated using the precursors methyl methacrylate (MMA) and copper(II) acetylacetonate [$Cu(acac)_2$, as listed in Table 1], respectively, are especially the objects of our research in this dissertation though some preliminary attempts were also made to use ethylene as the monomer for polyethylene (PE) or hydrocarbon film deposition. Note that we call the plasma polymerized films fabricated using MMA as PMMA films since they have been demonstrated to have similar characteristics to those in pure PMMA (shown in Section 4). However, we use "PE or hydrocarbon films" here to present the films obtained by ethylene as no further measurement of their chemical compositions was performed. A rather extensive experimental study of the as-deposited PMMA films and copper films will be presented in the later sections.

3.3.1 Polymer Film Deposition in Ambient Air

Figure 16(a) schematically shows the experimental apparatus of the PMMA film deposition system in ambient air. Instead of the use of a chamber in Figure 12, this system simply consists of a gas feed system and an atmospheric pressure floating-

electrode DBD jet. Similarly, the working gas helium flow rate was controlled in the range of 2–3 slm. The flow rate of the helium carrier gas, fed to the bubbler filled with MMA liquid monomers, was in the range of 0.05–0.2 slm. In this case, the total helium flow rate, which is the combination of the working gas flow rate and the carrier gas flow rate, was maintained at 3 slm. The concentration of MMA in the mixture was thus in the range of 800–3600 ppm, which was obtained by measuring the consumed quantity of the liquid MMA after 30-min operation. The mixture of helium and MMA was then allowed to flow into the floating-electrode DBD jet.

The floating-electrode atmospheric DBD jet employs a borosilicate glass tube with 120 mm in length, 6.35 mm in the outer diameter and 4 mm in the inner diameter. A cross-sectional schematic diagram of the floating-electrode DBD jet is illustrated in Figure 16(b). A 30 mm long metallic tube, which was used as the high-voltage (HV) powered electrode, fit tightly around the glass tube with the downstream end at a distance of 15 mm from the tube end. The powered electrode was connected to the AC high voltage power supply with a fixed frequency of 28.5 kHz and sinusoidal waveform for discharge generation. An aluminum substrate holder was employed as the second electrode (grounded or at a floating potential when a resistor was present for discharge current measurement) and placed downstream of the nozzle. The substrate used for thin film growth was placed on top of the holder, and the gap between the substrate and the tube end was set to 10 mm. When the discharge was ignited, it extended downstream from the powered electrode to the substrate surface. In addition, a thermocouple probe

was buried in the substrate holder and positioned directly underneath the substrate which was treated by the DBD jet to measure the deposition temperature.

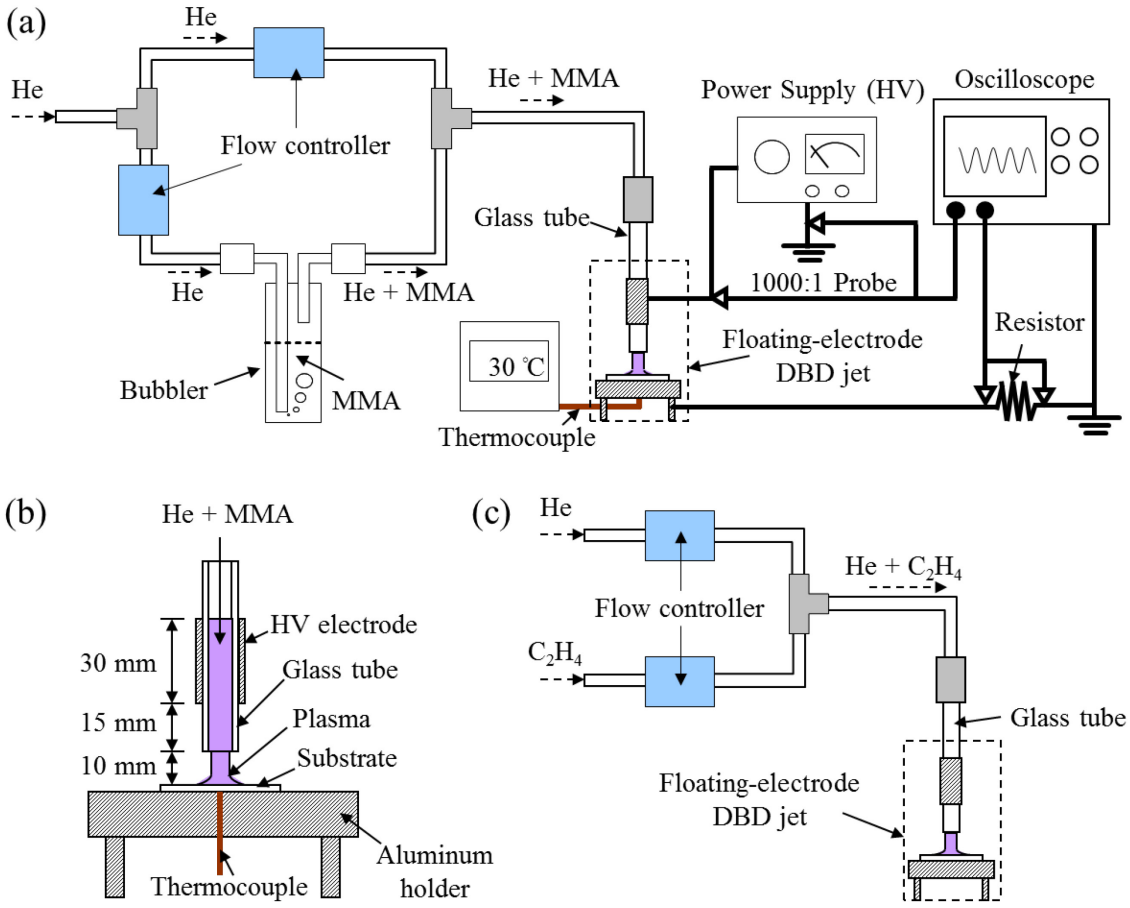

Figure 16. (a) Schematic diagram of DBD jet setup used for PMMA film deposition in ambient air; (b) cross-sectional view and specifications of the floating-electrode DBD jet; (c) schematic setup for PE film deposition.

For the measurement of the electrical characteristics (e.g., voltage, current and power) of the generated DBD jet, a LeCroy 1000:1 100 MHz high voltage probe was connected to the powered electrode to allow observation of waveform for the applied

voltage, as shown in Figure 16(a). To measure the discharge current, the substrate holder was electrically isolated from ground and an 816 ohm resistor (shunt) was placed between the metallic substrate holder and ground. The discharge current was obtained by dividing the voltage drop across the resistor by the resistance, and had a measured bandwidth greater than 500 MHz. Both signals of applied voltage and discharge current were monitored and recorded by a LeCroy 204MXi (2 GHz) oscilloscope. The instantaneous discharge power was obtained by multiplying the instantaneous applied voltage with the instantaneous discharge current. Furthermore, the average dissipated power of the DBD jet was calculated online by taking the average of the instantaneous discharge powers over several hundred voltage cycles.

To achieve polyethylene (PE) or hydrocarbon film deposition, the deposition system can be simply constructed as shown in Figure 16(c) since the ethylene (C_2H_4, Acetylene Oxygen Co, 99.995 %) is a gaseous precursor which can be fed into the DBD jet system directly. Similar to the case in PMMA film deposition, the flow rate of helium was set to be 3 slm, whereas the ethylene flow rate was in the range of 0.005–0.01 slm. A gap distance of around 3 mm between the tube end the substrate surface was utilized in this case.

Figure 17(a) shows a photograph of the DBD-jet-based AP-PECVD system operating in ambient air. A microscope slide with a thickness of 1 mm was employed for thin film deposition. After 30-min PMMA deposition using the He/MMA DBD jet, both the transparent film and opaque film, which are similar to the films shown in Figure 13 with the use of a chamber, were observed, as displayed in Figure 17(b) and Figure 17(c),

respectively. Again, the opaque film deposition occurred by using a relatively high power. The opaque film obtained here is smaller than that in Figure 13(b) as a gap distance of 10 mm was used in this case instead of a 3-mm gap. A detailed study of the relationship between the PMMA film morphology and the applied discharge power, the microstructures and the formation of the opaque film, and the PMMA film composition will be reported in the next section.

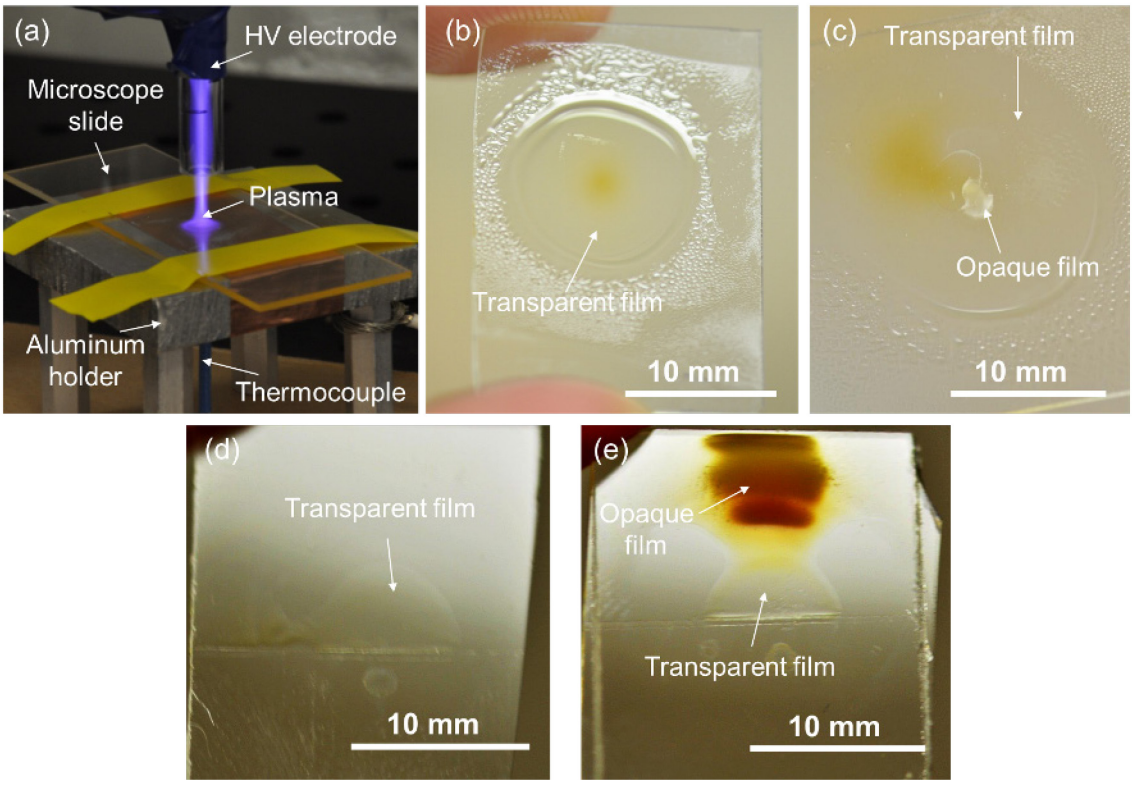

Figure 17. (a) Photograph of the DBD jet used as the AP-PECVD system in ambient air; (b) as-deposited transparent PMMA film; (c) opaque PMMA film growth at the center of the transparent film when a relatively high discharge power was applied; (d) as-deposited film with a transparent appearance by the He/C_2H_4 DBD jet; (e) opaque film growth at the edge of the transparent film by the He/C_2H_4 DBD jet when a relatively high discharge power was applied.

Transparent films and opaque films were also observed when the ethylene was used as the deposition precursor. The image in Figure 17(d) presents a transparent film growth on top of the microscope slide. Similar to the PMMA case, a higher discharge power leads to the formation of the opaque film, as shown in Figure 17(e). However, the opaque film was grown at the edge of the transparent film rather than at the center of the transparent film in the PMMA case. The reason of this difference is yet unclear.

Surface free energy of the coating deposited on the microscope slide by the He/C_2H_4 DBD jet was measured using a contact angle goniometer (VCA Optima). The static water contact angle measurements of the microscope slide surface before and after the treatment by a pure helium DBD jet were also performed for comparison and the results can be seen in Figure 18(a) and Figure 18(b), respectively. It shows that after being treated by the helium DBD jet the surface of the microscope slide becomes more hydrophilic, compared to that without treatment. When the hydrocarbon (or PE) coating was applied to the microscope slide, the water contact angle was significantly increased, as displayed in Figure 18(c). Similar contact angle result was also reported by Fanelli *et al.* in their work, which employed He/C_2H_4-fed glow (diffuse) DBD to grow the hydrocarbon films [116]. This result demonstrates that the wettability of the substrate surface can be tailored by this technique when a proper precursor is fed into the helium DBD jet.

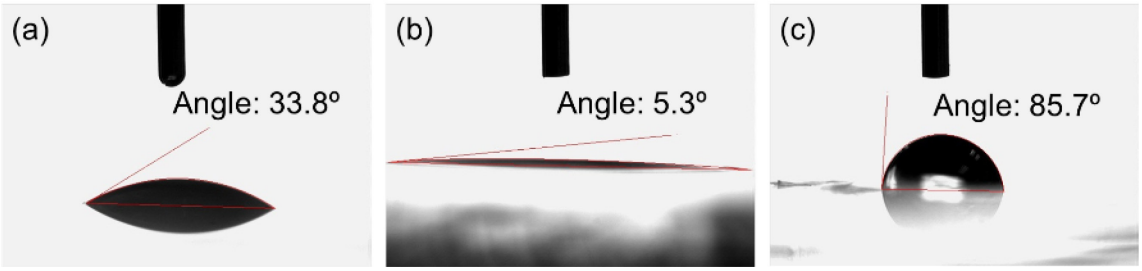

Figure 18. Static water contact angle measurements of (a) the microscope slide before plasma treatment, (b) the microscope slide after 1-min helium DBD jet treatment, and (c) the microscope slide coated with a PE or hydrocarbon film achieved by the helium/ethylene DBD jet.

3.3.2 Metal Film Deposition in Ambient Air

Metal film deposition can be also achieved in open air using the helium DBD jet. Copper(II) acetylacetonate [$Cu(acac)_2$, Sigma-Aldrich, 97 %], which is an metal-organic compound in a solid form, was employed as the precursor for copper film deposition. Note that "(II)" means that the compound is formed based on +2 oxidation state of copper. The main difference between the "organometallic" (e.g., ferrocene) and the "metal-organic" precursors is whether they contain metal-carbon bonds in addition to the organic ligands [145]. Organometallic precursors have the metal-carbon bonds, while no metal-carbon bonds exist in the metal-organic precursors. Copper was selected as our deposition product due to its slow reaction with atmospheric oxygen. In addition, copper oxidation typically leads to the formation of a layer of brown copper oxide, which can prevent further corrosion in the bulk copper.

The copper deposition system setup using the helium DBD jet is illustrated in Figure 19. The precursor supply system is similar to that in Figure 14 as the $Cu(acac)_2$ is in a form of powdered solid. In addition to the helium working gas, hydrogen is required

to accomplish the copper deposition since typically copper films are grown by the hydrogen reduction of $Cu(acac)_2$ [146-148]. Hydrogen has also been demonstrated to be essential to reduce oxygen and carbon impurities in the deposited copper films. The vapor pressure of the $Cu(acac)_2$ is about 1.7×10^{-4} Torr at room temperature [147], which is one order smaller than that of ferrocene. It was found that the flow rate of the $Cu(acac)_2$ at room temperature was so low that no film growth was observed after 10-min deposition. Heating up the precursor is thus needed to increase the vapor pressure of the $Cu(acac)_2$, further elevating the deposition rate. A cartridge heater was utilized as the heat source of the precursor and was directly attached to the bottom of the precursor container. To achieve uniform heating, the precursor container was wrapped by aluminum foil (not shown). A temperature controller was used to bring the container temperature to a desired value by the feedback of the thermocouple readings. The mixture of helium, hydrogen, and $Cu(acac)_2$ vapor then flowed into the floating-electrode DBD jet generator for copper film deposition. The detailed specifications of the DBD jet were identical to those in Figure 16(b) except that a shorter gap distance (2–5 mm) between the tube end and the substrate was set in this case.

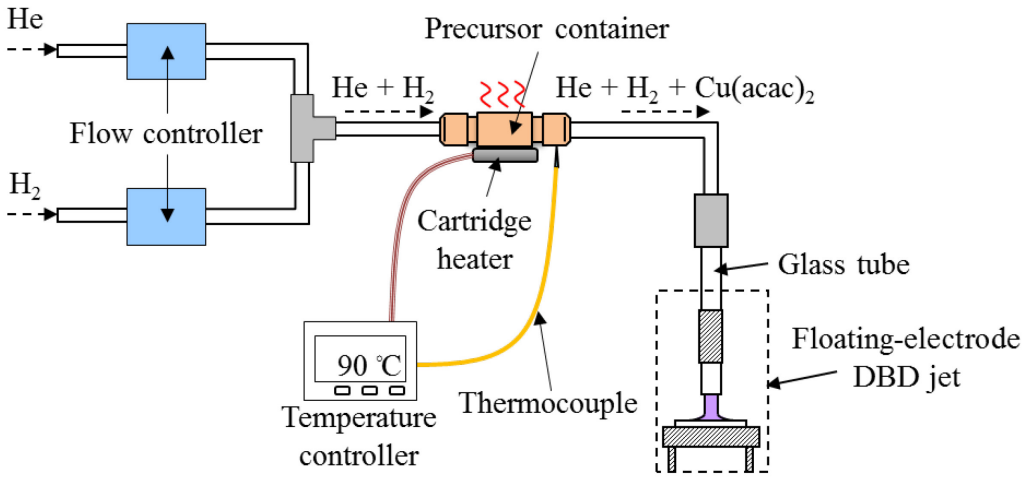

Figure 19. Schematic experimental setup for copper film deposition in ambient air using the helium DBD jet.

Figure 20(a) shows the image of the AP-PECVD experimental setup for copper deposition using the He/H_2/Cu(acac)$_2$ DBD jet. Similarly, microscope slides were employed as the substrates for the test. Note that in this picture the aluminum foil was not used to cover the precursor container to better show the setup. After around 5-min deposition, the growth of a copper film on the microscope slide can be observed [Figure 20(b)]. In this case, the helium flow rate was 3 slm and the hydrogen flow rate was 0.1 slm. The gap distance between the tube end and the substrate was set to be 5 mm. 90 ºC precursor temperature and 3 W discharge power were utilized to achieve copper film deposition. Figure 20(c) displays the as-deposited copper film after 10-min deposition. It shows that the film consists of three regions which exhibit distinct colors. The central region of the film appears copper color (reddish brown region) with a diameter of around 3 mm, which is slightly smaller than the inner diameter (4 mm) of the glass tube. However, a dark blue region was seen at the edge of the reddish brown region. This is

likely due to the thin thickness at this film region, which has also been observed in the prior art [148]. The radially distributed plasma discharge on the microscope slide, as shown in Figure 20(b), leads to the formation of filamentary patterns at the dark blue region. There also exists a yellowish region at the outer portion of the copper film, as indicated in Figure 20(c). This region may be attributed to the low-power surface discharge at the outer plasma zone.

Deposition without the addition of hydrogen and without plasma generation was also tested for comparison. Figure 20(d) presents the experimental result after 10-min treatment when hydrogen was not fed into the DBD jet. It can be clearly seen that with the absence of hydrogen instead of copper films only a brownish ring-shaped pattern was obtained at the outer area. When only the gas mixture (helium/hydrogen with 90 ºC precursor) flowed onto the substrate surface without plasma, no copper film was deposited. Only a white cloud pattern formed on the microscope slide, as shown in Figure 20(e), likely due to the condensation of the hot precursor gas when it reached the relatively cool surface. Figure 20(f) shows the copper film deposition result after 10-min deposition when a 10-mm gap distance was utilized. Compared with the film obtained using 5-mm gap in Figure 20(c), one yellowish region instead of three distinct regions was observed in this case. This may be due to the relatively low deposition rate when a relatively large gap distance was applied. These results showed that the use of both the hydrogen and plasma discharge and the requirement of a short discharge gap were necessary to accomplish copper film deposition with an efficient deposition rate.

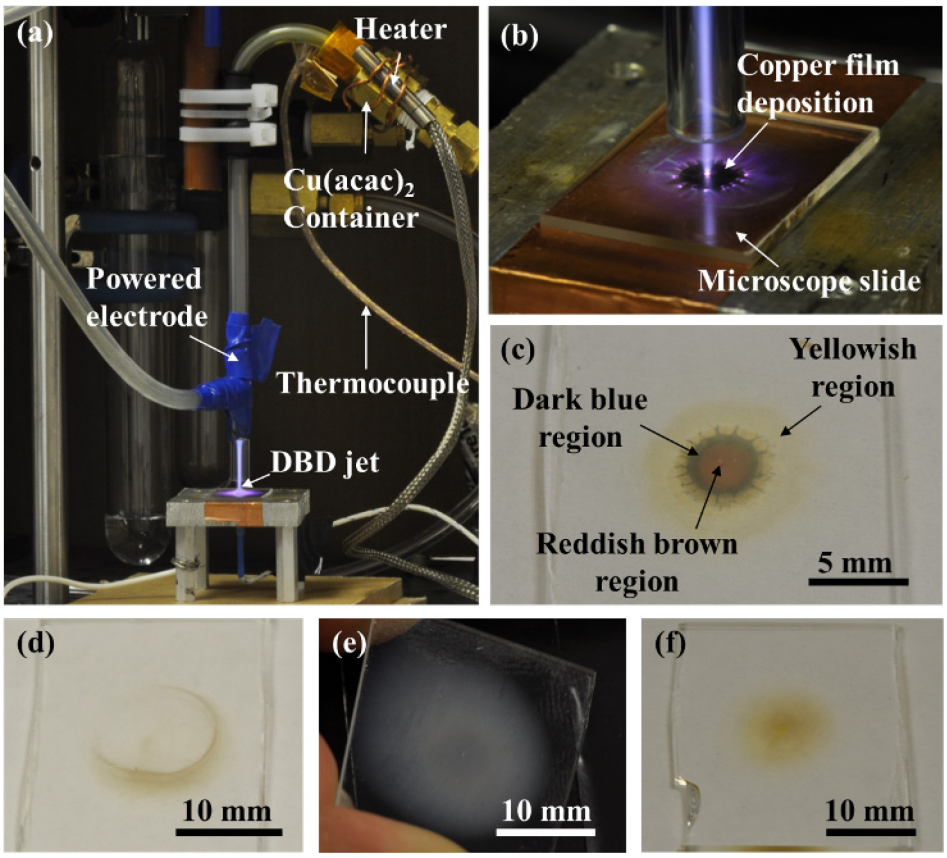

Figure 20. (a) Photograph of the experimental setup for copper film deposition in ambient air; (b) image of copper film growing on the microscope slide; (c) as-deposited copper film showing three different regions after 10-min deposition with a 5-mm gap; (d) as-deposited result without the addition of hydrogen; (e) white cloud pattern formation when no plasma was employed; (f) as-deposited film when a 10-mm gap was used.

3.3.3 Micro/Nanostructured Film Deposition in Ambient Air

Similar to those traditional PECVD systems, this DBD jet deposition system we developed in this study can also achieve even more complicated coatings, e.g., thin films with micro or nanostructured surfaces, by using more than one type of precursors concurrently. Figure 21 illustrates an example of the microstructured metal/polymer composite film deposition using the DBD jet fed by both $Cu(acac)_2$ and MMA precursors. A push connect tee was utilized to connect the $Cu(acac)_2$ supply system and

the MMA bubbler to allow the mixture gas ($He/H_2/Cu(acac)_2/MMA$) to flow into the DBD jet generator. Preliminary test employed the helium flow rates at 2.95 slm and 0.05 slm to carry the $Cu(acac)_2$ precursor and the MMA precursor, respectively. The precursor temperature was set to be 100 ºC and the gap distance was 5 mm. After the DBD jet was driven by 3.6 W for 10 min, a white opaque film with microscale structures was deposited. Optical microscopy was used for clear observation of the microstructures, as shown in Figure 21(b). It can be seen that the film contains many spherical microstructures with diameters of about 1–2 μm on the surface. The microstructure dimension can be tailored by adjusting the concentration ratio of $Cu(acac)_2$ to MMA. Figure 21(c) shows the optical microscopy image of the deposition result when the helium carrier flow for $Cu(acac)_2$ and that for MMA were set to be 2.97 slm and 0.03 slm, respectively. The higher $Cu(acac)_2$ to MMA concentration ratio, compared to the case in Figure 21(b), leads to the formation of greater spherical microstructures. In addition to the 1–2 μm microspheres (microstructure 1), which are similar to those observed in Figure 21(b), large microspheres with 4–7 μm diameters (microstructure 2) were obtained in this case. These results indicate that this technique has the potential of micro- (even nano-) structured film fabrication in ambient air, further implying that micro/nanostructured materials could be synthesized on the biological substrates. Such films may be also achieved by feeding two different polymer monomers into the helium DBD jet for self-assembled copolymer growth though more studies are required in the future [149, 150].

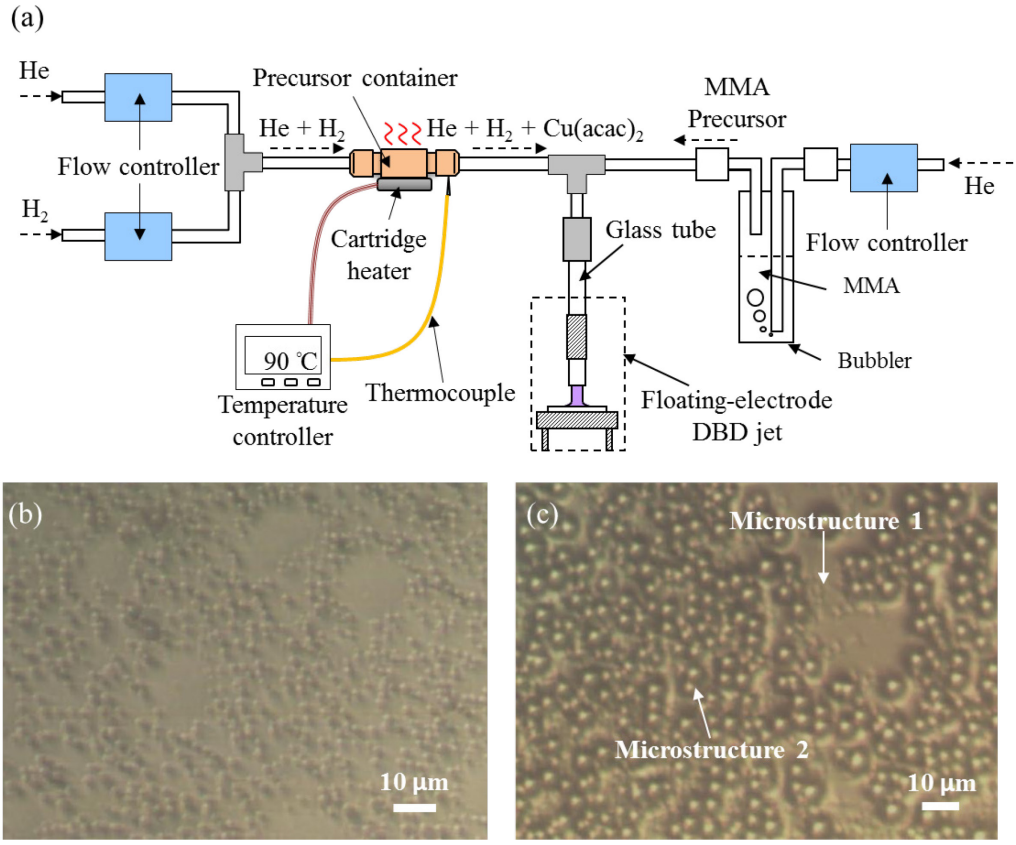

Figure 21. (a) Illustration of the experimental setup using the helium DBD jet to fabricate micro/nanostructured films: an example using $Cu(acac)_2$ and MMA precursors; As-deposited films containing (b) 1–2 μm spherical microstructures and (c) spherical microstructures with two different sizes (microstructure 1: 1–2 μm and microstructure 2: 4–7 μm).

3.4 Section Conclusions

Several different types of material processing systems were constructed using He DBD jets in this section. In addition to simply depositing thin films, the DBD-jet-based system is able to synthesize nanoparticle, carbon nanotubes nanoparticle and micro/nanostructured metal/polymer composite films by slightly modifying the system and using different precursors. Initially a chamber was employed to build up the deposition system as additional concerns were oxidation and combustion of the

monomers. Thin film deposition in open air conditions was then achieved without the use of the chamber. Three different precursors, MMA, ethylene, and $Cu(acac)_2$, were employed to accomplish the deposition of PMMA, PE (or hydrocarbon), and copper films, respectively. In both PMMA and PE/hydrocarbon films, it was found that not only the most common transparent films were deposited, but also white opaque films can be obtained when a relatively high discharge power was applied. This result showed that the film morphology is able to be tailored by adjusting the plasma conditions. In copper film deposition heating $Cu(acac)_2$ up to 90 ºC was required to efficiently deliver the precursor vapor due to its low vapor pressure. The addition of hydrogen was required to decompose the ligands of $Cu(acac)_2$ through the hydrogen reduction mechanism. All these results demonstrated that the He DBD jet has the potential to be used in our "PECVD on living substrates" as the open air deposition of materials with variety and functionality can be attained.

4. PMMA FILM DEPOSITION AND CHARACTERIZATION*

4.1 Introduction

This section presents detailed experimental results of the PMMA deposition in ambient air, including the operation modes of the He/MMA DBD jet, PMMA deposition rate, film morphologies, and the chemical characterization of the as-deposited PMMA films with respect to different discharge powers. Various substrates including commonly-used glasses and silicon wafers as well as temperature-sensitive materials (e.g., plastic, rubber, onion, and even fingernail) were also tested in the deposition. The results in this section have been published in a recent paper [45].

4.2 Experimental Methods

The way to achieve PMMA film deposition and to monitor the electrical characteristics (e.g., applied voltage, discharge current, and discharge power) of the DBD jet has been illustrated in Figure 16(a) and described in Section 3.3.1. For visualization of the PMMA film surface morphology, scanning electron microscopy (SEM, JEOL JSM-7500F) and atomic force microscopy (AFM, Veeco Digital Instruments Nanoscope AFM/STM) were utilized to acquire the images of the film surface. The film thickness after 30 minutes and the film deposition rates were obtained by measuring the step height using a stylus profilometer (KLA Tencor P-6) at the mask

*Part of this section is reprinted with permission from "Low-temperature Polymer Deposition in Ambient Air Using a Floating-electrode Dielectric Barrier Discharge Jet" by T.-C. Tsai and D. Staack, 2011. *Plasma Processes and Polymers,* vol. 8, pp. 523-534, Copyright [2011] WILEY-VCH Verlag GmbH & Co. KGaA, Weinheim.

edge of films deposited on partially masked substrates after removing the mask. X-ray photoelectron spectrometer (XPS, Kratos Axis Ultra Imaging) was used to study the chemical composition of the as-deposited PMMA film surface. It should be mentioned that all measured films in SEM and XPS were tested as deposited. Generally the films appear hard and the films should not be influenced by the high vacuum environment. A potential exception is for the apparently partially cured film obtained at low power (1 W), discussed in detail later. However, the high vacuum of the XPS system showed no significant influence on the partially cured film due to the fact that similar XPS results were obtained even if multi-samples with the same experimental conditions (1 W) and different times exposed to high vacuum were measured. The chemical structures of the PMMA films were characterized by using attenuated total reflection Fourier-transform infrared spectroscopy (ATR-FTIR, Bruker Optics ALPHA-P 10098-4). Note that most of the PMMA deposition experiments were performed on the microscope slide with a thickness of 1 mm. For the ATR-FTIR analysis, silicon wafers were employed for PMMA film deposition. Additionally, the optical emission spectroscopy (OES) was performed to detect the excited species in the He/MMA DBD jet by using a USB spectrometer (Edmund Optics 64813, TE cooled USB spectrometer UV-VIS). A DBD jet using pure helium (He DBD jet) was also analyzed for comparison.

4.3 Experimental Results

In this subsection, before the characterization of as-deposited PMMA films was given, the operation modes of the He/MMA DBD jet were presented since it was found

that the modes showed significant influence on the film properties, such as the film morphologies, film compositions, and chemical structures. It should be mentioned here that different precursors fed into the DBD jet may result in various discharge operation modes. When different precursors are used, it is thus quite important to observe and investigate how the precursors affect the operation modes of the DBD jet before the measurement of the deposited film properties is performed.

4.3.1 Operation Modes of He/MMA DBD Jet

After the DBD jet is ignited, two distinct modes of the discharge, namely a diffuse mode and a concentrated mode, are observed as the applied voltage is changed, as shown in Figure 22(a)–(d). Figure 22(a) shows a diffuse discharge (diffuse mode) which is observed immediately after discharge is generated. In this operation mode, the discharge color shows uniform distribution, as presented in several studies [98, 108]. The increase of the applied voltage results in the change of the discharge appearance. The central part of the discharge along the axial direction starts to be brighter, compared with the part near the inner wall of the dielectric glass tube. This transition image can be seen in Figure 22(b). The discharge at this point is in transition from the diffuse mode to the concentrated mode. The concentrated mode can be further divided into two types based on the discharge position; that is, centered concentrated mode and off-centered concentrated mode. As the input power is increased sufficiently, the discharge contracts in the radial direction and becomes a thin bright line located in the middle of the tube (centered concentrated mode), as shown in Figure 22(c). The discharge in this mode

appears to contract to a size smaller than the tube inner diameter. As an even higher power is applied, the discharge starts to move from the tube centerline to the inner wall of the tube (off-centered concentrated mode), as can be seen in Figure 22(d).

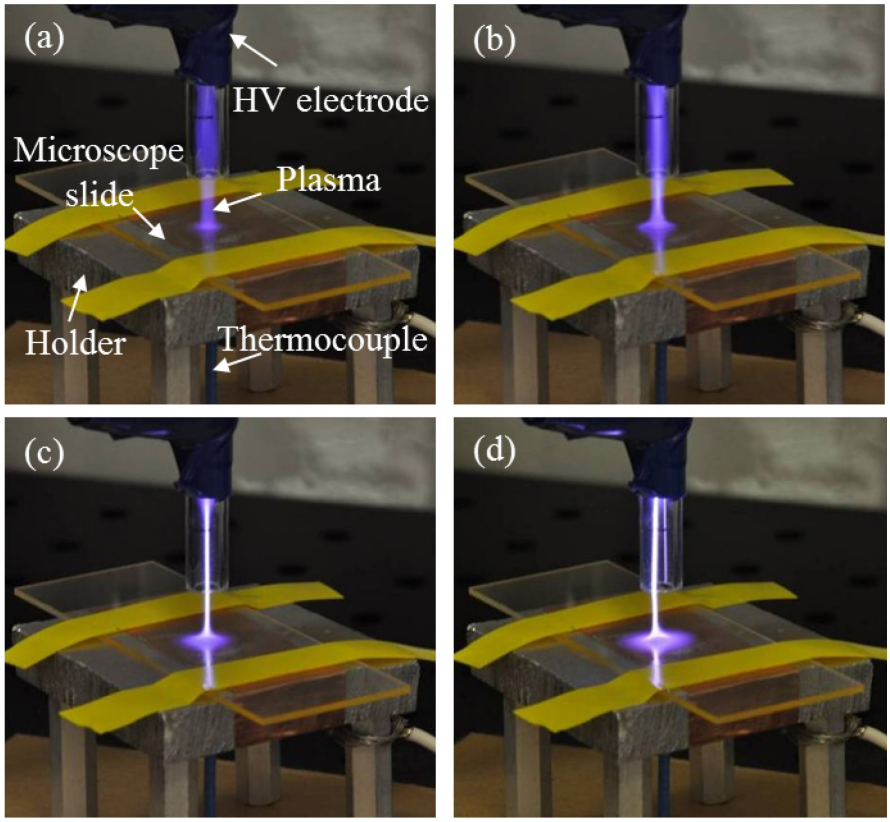

Figure 22. Four types of the He/MMA DBD jet appearance (a) in diffuse mode, (b) during transition, (c) in centered concentrated mode, and (d) in off-centered concentrated mode.

The discharges in these modes show not only different visual appearance, but also different behavior in their current waveforms. Multiple current pulses, which have been observed in the traditional parallel-plate helium DBD reactors in several prior studies (see Section 2.2.2) [17-19, 113-116], also occur in our discharge currents.

Similar to the features in these prior studies, the number of current pulses per half cycle increases as the discharge power is raised. In the diffuse mode, only one current pulse is observed within each half cycle as shown in Figure 23(a). When the DBD jet is operated under the transition condition, second pulses appear on the half cycles of the current waveforms [Figure 23(b)]. However, the second pulses are sporadically ignited, i.e., not every half cycle has two pulses during the transition operation. It is seen that the probability of occurrence of the second pulses grows with rising power. As a relatively high power is applied and the discharge switches to the concentrated mode, two strong pulses on every half cycle are always observed. Further increase of discharge power can make the third pulse generation on each half cycle, as presented in Figure 23(c). Note that in a pure helium DBD jet without the addition of any precursors the current waveforms exhibit only current pulse regardless of the applied voltage. However, if either pure helium (He DBD jet) or the mixture of helium and a small amount of MMA (He/MMA DBD jet) are used as the working gas the change between diffuse and concentrated modes are attainable. Visually the discharge shows different behavior and colors due to the existence of the impurity (MMA in this case) in the helium. In addition to discharge power and precursor concentration, the mode change phenomenon is found to be related to several parameters, such as the position of the powered electrode, the gap distance between the nozzle and the substrate, and the dimension and the material used in the dielectric tube. The factors influencing the mode change in the DBD jet and the evolution of discharge currents will be discussed and reported in more detail in Section 6.

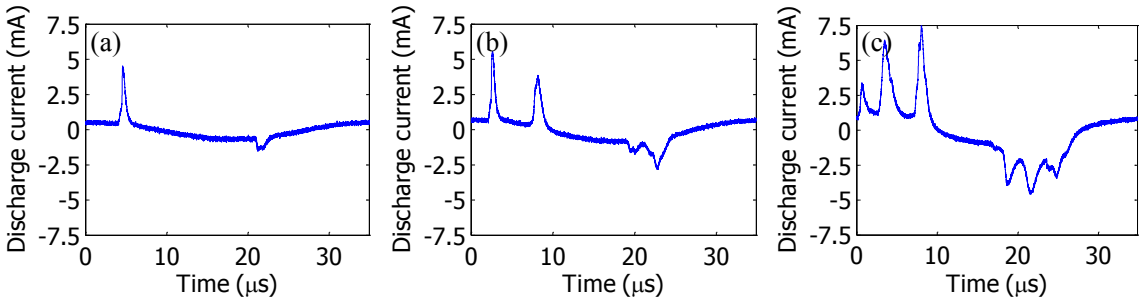

Figure 23. Current waveforms over one complete cycle in the DBD jet fed by helium and MMA (a) in diffuse mode (0.7 W); (b) during transition (1.7 W); (c) in concentrated mode with relatively high power (6.0 W).

4.3.2 PMMA Deposition Rate

Figure 24(a) shows the PMMA deposition rates with various discharge powers when the helium working gas and carrier gas flow rates are 2.9 slm and 0.1 slm, respectively. In this case, the MMA concentration is about 1800 ppm. In these results, the thickness at the film center is measured and the corresponding deposition rate is computed by dividing the thickness value by the deposition time (30 min). When the DBD jet is ignited and the discharge power is set to less than 1 W, the discharge is observed in the diffuse mode. It can be seen that the deposition rate in the diffuse mode is lower than 0.5 nm·sec^{-1}. As discharge power is increased, the central axis of the discharge starts to become brighter and the discharge mode of operation enters the transition status to the concentrated mode. The deposition rate during the transition increases as the power is increased. When the discharge power is larger than 3 W and the discharge switches to the concentrated mode, a maximum of the PMMA deposition rate is observed (22 nm·sec^{-1}). The deposition rate is found to be 3-10 times higher than those in the prior works which also employ atmospheric pressure plasma jets as their

depositing tools [27, 72, 85]. Initially an increase of discharge power results in no significant change in deposition rate. However, the deposition rate starts to decrease with a further increase of power, as displayed in Figure 24(a). When the power is increased to 6.5 W, the deposition rate of merely 7 $nm \cdot sec^{-1}$ is observed. The unchanged and reduced deposition rates under high power operation (>4 W), depicted by triangular markers with dash lines, are due to the fact that the concentrated discharge starts to be unstable and shifts from the central axis to the inner wall of the dielectric tube. This causes that the position where the greatest film thickness occurs also shifts from the film center to the outer region. Therefore, the measured thickness and deposition rate at the film center may be smaller than the maximum deposition rate at these relatively higher discharge powers. At these powers (>4 W) the film thickness is also topologically less symmetric. The substrate temperature is also monitored during deposition by using a thermocouple, as shown in Figure 16(a). The corresponding substrate temperature after 30-min deposition is recorded, as presented in Figure 24(b). It can be seen that the temperature rises linearly with the increasing power. Besides, the results show that the highest deposition rate (22 $nm \cdot sec^{-1}$) can be obtained with the substrate temperature merely rising to 39 °C, which is quite suitable for films deposition on temperature-sensitive substrates, such as polymers or biological surfaces.

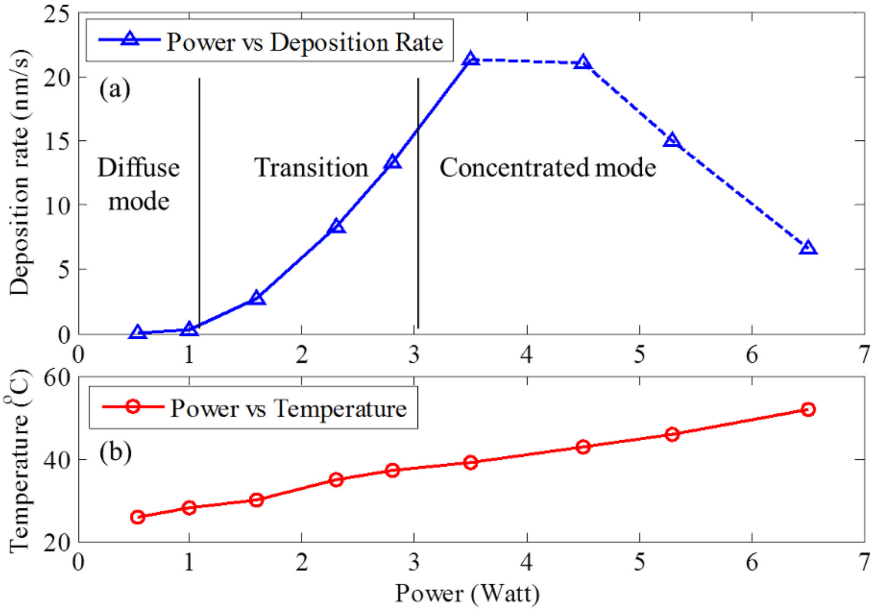

Figure 24. (a) Deposition rate as a function of discharge power; (b) substrate temperature as a function of discharge power.

4.3.3 Transparent and Opaque Films

The images of the PMMA films obtained by the floating-electrode DBD jet after 30-min deposition are shown in Figure 25. As can be seen in these images, not only typical transparent films are deposited, but also white opaque films can be fabricated by adjusting discharge parameters. Under diffuse mode operation with 1 W discharge power, the size of the PMMA film is around 8 mm in diameter, which is similar to the plasma spot size on the glass substrate in Figure 22(a) and is about double the size of the inner diameter of the dielectric tube (4 mm), as shown in Figure 25(a). The thickness at the film center is about 0.6 μm, and many droplet-like patterns surrounding the circular transparent film are also seen in this figure. It is found that the surfaces of the films deposited by the low power diffuse mode feel sticky when touched by bare hands.

Visually the films appear to have a very high viscosity but with some liquid-like properties and can be dissolved in ethanol. The partially cured properties can be also distinguished by visible deformation of the film surface which is obtained when the excessive tapping of the profilometer is used during measurements of the film thickness. This deformation did not occur for all other films tested. Figure 25(b) shows the PMMA film with a thickness of about 39 μm by using concentrated mode discharge (3.5 W). In this case, the film dimension increases as the discharge spot size on the glass substrate expands [discharge image is in Figure 22(c)]. Since locally high temperature is generated by the highly concentrated discharge, a yellow spot at the film center is observed. The films deposited with the relatively high power operation appear to be hard and their surfaces are less sticky, compared to the films obtained in the diffuse mode. Further increase of the discharge power (7.7 W) leads to the occurrence of a white opaque film growth, as displayed in Figure 25(c). Besides, the transparent film region under high power operation becomes greater in size than the case in Figure 25(b). In this case, the substrate temperature rises to 56 °C and the thickness of the film center decreases to slightly less than 10 μm due to a shift in the concentrated discharge position, as mentioned in the previous subsection. It should be noted that Figure 25(a), (b) and (c) are the results when the gap between the substrate and the exit of the dielectric tube is set to 10 mm. If a small gap (3 mm) is adopted and the concentrated mode with similar high power is applied, a large and circular opaque pattern can be obtained, as indicated in Figure 25(d). The transparent film surrounding the opaque one is seen to be larger in diameter than the case in Figure 25(c) due to the shorter nozzle-to-substrate distance.

The average thickness of the opaque region is around 6 μm and a substrate temperature of 53 °C after 30-min deposition is measured. It should be mentioned that the opacity of the film is not a result of film thickness. Evidence can be seen from the opaque film (6 μm) in Figure 25(d), which is thinner than the transparent film (39 μm) in Figure 25(b), and during the deposition process as the film is growing (prior to the 30-min termination) an opaque film can be seen. Also the structure of the opaque film is different as discussed in the next subsection. The opaque feature is found to occur only when the concentrated mode discharge is used with a sufficient high discharge current. The same feature can be also achieved by heating up the glass substrate to 150 °C with low power diffuse mode operation. Therefore, it is suggested that thermal effect is one of the critical factors for opaque films generation.

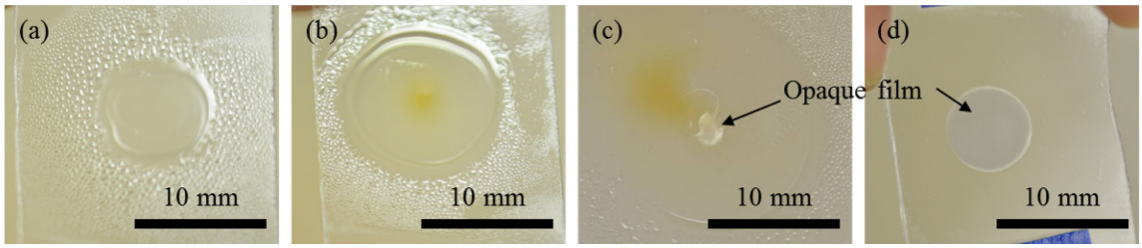

Figure 25. PMMA films obtained under different modes of operation: (a) diffuse mode (1 W); (b) concentrated mode (3.5 W); (c) concentrated mode with relatively high power (7.7 W) by which an opaque film region is deposited at the center of the film; (d) concentrated mode with relatively high power and short distance (3 mm) between the nozzle and substrate.

4.3.4 SEM and AFM Results

In order to distinguish the microstructures between the transparent film and the opaque film obtained in this work, SEM and AFM are utilized to acquire the surface

images of the films. Figure 26(a) shows the SEM image of a transparent film with 10 μm thickness deposited using the concentrated mode. The surface of the PMMA coating is seen to be smooth and uniform without particle formation. The smoothness in surface morphology of the transparent film is also examined by using AFM on a small Z-scale (10 nm·div^{-1}), as shown in Figure 26(b). The root-mean-square (RMS) roughness value is merely 0.4±0.1 nm, which shows that high quality of the polymer films can be accomplished by our deposition approach. Compared to the transparent film without any microstructure formation, the opaque film (average thickness approximately 6 μm) consists of clear wrinkled microstructures, as presented in Figure 26(c). The width of the microstructures, which depends on the discharge power, is measured in the range of 2 μm to 10 μm. These wrinkled micropatterns appear similar to those in thin oxide films obtained by Takahashi *et al.* [151]. In their work, UV curing technique was employed to achieve fast polymerization, and "buckling effects" are induced to form wrinkled microstructures on their films. Similar to their results, wrinkled microstructures in the middle while ordered grating patterns at the edge are also observed in our opaque film. Thus, in our case it is suggested that fast polymerization of the PMMA films occurs due to locally high temperature generated in the concentrated discharge, further causing buckling effects in the deposited PMMA films. The measurement of surface morphology of the opaque film is also performed by AFM, as shown in Figure 26(d). Quite large RMS roughness value (355 nm) is measured due to the wrinkled microstructures in the opaque films.

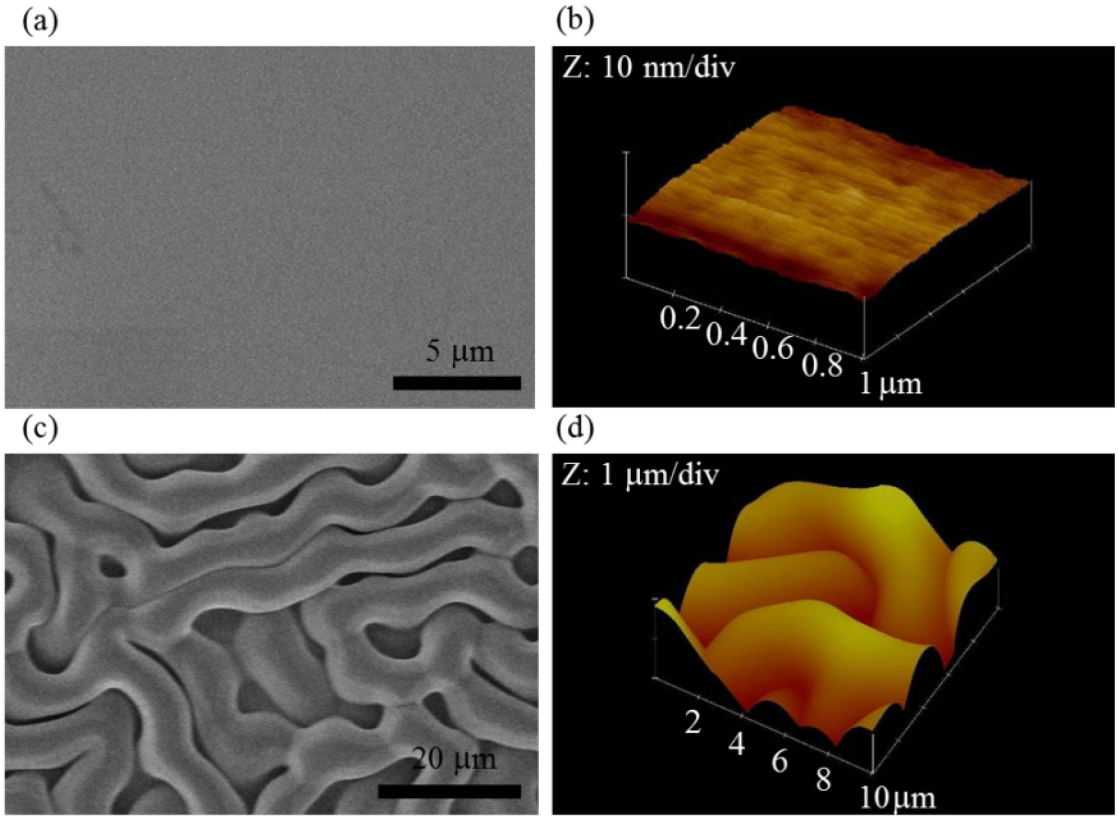

Figure 26. Transparent film images acquired by using (a) SEM, (b) AFM; opaque film images obtained by (c) SEM, (d) AFM.

4.3.5 XPS Analysis

4.3.5.1 Spatial Variation

In addition to the measurement of surface morphology of the deposited PMMA films, the chemical composition of both the transparent and opaque films is analyzed by XPS. For a transparent film obtained at medium power (2.8 W) with 37 °C deposition temperature and 10 mm nozzle-to-substrate distance, three positions on the film, from the center to the edge, are measured by XPS, as indicated in Figure 27(a). Position (1) is the film center, and position (2) and (3) are about 2.5 mm and 5 mm away from the film

center, respectively. The lower edge of the film is formed by covering a mask during deposition for further measurement of the film thickness. The atomic compositions for these three positions are given in Figure 27(b). Experimental errors are determined by assessing the deviations from the measurement results of multi-samples which are obtained with the same experimental parameters. When not shown, the error bar is smaller than the size of the symbol. At the center of the PMMA film, the carbon concentration (77 at.%) appears to be about 9 % higher than those at the other two outer positions, while the oxygen concentration (23 at.%) is lower. The C:O ratio at the film center is 6.7:2, which is higher than that in a typical PMMA film (C:O = 5:2). At position (2) and (3), the C:O ratios are observed to be similar (4.9:2 and 5:2) and they are lower than the C:O ratio at position (1). The results show that under higher power treatment [position (1)] the film contains more carbon and less oxygen, which was also observed in the prior work by De Geyter *et al.* [22]. In addition, a slight amount of nitrogen (between 0.4% and 1.5 %) is detected in the deposited transparent film. Nitrogen in ambient air likely also participates in the plasma polymerization. However, measurement uncertainties at these low concentrations preclude a detailed analysis of nitrogen incorporation in the film.

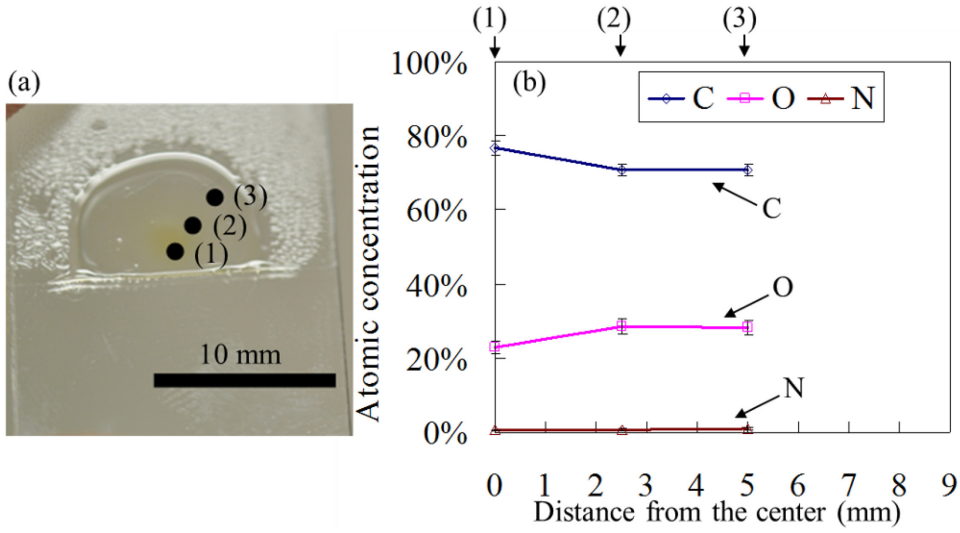

Figure 27. (a) XPS analysis on three different positions of the transparent film; (b) atomic composition of the three positions.

To compare the difference between the transparent film and the opaque film, XPS analysis is also performed to measure the surface chemical composition of the film with a clear circular opaque region [Figure 25(d)], which is obtained by using the concentrated mode discharge (deposition temperature of 53 °C) and a short nozzle-to-substrate distance (3 mm). Similarly, three points are selected for XPS analysis, as indicated in Figure 28(a). Position (1) is located at the film center, and the distances of 5 mm and 8.5 mm from the center are selected for position (2) and (3), respectively. Figure 28(b) shows the atomic composition of the three positions on this film. At the position (1) (opaque region), the carbon concentration (86 at.%) appears highest in these three points, while lowest oxygen concentration (14 at.%) is observed. The C:O ratio is evaluated to be 12:2, which shows less retention of the atomic composition (C:O = 5:2) in typical PMMA than the case at the center of the transparent film (6.7:2). Similar to the

result in the transparent film, the C:O ratios at the outer positions [position (2) and (3)] are lower than that at the film center. Nitrogen signals are also detected in this case except for the zero nitrogen composition at the central region [position (1)]. This may be attributed to the quite small gap (3 mm) between the nozzle and the glass substrate in this case. Therefore, no ambient air can react with plasma at the central region when the working gas starts flowing out of the tube.

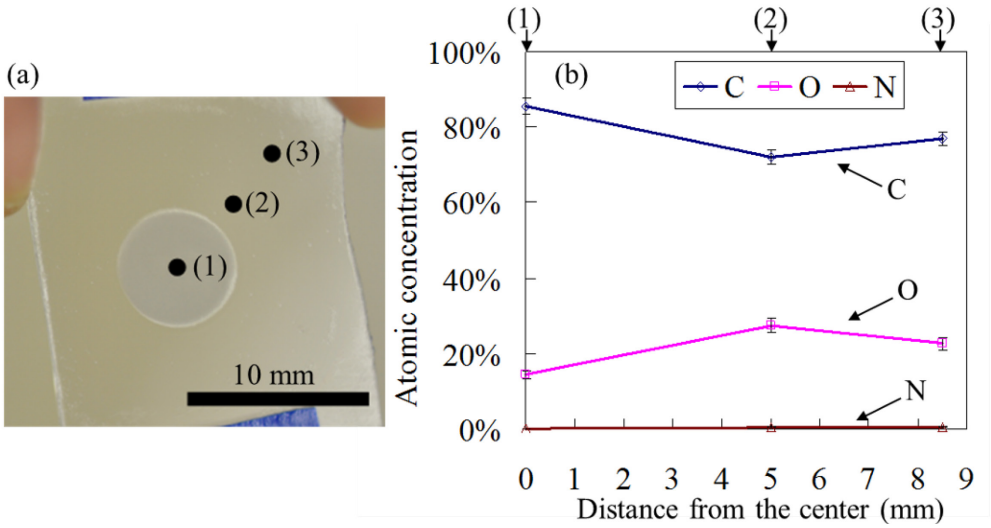

Figure 28. (a) XPS analysis on three different positions of the opaque film; (b) atomic composition of the three positions.

A deconvolution of the O 1s and C 1s spectra is performed to obtain the chemical bonds in the deposited PMMA films. A constant value of 1.2±0.1 eV is used for the full width at half maximum (FWHM). However, the typical four-peak C 1s and two-peak O 1s deconvolution for PMMA is not suitable for our films [152]. It is due to the fact that the O 1s spectrum for the deposited PMMA appears different from typical pure PMMA.

The O 1s spectrum in typical PMMA is symmetrical around 532.9 eV due to the same amount of the two oxygen atoms in the O=C–O group, which are indicated as O^1 and O^2 in Figure 29(a). However, the O 1s spectrum in our plasma-polymerized PMMA films shows an asymmetrical shape, as presented in Figure 29(b). The O1 peak (O=C/O=C–O) appears higher than the O2 peak(O=C–O–C), and one additional peak (O') is required to obtain a good fit. The greater O1 area implies that in addition to the typical ester group (O=C–O), O=C also exists in the deposited PMMA films. The appearance of O' group shows the existence of C–O–C or H–O–C group. These additional groups are generated in the films likely due to the fact that the ester methoxy group is broken by energetic radicals in plasma [87, 153]. The corresponding binding energies and possible bond candidates for XPS deconvolution are summarized and listed in Table 2 [154].

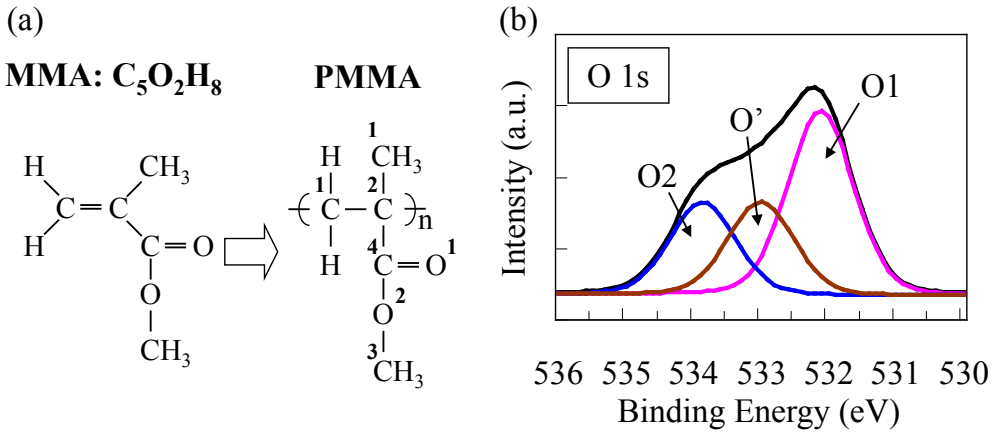

Figure 29. (a) Illustration of the chemical structures of a MMA monomer and PMMA; (b) O 1s XPS spectra of the deposited PMMA film by our DBD jet.

Table 2. Binding energies and relative bond candidates of the fitted C 1s and O 1s peaks.

Spectrum	Peak	Binding Energy	Bond Candidates
		eV	
O 1s	O1	532.1±0.1	O=C or O=C–O
	O’	532.8±0.2	C–O–C or H–O–C
	O2	533.7±0.2	O=C–O–C
C 1s	C1	285.0	–CH_n (e.g., Methyl)
	C2	285.7±0.1	C–COOR (e.g., Ester/Carboxylic acid)
	C3	286.6±0.2	C–O
	C’	287.7±0.2	C=O or O–C–O
	C4	288.9±0.2	O=C–O (e.g., Ester/Carboxylic acid)

Since the existence of the additional groups mentioned above, the C 1s curves of the three positions of the transparent PMMA film [Figure 27(a)] are deconvolved into five peaks at 285.0, 285.7, 286.6, 287.7 and 288.9 eV, as listed in Table 2. Figure 30 shows the deconvolved peaks for the three positions in the transparent film. A slight amount of C’ group (C=O or O–C–O), which does not exist in typical pure PMMA, is observed at these three positions. As can be seen in this figure, the –CH_n group (C1) decreases but the ester group (C2 and C4) increases as the distance from the film center [position (1)] increases. The detailed variation of the bonds concentration can be seen in Figure 31(a). It also shows that the C3 group, including C–O in the methoxy group of the ester or C–O in ether/alcohol groups, increases from the film center [position (1)] to the edge [position (3)]. Besides, no significant change in C’ group is observed. Similarly, the deconvolved C 1s peaks for the opaque film in Figure 28(a) can be obtained and their

concentrations are also depicted in Figure 31(b). Again, similar trends can be seen in these two figures for the transparent film and the opaque film, respectively. Higher C1 concentration and slightly lower C2, C3, C4 and C' concentrations are observed at the position (1) of the opaque PMMA film, which is deposited with higher discharge current than the transparent film. It can be suggested from the results that the film deposited with higher power operation, such as at the position (1), has less retention of the monomer ester groups and lower concentration of C–O groups. However, at every position of both the transparent film and the opaque film, the C3 concentration (C–O groups) appears much higher than C2 (and C4), which suggests that a certain amount (5-15%) of ether/alcohol groups exists in the plasma-polymerized PMMA film.

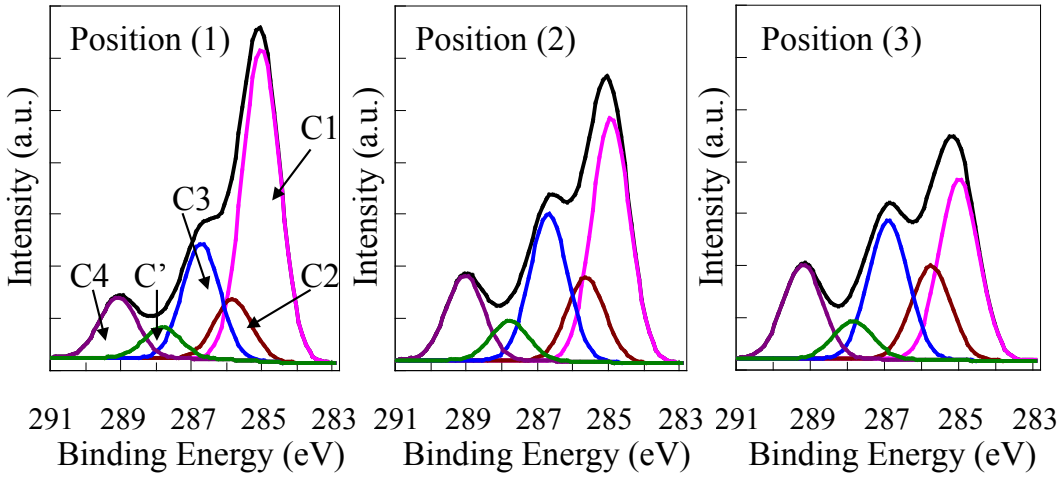

Figure 30. Deconvolved C 1s peaks of the transparent PMMA film for three different positions in Figure 27(a).

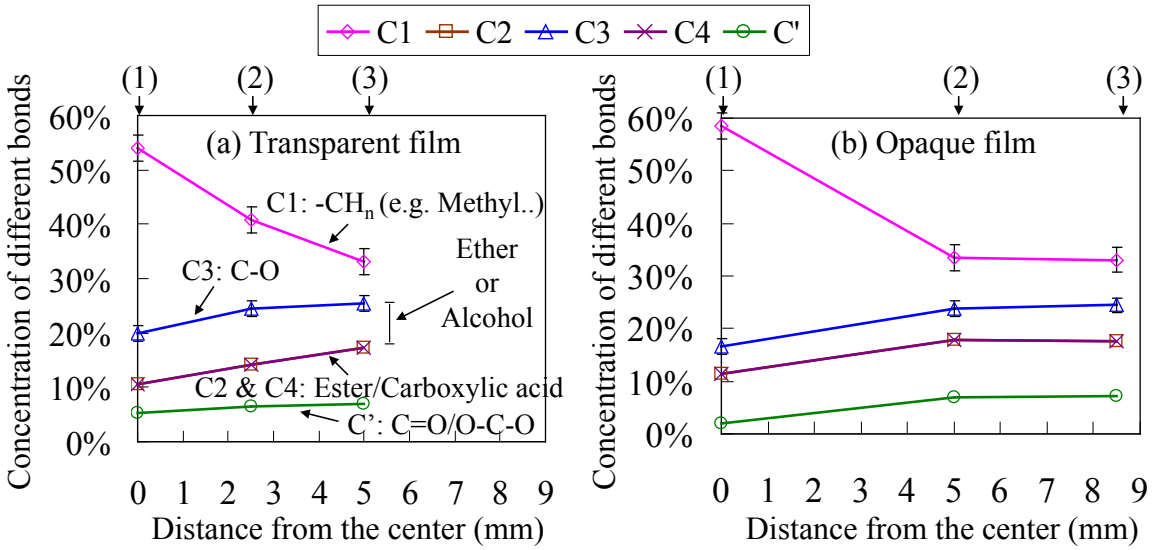

Figure 31. Concentrations of different bonds in C 1s for three different positions in (a) the transparent PMMA film, and (b) the opaque film.

4.3.5.2 Different Discharge Powers

To gain further insight into the influence of discharge power on the chemical compositions of the deposited PMMA films, the transparent PMMA films with 10 mm nozzle-to-substrate distance at different powers are analyzed by XPS. Figure 32 shows the atomic concentrations of the deposited transparent films at discharge powers of 1, 1.6, 2.8 and 4.5 W. In the presented data, only the film center is measured. The results show the further evidence that the film deposited at higher power contains more carbon composition and less oxygen composition. The C:O ratio of the film increases from 4.5:2 to 7.3:2 with the rising discharge power. It shows that the film deposited by the higher power appears to be more different from typical PMMA with C:O ratio of 5:2. Again, a slight amount of nitrogen is observed in the analysis results.

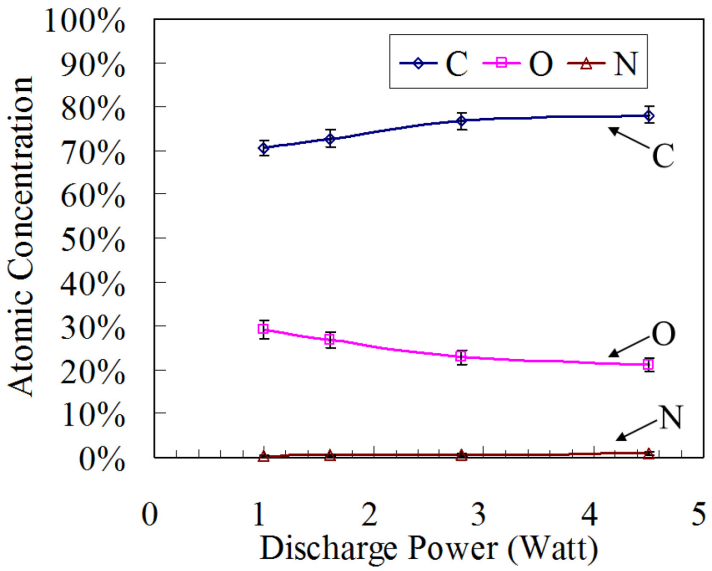

Figure 32. Atomic composition of the deposited films at different powers.

The deconvolution of C 1s peaks for the films at different powers is also performed to distinguish the detailed difference among the chemical bonds in the films. As depicted in Figure 33, very low concentration of C1 groups ($–CH_n$) is observed in the film at the power of 1 W, which is operated in the diffuse mode. The film deposited at 1 W consists of a relatively large amount of C–O (C3) and ester (C2 and C4) groups, and the C1 and C3 groups have similar concentrations. It implies that almost half the amount of C1 groups ($–CH_n$) in the MMA monomers is lost during deposition. When the discharge enters the transition (1.6 and 2.8 W) to the concentrated mode, the concentration of C1 groups starts to rise while C–O and ester groups diminish. As the discharge power increases, the difference between the concentrations of C1 groups and C–O/ester groups appears greater. Further increase of the power leads to less retention of ester groups in the film, i.e., the film obtained at 4.5 W with the concentrated mode.

However, the C' groups (C=O/O–C–O) in the deposited transparent films show no significant difference in concentrations as the power changes. In addition, it is observed that a certain amount of ether/alcohol groups exists in the plasma-polymerized films regardless of the discharge operation mode. These results agree well with those obtained at different positions of a film as described above.

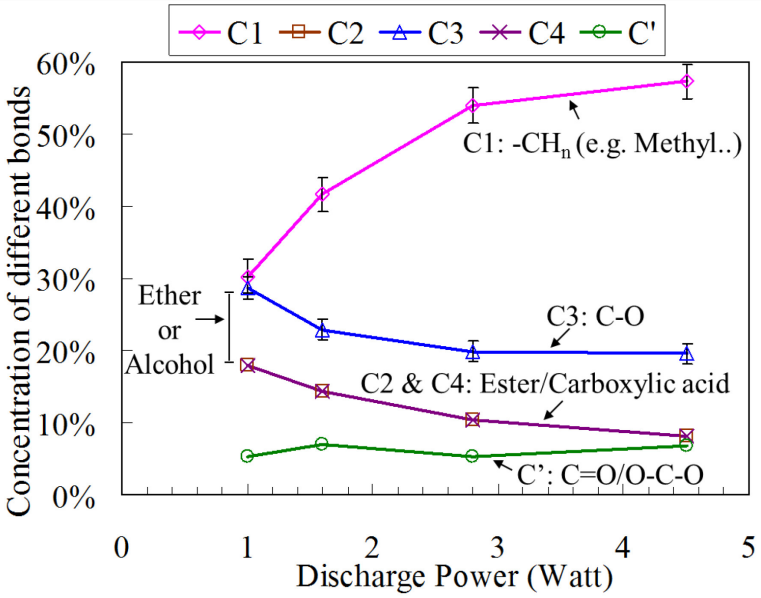

Figure 33. Concentrations of different bonds in C 1s for the transparent films with various discharge powers (1.0, 1.6, 2.8, and 4.5 W).

4.3.6 FTIR Analysis

The PMMA films deposited using the DBD jet with various powers are prepared on silicon wafers for FTIR analysis. For comparison, the FTIR spectrum of a pure PMMA is shown in Figure 34(a) [155]. Figure 34(b) presents the FTIR spectra (normalized with respect to the peak at 1730 cm^{-1}) of three deposited PMMA samples

with discharge powers at 1, 2.8, and 4.5 W. High retention of the functional groups in pure PMMA is observed in all the deposited films. The apparent peak of ester C=O stretch at 1730 cm^{-1} shows highly retained ester groups in the deposited PMMA films. The C–H stretches (3000-2850 cm^{-1}), C–H deformation vibrations of CH_2 and CH_3 (1480-1420 cm^{-1}), C–H bending modes in ester (1149-1192 cm^{-1}), and C–C rocking modes (750 cm^{-1}) are all comparable to those in the pure PMMA. It is seen that a peak at 1620 cm^{-1} appears in the plasma-polymerized films due to the C=O stretch of hydrogen bonded carboxylic acid [156]. It is likely due to the scission of some ester methoxy groups in MMA monomers, further creating a radical site and forming hydrogen bonded carboxylic acid groups by reaction with hydrogen radicals. A broad band between 3100 and 3600 cm^{-1} is also observed in the films deposited by the DBD jet due to hydroxyl groups. The hydroxyl groups could be attributed to the presence of alcohol or ether groups, as mentioned in the XPS analysis earlier. Besides, another broad band at 1060 cm^{-1}, which typically represents the C–O stretching vibrations of ethers and alcohols, provides the further evidence of the existence of ether/alcohol groups in the PMMA films deposited by the DBD jet. The FTIR results also show similar trends to the XPS results in the dependence of the concentrations of functional groups on discharge power. In Figure 34(b), which are normalized with respect to the C=O stretch of ester (1730 cm^{-1}), it is observed that the quantity of C–H stretches (3000-2850 cm^{-1}) increases with rising power, as shown in the inset. This implies that a higher discharge power used in the deposition results in more $–CH_n$ groups in the film, which agrees well with the XPS results in Figure 33. Thus, from the results of XPS and FTIR analysis, it can be

concluded that a plasma-polymerized film with similar characteristics to the pure PMMA can be obtained by the DBD jet technique at a relatively low temperature with a proper operation power.

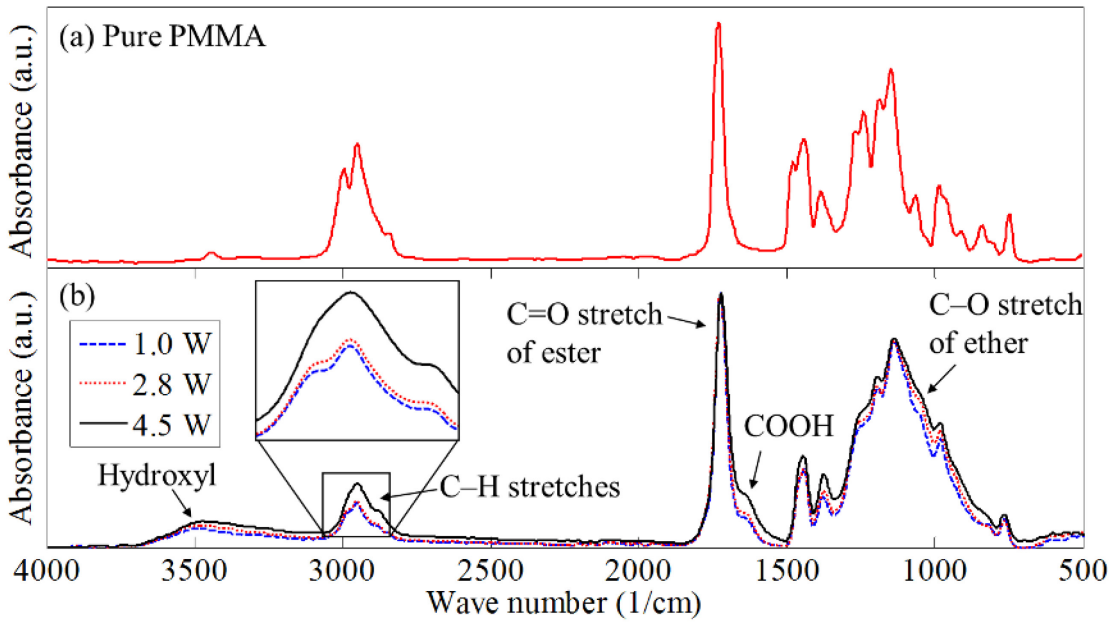

Figure 34. FTIR spectra of (a) pure PMMA [155] and (b) the deposited PMMA at 1.0, 2.8, and 4.5 W.

4.3.7 OES Analysis

Excited species generated from the DBD jet were detected by optical emission spectroscopy (OES). The light emitted from the DBD jet at the point 2.1 mm downstream of the dielectric tube end was collected and analyzed. To examine the effect of the MMA precursor on the excited species, pure He DBD jet was employed in the analysis before the MMA precursor was added. Figure 35 shows the resulting spectra of the He DBD jet at different powers (0.7, 1.7, and 3.0 W). The species observed in the He

DBD jet are mainly due to NO ($A^2\Sigma^+, \upsilon' - X, \upsilon''$), OH, N_2 second positive ($C^3\Pi_u - B^3\Pi_g$), N_2^+ first negative ($B^2\Sigma_u^+ - X^2\Sigma_g^+$), He, and O transitions. Note that all the spectra were normalized with respect to the nitrogen peak at 337 nm. As the applied power rises (from the diffuse mode to the concentrated mode), the intensities of the NO lines become stronger. However, the OH, N_2^+, He, and O lines are observed to be reduced with the rising power. The relative height between the lines of N_2 remains similar.

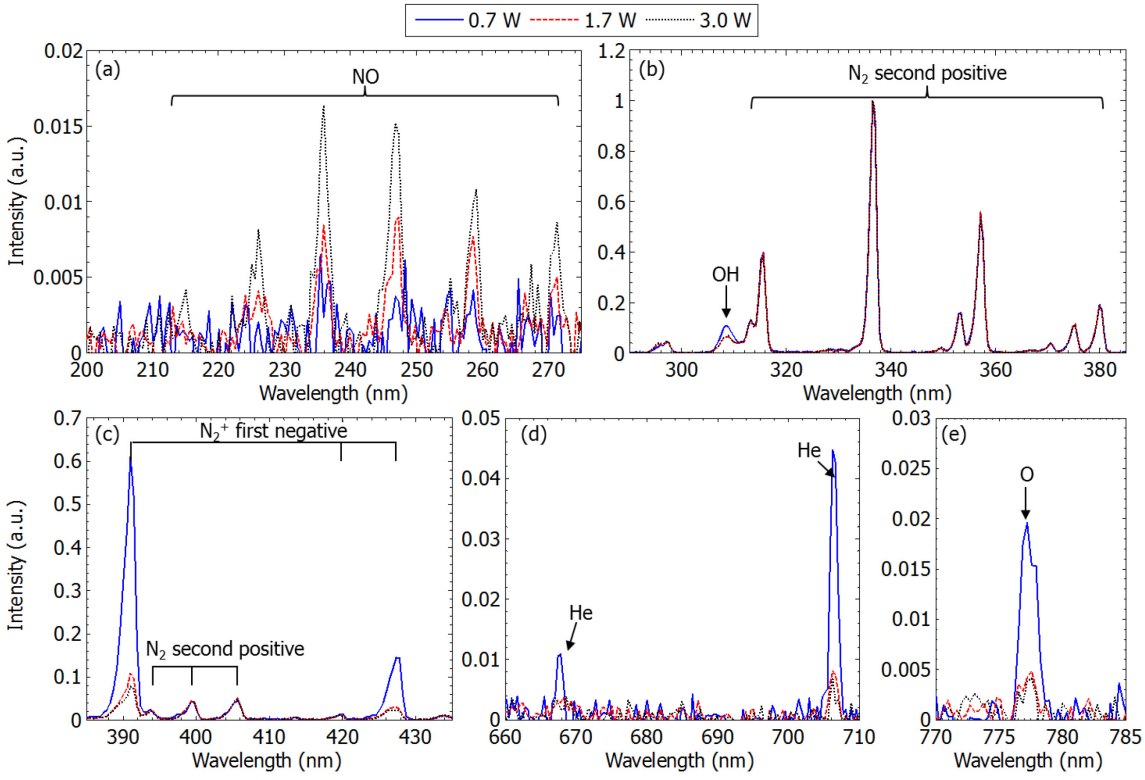

Figure 35. Optical emission spectra of He DBD jet at 0.7, 1.7, and 3.0 W: (a) 200–275 nm (NO), (b) 290–385 nm (OH and N_2), (c) 385–435 nm (N_2 and N_2^+), (d) 660–710 nm (He), and (e) 700–785 nm (O).

After the MMA precursor was fed into the He DBD jet, some disparity in the emission lines was observed Figure 36, compared with the case using pure He DBD jet. Figure 36(a) and Figure 36(b) shows that no NO emission lines (ultraviolet region: 200–275 nm) and OH line (308 nm), respectively, were detected regardless of the discharge power. Similarly to the results using He DBD jet, a higher discharge power leads to the reduction in the intensities of N_2^+, He, and O lines.

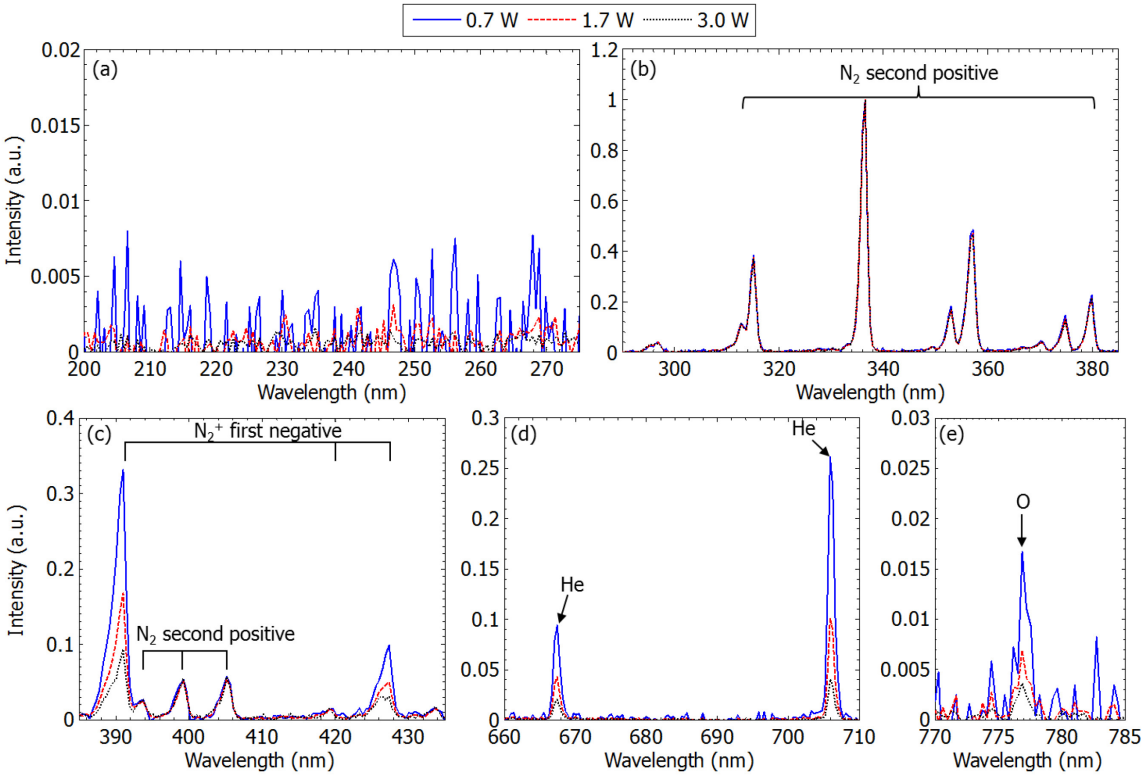

Figure 36. Optical emission spectra of He/MMA DBD jet at 0.7, 1.7, and 3.0 W: (a) 200–275 nm (NO), (b) 290–385 nm (OH and N_2), (c) 385–435 nm (N_2 and N_2^+), (d) 660–710 nm (He), and (e) 700–785 nm (O).

These OES results of the He DBD jet and He/MMA DBD jet both show that a higher applied power results in more intense light emitted from the nitrogen species (i.e., higher N_2/He ratio). This may indicate that more nitrogen molecules in the entrained air can be electronically excited by a stronger applied electric field. An increase in the discharge power also leads to a decrease of N_2^+ / N_2. It may be attributed to either a reduction in the nitrogen ion density or an increase in the electronic excitation temperature (T_{elex}) since the intensity of an emission line can be written as [157, 158]:

$$I_{n' \to n} \propto n_0 \cdot e^{-\frac{E_{n'}}{kT_{elex}}} \quad \textbf{(Equation 2)}$$

where $I_{n' \to n}$ is the intensity of the emitted light generated when an electron of an atom or molecule transitions from a higher excited energy state *n'* to a lower state *n*, n_0 is the density of the fundamental state, $E_{n'}$ is the upper state energy (cm^{-1} or eV), and *k* is the Boltzmann constant (0.695 $cm^{-1}K^{-1}$ or 8.617×10^{-5} $eV \cdot K^{-1}$). The value of $E_{n'}$ is readily available in the spectra database provides on NIST website [159]. Thus a further estimation of T_{elex} at various powers is required to determine whether a change in the intensity of an emission line is due to a change in the density of the corresponding species.

To show clearer comparison between the spectra of He DBD jet with and without the MMA addition, the OES results of He DBD jet and He/MMA DBD jet at 1.7 W were presented on the same plot in Figure 37. This result shows that the presence of MMA precursors in the He DBD jet inhibits the generation of NO and OH excited species. In

addition to the disappearance of NO and OH lines, the intensities of N_2^+ and He lines appear to be relatively stronger with the addition of MMA precursors.

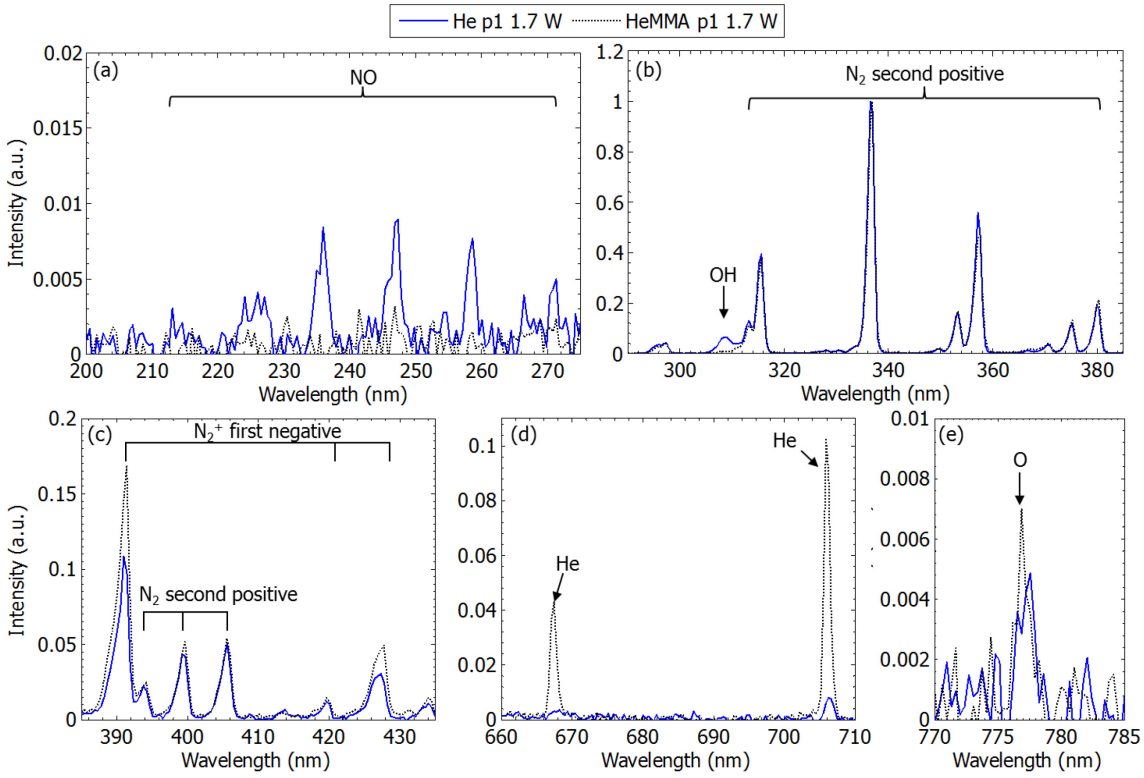

Figure 37. Comparison of optical emission spectra of He DBD jet and He/MMA DBD jet at 1.7 W: (a) 200–275 nm (NO), (b) 290–385 nm (OH and N_2), (c) 385–435 nm (N_2 and N_2^+), (d) 660–710 nm (He), and (e) 700–785 nm (O).

4.3.8 Various Substrates

It was observed that the discharge and the deposited film appearance show dependence on the types of the substrates used for deposition. Figure 38(a) [same picture as Figure 22(a)] and Figure 38(b) show the He/MMA DBD jet images at 1.0 W when a microscope slide and a silicon wafer were used as the substrates, respectively. The

plasma spot diameter (~6 mm) on the microscope slide appears larger than that (~2 mm) on the silicon wafer. Similar spot size to that on the silicon wafer was also observed when an aluminum sheet was employed as the deposition substrate. A relatively large plasma spot was observed on the microscope slide as the dielectric material (microscope slide) distributes the discharge over the entire surface (i.e., surface discharge) [7]. This is a common phenomenon in the DBD plasmas. In contrast, the conductive/semi-conductive substrates (e.g., aluminum and silicon wafer) allow the discharge current to flow through, leading to the plasma spot size similar to the dimension of the plasma jet. The plasma spot size further affects the growth area of the deposited film. Figure 38(c) [same picture as Figure 25(a)] and Figure 38(d) show the as-deposited PMMA films on the microscope slide and silicon wafer, respectively, for comparison. The PMMA film on the microscope slide is around 8 mm, whereas that on the silicon wafer is about 2 mm. Note that here we refer to the relatively continuous and uniform pattern formed directly downstream of the DBD jet as the "film" in the figure. These images indicate that the plasma spot size on the substrate determines the film dimension. The larger the discharge spot, the greater the continuous deposited film. This further confirms the results in Section 4.3.3, in which we showed that an increase in the discharge power (i.e., an increase in the plasma spot size) leads to the expansion of the film diameter. It can be observed from Figure 38(c) and Figure 38(d) that both deposited results contain the droplet-like patterns in the outer region. As shown in Figure 38(d), there exists an outer thin, continuous film between the film edge and the droplet-like patterns on the silicon wafer. Film thickness measurement using the profilometer shows that the thickness

(several micrometers) of the central film deposited directly in the plasma spot is significantly greater than that (several tens of nanometers to several hundreds of nanometers) of the outer thin film. The formation of the outer thin film is likely due to the presence of those longer-lived species in the plasma afterglow to activate the continuous film formation.

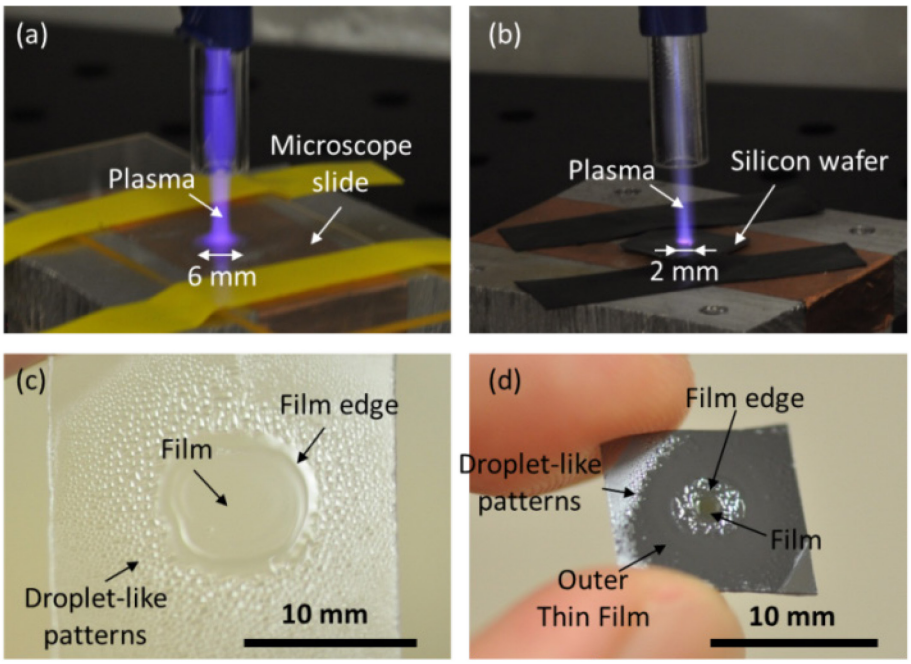

Figure 38. Comparison of images of (a) discharge on microscope slide, (b) discharge on silicon wafer, (c) as-deposited PMMA film on microscope slide, and (d) as-deposited PMMA film on silicon wafer at 1.0 W.

In order to demonstrate that this technique is suitable for temperature-sensitive substrates, various substrate materials, such as plastic, rubber, onion, and even fingernail, were employed in the PMMA deposition. Figure 39 shows the photos of the deposition results on these different substrates. In each case, a power of about 2–3 W is utilized to

generate the DBD jet within the transition regime, and as before the gap between the tube end and the substrate is set to 10 mm. As shown in Figure 39(a), a half-circle PMMA film can be observed on a sheet of transparent polyethylene plastic. The lower edge of the film is formed by covering a portion of the substrate with a tape mask during deposition. This makes the observation of the film clearer. Figure 39(b) presents the PMMA deposition result on a piece of EPDM rubber. No mask is used in this case since the difference between the film and the substrate can be easily distinguished.

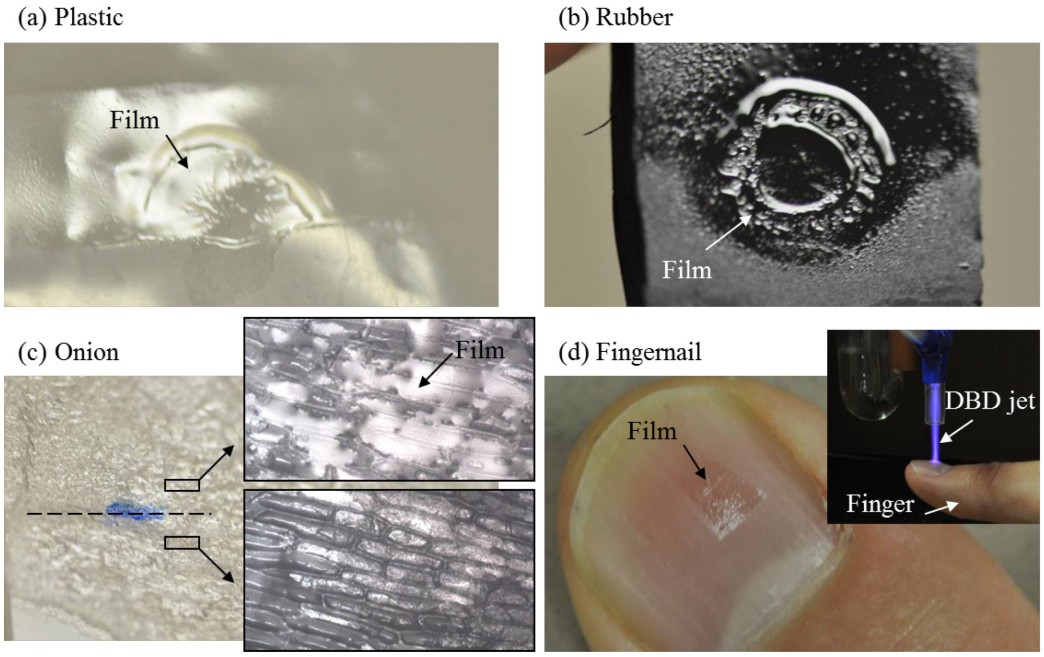

Figure 39. Photographs of PMMA deposition results on different substrates: (a) plastic; (b) rubber; (c) onion epidermis; (d) fingernail.

To gain an insight into the influence of the low-temperature DBD jet on the organic material, a piece of onion epidermis (a monolayer of onion cells) is also peeled

off and fixed to a microscope slide for PMMA deposition. Figure 39(c) displays the image of the onion epidermis after deposition. Masking using a cover slip was employed to facilitate visualization of the PMMA film edge indicated by the dash line on Figure 39(c). The region above the line is coated with PMMA, while the region below the line is uncoated. The clear difference between the coated and the uncoated surfaces can be seen by the insets, which are the images obtained by optical microscopy. Compared to the image of the uncoated part with distinct plant cells (bottom inset), the top inset clearly shows that there are PMMA films covering on top of the cells. Certain of the cell wall structures appear intact beneath the film layer. In deposition onto the cells certain yet unexplained non-uniformities are observed in the coating. Additional issues are the potential gas emission from the organic substrate which may cause porosity in the films. Furthermore, PMMA deposition is achieved on a fingernail, as shown in the inset of Figure 39(d). Tape was used as a mask to create the edge of the film for easy observation (not shown in the figure). A clear PMMA pattern on the fingernail can be seen in Figure 39(d) after 10 minutes of deposition.

4.4 Section Conclusions

A polymer deposition system by using a floating-electrode DBD jet was developed, which enables active plasma and energetic species to be generated in the vicinity of the substrate. This floating-electrode DBD jet deposition technique can be operated not only at atmospheric pressure but also in ambient air with a large gap distance from the tube end to the treated objects. Two distinct modes, which are diffuse

mode and concentrated mode, were observed in the DBD jet with the rising applied power. MMA was employed experimentally as the monomer for depositing PMMA films. The operation modes of discharge were found to result in different influences on the film deposition rates, while the deposition temperature increases linearly as the discharge power rises. The results showed that quite high deposition rate (22 $nm \cdot sec^{-1}$), which is 3-10 times higher than those in many prior works using atmospheric plasma jets as their depositing tools, can be attained with discharge power of 3.5 W and 39 °C deposition temperature. In addition to typical transparent PMMA films, opaque films with wrinkled microstructures can be obtained by using the concentrated-mode DBD jet with relatively high-power operation likely due to a buckling effect. High quality (RMS roughness is 0.4±0.1 nm) of the deposited transparent films was also demonstrated by SEM and AFM imaging techniques. Similar functional groups were observed comparing pure PMMA and the films deposited at different powers by using FTIR, though there are variations in the concentrations of different bonds in the films surfaces as the discharge power is changed. It was also shown that higher power operation leads to higher C:O ratio in the deposited films. Besides, the higher the power of DBD jet is applied, the less retention of ester groups and the higher concentration of the $–CH_n$ groups are observed. Additional C=O/O–C–O bonds were seen from the XPS analysis. This could be attributed to the scission of the ester groups in MMA monomers. The existence of ether/alcohol groups in the deposited films were also proven by both XPS and FTIR results. OES results showed the light emitted from the He DBD jet is mainly due to the NO, OH, N_2, N_2^+, He, and O transitions. It was also observed that the higher the

discharge power the weaker the N_2^+, He, and O lines relative to the N_2 lines. The MMA addition to the He DBD jet inhibited the generation of NO and OH excited species. By using this proposed ambient polymer deposition technique with floating-electrode DBD jet, rapid polymer film growth can be achieved on various types of temperature-sensitive substrates (e.g., plastic, rubber, onion, and fingernail) with similar characteristic features to the conventional polymer films.

5. COPPER FILM DEPOSITION AND CHARACTERIZATION

5.1 Introduction

After a detailed study of the PMMA film deposition, similarly, in this section we will report several experimental results of copper film deposition using $Cu(acac)_2$ precursors. The following subsection (Section 5.2) will present the methods used to grow and characterize the copper films. Section 5.3 shows experimental results, starting with the different operation modes observed in the $He/H_2/Cu(acac)_2$ DBD jet, compared to those observed in He/MMA DBD jet. It is then followed by the results on deposition rates, electrical resistivity, film morphologies, and the chemical characterization of the as-deposited copper films with respect to different discharge powers. Copper deposition on various substrates, such as glasses, silicon wafers, cardboard, and plastic, will be also presented.

5.2 Experimental Methods

Copper AP-PECVD using the helium DBD jet was achieved using the setup which has been shown in Figure 19 and the method to measure the electrical characteristics (e.g., applied voltage, discharge current, and discharge power) of the DBD jet was similar to that in the PMMA deposition experiment [Figure 16(a)]. The copper film thickness was obtained by measuring the film step height, created at the mask edge of films deposited on partially masked substrates after removing the mask, by

a stylus profilometer (KLA Tencor P-6). The measured film thickness along with its deposition time can be further used for the estimation of film deposition rates.

A two-terminal sensing technique was used for preliminary electrical resistance measurement of the deposited copper films, as shown in Figure 40(a). The resistance value was read through an ohmmeter (Fluke 115 Digital Multimeter) with 0.1-ohm resolution and ± (0.9% + 1) accuracy. For more accurate measurements four-terminal sensing can be employed in the future to eliminate the effects of contact resistance present in the two-terminal method. Electrical resistivity (ρ_{film}) can be computed by

$$\rho_{film} = C_1 \times R_{film} \times \frac{A_{film}}{L_{film}} \qquad \textbf{(Equation 3)}$$

where R_{film}, A_{film}, and L_{film} are the electrical resistance, cross-sectional area, and length of the deposited film, respectively, as illustrated in Figure 40(b). Note that R_{film} was calculated by subtracting the resistance of the probes (0.6±0.2 ohm) from the value read on the ohmmeter when the film was measured. The cross-sectional area (A_{film}) of the film can be obtained by multiplying the film width (W_{film}) by the film thickness (T_{film}), which was measured by the profilometer. $C_1 (\leq 1)$ is a calibration constant which is determined by the probe configurations. In our case using two pin-shaped probes, the electric current flowing from one probe to another one through the film can be drawn as shown in Figure 40(c) [160]. It can be seen that the current does not travel through the entire film. This results in a higher measured resistance, compared to the actual resistance of the film. Thus in this case C_1 is less than 1. However, it is difficult to determine the value of C_1. In order to simplify this question, we assumed that $C_1 = 1$ in all the following resistivity

estimations. When C_1 is equal to 1, it resembles the case with sensing probes contacting all the way across the film, as illustrated in Figure 40(c). Therefore, with this assumption, the actual electrical resistivity values of the deposited copper film are lower than those estimated resistivity results as presented in this section. Figure 40(d) shows the actual image of the simple, handmade two-terminal sensing device. A two-way pin header was employed as the sensing probes. The spacing ($L_{spacing}$) between the two pins was 2.5 mm. Samples coated with copper films were placed directly underneath the probes for electrical resistance measurement. In this case, $L_{spacing}$ was thus used as the film length (L_{film}) for resistivity computation (i.e., $L_{spacing} = L_{film}$).

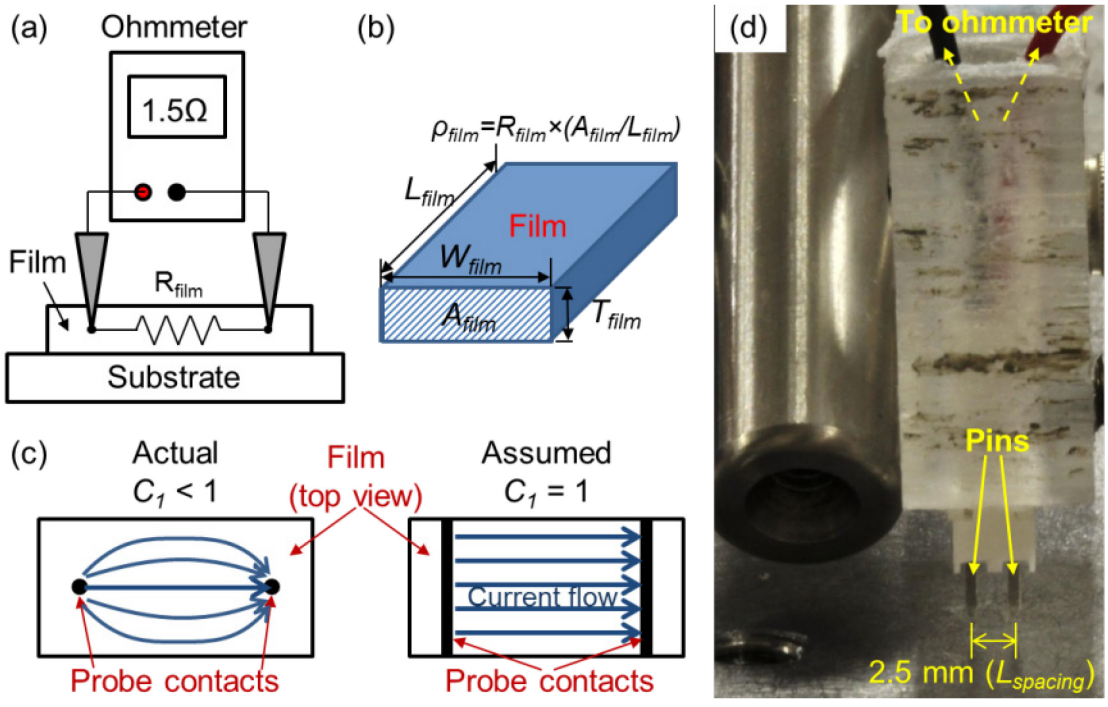

Figure 40. (a) Schematic setup of film resistance measurement using two-terminal sensing; (b) illustration of the electrical resistivity estimation for copper films in this study; (c) schematic top views of electrical current flows in the samples with different probe geometry; (d) image of the experimental setup for resistance measurement.

To visualize the copper film surface morphology, scanning electron microscopy (SEM, JEOL JSM-7500F) was utilized to acquire the images of the film surface. The chemical composition of the as-deposited copper film surface was analyzed by an X-ray photoelectron spectrometer (XPS, Kratos Axis Ultra Imaging). Optical emission spectroscopy (OES) was performed to detect the excited species in the DBD jet by using a USB spectrometer (Edmund Optics 64813, TE cooled USB spectrometer UV-VIS).

5.3 Experimental Results

In this subsection, different modes present in the $He/H_2/Cu(acac)_2$ DBD jet from those seen in the He/MMA DBD jet will be shown first. Similar to the previous section (Section 4) which reported the results of PMMA films, we applied various discharge powers to the $He/H_2/Cu(acac)_2$ DBD jet and investigated the deposition rates and chemical compositions of the as-deposited copper films obtained by different powers. The electrical resistivity of the copper films with respect to different powers was also measured and compared. Furthermore, copper film deposition on several temperature-sensitive substrates was achieved.

5.3.1 Operation Modes of $He/H_2/Cu(acac)_2$ DBD Jet

The operation modes of the $He/H_2/Cu(acac)_2$ DBD jet were studied when a helium flow rate of 2.9 slm, hydrogen flow rate of 0.1 slm, and a gap distance of 2.5 mm were used during operation. When the precursor temperature was set to be lower than 90 °C, it was found that the operation modes of the $He/H_2/Cu(acac)_2$ DBD jet were similar

to the He DBD jet and the He/MMA DBD jet; that is, a diffuse mode was observed in the $He/H_2/Cu(acac)_2$ DBD jet at lower powers and an increasing applied power led to the occurrence of a concentrated mode. The concentrated mode also includes a centered concentrated mode and an off-centered concentrated mode, as presented in Figure 22 in the prior section.

However, when the precursor container is heated up to 100 °C, a different operation mode instead of the concentrated mode was observed at a relatively high discharge power. It should be mentioned that in this case the diffuse mode is also followed by the transition from the diffuse discharge to the concentrated discharge as the applied voltage is increased. During the transition, as shown in Figure 41(a), in the $He/H_2/Cu(acac)_2$ DBD jet a concentrated discharge (plasma channel) can be seen along the central axis of the glass tube in addition to the diffuse discharge. If the precursor temperature is lower than 90 °C, further increase of the discharge power leads to a mode change to the centered concentrated mode. Nevertheless, in this case with a precursor temperature at 100 °C, the discharge starts to bend to form a curve and spin in the tube around the central axis with a rising power [Figure 41(b)], instead of the occurrence of a straight, centered concentrated discharge. This mode is referred to as a "helical mode" as the discharge exhibits a helical motion in the glass tube. A more detailed description and characterization about these mode changes in the $He/H_2/Cu(acac)_2$ DBD jet will be reported in Section 7.

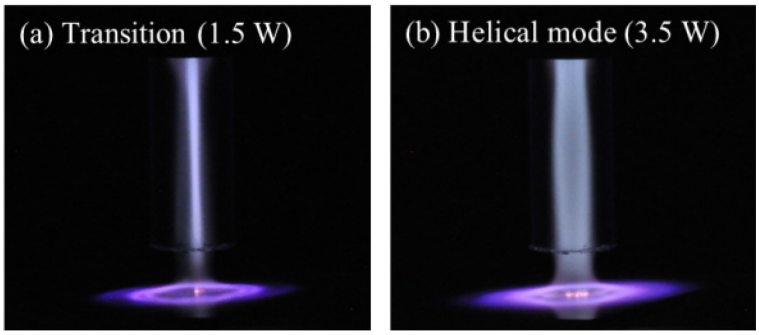

Figure 41. Plasma images (a) during transition at 1.5 W and (b) in the helical mode at 3.5 W observed in $He/H_2/Cu(acac)_2$ DBD jet when the precursor temperature was set to be 100 °C.

The discharge current waveforms over one complete voltage cycle of the $He/H_2/Cu(acac)_2$ DBD jet with a precursor temperature of 100 °C are given in Figure 42. Unlike the multiple current pulses observed in He/MMA DBD jet (Figure 23), only one broad current pulse was seen in this case regardless of the applied power. At 0.5 W in the diffuse mode, similar to that in He/MMA jet [Figure 23(a)], both the positive half cycle and the negative half cycle have a distinct current pulse [Figure 42(a)]. The current pulse in the negative cycle is comparable in amplitude to that in the positive cycle, whereas the negative pulse (~ 10 μs) appears to have longer duration than that of the positive pulse (~ 4 μs). As the discharge power rises, the current pulses in both the positive cycle and negative cycle last longer in duration, as shown in Figure 42(b). In the positive half cycle the broad current pulse with duration of ~ 7 μs contains several peaks. It was found that more and more subsequent current peaks, as indicated in the figure, were generated with the rising power, further broadening the current pulse. This result implies that there actually exist multiple current pulses at each positive half cycle and they overlap to form a broad current pulse. An increase of the discharge power results in

even broader current pulses in both the positive and negative cycles. Figure 42(c) shows the current waveform at 5.0 W in the helical mode. About eight subsequent current peaks, which form a ~10 μs broad current pulse, can be observed at the positive half cycle. A negative current pulse with longer duration was also obtained by the higher applied power. Though the current waveforms in the $He/H_2/Cu(acac)_2$ DBD jet are different from those seen in the He/MMA plasma, they are similar to the waveforms in the pure helium DBD jet (i.e., only one broad current pulse during each half cycle at any powers). Besides, similar current waveforms with only one broad current pulse at each half cycle were observed even if a lower precursor temperature was used. A further comparison of the discharge appearances and current waveforms in the pure He, He/MMA, and $He/H_2/Cu(acac)_2$ DBD jets will be given in Section 7. In this section we mainly focus on the characterization of the copper films obtained by the precursor temperature of 90 °C, with which no helical mode is induced.

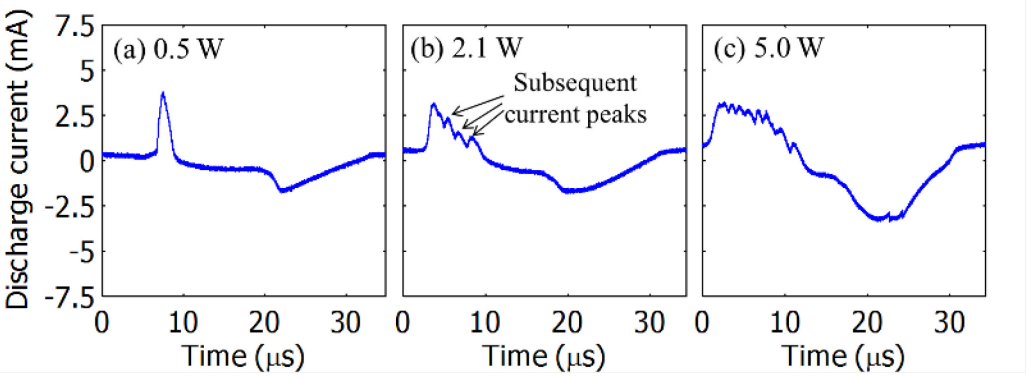

Figure 42. Current waveforms over one complete cycle in the $He/H_2/Cu(acac)_2$ DBD jet with a precursor temperature of 100 °C (a) in the diffuse mode (0.5 W); (b) during transition (2.1 W); (c) in the helical mode (5.0 W).

5.3.2 Copper Film Thickness Profile and Deposition Rate

The thickness of the as-deposited copper films using the $He/H_2/Cu(acac)_2$ DBD jet was measured by the profilometer. Figure 43(a) shows the image of an copper film on a microscope slide deposited using the 1.7-W $He/H_2/Cu(acac)_2$ DBD jet. The experimental parameters used were 2.9-slm helium, 0.1-slm hydrogen, 5-mm gap distance, 90-°C precursor temperature, and 30-min deposition time. Compared with the film after 10-min deposition shown in Figure 20(c), in addition to the three distinct regions (reddish brown, dark blue, and yellowish regions) a bright yellowish spot was observed at the center of the copper film after 30-min deposition, as can be seen in Figure 43(b). The bright yellowish spot was typically obtained when a relatively long treatment time was utilized. The left and right edges of the film were created by covering tape masks on the microscope slides in order to facilitate the film thickness measurement using the profilometer. Figure 43(b) also displays the stylus scanning path (dashed line from a to a') employed to obtain the film surface profile. The scanning result along a-a' is shown in Figure 43(c), which was obtained using the software accompanying the profilometer. The figure shows that the maximum thickness was seen at the film center and the film was thinner toward the edges. Additionally, the film center (i.e., bright yellowish spot) exhibits a profile with relatively bumpy surface, compared to the outer portions of the film. This indicates that the bright yellowish region is likely due to its rough surface structure. The average step height of the film center [the highlighted region by "R1" vertical cursors in Figure 43(c)] is about 199 nm as measured by the profilometer.

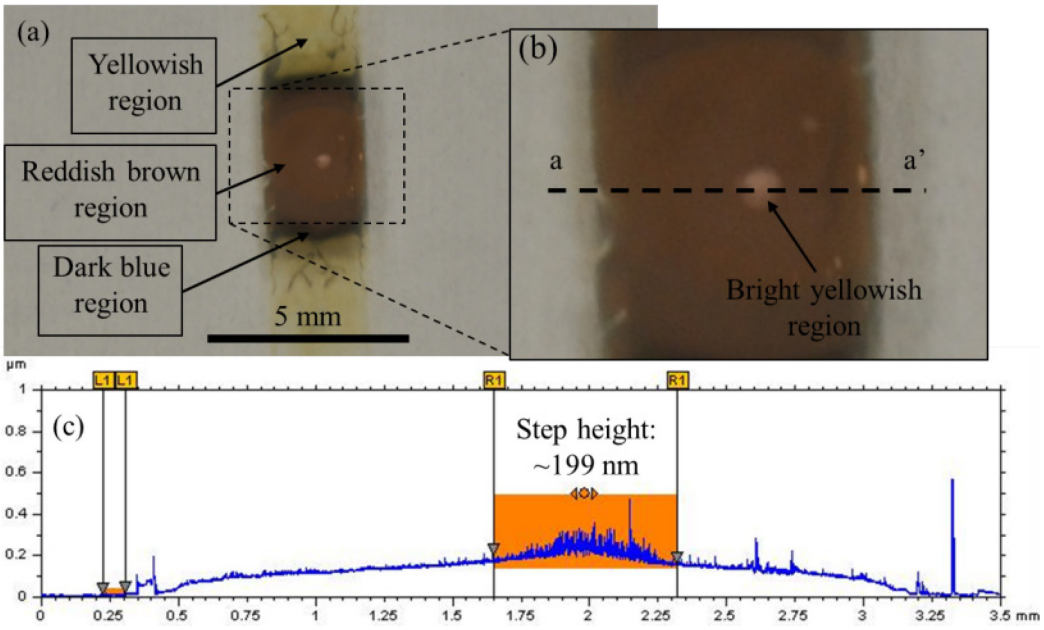

Figure 43. (a) Snapshot image of the as-deposited copper film using 1.7 W discharge, (b) magnified image of the copper film to show the scanning path (from a to a') of the profilometer, and (c) the corresponding surface profile along a-a' as measured by profilometer.

To get the thickness profile of the entire copper film including the three distinct regions, multiple scans were employed. Figure 44(a) shows the points (point A-I) measured by scanning spatially different positions for constructing the deposition profile of the copper film. Only the thickness at the right half of the film in Figure 44(a) was measured as the film growth should be nearly symmetric with respect to the center. These thickness data (from the film center to the outer film area) along the radial direction are plotted in Figure 44(b). The result shows that the film center (point A), which exhibits a rough surface, has the greatest thickness (~199 nm), as mentioned earlier. As the measured point was farther away from the center in the reddish brown region and closer to the dark blue region (points B-D), the obtained thickness was decreased. At a distance of around 2.4 mm away from the center (point E, ~0.2 mm

away from the dark blue region), a local maximum (~194 nm) in the thickness was observed. The thickness at the outer yellowish film region (points F-H) was seen to drop again. At point I (8 mm away from the center), where the film appeared transparent, a thickness of around 86 nm was still measured. These results imply that the deposited film is greater than 16 mm in diameter though the visible film region is relatively smaller. A similar thickness profile has been reported using a RF microplasma jet for a-C:H film deposition in [72], in which the maximum thickness of the film was observed to be located at 0.5 mm away from the film center when a relatively small gap distance (1 mm) was employed . When the authors used a 2-mm nozzle-to-substrate distance, the deposition had its maximum at the film center. It was suggested that the deposition profile mainly depends on the combination effect of plasma density and precursor density profiles. Thus, similarly, the plasma density, H_2 density, and $Cu(acac)_2$ density profiles in our DBD jet may determine the deposition rates at spatially different positions of the film. Since these density profiles vary along the axial direction of the dielectric tube, the gap distance between the tube end and the substrate surface affects the deposition profile.

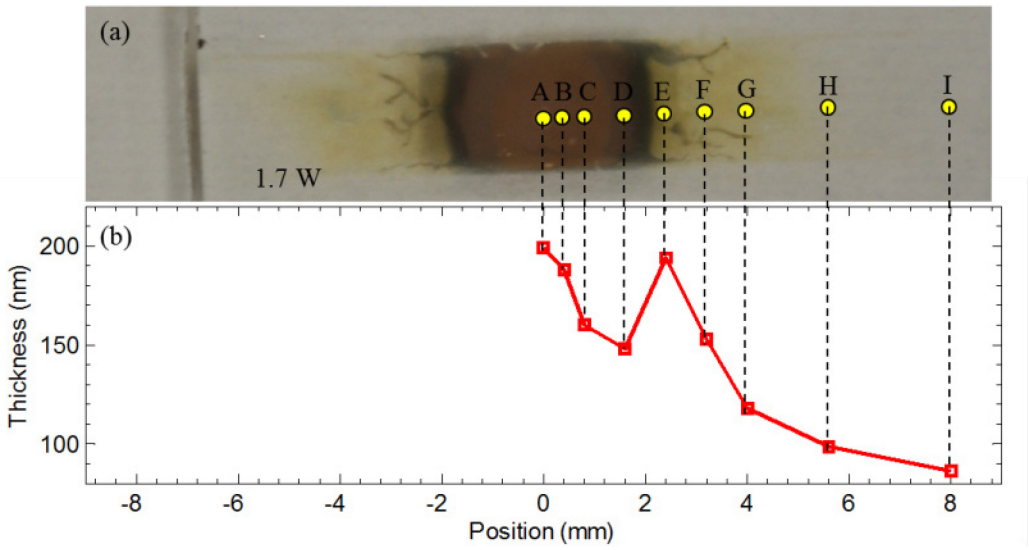

Figure 44. (a) Snapshot image of the copper film (1.7 W) showing several different positions measured by multiple scans using profilometer, and (b) the corresponding deposition profile of the right half of the film obtained by multiple scans using profilometer.

Deposition rates of the copper films obtained by varying discharge powers were also estimated. Copper films with discharge powers of 0.7, 1.7, 3.0, and 6.0 W were grown on microscope slides using, again, 2.9-slm helium, 0.1-slm hydrogen, 5-mm gap distance, 90-°C precursor temperature, and 30-min deposition time for the comparison of deposition rates. The images of the as-deposited films can be seen at the upper panel in Figure 45. As can be seen in Figure 45, similar to the prior result, most of the copper films exhibit a bright yellowish spot at their centers. This is likely due to the relatively high film growth rate (relatively great thickness) at the position under the center of the plasma jet. In the case using a discharge power of 3.0 W, the bright yellowish spot with a relatively great dimension can be seen due to the occurrence of the concentrated mode in the plasma discharge. The formation of the thin, bright plasma channel during the concentrated mode further increases the film deposition rate at the region directly treated

by the concentrated discharge. However, at 6.0 W more than one bright yellowish spots were observed since in this case the concentrated discharge was slightly unsteady in position instead of being fixed at the tube central axis. The concentrated discharge thus was not constantly located at the film center, resulting in the non-uniform growth of the copper film.

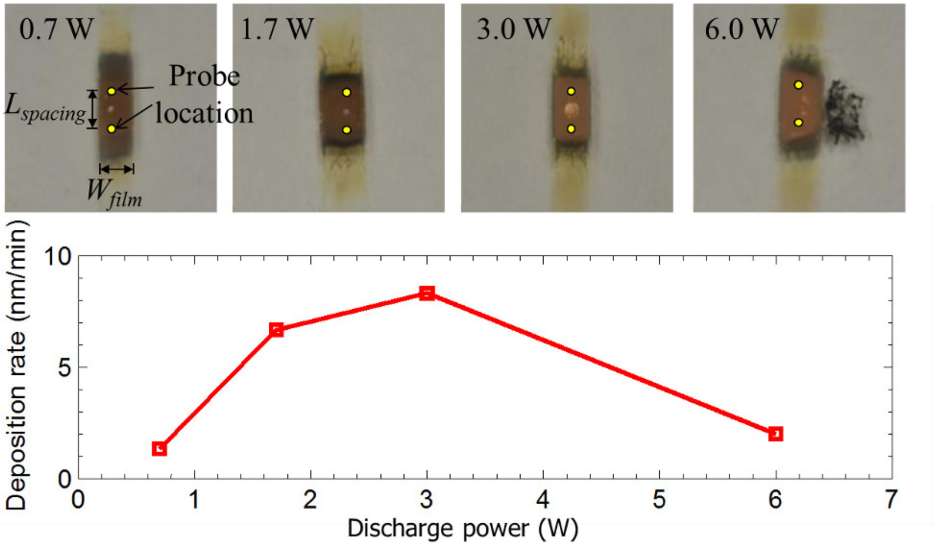

Figure 45. Snapshots (upper panel) of as-deposited films at different discharge powers and their corresponding deposition rates (lower panel).

For the deposition rate estimation, the thickness of the film center was measured. The copper film deposition rates with different powers can be seen at the lower panel of Figure 45. The copper deposition rates were in the range from 1 to 10 nm/min, which are much lower than those of PMMA films obtained using the He/MMA DBD jet shown in the Section 4. It is likely due to the fact that the vapor pressure of MMA is much higher than that of $Cu(acac)_2$ even though the $Cu(acac)_2$ was heated to 90 °C. The deposition

rate is increased when the power of the $He/H_2/Cu(acac)_2$ DBD jet rises from 0.7 W (diffuse mode) to 3.0 W (concentrated mode), whereas the rate drops at a power of 6.0 W. The growth rate increase is probably due to the formation of the plasma channel in the discharge as a higher power is applied. The relatively high intensity in the plasma channel enables more species generation, thus inducing more decomposition of the precursors and increasing the deposition rate. The decrease in the deposition rate at 6.0 W may be attributed to the spatial instability of the concentrated discharge and/or the occurrence of precursor depletion due to a higher deposition temperature induced by the higher power discharge.

5.3.3 Electrical Resistivity of Copper Films

Based on Equation 3, the measurement of the width (W_{film}), cross-sectional area (A_{film}) and resistance (R_{film}) of the copper film is required to obtain the film electrical resistivity. The copper films shown in Figure 45 were employed in the analysis. The width of the film, W_{film}, is thus that created by the tape mask, as indicated in Figure 45. R_{film} was measured using two-terminal sensing, as mentioned earlier (Figure 40). The locations the resistance sensing probes were placed at and the spacing ($L_{spacing}$) between the probes are also shown in Figure 45. It should be mentioned that only the films with reddish brown color are electrically conductive. The outer dark blue and yellowish regions of the film were found to have high resistance (non-conductivity) when measured. Similar to the CVD copper film in prior art [148], the films deposited using the DBD jet also exhibited dark blue color and are not conductive when the films are

relatively thin in thickness (i.e., grown using a short deposition time). The cross-sectional area, A_{film}, was computed by integrating the film thickness data, which were obtained using profilometer, over the film width. Table 3 summarizes these parameters of the as-deposited copper films at different applied powers. The variation on A_{film} shown in the table is attributed to the thickness difference at different positions of the film. The electrical resistivity (ohm-m) for each sample can thus be calculated using these parameters through Equation 3. Figure 46 displays the electrical resistivity values of these copper films. The error bars represent the uncertainties in the measurement of resistances (including the resolution and accuracy of the ohmmeter) and in the estimation of cross-sectional areas (A_{film}). The resistivity of bulk iron and that of bulk copper are also shown as the two dashed lines on the plot. It can be seen that all the copper films have resistivity values in the range between the resistivity of bulk copper (1.68×10^{-8} ohm-m) and that of bulk iron (1×10^{-7} ohm-m). This result shows that no significant change is observed in the resistivity of the copper films obtained by the $He/H_2/Cu(acac)_2$ DBD jet regardless of the applied powers though their deposition rates vary with different powers.

Table 3. Summarized parameters of the as-deposited copper films prepared for resistivity estimation.

Power (W)	W_{film} (m)	A_{film} (m^2)	$L_{spacing}$ (m)	R_{film} (ohm)
0.7	2.1×10^{-3}	5.4×10^{-11} – 12.9×10^{-11}	2.5×10^{-3}	1.9±0.2
1.7	2.7×10^{-3}	30.7×10^{-11} – 32.9×10^{-11}	2.5×10^{-3}	0.9±0.2
3.0	2.3×10^{-3}	7.5×10^{-11} – 15.2×10^{-11}	2.5×10^{-3}	1.4±0.2
6.0	2.5×10^{-3}	9.8×10^{-11} – 14.1×10^{-11}	2.5×10^{-3}	1.1±0.2

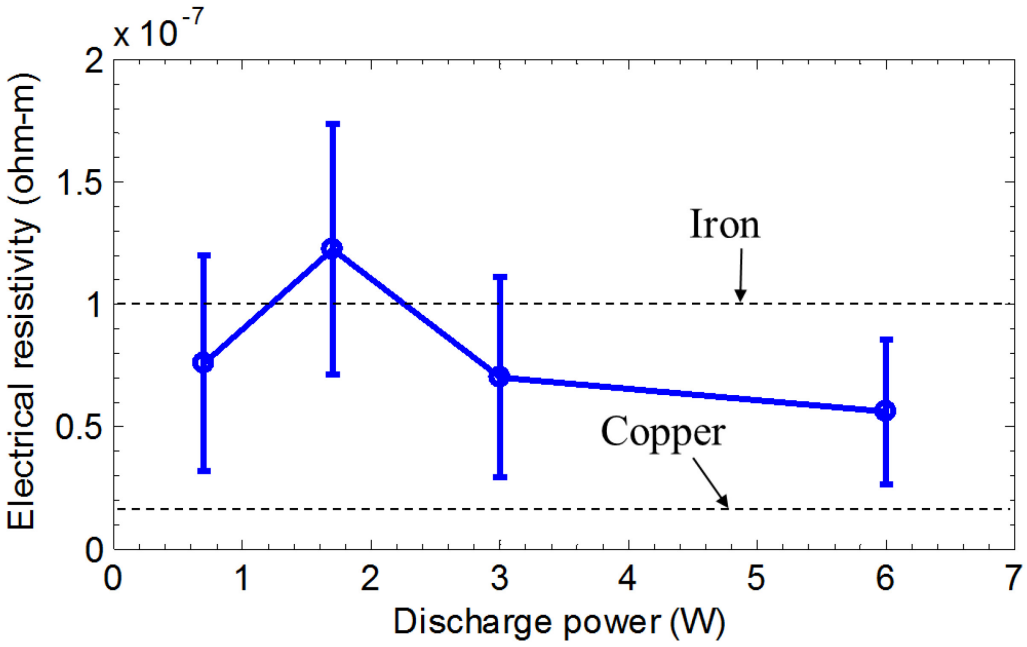

Figure 46. Electrical resistivity of the as-deposited copper films obtained by various powers.

5.3.4 SEM Analysis

The as-deposited copper film obtained by a helium flow rate of 3 slm, a hydrogen flow rate of 0.1 slm, a gap distance of 5 mm, a precursor temperature of 90 ºC, a power of 3 W, and a deposition time of 10 min was utilized for surface morphology observation using SEM. A snapshot of the copper film is shown in Figure 47(a). Figure 47(b) shows the SEM image of the film portion in the dashed box in Figure 47(a). Similar to the film image taken by the regular camera, the film appearance under SEM also exhibits distinct regions, indicating different surface properties at these regions. A magnified SEM image of the center of the main copper film region (point A) is given in Figure 47(c). It can be observed that the film in this region appears to consist of nano-grains, implying that the copper film is formed due to the island growth. Similar surface morphologies have been

shown in several prior studies using traditional CVD methods [161, 162]. The region in the dashed rectangle in Figure 47(c) is enlarged and shown in Figure 47(d) for better observation. It can be seen that the copper grain size is around 50 nm. Point B is at the dark blue region, on which a white ring-shaped pattern is also observed. A magnified SEM image of point B is displayed in Figure 47(e). Not only the grain-structured film is observed, but also visually relatively bright nano-particles exist on the film surface. These particles likely result in the observation of the white ring-shaped pattern. They may be formed in the helium stream when the gas-phase $Cu(acac)_2$ precursors reach the plasma zone, and blown to the edge of the main copper film region. However, the compositions of these particles are yet unclear and a further elemental analysis is required. The outer yellowish region has different surface morphology from that of the main copper region. Figure 47(f) shows the magnified SEM image at point C, where is the yellowish region between the dark blue filamentary patterns. A continuous film instead of grains is seen at this region. Similar to the image at point B, some particles are present on the surface of the dark film area. These results indicate that the brown reddish region (point A) and the dark blue region (region B) exhibit similar surface morphology (nano-grain structure) though visually they show distinct colors. In fact, these three regions also have various chemical compositions and the results will be reported in the next subsection using XPS.

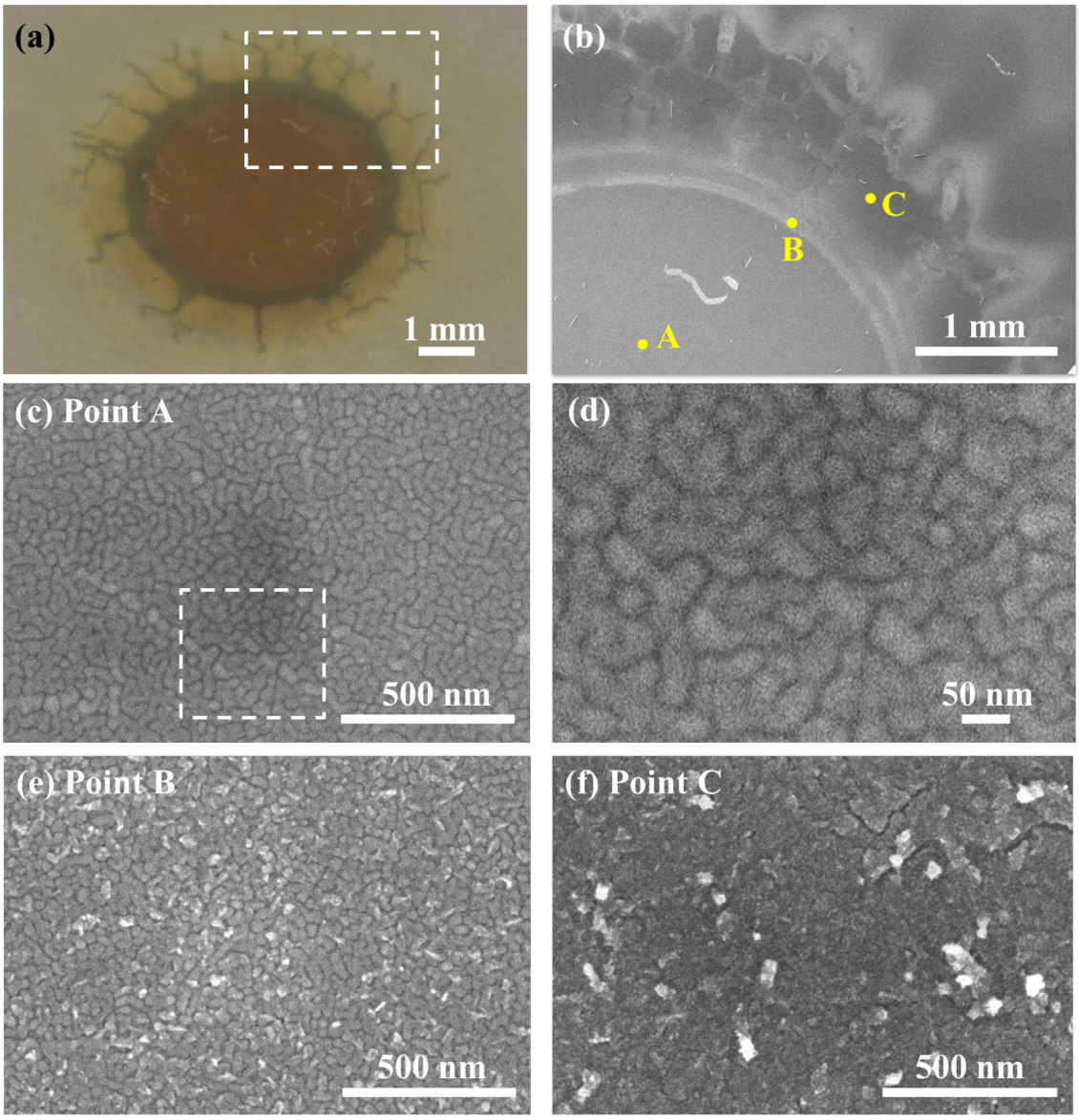

Figure 47. (a) Snapshot of copper film used in the SEM analysis and its SEM images at different positions: (b) the portion of the copper film in the dashed box in (a); (c) point A on figure (b); (d) magnified image of the dashed box in figure (c); (e) point B on figure (b); (f) point C on figure (b)

5.3.5 XPS Analysis

5.3.5.1 Spatial Variation

The copper film, which was prepared using 3-slm helium, 0.1-slm hydrogen, 5-mm gap, 90-ºC precursor temperature and 3-W discharge power, was analyzed by XPS to investigate the spatial variation in the chemical compositions of the film. Three points [A, B, and C as indicated in Figure 48(a)] on the film were selected for analysis to study the atomic concentrations of the central reddish brown region, the dark blue region, and the outer yellowish region, respectively. Point A is the center of the main copper film region (reddish brown region). Point B, about 2 mm away from the film center, is at the dark blue film region. A point (point C, 4.5 mm away from the film center) at the outer yellowish region was also selected in the analysis for comparison. The XPS analysis results can be seen in Figure 48(b). The main measured compositions are copper, oxygen, and carbon. The oxygen and carbon observed in the film can be attributed to the acetylacetonate ligands in the metal-organic precursor [$Cu(acac)_2$] used in this study. In all these three different positions, the major composition is copper (> 60 at.%). This result shows that all the three regions mainly consist of copper though they show different colors. At the film center [point A], where the film is reddish brown in color and is electrically conductive, the copper concentration is about 82 at.%, and the oxygen and carbon concentrations are about 10.7 at.% and 7.3 at.%, respectively. At the dark blue region (point B), a lower concentration of copper (69.6 at.%) but higher concentrations of oxygen (13.2 at.%) and carbon (17.2 at.%) were observed, compared to those in point A. Similar results were seen in point C, in which an even lower copper

concentration (63.5 at.%), a higher oxygen concentration (20.5 at.%), and a similar carbon concentration (16 at.%) were detected. These results show that under higher power treatment (point A) the film contains more copper and less oxygen and carbon. It has been shown that atomic hydrogen is the main species which induce the reduction of copper oxide in an atmospheric-pressure glow discharge [163]. Thus it is suggested that in our case more atomic hydrogen species are generated at the region with more intense plasma (e.g., point A), further leading to more complete precursor reduction and copper film deposition. It should be mentioned here that no detectable nitrogen signals from the ambient air were obtained by XPS. This may be due to the use of a small gap distance (5 mm) between the tube end and the microscope slide in this case. Thus the amount of air participating in the reaction may be too small to be measured.

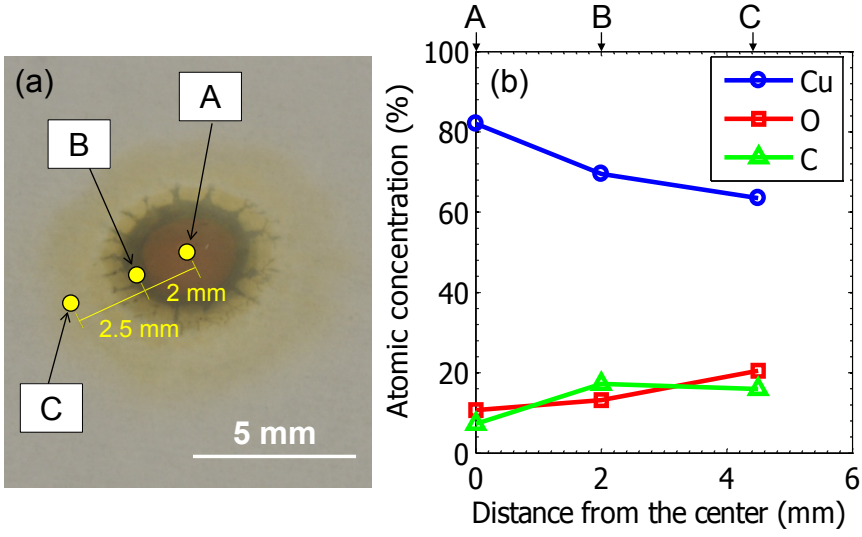

Figure 48. (a) Snapshot of the as-deposited film used for XPS analysis and (b) atomic concentrations of copper, oxygen, and carbon at the three corresponding different spatial locations [A, B, and C as labeled on figure (a)] in the copper film.

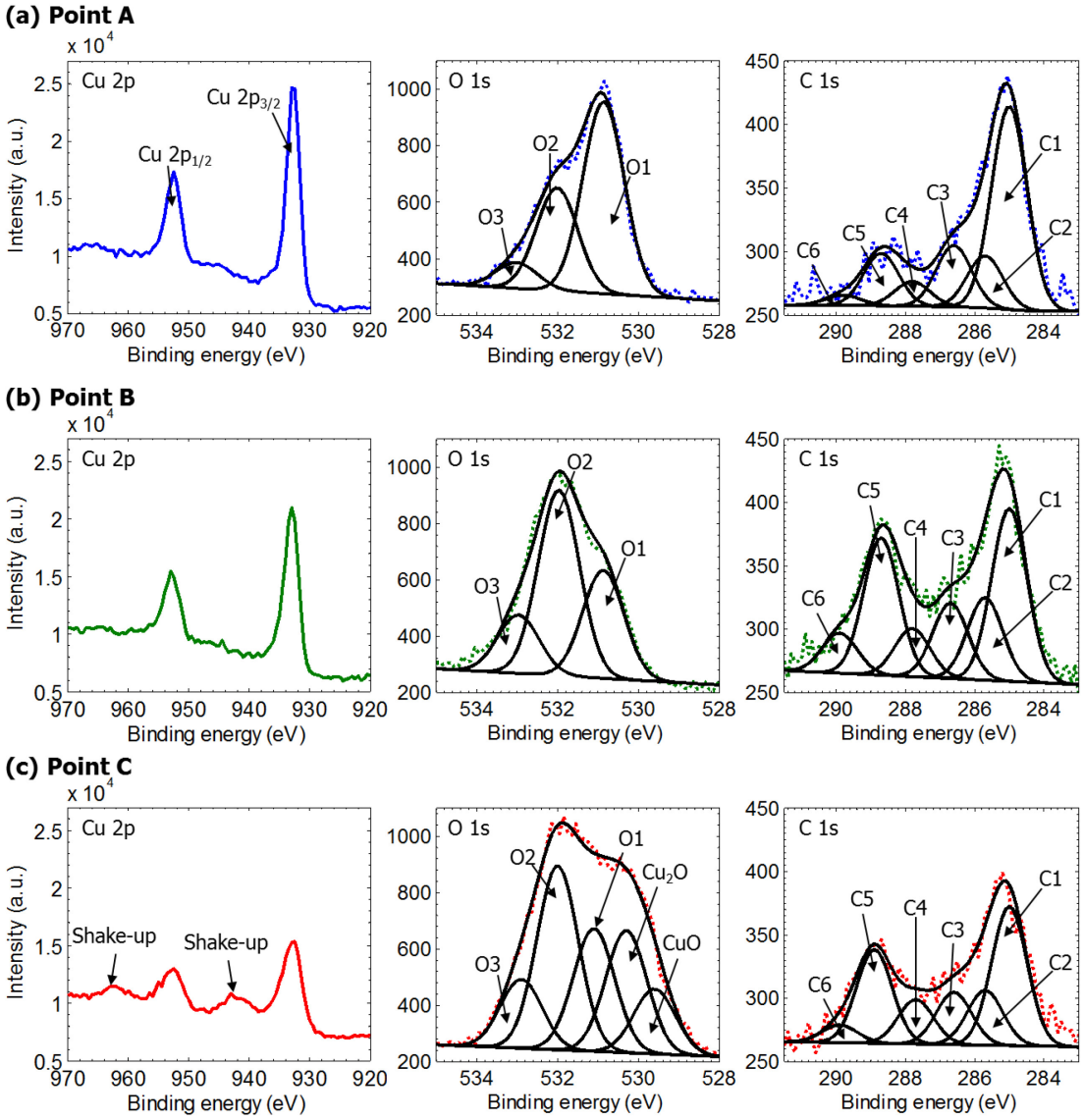

Figure 49. Cu 2p, O 1s, and C 1s XPS spectra of points (a) A (reddish brown region), (b) B (dark blue region), and (c) C (yellowish region).

Figure 49 shows the spectra of Cu 2p, O 1s, and C 1s obtained by XPS for the three different spatial points (A, B, and C) shown in Figure 48(a). The Cu 2p spectrum of point A (reddish brown region) exhibits two distinct peaks at 952.7 eV and 932.7 eV, which represent Cu $2p_{1/2}$ and Cu $2p_{2/3}$, respectively [Figure 49(a)]. This spectrum

indicates that the copper composition measured by XPS is due to the metallic copper on the surface of the reddish brown region [164-167].

More evidence regarding the presence of metallic copper instead of copper oxide at point A can be seen after the deconvolution of the O 1s spectrum. To obtain a good fit, three peaks at 531.3 (O1), 532.1 (O2), and 532.8 (O3) eV are required for the O 1s spectrum at point A in Figure 49(a). The O1 peak is typically attributed to the presence of the copper hydroxide [$Cu(OH)_2$] and/or copper carbonate ($CuCO_3$) on the surface [164, 165, 167-171]. $Cu(OH)_2$ may result from the adsorption of water from the ambient air and/or that generated during the hydrogen reduction of copper oxide [170, 172, 173]. It has been observed that the chemical reaction of copper with carbon dioxide (CO_2) from the ambient air causes the formation of $CuCO_3$ [169, 171, 174]. The O2 peak (O=C/O=C–O) is likely due to the acetylacetonate ligands of the $Cu(acac)_2$ precursors. The O3 peak, due to the alcohol (H–O–C) and ether (C–O–C) groups, can also be attributed to the acetylacetonate ligands. It can be found that the O2 peak appears higher than the O3 peak, which implies that after the reaction with plasma, the $Cu(acac)_2$ precursors tend to be decomposed into carbonyl groups (e.g., aldehyde, ketone, carboxylic acid, and ester groups) rather than alcohol or ether groups. However, no ester group (O=C–O–C) is observed as no peak at 533.7 eV is present in the O 1s spectrum. In addition, no peaks at 529.7 and 530.5 eV, which represent cupric oxide (CuO) and cuprous oxide (Cu_2O), are seen, showing that the copper composition at point A is mainly owing to metallic copper. The binding energies and the corresponding possible bond candidates for XPS deconvolution are summarized and listed in Table 4 [154, 164-

174]. It should be mentioned that a constant value of 1.2±0.1 eV was used for the full width at half maximum (FWHM) to deconvolve all the spectra in Figure 49.

The right panel of Figure 49(a) displays the C 1s spectrum with six carbon deconvolved peaks at 285.0, 285.7, 286.6, 287.7, 288.9, and 289.6 eV [154, 169, 171, 174], as listed in Table 4. The first five peaks can be attributed to the decomposition products of the acetylacetonate ligands. Besides the main peak at 285.0 eV showing the $–CH_n$ group (C1), the intensity of the peak at 288.9 eV (C5), representing O=C–O, is noticeable. The appearance of C5 group typically shows the existence of ester or carboxylic acid. Since the O 1s spectrum exhibits no ester group in this case, the C5 group mainly consists of the carboxylic acid (i.e., –COOH). It can be seen that the C5 concentration is higher than that of C4 peak (C=O or O–C–O). This indicates that more carboxylic acid groups than aldehyde and ketone groups are formed on the surface of the reddish brown film region due to the decomposition of the $Cu(acac)_2$ ligands. Additionally, in the C 1s spectrum a peak at 289.6 eV (C6) was detected, showing the existence of a small amount of carbonate groups ($CuCO_3$).

Table 4. Binding energies and relative bond candidates of the fitted C 1s and O 1s peaks in copper samples.

Spectrum	Peak	Binding Energy	Bond Candidates
		eV	
O 1s	CuO	529.7±0.3	CuO (Cupric oxide)
	Cu_2O	530.5±0.3	Cu_2O (Cuprous oxide)
	O1	531.3±0.4	$Cu(OH)_2/CuCO_3$
	O2	532.1±0.1	O=C or O=C–O
	O3	532.8±0.2	C–O–C or H–O–C
C 1s	C1	285.0	–CH_n (e.g., Methyl)
	C2	285.7±0.1	C–COOH (Carboxylic acid)
	C3	286.6±0.2	C–O
	C4	287.7±0.2	C=O or O–C–O
	C5	288.9±0.2	O=C–O (Carboxylic acid)
	C6	289.6±0.3	$CuCO_3$ (Carbonate)

At point B, the dark blue region, there still only exist two copper peaks (952.7 and 932.7 eV) in the Cu 2p spectrum [Figure 49(b)], while their intensities are relatively weak, compared with those at point A. This result shows that the surface of the dark blue region still mainly consists of metallic copper because, again, no copper oxide peaks (529.7 and 530.5 eV) are observed in the O 1s spectrum. However, the peak height of O2 signal (O=C/O=C–O) in the dark blue region is greater than that of O1 [$Cu(OH)_2/CuCO_3$] and the O3 peak also becomes comparable to the O1 peak, which is different from the case at point A. Both O2 and O3 peaks represent those oxygen-carbon functional groups which are mainly provided by the ligands of $Cu(acac)_2$. This implies that the deposited film at point B has more residual precursor ligands than those at point

A. The C 1s spectrum at this point also shows a different result, in which the C5 peak appears quite comparable to the C1 peak. The strong signals observed at both O2 and C5 peaks show that more carbonyl groups are deposited with the copper film, compared to the case at the reddish brown region. In addition, compared with the case at point A, a relatively higher concentration of the carbonate groups (C6) were observed in this region.

The Cu 2p spectrum at point C (outer yellowish region) shows the presence of two additional peaks at around 962 eV and 942 eV in addition to the two copper peaks [Figure 49(c)]. These two "shake-up" features can be attributed to the existence of CuO [i.e., so-called cupric oxide or copper(II) oxide, where the copper is in the +2 oxidation state] on the surface of the outer yellowish region [165, 175, 176]. In pure CuO the XPS peaks at 962 and 952.7 eV typically exhibit similar intensity. The relatively weak peak at 962 eV, compared with the Cu $2p_{1/2}$ peak at 952.7 eV, observed in this case is likely due to the coexistence of CuO, Cu (metallic copper), and/or Cu_2O [i.e., cuprous oxide or copper(I) oxide, where the copper is in the +1 oxidation state] [165, 167, 170]. The O 1s spectrum at this point requires two more peaks at 530.5 and 529.7 eV to obtain a good fit since a relatively broad spectrum was measured, as shown in Figure 49(c). These two peaks correspond to Cu_2O and CuO, respectively, further showing the coexistence of CuO and Cu_2O in this yellowish region. Note that the concentrations of O1, O2, and O3 in this region are similar to those in the dark blue region (i.e., O2 > O1 > O3). In the C 1s spectrum at point C, the $CuCO_3$ groups are also present and similar concentrations of the carbon functional groups to those at point B are observed; that is, the C5 peak is comparable to the C1 peak.

It has been shown that reduction of copper oxide to metallic copper can be achieved by UV radiation as well as atomic hydrogen [163, 165, 173]. Thus the presence of copper oxide at the outer yellowish region (point C) is likely due to the weaker intensity of the UV radiation and/or the lower concentration of the atomic hydrogen in the less-intense plasma region, where is farther away from the central axis of the tube. In contrast, the reddish brown region and the dark blue region are mainly composed of metallic copper probably because in these two regions, where are under and close to the direct plasma treatment, the hydrogen reduction of $Cu(acac)_2$ and copper oxide can be effectively induced by the sufficiently intense UV radiation and high atomic hydrogen concentration.

5.3.5.2 Different Discharge Powers

Copper films deposited using four different discharge powers (0.7, 1.7, 3.0, and 6.0 W), as shown in Figure 45, were also analyzed by XPS to study the effect of the plasma power on the elemental compositions in the film. The deposition of these copper films was achieved using 2.9-slm helium, 0.1-slm hydrogen, 5-mm gap, 90 ºC precursor temperature, and 30-min deposition time. The measurement was performed at the film center (reddish brown region) of each copper sample. Figure 50 displays the atomic concentrations of copper, oxygen, and carbon in the films obtained from the XPS analysis. At a power of 0.7 W (diffuse mode), 57.16 at.% copper, 22.38 at.% oxygen, and 20.46 at.% carbon were measured in the film. As a higher discharge power was used to deposit copper film, the copper concentration was observed to rise, whereas the

oxygen and the carbon concentrations dropped. When a discharge power of 6.0 W (concentrated mode) was applied, the concentrations of copper, oxygen, and carbon of 76.68, 12.27, and 11.05 at.%, respectively, in the as-deposited film were obtained. This result again demonstrated that a higher discharge power leads to the deposition of a copper film with higher purity. The impurities (i.e., oxygen and carbon) in the film can be reduced by the increasing power likely due to the fact that the higher power can cause more complete dissociation of acetylacetonate ligands from the $Cu(acac)_2$ precursors.

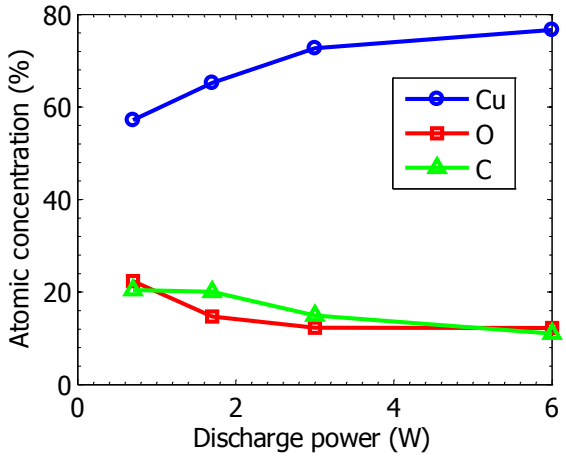

Figure 50. Atomic concentrations of copper, oxygen, and carbon in the copper films with various powers (0.7, 1.7, 3.0, and 6.0 W).

The detailed Cu 2p, O 1s, and C 1s spectra of the copper films deposited using different powers are shown in Figure 51. The Cu 2p spectra of all these samples show only two copper peaks at around 952.7 and 932.7 eV. Additionally, no copper oxide signals (i.e., CuO at 529.7 eV and Cu_2O at 530.5 eV) are observed in their O 1s spectrum. This result indicates that the copper compositions at the surfaces of these four

films detected by the XPS result from the metallic copper. It further demonstrates that the reason for the low electrical resistivity (~10^{-8} –10^{-7} ohm-m) measured in these films. Similar to the prior results, all these samples obtained by different powers contain not only metallic copper but also copper hydroxide, copper carbonate, and several different carbon-oxygen groups from the precursor ligands.

The XPS spectra after deconvolution show that the concentrations of functional groups depend on the discharge power. In the O 1s spectrum of the 0.7 W film [Figure 51(a)], the O2 peak (O=C/O=C–O) is seen to be higher than the O1 peak (hydroxide or carbonate groups). As the discharge power rises, the O2 peak is decreased in intensity and becomes lower than the O1 peak when the discharge power is 3.0 W or higher, as shown in Figure 51(c) and (d). It implies that the number of the aldehyde, ketone, and carboxylic acid groups is reduced with the rising power. Similar trend is observed in the C5 peak (O=C–O) in the C 1s spectrum; that is, higher discharge power leads to lower concentration of the O=C–O in the deposited film. These results are found to be similar to the results shown in Figure 49(a) and Figure 49(b), in which both the O2 and C5 peaks at point A, where is deposited by a higher discharge power, are weaker in intensity than those at point B. It shows that less carbonyl groups, which mainly come from the ligands of the $Cu(acac)_2$, are retained in the deposited film when a higher power is used. It thus can be concluded that a sufficiently higher discharge power is required for more efficient precursor decomposition.

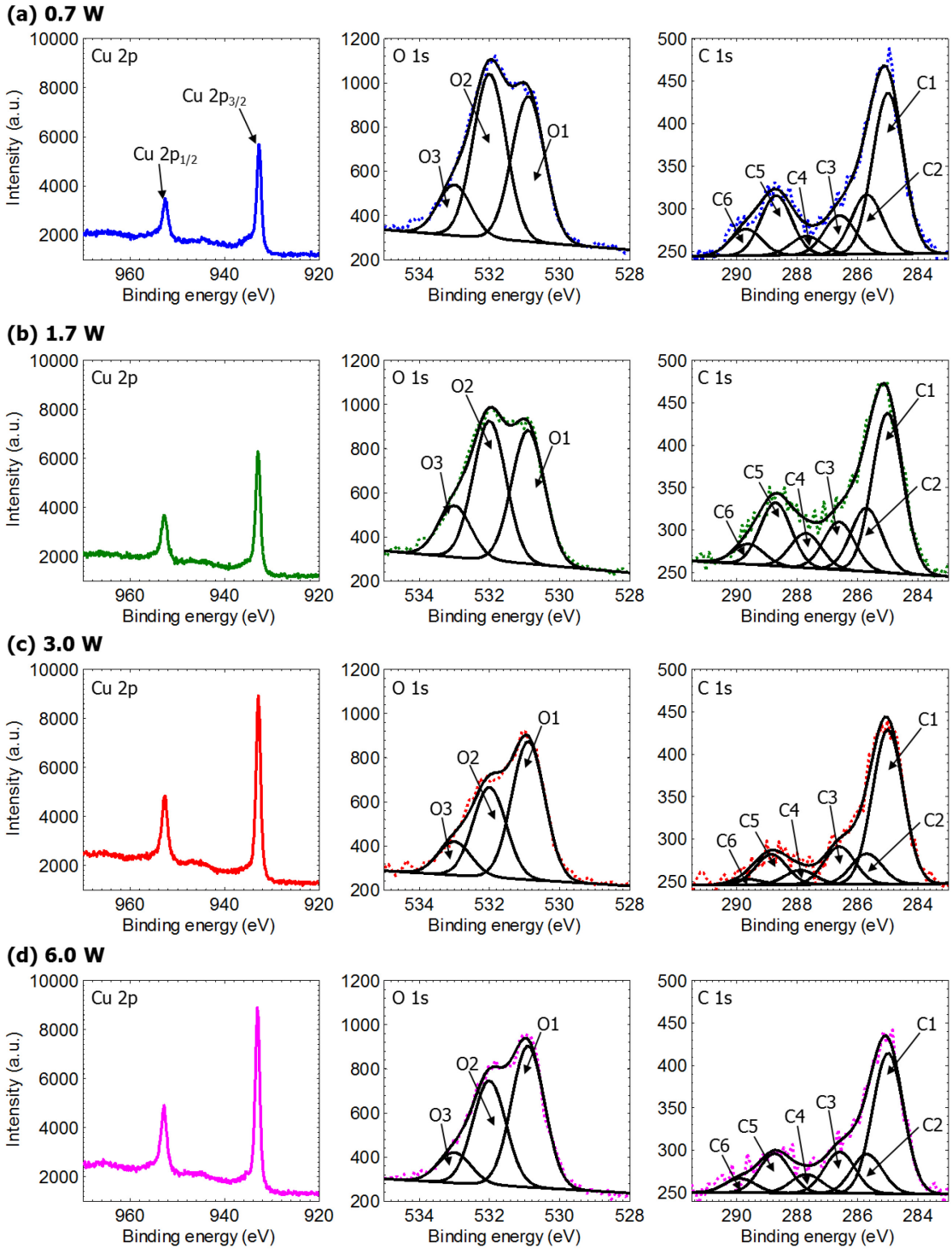

Figure 51. Cu 2p, O 1s, and C 1s XPS spectra of the as-deposited copper films obtained by discharge powers of (a) 0.7 W, (b) 1.7 W, (c) 3.0 W, and (d) 6.0 W.

It should be mentioned that the stability of the copper films obtained using the $He/H_2/Cu(acac)_2$ DBD jet were also compared to that of the films (with thickness < 100 nm) deposited by using thermal evaporation (PVD method). After deposition, we stored all the copper films in small plastic boxes, which were placed on a workbench in our laboratory. The plastic boxes resemble those plastic cases for pill/medicine storage, which are not controlled environments and similar to ambient air conditions. After being stored in the box for one day, the PVD copper coatings appeared to be dark brown in color instead of the reddish brown copper color, likely due to the oxidation of the copper films. Longer storage time (> 2 days) led to the presence of greenish color on the film surface. This usually indicates the copper corrosion, which can be attributed to the formation of copper carbonate (blue-green in color). Note that the PVD films with greater thickness can remain reddish brown shiny color for a longer period of time. In contrast, the DBD-jet-deposited copper coatings regardless of the thickness appear to be more stable than the PVD coatings. Visually no significant change in the appearance of copper films deposited by the DBD jet was observed after leaving them in the plastic box for several weeks. Even after almost one-year storage, the copper films still exhibited reddish brown shiny color though the films appeared to be slightly reduced in dimension and thickness, likely due to the occurrence of slow, gradual corrosion. A comparison between the images of the as-deposited film (0.7 W, same as the one in Figure 45) and the film after almost one year can be seen in Figure 52(a) and Figure 52(b), respectively. The relatively high stability observed in the copper films obtained using the $He/H_2/Cu(acac)_2$ DBD jet probably can be attributed to the formation of thin

polymer layers on top of the copper films. The polymer layers, which serve as the barriers preventing the underneath copper from being exposed to air, may be formed by the plasma polymerization of the functional groups of the acetylacetonate ligands in the $Cu(acac)_2$ precursors. The C 1s spectra shown in Figure 49 and Figure 51 are likely an indication of the presence of the polymer layer since the spectra resemble those detected in the PMMA films polymerized by the He/MMA DBD jet, as shown in Section 4.3.5.

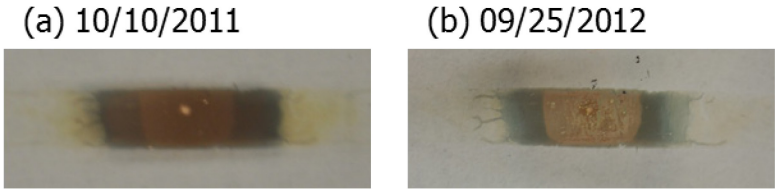

Figure 52. Comparison of the photographs of copper films at 0.7 W taken on (a) October 10, 2011 and (b) September 25, 2012.

5.3.6 OES Analysis

Optical emission spectroscopy (OES) was used to obtain the species generated from the $He/H_2/Cu(acac)_2$ DBD jet. The DBD jet in this study was generated by 2.9-slm helium flow, 0.1-slm hydrogen flow, 90 ºC precursor temperature, and 3-W discharge power with 5-mm gap distance. As shown in the insets in Figure 53, two different positions in the axial direction of the plasma jet were measured. The spectrum of the emitted light coming out of the glass tube portion at a height of 14 mm (upstream discharge) is displayed in Figure 53(a). The main excited species result from the atomic copper (324 and 327 nm) and atomic hydrogen (H_α at 656 nm). Several relatively small peaks at 308 (OH), 337 (N_2 second positive 0–0), and 486 (H_β) nm were also observed.

No signal with the wavelength smaller than 265 nm was seen as the glass tube served as a filter blocking most of the light below 300 nm.

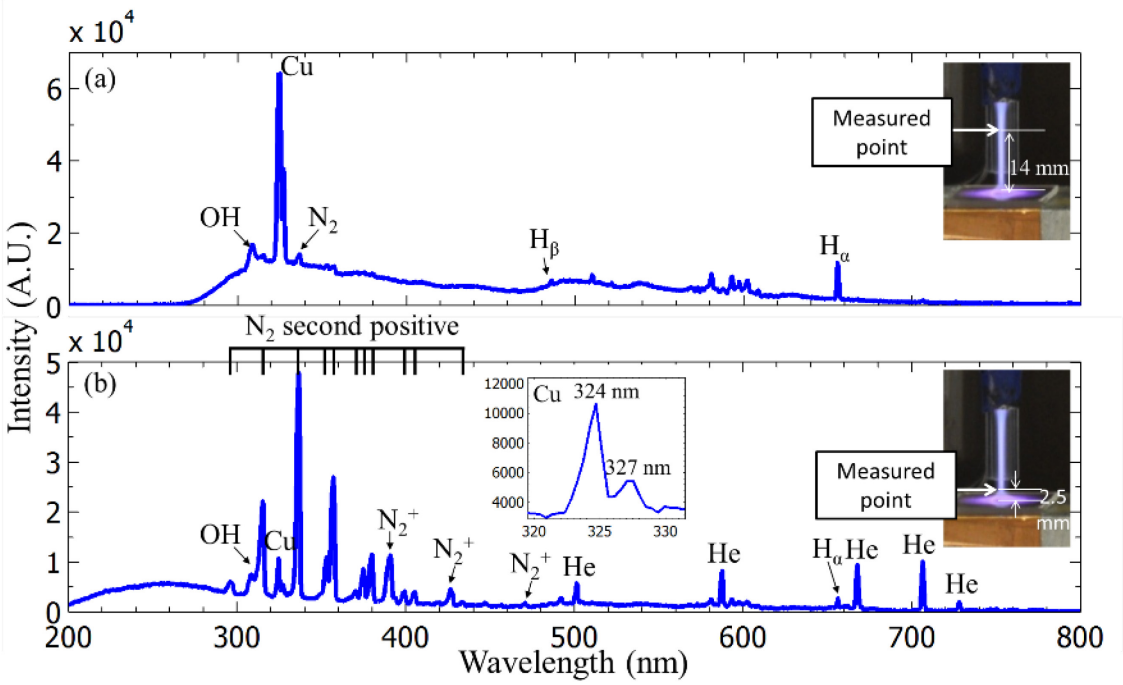

Figure 53. Optical emission spectra from 200 to 800 nm of the He/H_2/Cu(acac)$_2$ DBD jet at the measured points (a) 14 mm away from the substrate and (b) 2.5 mm away from the substrate.

When we measured the light emission from the downstream discharge in the ambient air at a height of 2.5 mm [Figure 53(b)], more abundant excited species were detected by the OES, compared with the case in the tube. In addition to the OH, copper, and hydrogen emission lines, the N_2 second positive transitions, N_2^+ first negative transitions, and atomic He lines are visible. The presence of N_2 second positive and N_2^+ first negative transitions with comparable peak heights can be attributed to the high concentration of N_2 in the entrained air. The appearance of the Cu atomic emission lines

in both upstream and downstream positions shows that the decomposition of $Cu(acac)_2$ precursors occurred and metallic copper was formed when the precursors reached the plasma zone. In addition, these results demonstrate that in our DBD jet there exists atomic hydrogen, which may be the species activating the precursor decomposition and inducing the copper film deposition.

5.3.7 Various Substrates

Similar to the PMMA deposition presented in the previous section (Section 4), various substrates were treated by the $He/H_2/Cu(acac)_2$ DBD jet for copper film deposition. Figure 54(a) shows the copper film growth on a silicon wafer. In this case, a helium flow rate of 1.5 slm, a hydrogen flow rate of 0.1 slm, a gap distance of 2.5 mm, precursor temperature of 90 ºC, a discharge power of 3.0 W, and deposition time of 10 min were employed to achieve the deposition. The dimension of the silicon wafer was around 1×1 cm^2. It can be seen that the reddish brown copper region on the silicon wafer is much smaller than that on the microscope slide. This result is similar to that observed using He/MMA DBD jet shown in Section 4.3.7, in which the PMMA film on the silicon is also smaller in diameter than that on the microscope slide. The dimension difference can be attributed to the electrical conductivity of the substrate. A smaller copper pattern formed on the silicon wafer is due to a smaller plasma spot on the more conductive substrate, compared with the case using the dielectric substrate (microscope slide). Temperature-sensitive substrates were also utilized in the copper deposition. The copper film deposition was achieved on a sheet of transparent polyethylene plastic, as shown in

Figure 54(b). In this case, we used 3 slm helium and 0.05 slm hydrogen as the working gas. The precursor temperature was set to be 90 ºC and the gap distance was 4 mm. An applied power of 3.0 W was employed to ignite the plasma. The film was obtained after 20 min deposition. It can be seen that the copper film was well-attached to the plastic substrate even if we bent the plastic sheet. The $He/H_2/Cu(acac)_2$ DBD jet was also applied to a piece of cardboard. The copper film growth on the cardboard is shown in Figure 54(c). The film deposition was accomplished using a helium flow rate of 3 slm, a hydrogen flow rate of 0.1 slm, a precursor temperature of 90 ºC, and a gap distance of 5 mm after 30 min at 3.0 W. Non-uniform copper film growth appears on the cardboard likely due to the fiber structures in the cardboard which provide a rough surface for deposition.

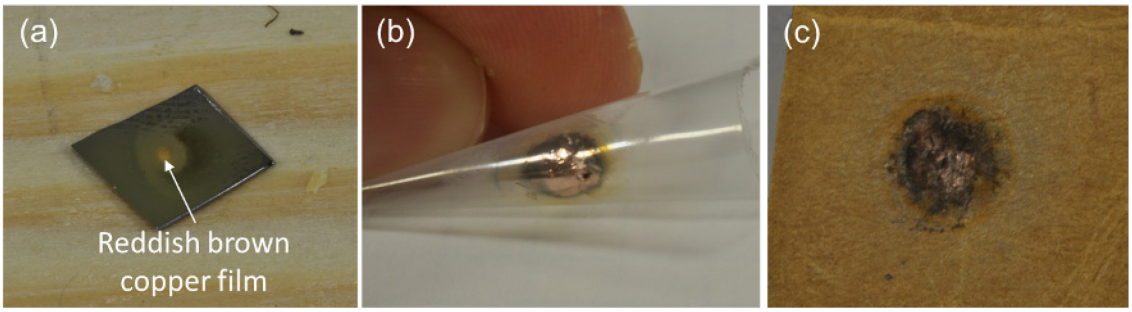

Figure 54. Copper film deposition on (a) silicon wafer, (b) plastic sheet, and (c) cardboard.

5.4 Section Conclusions

Deposition of metallic copper films were accomplished at ambient air conditions using the helium DBD jet with the addition of hydrogen and $Cu(acac)_2$ vapor, which was sublimed from its solid state at 90 °C. The change in the operation mode of the DBD jet

was observed with the rising applied power. Initially a diffuse mode was present at the low power. Higher power led to the transition to a concentrated mode, in which a plasma channel with relatively high intensity was formed. The mode change also showed dependence on the precursor temperature. When the precursor was heated up to 100 °C, a helical mode, in which the discharge bent to form a curve and spun in the tube around the central axis, occurred instead of the centered concentrated mode. The deposition profile obtained by the profilometer showed that in general the as-deposited copper film is thicker at the center and thinner toward edges. At a power of 3.0 W, a deposition rate of 8.3 nm/min and an electrical resistivity of $\leq 1\times10^{-7}$ ohm-m, which is close to that of bulk iron, can be obtained. Similar to those copper films deposited by traditional CVD methods, the films obtained using the $He/H_2/Cu(acac)_2$ DBD jet consisted of nano-grains (~ 50 nm in size), indicating the island growth mechanism. The XPS results showed that the surface of the conductive portion (reddish brown region) of the as-deposited film was mainly composed of metallic copper (60–80 at.% in total), rather than copper oxide, whereas carbon and oxygen (20–40 at.% in total) were still observed. The concentrations of the carbon and oxygen impurities, mainly attributed to the precursor ligands, can be significantly reduced by applying a higher discharge power. It was also shown that a higher power led to a lower concentration of the carbonyl groups in the film. In addition, the copper films exhibit better stability (more resistant to corrosion), compared to the copper films deposited using thermal evaporation. This $He/H_2/Cu(acac)_2$ DBD jet enables the copper films to be deposited on various substrates (e.g., glass, silicon, plastic, and cardboard) at low temperature.

6. FUNDAMENTAL STUDIES OF DBD JETS: PRECURSOR-DEPENDENT MULTIPLE BREAKDOWNS*

6.1 Introduction

In this section, we focus on the electrical, imaging and optical characterization of the multiple current pulses and the mode change observed in the floating-electrode helium DBD jet with the addition of MMA precursor gas (He/MMA DBD jet) when a dielectric substrate was placed downstream of the plasma. A helium-only DBD jet (He DBD jet) was also used for comparison. Resolving the temporal and spatial evolution of the discharges in the DBD jet was achieved by nanosecond resolved electrical, imaging and optical characterization methods. This section will show that each broad current pulse observed in both the He and He/MMA DBD jets is actually composed of several short-duration current pulses. Each short-duration current pulse is induced by a leading ionization wave and a plasma channel formed subsequently. The applied voltage influences the number of the short-duration current pulse, the time between the pulses as well as their spatial dimensions and brightness. The characterization of both the DBD jets with various discharge powers (and various operation modes) was performed and compared. This section provides several new results for the underlying physical mechanisms of a floating-electrode DBD jet as a film depositing tool with the presence of a substrate. The results in this section have been published in a recent paper [46].

*Part of this section is reprinted with permission from "Characteristics of Precursor-Dependent Breakdown in Helium Dielectric Barrier Discharge Jet" by T.-C. Tsai and D. Staack, 2012. *Plasma Science, IEEE Transactions on,* vol. 40, pp. 2931-2945, Copyright [2012] IEEE.

6.2 Experimental Setup and Methods

The experimental setup for generation and electrical characterization of the He/MMA DBD jet is similar to that in Figure 16(a) except the use of a thermocouple. Its schematic diagram is re-drawn here in Figure 55(a) for better illustration of the experimental methods in this subsection. Similar to the parameters used in the PMMA deposition, the helium flow rates of the working gas and carrier gas were set to 2.9 slm and 0.1 slm, respectively. A total helium flow rate combining the working gas and carrier gas was maintained at 3 slm. It results in a MMA concentration of about 1800 ppm in the helium gas stream. The mixture of helium and MMA then flowed into a floating-electrode DBD jet generator, as shown in the dashed box in Figure 55(a). A He DBD jet without MMA precursors at a flow rate of 3 slm was also used for comparison.

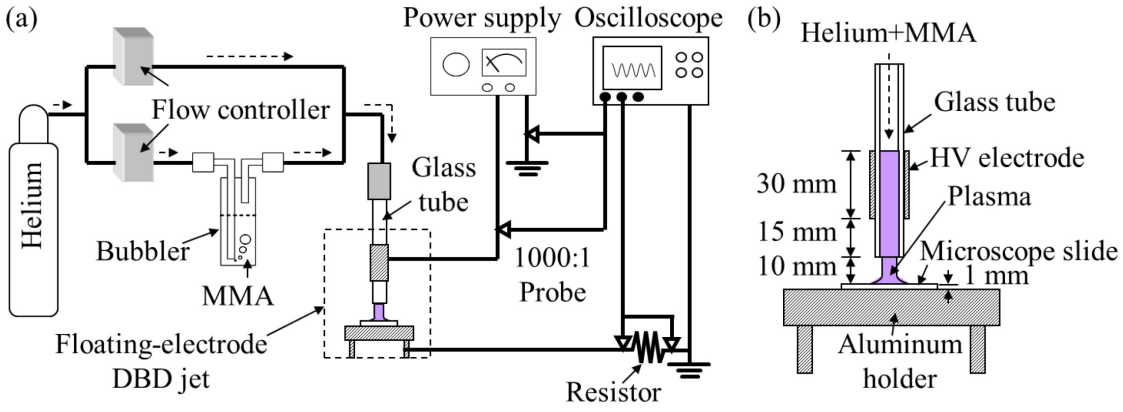

Figure 55. (a) Schematic diagram of the experimental setup used for generation and electrical diagnostics of a floating-electrode helium/MMA DBD jet; (b) schematic cross-section of the floating-electrode DBD jet in this study.

The detailed specification of the atmospheric-pressure floating-electrode DBD jet, which has been illustrated in Figure 16(b), is also re-drawn in Figure 55(b) and reiterated here. A borosilicate glass tube with 120 mm in length, 6.35 mm in the outer diameter, and 4.0 mm in the inner diameter was used as the dielectric barrier in the DBD jet. The glass tube was covered tightly by a 30 mm long metallic tube, which was employed as the high-voltage (HV) powered electrode and had its downstream end at a distance of 15 mm from the glass tube end. An aluminum holder was used as the second electrode (grounded or at a floating potential when a resistor is present for current measurement) and placed directly downstream of the tube end. A microscope slide with 1 mm thickness on top of the holder served as the second dielectric barrier and the substrate for PMMA film deposition. The distance between the glass tube end and the slide was set to 10 mm. The ignition of the plasma jet between the powered electrode and the slide surface was achieved using an AC high voltage (~kV) power supply with a frequency of 28.5 kHz. The applied voltage, discharge current and discharge power of the DBD jets were monitored and recorded by a LeCroy 204MXi (2 GHz) oscilloscope, as described in Section 3.3.1.

The light emission studies of the floating-electrode DBD jets were performed by using a photomultiplier tube (PMT, Hamamatsu R928, with rise time 2 ns), as displayed in Figure 56. The signal output of the PMT was also connected to the oscilloscope for comparison with the discharge current waveform. In order to obtain the time-resolved images of the ionization wave propagation and the discharge behavior in the DBD jet, a high-speed gated intensified charge coupled device (ICCD, Stanford 4Picos ICCD)

camera was utilized. For both PMT and ICCD measurement, a UV/Vis lens was employed to bring the light to a clear focus on the collector.

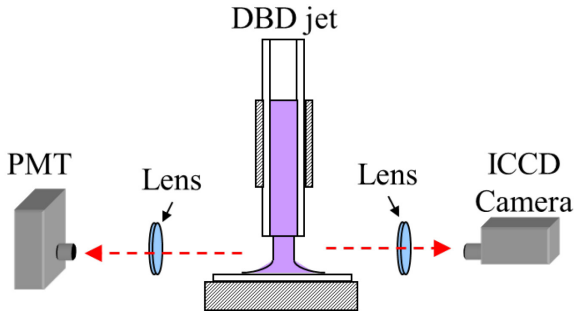

Figure 56. Schematic setup for measurement of photoemission and time-resolved images of the discharge.

6.3 Experimental Results

This subsection is divided into four parts, in which both the He DBD jet and the He/MMA DBD jet are presented and compared. The first part (Section 6.3.1) gives the experimental results regarding the visual appearance, the electrical characteristics of the operation modes, and the detailed current waveforms with respect to different powers in both DBD jets. And then it is followed by the time-resolved imaging results acquired by the ICCD camera showing the highly time-dependent variation in the discharges (Section 6.3.2). In Section 6.3.3, the PMT results are presented and used to correlate with the results obtained from the discharge current traces and the ICCD images. Finally the phenomena observed in the experimental results are discussed and several possible reasons are proposed in Section 6.3.4.

6.3.1 Operation Modes and Electrical Characteristics

During electrical breakdown, two distinct operation modes, namely a diffuse mode and a concentrated mode, were observed with the rising applied voltage. Figure 57(a)–(d) present the images of the He/MMA DBD jet with variations on the discharge appearance as the applied voltage is changed. Immediately after the DBD jet is ignited a discharge with diffuse color (diffuse mode) is observed, as shown in Figure 57(a). Similar appearance of a DBD jet with uniform color distribution has been reported in several studies [98, 108]. As the applied voltage is raised, the central axis of the discharge begins to be brighter than the outer parts of the discharge near the tube wall, as presented in Figure 57(b). The discharge at this point is in transition from the diffuse mode to the concentrated mode. The concentrated mode can be further divided into two types based on the discharge position; that is, centered concentrated mode and off-centered concentrated mode. Figure 57(c) displays the centered concentrated operation mode of the discharge by a sufficient increase of the applied voltage. The discharge appears to be a thin bright line located in the middle of the dielectric tube due to the contraction of the discharge in the radial direction. Further increase of the applied voltage results in the discharge movement from the tube centerline to the inner wall of the tube (off-centered concentrated mode), as can be seen in Figure 57(d). In this mode the direction in which the concentrated discharge moves is random and adjustment of the applied voltage can make the discharge shift to other positions on the tube inner wall. The reason for the variation on discharge position is yet unclear.

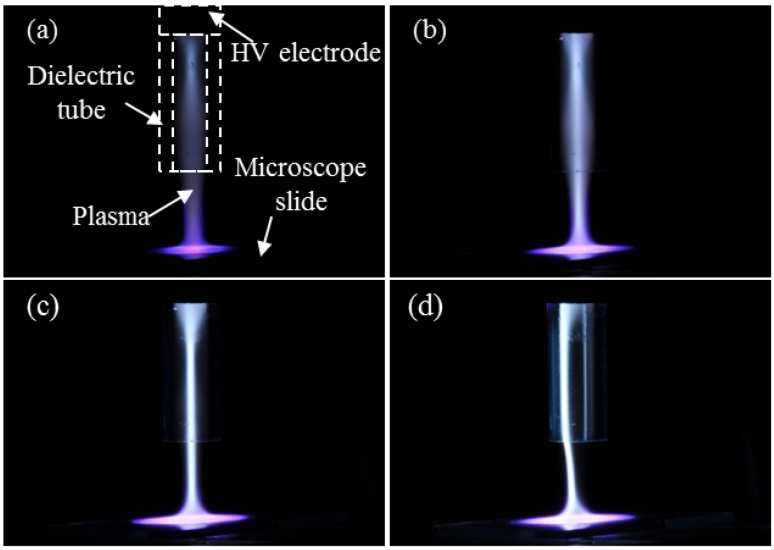

Figure 57. Types of discharge appearance using a digital camera with 4-s exposure time (a) in diffuse mode, (b) during transition, (c) in centered concentrated mode, and (d) in off-centered concentrated mode.

Figure 58 shows the spatial light intensity profiles of the discharges for the various operation modes. To avoid the saturation of the CCD pixels in the camera, shorter exposure time (1/15 s) was employed to acquire the discharge images for intensity estimation instead of the 4-s exposure time used for Figure 57(a)–(d). A region in the images extending from the dielectric tube exit to 0.5 mm downstream were used to calculate the intensity profiles as the reflection and refraction light from the dielectric tube influence the actual discharge intensity estimation inside of the tube. The intensity profile was obtained by taking an average of the grayscale values for each pixel and then calculating the mean value of each column of pixels. It can be seen from Figure 58 that the intensity profile is narrower and has a greater peak value when the operation mode changes from the diffuse mode to the concentrated mode. The off-centered concentrated discharge is observed to be located at –1.4 mm in this case.

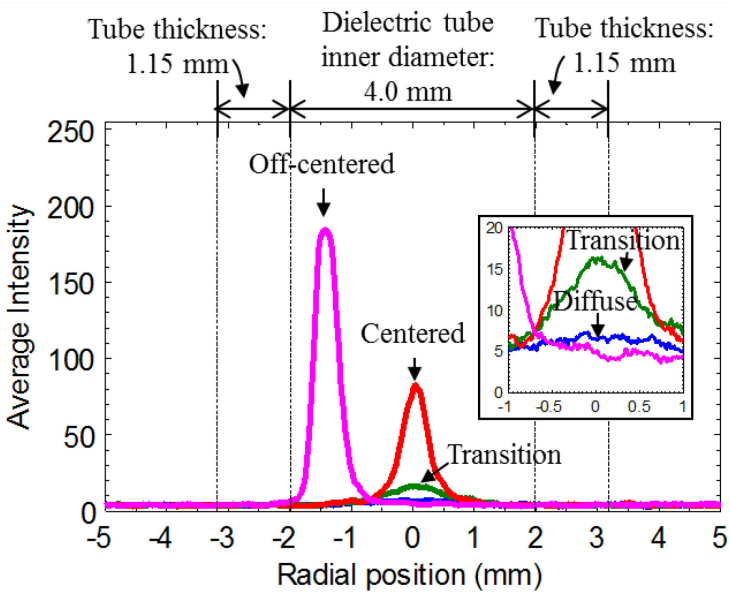

Figure 58. Intensity profiles of the discharge images at different operation modes.

Both the He DBD jet and He/MMA DBD jet have the mode change in their discharge appearance but visually with slightly different colors. The mode change in the discharge was found to significantly depend on several parameters, such as the precursor type, the precursor concentration, the position of the powered electrode, the nozzle-to-slide distance, the dimension and the material used in the dielectric tube, the parasitic capacitance in the circuit and the conductivity of the material placed on the holder. The occurrence of the off-centered concentrated mode is especially sensitive to these parameters. It was found that the off-centered concentrated mode can occur directly after transition without occurrence of the centered concentrated mode when different gap distance, precursor concentration, or various experimental parameters are employed.

The He DBD jet and the He/MMA DBD jet show different relationships between the root-mean-square (RMS) applied voltage and the discharge power though similar

operation modes were observed in both of them. It can be seen from Figure 59 that the He DBD jet requires lower applied voltage (RMS voltage of ~2 kV) for discharge breakdown, compared to the 2.5-kV RMS voltage required in the He/MMA DBD jet. This result indicates that precursors in a He DBD jet increase the required electric field for discharge breakdown, as might be expected. Additionally the different operation modes in both cases result in distinct slope changes in the data lines. As can be observed in the He DBD results, in the diffuse mode the power appears to increase exponentially with the RMS voltage up to around 1.3 W. It then exhibits nearly linear growth during transition and its slope increases to about 5 W/kV in the concentrated mode. Dashed trend lines along with their fit equations (obtained by a least squares method in Matlab) are shown on Figure 59 to assist in identifying the mode changes. These results imply that the electrical conductivity of the discharge in the He DBD jet is altered by the mode change. The concentrated mode has higher electrical conductivity than the diffuse mode. The trend (two distinct slope changes) in the He DBD jet is repeatable and similar to that observed by Walsh *et al.* although a metallic substrate was used in their study [108]. A slope change in the data curve is also observed in He/MMA DBD jet. Compared to the case in the He DBD jet, in the diffuse mode in the He/MMA DBD jet the data line increases linearly with a slope of around 0.6 W/kV, although in the transition and the concentrated modes, it has a slope comparable to 5 W/kV. Similar steep inclines of the data lines in the centered and off-centered concentrated modes are seen in both the He DBD jet and the He/MMA DBD jet. It may indicate that the electrical conductivity of the discharge shows no significant dependence on the position of the concentrated

discharge. The horizontal error bars show the variation on the RMS voltages in multiple measurements when the discharge powers were set to those desired values. It should be reiterated that the mode change is very sensitive to the experimental parameters mentioned previously. Therefore, the lines for differentiation between modes in Figure 59 may be located at different positions if some parameters are altered. The results shown in Figure 59 were measured immediately after the dielectric tube was cleaned (carefully controlled electrode surface properties) and the bubbler for the MMA monomer was refilled to a preset level (corrected the minor variations in precursor concentration).

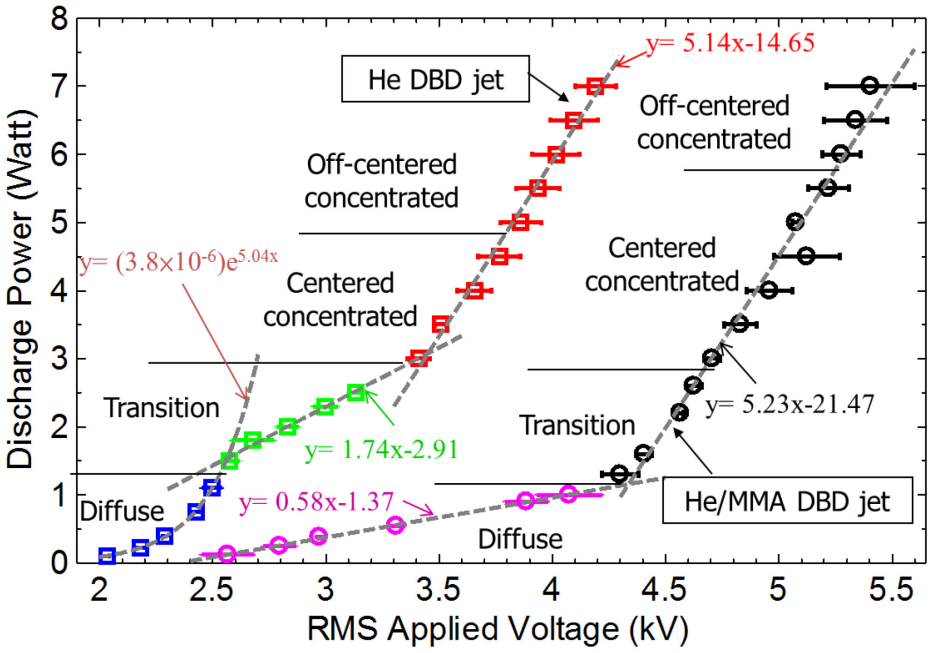

Figure 59. Discharge powers in the He DBD jet and the He/MMA DBD jet as a function of the RMS applied voltages.

Figure 60(a)–(d) show the waveforms of the He DBD jet at the powers of 0.7, 1.7, 3.0, and 6.0 W, respectively. At 0.7 W in the diffuse mode [Figure 60(a)], sporadic ignition is observed in each cycle, i.e., not every cycle has one current pulse in this mode. It should be noticed that the positive half cycle always has a more distinct current pulse than the negative half cycle likely due to the asymmetric electrode geometry in our DBD jet. As the applied voltage is increased, the probability of occurrence of the current pulses grows. When the discharge enters the transition to the concentrated mode, almost every positive and negative cycle has a current pulse but with different magnitude, as shown in the case at 1.7 W in Figure 60(b). Current pulses with similar magnitude are then observed when the discharge power keeps rising and the breakdown is seen to be periodic at the driving frequency. After the operation mode switches to the concentrated mode with the rising power, the duration of current pulses in the positive half cycles appears to be wider than those in the diffuse mode, as displayed in Figure 60(c) with a power of 3.0 W. Also, the current pulses in the negative cycles become comparable in magnitude. A power of 6.0 W in the He DBD jet leads to the off-centered concentrated mode, and its current waveform [Figure 60(d)] shows greater amplitude and longer duration in the current pulses, compared to those at a lower power.

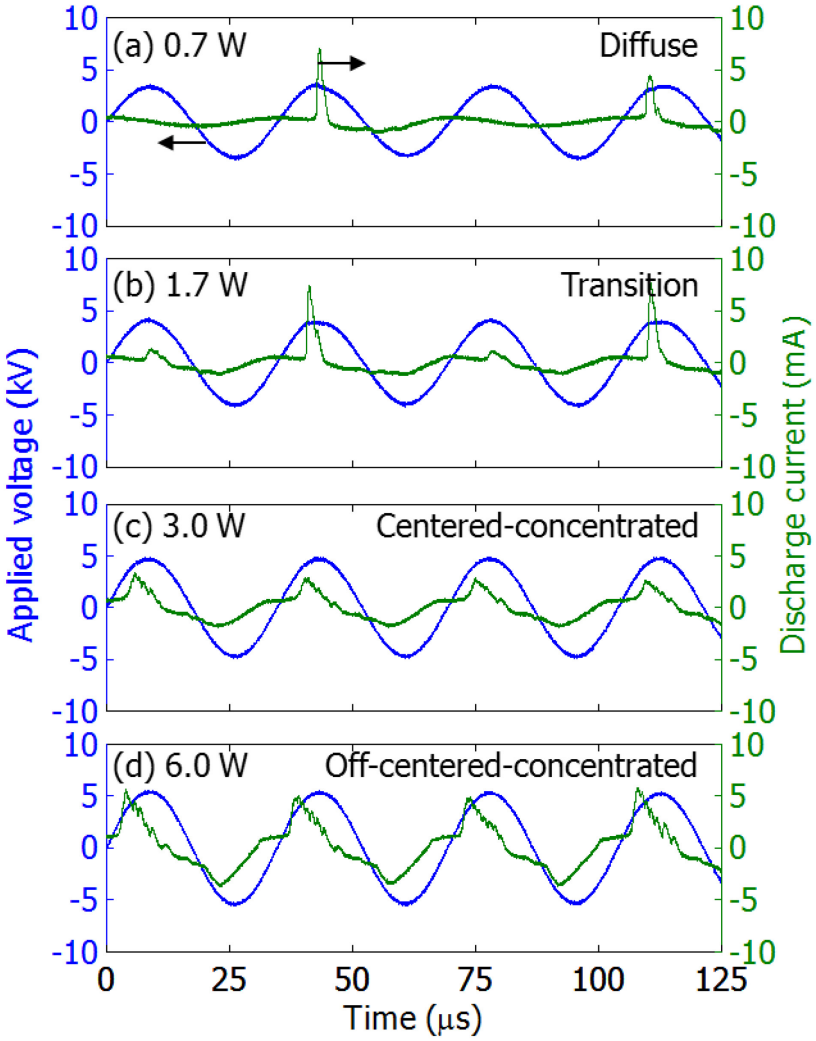

Figure 60. Voltage and current waveforms of He DBD jet at (a) 0.7 W, (b) 1.7 W, (c) 3.0 W, and (d) 6.0 W.

The voltage and current waveforms with identical power settings in the He/MMA DBD jet are given in Figure 61(a)–(d). Different current waveforms are observed in this case. At 0.7 W in the diffuse mode [Figure 61(a)], one current pulse is seen within each positive half cycle. However, one or two current pulses appear in each negative half cycle. Different from the case in the He DBD jet, these current pulses in the negative

cycle are comparable to those in the positive cycle in the He/MMA DBD jet. When the discharge power is increased and the He/MMA DBD jet enters the transition condition, second pulses appear in the positive half cycles sporadically. Besides, the probability of occurrence of the second pulses in the negative half cycles grows with the rising voltage and finally two current pulses with different magnitude are observed in each negative half cycle with sufficient applied voltage. One example at a power of 1.7 W during the transition can be seen in Figure 61(b). As the power rises, similar to the pulses in the negative half cycles, the second pulses occur in the positive half cycles more frequently. Eventually two strong pulses in every positive half cycle are always observed when a relatively high power is applied and the discharge switches to the concentrated mode, as shown in Figure 61(c) with a power of 3.0 W. Also, in this case every negative cycle has three distinct current pulses. Further increase of discharge power can generate the third pulse in each positive half cycle. Figure 61(d) shows three strong current pulses in both the positive and negative cycle at 6.0 W. From these results, it can be concluded that in both cases (He DBD jet and He/MMA DBD jet) the higher applied voltage results in the longer duration of discharge breakdown in each half cycle. Additionally, in the He/MMA case, it is seen that the number of pulses in the negative half cycle grows faster than that in the positive cycle. There is a stochastic nature to the breakdown in transitional modes nonetheless the average behavior and observable trends are repeatable.

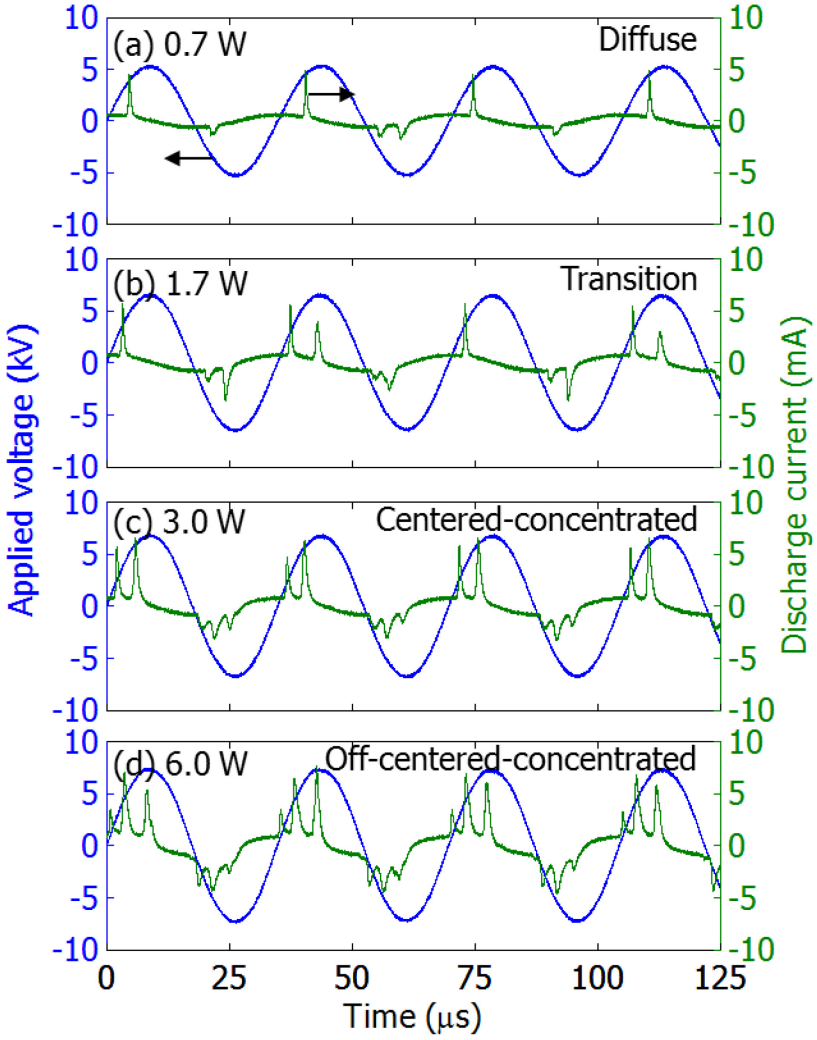

Figure 61. Voltage and current waveforms of He/MMA DBD jet at (a) 0.7 W, (b) 1.7 W, (c) 3.0 W, and (d) 6.0 W.

For a better understanding of the 'structure' of the discharge current pulses and the evolution of the current waveforms with respect to the power, the current waveforms over one complete cycle at various powers in Figure 60 and Figure 61 are extracted and re-plotted in Figure 62 for comparison.

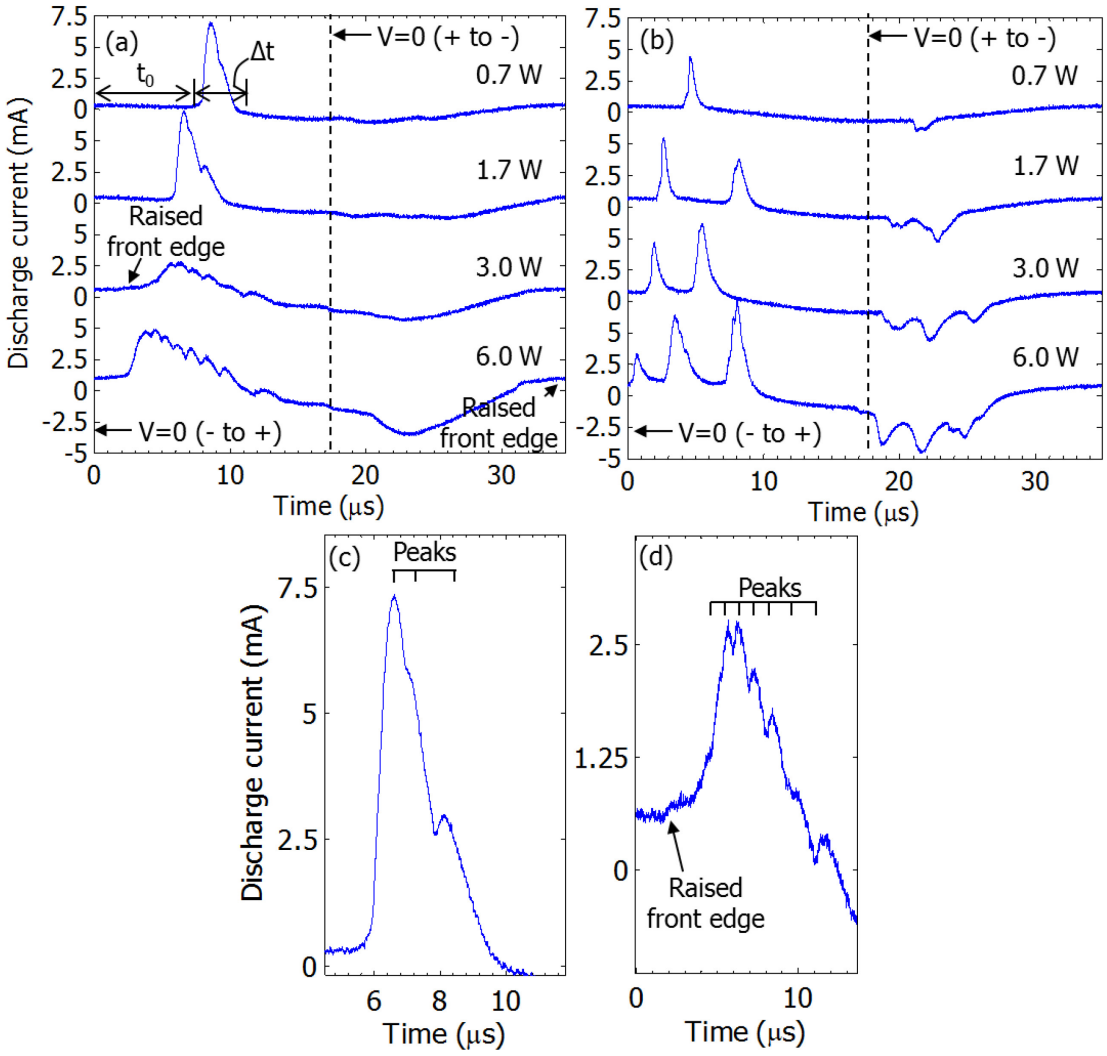

Figure 62. Evolutions of current pulses with rising power in (a) He DBD jet and (b) He/MMA DBD jet; the magnified current pulse which composed of small pulses (c) in He DBD jet at 1.7 W and (d) in He DBD jet at 3.0 W in the concentrated mode with raised current edge.

In this figure, the zero-crossing point from negative voltage to positive voltage is located at the time of 0 μs, whereas the point from positive voltage to negative one is at the time of around 17.5 μs, as indicated by a dashed line. It can be clearly seen that the current pulses in the He DBD jets consist of several short-duration (1–2 μs) pulses in the

positive half cycle though visually only one strong broad pulse (4–16 μs) appears on it, as shown in Figure 62(a). As the discharge power is increased from 0.7 W (diffuse mode) to 1.7 W (transition), the number of the relatively small (short-duration) pulses, which overlap to form the strong current pulse in the positive half cycle, increases. This further prolongs the pulse duration, Δt, as illustratively shown in Figure 62(a). Δt is determined by the time interval between the breakdown initiating time t_0 [when the $|dI/dt|>200$ (A/s)] and the pulse disappearance time when the $|dI/dt|<200$ (A/s). A magnified waveform of the current pulse at 1.7 W is shown in Figure 62(c). As can be observed, after the greatest peak appearing at 6.8 μs, there are two relatively small peaks following it at 7.2 and 8.2 μs, respectively. It shows that a strong current pulse can be deconvolved into several short-duration pulses, and each pulse may correspond to a breakdown. To be clear, we refer to the strong current pulses as the "broadened current pulses". It should be mentioned that at a fixed power not all current pulses at each half positive cycle contain the same numbers of short-duration pulses, i.e., some broadened pulses contain more peaks but some have fewer. The detailed breakdown phenomenon will be presented in the later subsections by using ICCD and PMT. As the discharge power rises, more small pulses following the most intensive peak occur, leading to a broadened pulse with longer duration. However, after the discharge in the He DBD jet switches to the concentrated mode, not only more small pulses in the positive half cycle are observed, but also the front edge of the broadened pulse is raised before the occurrence of those short-duration pulses. A clear broadened current pulse in the concentrated mode can be seen in Figure 62(d), which is an enlargement of the case at

3.0 W in Figure 62(a). It should be emphasized that the 'raised front edge', which is an initiating breakdown shown in the later subsections, is only observed in the concentrated mode in the He DBD jet, and not for the He/MMA case. Further increase of the discharge power results in more subsequent short-duration pulses, such as the case at 6.0 W in Figure 62(a). Additionally, the initiating time (t_0) of breakdown are seen to be shorter with the rising power. Note that the raised front edges begin in the negative half cycles of voltage (t_0<0) when the power of 6.0 W is used in the He DBD jet. Similar to those DBD devices, the 'early breakdown' (t_0<0) at higher power is due to the fact that more residual charges from the previous half cycle are present on the dielectric surface. Thus lower voltage potential difference is required to induce breakdown. The initiating time (t_0) of breakdown and the broadened pulse duration (Δt) per each half cycle at various powers are summarized in Table 5.

Table 5. Initiating time (t_0) of breakdown and the duration time (Δt) of the broadened current pulses during both positive and negative half cycles at various powers in He DBD jet

Power (W)	Positive half cycle		Negative half cycle	
	t_0 (μs)	Δt (μs)	t_0 (μs)	Δt (μs)
0.7	7.0	4.0	18.8	8.2
1.7	5.2	4.8	18.0	11.0
3.0	1.6	11.9	16.7	15.3
6.0	-1.5	15.5	16.7	15.3

When the MMA is added to the He DBD jet, the current pulses in the He/MMA DBD jet evolve in a different way [Figure 62(b)], as compared with the He DBD jet. Each broadened current pulse in this case is similar to those in the He DBD jet during the diffuse mode and the transition as given in Figure 62(c). It is also composed of several small pulses (will be shown in the later results) though in this case with MMA no distinct subsequent short-duration current pulse can be observed. However, the current pulse in the He/MMA DBD jet is observed to have shorter duration (~1.9 μs at 0.7 W) than that of the pulse in the He DBD jet (~4.0 μs at 0.7 W). Also, a rising power leads to the generation of multiple separated broadened current pulses per half cycle instead of the increasing number of the subsequent short-duration pulses in every single broadened pulse. Thus it can be seen that every broadened pulse occurring in the He/MMA DBD jet has no significant difference between their pulse widths (about 2–4 μs) regardless of the power. Like the case in the He DBD jet, the initiating breakdowns (or the first broadened current pulses in this case) move toward the voltage zero with the rising discharge power, and the time between the broadened current pulses also decreases. When two broadened pulses in the positive half cycle are close to each other, the first current pulse is found to usually have weaker amplitude than the second one, as shown in the cases of 3.0 W and 6.0 W in Figure 62(b). However, the reason is yet unclear. In the negative half cycle, the number of the strong current pulses grows as the discharge power rises but the time between the pulses always remains short (~0 μs, i.e., successive negative current pulses). Similarly, summarized parameters of the broadened current pulses in the He/MMA DBD jet are given in Table 6.

Table 6. Initiating time (t_0) of breakdown and the duration time (Δt) of the broadened current pulses during both positive and negative half cycles at various powers in He/MMA DBD jet; the notations Δt_1, Δt_2 and Δt_3 represent the duration time of the first, second and third current pulse, respectively

Power (W)	Positive half cycle				Negative half cycle			
	t_0 (μs)	Δt_1 (μs)	Δt_2 (μs)	Δt_3 (μs)	t_0 (μs)	Δt_1 (μs)	Δt_2 (μs)	Δt_3 (μs)
0.7	3.9	1.9	-	-	20.9	2.0	-	-
1.7	2.0	1.9	2.9	-	19.0	2.1	3.5	-
3.0	1.2	2.8	3.8	-	18.6	2.5	3.5	3.4
6.0	0	2.6	3.8	3.8	16.7	3.6	3.3	5.3

6.3.2 Time Resolved Imaging Characteristics

In order to correlate the features (e.g., current peaks and valleys) on the discharge current waveforms with the time-resolved discharge appearances, the ICCD camera and the oscilloscope were both employed. The ICCD gating was controlled by the trigger signal generated from the oscilloscope to achieve this synchronicity. The trigger point was set at the strongest positive peak of each current waveform over one complete cycle. The image corresponding to any specific time point on the current trace can be acquired by adjusting the time delay of the ICCD gating. The following ICCD results are single-shot images taken with 10 ns exposure time in order to acquire the clear image of plasma propagation as well as to avoid saturation of the ICCD camera. To more clearly show the discharge features the ICCD images were converted into false-color with an intensity range from 0 to 20 using the mapping shown in the intensity color bar.

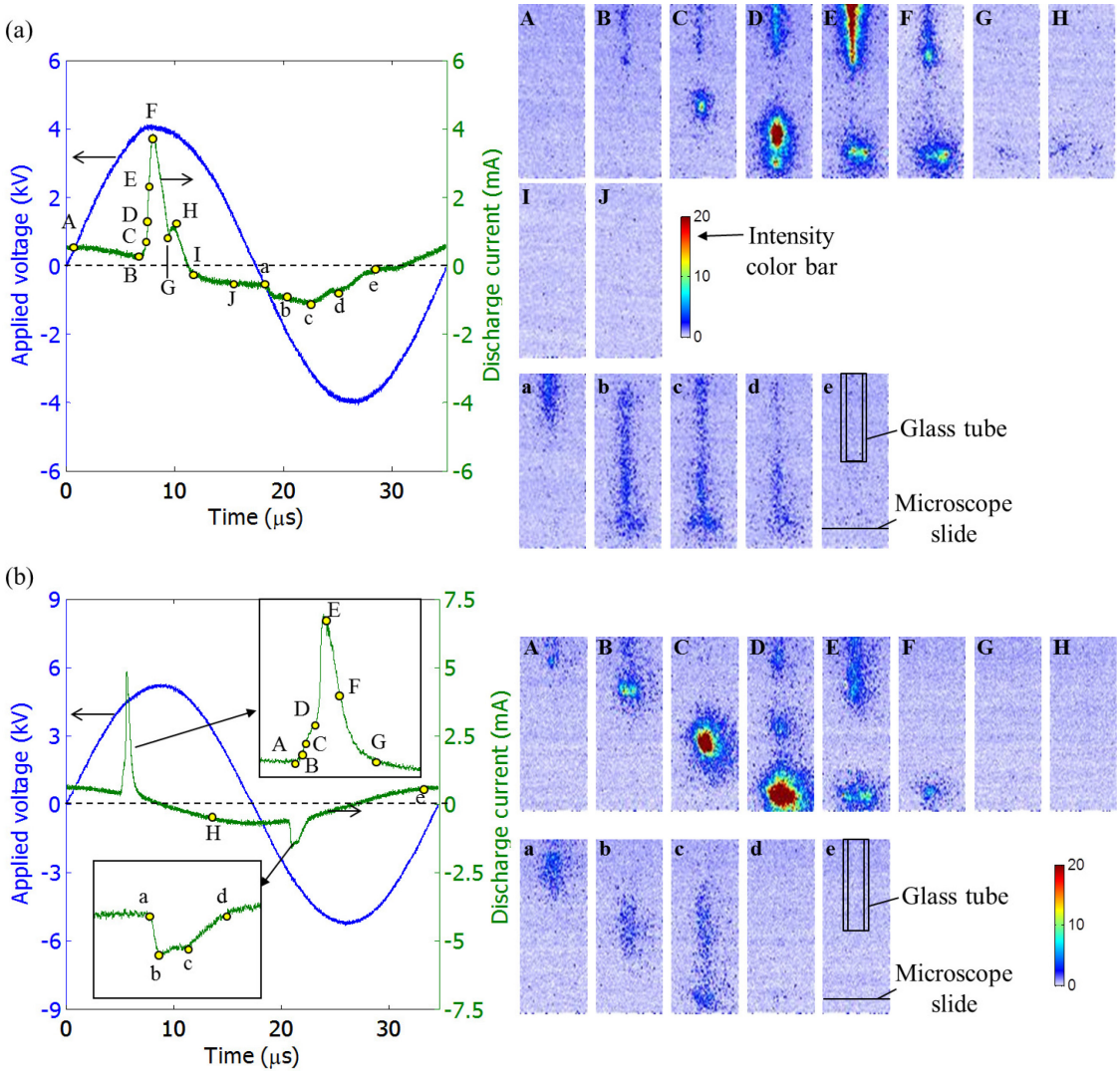

Figure 63. Voltage and current waveforms over one complete cycle (left) and the corresponding false-color ICCD images (right) with 10-ns exposure time in the (a) He DBD jet and (b) He/MMA DBD jet at 0.7 W (diffuse mode).

Figure 63(a) and Figure 63(b) show the voltage and current waveforms (left panel) and the corresponding false-color ICCD images (right panel) in the He DBD jet and the He/MMA DBD jet at a power of 0.7 W (diffuse mode), respectively. Capital letters on the current trace and the ICCD images represent that those images were taken

during the positive half cycle, whereas the images acquired during the negative half cycle are labeled by lower case letters. As can be observed from the onset of broadened positive current pulse [labels (B)–(D)] in Figure 63(a), a bright light emitting region is ejected from the dielectric tube (anode) and appears to move toward the microscope slide (cathode) with a velocity measured here of about 5×10^4 m/s. The observed light emission is attributed to the presence of a sufficient number of electrons with sufficient energy to excite atoms/molecules which subsequently decay yielding photons. The presence of these energetic electrons along with the propagation of the light emitting region (due to energetic electrons) thus infers the existence of an ionization wave moving from anode to cathode. As the ionization wave propagates, a partially ionized channel (or plasma channel) is developed right behind the ionization front. A portion of the plasma channel becomes observable when the wave reaches the cathode and the entire path is ionized [image (E)]. Most electrical current starts to flow through the plasma channel at this moment. And then, the current pulse increases in magnitude and reaches the peak while the plasma channel still exists, as displayed in the image (F). After the peak current, the current drops drastically to a local minimum [valley at label (G)], and its corresponding image shows a dim light on the cathode. This light is actually induced by a new ionization wave arriving at the microscope slide. At the subsequent peak [label (H)] in the positive half cycle, the ICCD image appears that the ionization wave is vanishing on the dielectric surface. This current peak also means that a new plasma channel is created by the ionization wave to allow more current to pass through though the channel is less observable. This implies that each short-duration current pulse

in the strong long-duration pulse is attributed to an ionization wave and a subsequent plasma channel. In other words, there are multiple ionization waves generated during one broadened current pulse but not all the wave propagation is noticeable (observable by ICCD). More evidence of these multiple ionization waves will be presented in the subsequent results. When the images were captured at points outside the current pulses [e.g., labels (I) and (J)], no discharge emission can be seen. Images (a) to (e) in Figure 63(a) were taken over the negative half cycle. In this case no evidence of ionization wave propagation was acquired. Instead, a faint discharge was first observed in the dielectric tube (cathode) at the initiating negative current pulse [image (a)]. Then a plasma channel with a distinct continuous structure (extends from one electrode to the other) occurs without any propagation front or generation of ionization waves as observed during the positive half cycle. The light intensity of the discharge appears to be related to the absolute current magnitude, i.e., the greater the absolute current magnitude, the brighter the current discharge in the negative cycle, as shown in the images (b)–(d) in Figure 63(a). Similarly, the light emission vanishes at the end of the current pulse [image (e)].

Figure 63(b) presents the ICCD imaging results in the He/MMA DBD jet at a power of 0.7 (diffuse mode). Similar to the case in the He DBD jet, the propagation of an ionization wave can be seen in the sequence of the images (A)–(D) in the positive half cycle. The average propagation velocity of the ionization wave is also around 5×10^4 m/s. A visible plasma channel following the ionization wave is created, as displayed in image (E) at which the discharge current reaches its maximum. The corresponding ICCD

images show similar results to the case in the He DBD jet at 0.7 W. Image (F) shows a new ionization wave arriving at the microscope slide, which, again, demonstrates that multiple small pulses make up the broadened pulse though in this He/MMA case no distinct subsequent short-duration current pulse can be observed within the broadened current pulse. Images (a) to (e) show the discharge variations over the negative half cycle. Similar to that in the He DBD jet, the plasma is first observed in the dielectric tube and then forms a long, continuous channel. However, the observable plasma channel reaches the microscope slide surface at the second peak [label (c)] instead of at the first peak [label (b)]. The same phenomenon will be shown in the PMT subsection.

As the discharge power rises and both the He DBD jet and the He/MMA DBD jet enter the transition states, different discharge images were observed in the two jets. In the He DBD jet, the positive broadened current pulse shows longer duration due to the occurrence of more short-duration pulses, compared to that at lower power. Figure 64 presents a sequence of the ICCD images at 1.7 W during the transition. Similar to the case in the diffuse mode, an ionization wave (also at a speed of about 5×10^4 m/s) is generated at the beginning of the positive current pulse and then a portion of the plasma channel created by the wave is visible [labels (B)–(F)]. In this case one more distinct subsequent current peak (local maximum) was seen [label (H)], compared to the previous case in Figure 63(a). Before the occurrence of this current peak, the image of the label (G) shows a distinct light pattern on the microscope slide, which is similar to the one observed in the image (G) of Figure 63(a), but with a brighter appearance. As mentioned earlier, this bright light is generated from an ionization wave reaching the

slide surface. Again, it is followed by a current peak as shown at label (H). The next valley at the point (I) and the final peak at the point (J) show similar images to the points labeled by (G) and (H) in Figure 63(a), respectively. The negative pulse [label (a)–(i)] is found to be similar to that in the diffuse mode in Figure 63(a) but has longer duration.

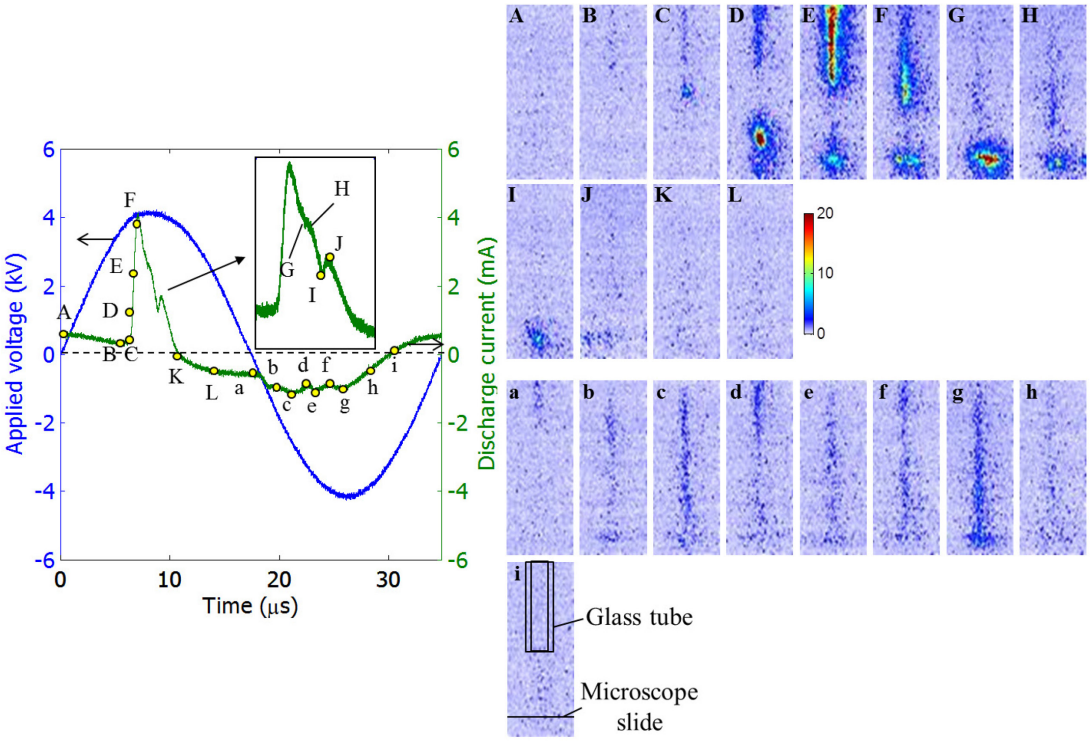

Figure 64. Voltage and current waveforms over one complete cycle (left) and the corresponding false-color ICCD images (right) with 10-ns exposure time in the He DBD jet at 1.7 W (transition).

It can be also observed that the plasma channels at each cycle become much brighter and thinner with the rising power. To show the discharge contraction in the radial direction as the power is increased, the spatial light intensity of the discharge from the downstream end of the powered electrode to the position 3-mm above the

microscope slide is extracted from the ICCD image. The average light intensity profile along the radial direction of the dielectric tube is then obtained by computing the mean intensity value of each column of pixels. Figure 65(a) shows an example of the intensity profiles of the ICCD images (D) and (E) in Figure 64. With the intensity profile, the corresponding full width at half-maximum (FWHM) can be determined to represent the radial dimension of the discharge. The FWHM values of all the discharges displayed in the ICCD images in Figure 63(a) (diffuse) and Figure 64 (transition) are collected and plotted in Figure 65(b) to compare the discharge dimensions in the He DBD jet. The capital letters and the lower case letters shown in Figure 65(b) represent those ICCD images with the same labels in Figure 63(a) and Figure 64. Note that the error bars represent the uncertainty in the determination of the half-maximum values in the light intensity profiles due to the presence of image noise. The larger error bars result from the dimmer images in which more noise is present. The figure presents that the discharge size is decreased when the operation mode enters the transition from the diffuse mode. This demonstrates that the discharge along the central axis becomes brighter than the rest parts with the rising power. Thus it causes the discharge non-uniform appearance during the transition displayed in Figure 57(b).

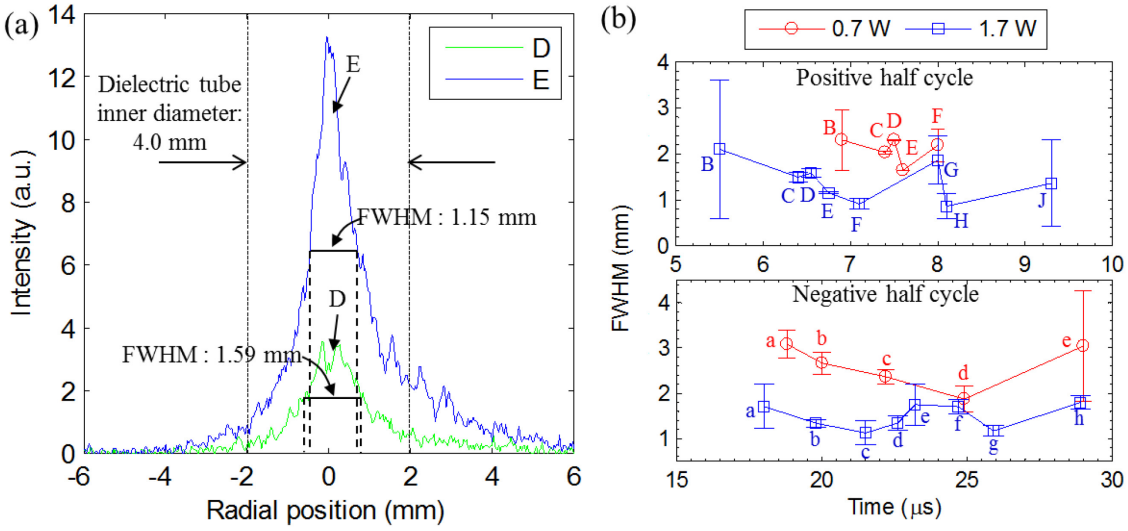

Figure 65. (a) Comparison of light intensity profiles of ICCD images (D) and (E) in Figure 64 and their corresponding FWHM during transition (1.7 W) in the He DBD jet; (b) plot of FWHM versus time for the discharges at the 0.7 W (diffuse) and 1.7 W (transition) in the He DBD jet.

In the He/MMA DBD jet during transition mode with 1.7 W, its current trace shows two strong current pulses in both the positive half cycle and the negative half cycle, as presented in Figure 66. The propagation of two ionization waves [image (B)–(D) and (I)–(K)] during the positive half cycle can be clearly observed. There is no significant difference between the velocities (~5×10^4 m/s) of these two waves. Also, each ionization wave is generated at the onset of each broadened current pulse. However, the second ionization wave [image (J)] appears to be smaller than the first ionization wave [image (C)] likely due to the fact that the path between the anode and the cathode after the disappearance of the first broadened current pulse still has residual charges. Thus fewer additional charges (an ionization wave with a smaller dimension) are required to create a conductive path bridging the anode and the cathode. In the negative half cycle, a second strong current pulse occurs right after the first relatively

small current pulse. The ICCD images of the first small current pulse are not shown here since they are similar to those over the negative cycle in Figure 63(b). The second pulse during the negative half cycle is seen to have a discharge with a relatively bright and thin structure [image (c)]. Besides, The subsequent discharges in images (L) and (M) in the positive half cycle exhibit the thin and bright appearance. Similar to the case in the He DBD jet, these lead to the non-uniform color distribution in the discharge appearance during the transition.

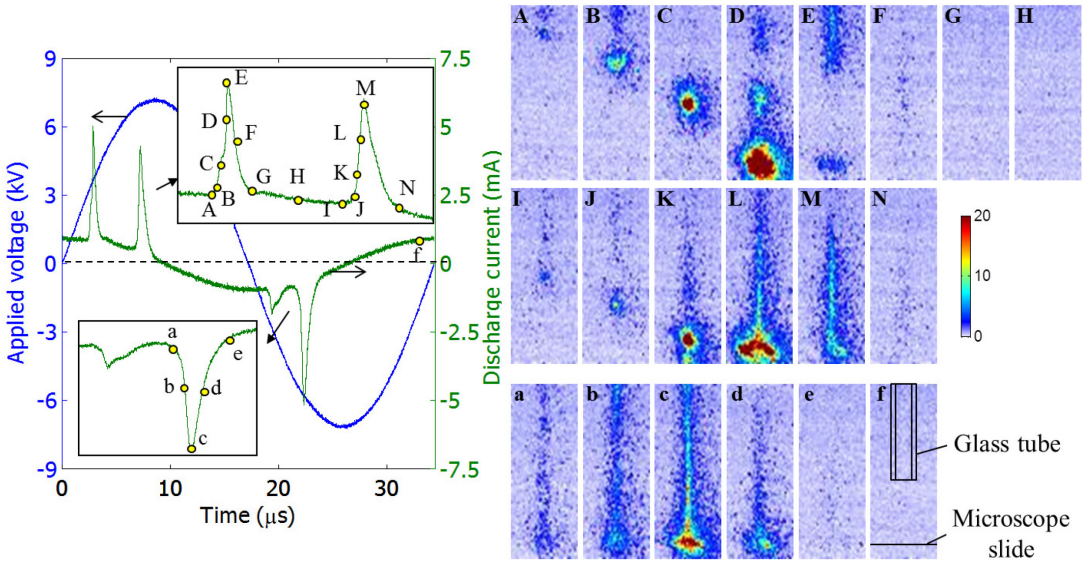

Figure 66. Voltage and current waveforms over one complete cycle (left) and the corresponding false-color ICCD images (right) with 10-ns exposure time in the He/MMA DBD jet at 1.7 W (transition).

When the He DBD jet switches to the concentrated mode (3.0 W), the ICCD images in Figure 67(a) show three main differences, compared to the cases in the diffuse mode and the transition status. The first difference is the early breakdown observed at the raised front edge [label (A)] during the positive half cycle. It can be seen that in the

image (A) a plasma channel is present in the discharge gap before the occurrence of the strong current pulse. The second one is that no apparent (or less-noticeable) ionization wave propagation is observed at the onset of the broadened current pulse in this case, as shown in the images (A)–(M) in the positive cycle. The last different feature is that the discharges [e.g., labels (C)–(I)] occurring after the raised front edge show a long spatially uniform structure extending from the powered electrode to the microscope slide instead of an appearance with a discontinuous structure as seen at a lower power. The faint area in the middle of the discharge results from the dielectric tube end, which influences the brightness of the emission light. Similarly, at the valleys of the current waveform [labels (H) and (J)] the corresponding images show bright emission light in the vicinity of the slide, implying that ionization waves reach the slide. Additionally, a large number of the distinct subsequent peaks, such as those labeled by (G), (I) and (K), indicate that several subsequent plasma channels are created to allow more electrical current to flow through during the positive cycle. In the negative half cycle, a broad and strong current pulse forms and the image corresponding to the peak [label (e)] shows a relatively bright discharge, compared to those observed in the lower power cases in Figure 63(a) and Figure 64. Thus it can be concluded that the concentrated mode is attributed to these thin and bright discharges. It should be also mentioned that further increase of the discharge power causes a continuous though low level emission along the entire discharge gap (from the tube end to the slide).

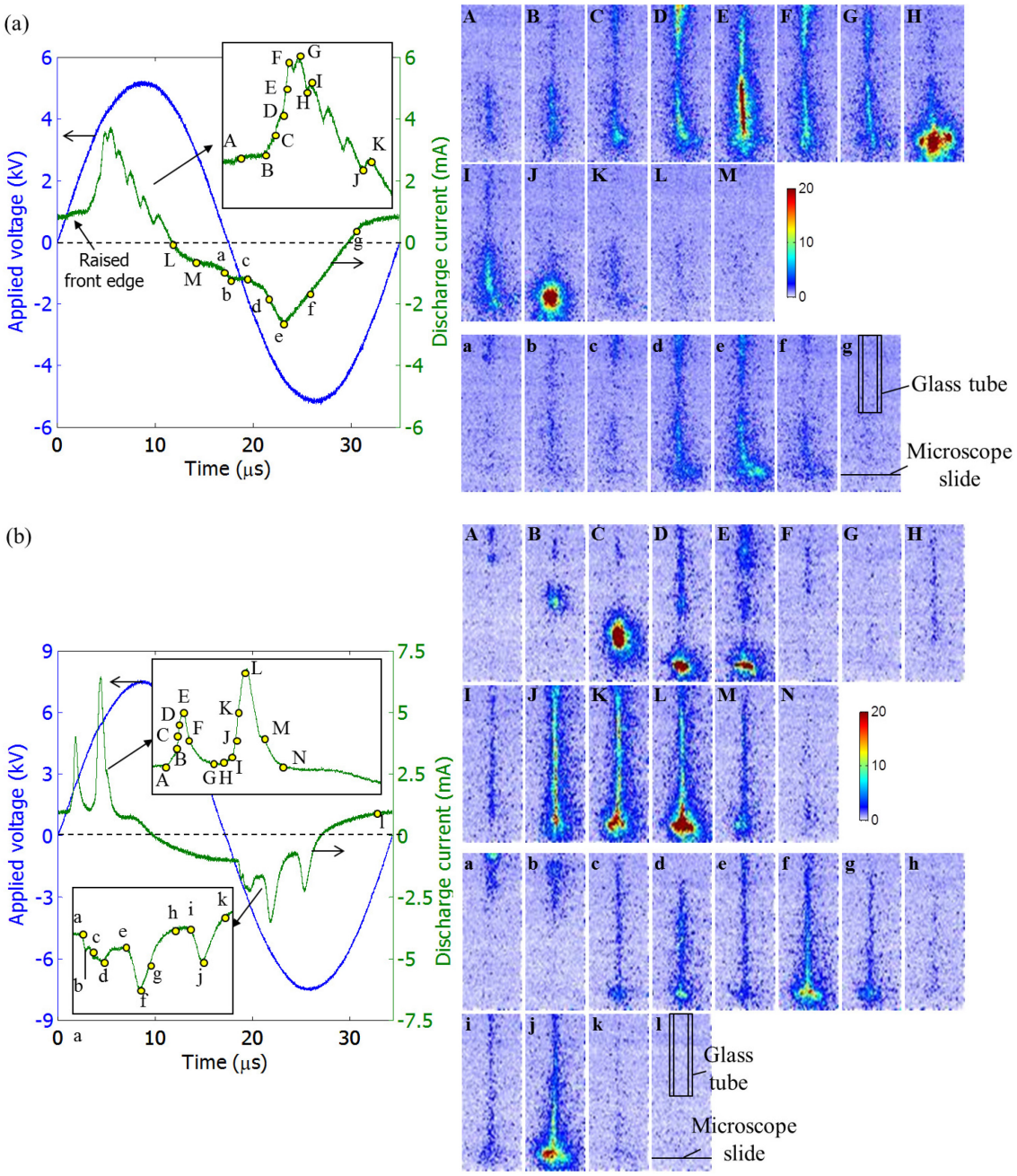

Figure 67. Voltage and current waveforms over one complete cycle (left) and the corresponding false-color ICCD images (right) with 10-ns exposure time in the (a) He DBD jet and (b) He/MMA DBD jet at 3.0 W (concentrated mode).

Further increase of the discharge power results in the decrease of the time between the two strong current pulses during the positive half cycle in the He/MMA DBD jet. Figure 67(b) shows such a case at a power of 3.0 W in the concentrated mode. In this case, an ionization wave can be still observed at the onset of the first broadened current pulse during the positive half cycle. It should be mentioned that all the ionization waves which have noticeable propagation processes were observed to have similar travel velocity (~5×10^4 m/s). Nevertheless, at the beginning of the second broadened pulse [image (H)], only a faint thin continuous discharge (plasma channel) can be seen instead of the second ionization wave propagation. As the current amplitude rises, the plasma channel becomes brighter, as presented in the sequence of images (J), (K), and (L). However, it should be noted here that there are still ionization waves propagating from the anode to the cathode during the occurrence of the second pulse though they are less noticeable in comparison to the bright channel. This can be proven by measuring the light emission from the slide surface through the PMT. The results will be introduced in the later subsection. In the negative half cycle, three distinct current pulses are observed. Again, the discharges at the negative current peaks exhibit thin, continuous structures occupying the whole path. Those thin and bright discharges shown in both the positive and negative half cycles form the concentrated discharge line observed in this mode. A sufficient increase of the discharge power can lead to the occurrence of the third current pulse during each positive cycle. Still, only the ionization wave propagation at the onset of the first broadened positive pulse can be observed.

From the above ICCD results it appears that the propagation process of an ionization wave can be clearly observed only when no plasma channel is present, whereas the existence of a plasma channel leads to a less-noticeable ionization wave though it can still be observed when the wave is arriving at the slide.

6.3.3 PMT Characteristics

In order to obtain more time-resolved information about the current pulses in the DBD jets, light emitted from a region near the surface of the microscope slide was acquired using the PMT. Figure 68(a) shows the discharge current waveform and the corresponding PMT trace of the He DBD jet at 1.7 W. Peaks are easier to identify in the PMT signal than those in the current trace during the positive half cycle. This is because the light emission is a more instantaneous measure of excitation processes than the current which is somewhat broadened by capacitance effects at the dielectric barriers. The inset displays the magnified view of the PMT signal in the dashed box for better observation. The first peak of the PMT signal right after the onset of the broadened current pulse is found to occur at the moment when the first ionization wave arrives at the microscope slide surface based on the previous ICCD results. Additionally, the line a–a' in Figure 68(a) indicates that the last trough of the current pulse and the last peak of the PMT trace during the positive half cycle happen at the same time, whereas at the negative half cycle the current peak and the peak of the PMT trace line up well. From the ICCD image (I) in Figure 64 it can be seen that at that moment the bright emission light occurs on the slide surface, inferring the arrival of the ionization wave.

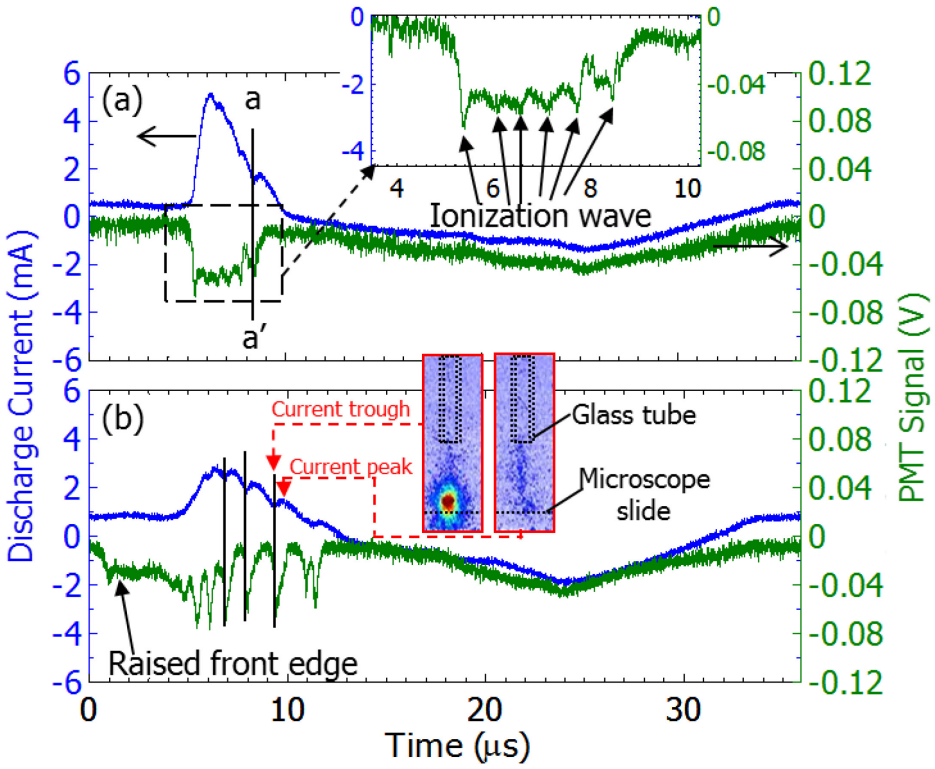

Figure 68. Discharge current waveforms and their corresponding PMT signals in He DBD jet at (a) 1.7 W and (b) 3.0 W.

These results imply that each peak in the PMT signal represents an ionization wave reaching the substrate during the positive half cycle. The PMT signal also indicates that between the occurrence of the first ionization wave and the peak of the broadened current there are still several subsequent ionization waves generated. More evidence can be seen in Figure 68(b), which shows the PMT signal in He DBD jet at 3.0 W. Several distinct and intense peaks were observed in the PMT trace, and they also line up with the troughs of the current trace, similar to the case with a lower power. Again, each intense peak of the PMT signal is induced by a new created ionization wave, as shown in the false-color ICCD insets of the figure. It should be mentioned that from the ICCD results

no clear propagation processes of the ionization waves are ever observed in this case though the images of the waves reaching the cathode can be captured. However, the PMT result confirms that there are still ionization wave propagating toward the cathode during the positive half cycle in the concentrated mode of the He DBD jet but the propagation process is less-noticeable, compared to that in the diffuse or transition status. The PMT results also confirm that a plasma exists during the raised front edge of the current trace in the concentrated mode during the beginning of each positive half cycle.

The current waveforms and their corresponding PMT traces of the He/MMA DBD jet at 1.7 W and 3.0 W are given in Figure 69(a) and Figure 69(b), respectively. Multiple peaks in the PMT signal are also observed within each broadened current pulse at each positive half cycle. It shows that each one broadened current pulse contains not only one breakdown (more than one ionization wave) though there are no distinct subsequent short-duration pulses in the positive current pulse. Additionally, the broader pulse (the second positive pulse) consists of more ionization waves than the pulse with shorter duration (the first positive pulse). It should be reiterated that the main difference between the He/MMA DBD jets at 1.7 W and 3.0 W regarding the ICCD images is that during the positive half cycle in the 3.0 W case a visible plasma channel is present at the onset of the second broadened current pulse instead of the observation of the ionization wave propagation [image (G)–(J) in Figure 67(b)]. However, from Figure 69(b) it displays that there is still an ionization wave arriving at the slide surface at the beginning of the second pulse due to an intense peak observed in the PMT waveform. Thus these

results indicate that if two short-duration current pulses are close to each other, the ionization wave propagation of the second current pulse becomes less noticeable likely due to the fact that the plasma channel created by the previous ionization wave is still present. Line a–a' in Figure 69(a) shows that no light emits from the slide surface during the occurrence of the first current peak at the negative half cycle, further confirming the image (b) in Figure 60(b).

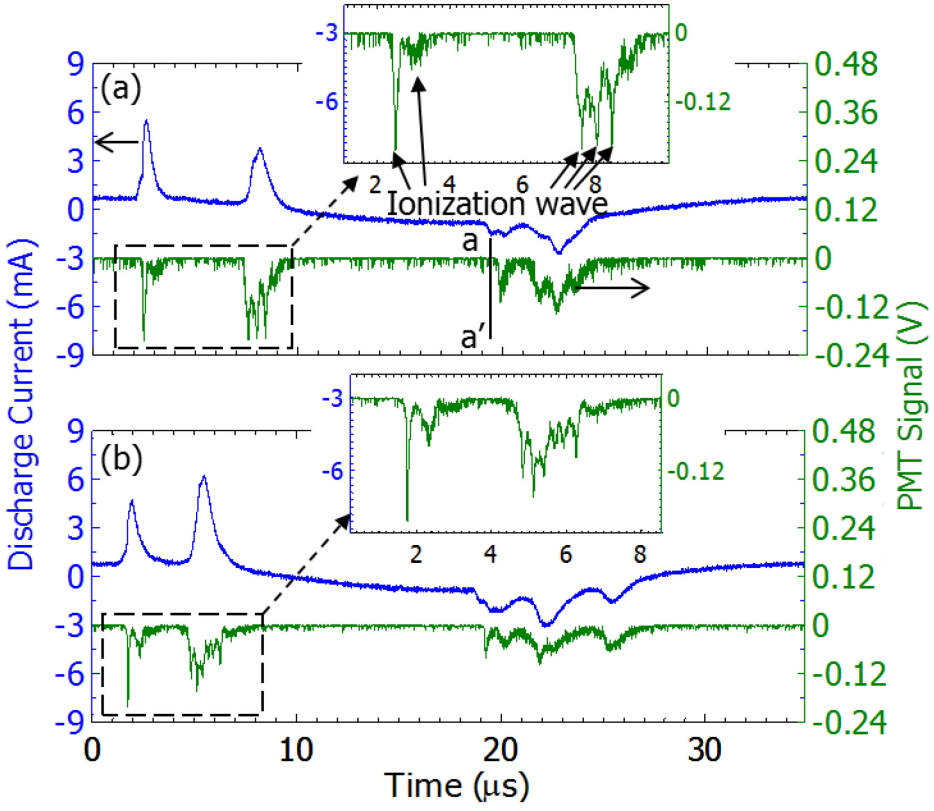

Figure 69. Discharge current waveforms and their corresponding PMT signals in He/MMA DBD jet at (a) 1.7 W and (b) 3.0 W.

6.3.4 Discussion

After correlating the results of electrical current waveforms, PMT signals and high-speed images from ICCD, we can conclude that during the positive half cycle each one broadened current pulse consists of several relatively small current pulses with short duration. Each short-duration current pulse is attributed to a large amount of electrical current flowing through a conductive plasma channel created by a leading ionization wave. It was observed that the time between two short-duration current pulses and the number of the short-duration current pulses during each half cycle significantly depends on the properties of the plasma working gas and the applied electric field.

For a better understanding of the time-resolved breakdown in the He and He/MMA DBD jets, a schematic illustration is presented in Figure 70. Figure 70(a) shows the case of the He DBD jet at a power of 1.7 W. The discharge current waveform and its corresponding PMT trace [the positive cycle of Figure 68(a)] are given at the left hand panel. The right panel gives the schematic diagrams showing the cross-sectional DBD jet and the discharge variation at the different time points (indicated by lines A–F on the left panel) of the broadened current. Around the onset of the discharge current [point (A)], an ionization wave is generated in the tube portion covered by the powered electrode (anode) and starts to propagate to the microscope slide (cathode). During the wave propagation, discharge current appears to increase in intensity. When the wave arrives at the slide, an intense peak of the PMT signal can be observed, as shown at the intersection of the line B and the PMT trace. At the same time, a plasma channel is created along the path the ionization wave passes through. After the ionization wave

vanishes, it leaves behind the plasma channel (diagram C). The existence of the plasma channel allows current to flow through until it dies out due to the reduction of the local electric field caused by accumulated charges on the dielectric surface and electron attachment processes. In this case since the applied voltage is still increasing, a new ionization wave is further produced when the previous plasma channel is still present, as illustrated in diagram (D). This new ionization wave moves toward the cathode and reaches the slide. Thus a new intense peak can be seen in the PMT signal (the intersection of the line E and the PMT trace) and, again, a plasma channel created by the new wave is then left behind (diagram F). It should be mentioned that not all plasma channels exhibit strong light emission. Similar processes, which include ionization wave propagation and plasma channel generation, repeat until the external applied voltage is unable to create a new breakdown. In this case using He DBD jet at 1.7 W, six ionization waves, as labeled by (1), (2)…(6) in Figure 70(a), are produced during the positive half cycle. However, the presence of the previously-created plasma channel leads to the less-noticeable propagation of the ionization waves (2)–(6). The onset time (t_i) and the corresponding applied voltage (V_i) of each ionization wave are listed in Table 7. The instantaneous time of the wave onset in the table is obtained by subtracting the travel time (0.5 μs) of the ionization wave from the time when the wave is arriving at the slide, i.e., the time when an intense peak is observed in the PMT trace. Here we assumed that all the ionization waves travel at the same velocity (5×10^4 m/s), so that 0.5 μs is required for the waves to propagate from the end of the insulated powered electrode to the surface of the microscope slide (the distance is 25 mm). Table 7 also presents the voltage

increment ($\Delta V_{i-(i-1)}$) between every two successive ionization waves. It can be seen that when the plasma channel is present, the voltage increment with only several hundred volts or lower is required to initiate a new ionization wave instead of several thousand volts needed for the first wave generation.

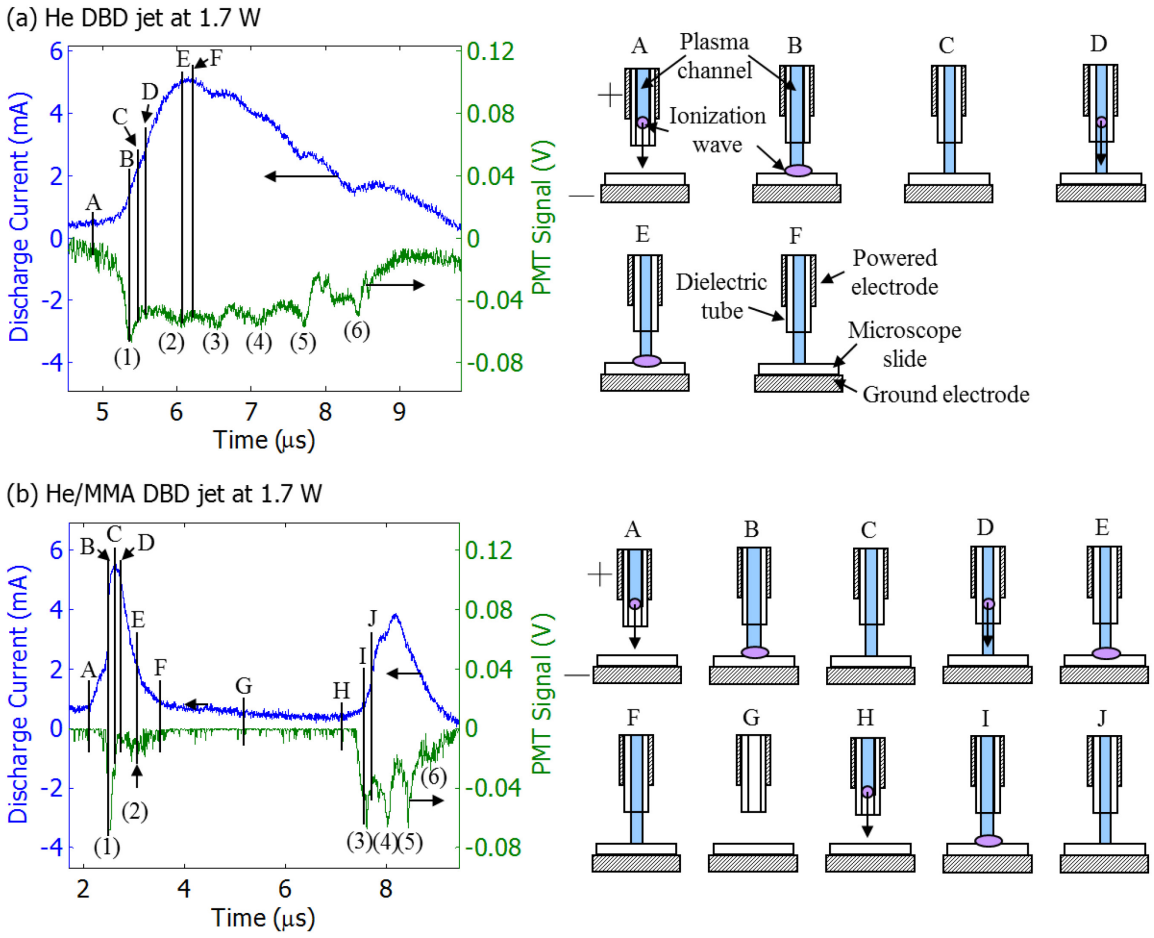

Figure 70. Discharge current and PMT traces (left panel) and the corresponding schematic sequence (right panel) of the discharge in (a) He DBD jet and (b) He/MMA DBD jet at 1.7 W at the positive half cycle.

Table 7. Instantaneous time (t_i) and applied voltage (V_i) of the onset of the successive ionization waves during the positive half cycle in He DBD jet at 1.7 W ($\Delta V_{i-(i-1)}$ represents the voltage difference between the onset of the i-th ionization wave and the (i-1)-th ionization wave)

Parameters	Onset of ionization waves					
	1st wave	2nd wave	3rd wave	4th wave	5th wave	6th wave
t_i (μs)	4.9	5.6	6.0	6.6	7.2	7.9
V_i(V)	3219.4	3504.2	3614.7	3692.2	3765.7	3810.7
$\Delta V_{i-(i-1)}$ (V)	-	ΔV_{2-1}	ΔV_{3-2}	ΔV_{4-3}	ΔV_{5-4}	ΔV_{6-5}
		284.8	110.5	77.5	73.5	45

An illustration (positive half cycle) for the He/MMA DBD jet at 1.7 W is given in Figure 70(b). The initiation time (t_i) of the ionization waves in the He/MMA case and the corresponding applied voltage (V_i) are presented in Table 8. There are also six ionization waves generated during the positive half cycle, and the numbers (1), (2)…(6) in Figure 70(b) are used as an indication of them. The first broadened pulse contains two ionization waves, and the breakdown processes [A–F in Figure 70(b)] including the ionization wave propagation and the plasma channel generation are the same as those in the He DBD case. However, the plasma channel vanishes before a new ionization wave can be initiated, as illustrated in the diagram G. This makes the DBD system return to a state which is similar to that at the beginning of the positive half cycle. In other words, it is required to apply a voltage near the breakdown voltage (several thousand volts) across the gap to initiate a new breakdown. Thus if the external applied voltage keep increasing and can provide a sufficiently high net electric field (= external electric field – the electric field created by accumulated charges on the dielectric surface), a new ionization

wave can be initiated. The result in Table 4 shows that a 3294.5 V increase (ΔV_{3-2}, from 2934.2 V to 6229.0 V) in the applied voltage after the first broadened current pulse leads to the 3rd ionization wave generation, as shown in the diagram H. Subsequently, the 4th, 5th and the last ionization waves during this positive half cycle are initiated in a way similar to those cases when a plasma channel exists between the two electrodes. Again, only several hundred volts or lower of the voltage increment are required to generate these subsequent ionization waves. In this case, only the propagation of the ionization waves (1) and (3) can be observed by ICCD as no plasma channel exists in the discharge gap prior to the wave.

Table 8. Instantaneous time (t_i) and applied voltage (V_i) of the onset of the successive ionization waves during the positive half cycle in He/MMA DBD jet at 1.7 W ($\Delta V_{i-(i-1)}$ represents the voltage difference between the onset of the i-th ionization wave and the (i-1)-th ionization wave)

Parameters	Onset of ionization waves					
	1st wave	2nd wave	3rd wave	4th wave	5th wave	6th wave
t_i (μs)	2.0	2.6	7.1	7.5	7.9	8.4
V_i(V)	2329.6	2934.2	6229.0	6362.4	6419.9	6430.2
$\Delta V_{i-(i-1)}$ (V)	-	ΔV_{2-1}	ΔV_{3-2}	ΔV_{4-3}	ΔV_{5-4}	ΔV_{6-5}
		604.9	3294.5	133.4	57.5	10.3

Not all the ionization wave propagation is noticeable though each one broadened current pulse in the positive half cycle includes the initiation of several waves. When the time between two short-duration current pulses is short enough, the propagation of the

subsequent ionization wave becomes less-noticeable using the ICCD technique since the plasma channel created by a previous ionization wave is still present between the electrodes. Typical examples are those subsequent ionization waves following the 1st wave in the same broadened current pulse. Some other examples worthy to be mentioned are the waves at the onset of the 2nd broadened pulse in the He/MMA DBD jet in the concentrated mode [Figure 67(b)] and the 1st wave in the broadened current pulse in the He DBD jet in the concentrated mode [Figure 67(a)]. However, as mentioned earlier, the wave fronts impinging on the microscope slide can still be observed by the ICCD camera and acquired by the PMT. Conversely, the propagation of the 1st ionization wave in a broadened current pulse without the presence of a previously-created plasma channel can be clearly observed. For instance, those 1st ionization waves in the diffuse mode and during transition in the He and He/MMA DBD jets as well as the wave at the onset of the 2nd broadened current pulse in the He/MMA DBD jet during transition are noticeable (Figure 63, Figure 64, and Figure 66).

Multiple broadened current pulses occur in the He/MMA DBD jet likely due to a combination of two reasons: (1) the electron density (n_e) in the He/MMA DBD decreases faster than that in the He DBD when the plasma is destructed (i.e., $|dn_e/dt|_{He/MMA} > |dn_e/dt|_{He}$) and (2) the breakdown voltage (V_b) of He/MMA DBD jet is higher than that in the He DBD jet ($V_{b,\,He/MMA} > V_{b,\,He}$). The decreasing rates of n_e ($|dn_e/dt|$) can be shown by the decay rates of the current pulses in the DBD jets. Every single short-duration current pulse in the He/MMA DBD vanishes faster than that in the case using pure He DBD jet. By differentiating the discharge current profiles in Figure

62 with respect to time, we found the peak current pulse decay rate in the He DBD jet is about 5 mA/μs, whereas around 10 mA/μs peak decay rate in the He/MMA case. It indicates that the current pulse in the He/MMA DBD jet dies out about two times faster than the pulse in the He plasma. The duration of a single current pulse depends on the net effect of chemical reactions in the plasma, such as ionization and attachment processes. When the MMA is fed into the He DBD jet, some of the energetic electrons generated in the plasma may tend to attach to the MMA radicals (electron attachment). Also the additional vibrational modes available for excitation in MMA mean the electron energy and ionization rate decrease more quickly. This reduces the net ionization in the plasma, further accelerating the vanishing rate of the electrons ($|dn_e/dt|$ is increased) in the He/MMA DBD jet. Therefore, the current pulses with shorter duration time (faster decay time) were observed when MMA is added to the He DBD jet. The second reason is the difference between the breakdown voltages, V_b, in the He DBD jet and the He/MMA DBD jet ($V_{b,\,He/MMA} > V_{b,\,He}$). Higher V_b in the He/MMA can be seen from its higher external RMS voltage for discharge breakdown shown in Fig. 4, compared to that in the He case, though the actual voltage in the discharge gap is hard to determine. This further denotes that it is more difficult to initiate the ionization wave in the He/MMA DBD jet than in the He plasma when the same external field is applied. An example can be seen in the comparison between Figure 60(d) (He DBD at 6.0 W) and Figure 61(a) (He/MMA DBD at 0.7 W). In these two cases the same applied voltage (peak voltage ~5.4 kV) was used. The He DBD jet has a broadened pulse (Δt = 15.5 μs) containing at least 7 short-duration small pulses at the positive half cycle, whereas a pulse with 1.9 μs

duration time is observed in the He/MMA case. It can be concluded that compared to the He DBD jet not only the breakdown is harder to occur in the He/MMA DBD jet but also the created plasma channel does not last as long. However, if a sufficiently strong, fast rising electric field [e.g., Figure 61(b)–(d)] is applied to the He/MMA multiple broadened current pulses can be induced even though the preceding plasma channel nearly disappears.

The ICCD images corresponding to the multiple current pulses in the He/MMA DBD jet are significantly different from those in the parallel-plate He DBD systems shown in [17] and [113], in which the DBDs exhibited the structures of a glow discharge. In the case using the He/MMA DBD jet, the occurrence of the current pulses involves the initiation of the ionization waves and the formation of the plasma channels instead of the generation of the glow discharges. Besides, it was confirmed that the multiple breakdowns in this study are not the Townsend discharge as proposed in [114] since the current density in our DBD jets is about 40 mA/cm^2, which is 2 orders of magnitude higher than the current density (0.05–0.1 mA/cm^2) in the Townsend discharge.

The generation of the multiple ionization waves (or multiple short-duration current pulses) per each positive half cycle in both the He and He/MMA DBD jets is found to result from the presence of the dielectric substrate (microscope slide) downstream of the plasma jet. When only the aluminum holder (conductive substrate) is used as the substrate, in the He DBD jet only one strong pulse without containing those small short-duration current pulses is observed. This is also the typical current pulse reported by the prior art [25], [97], and [108] when a metallic substrate is present.

Nevertheless, using He/MMA multiple strong current pulses are still obtained even if the aluminum substrate is employed. It thus can be inferred that the dielectric property of the substrate significantly influences the mechanism of the ionization wave generation.

6.4 Section Conclusions

In this section, we characterized the multiple-breakdown phenomenon in a floating-electrode He DBD jet when a treated dielectric substrate was present. It was observed that after MMA precursors were added to the He DBD jet, the discharge current pulse at each half cycle changed from a single broad pulse to multiple broad pulses when a sufficient voltage was introduced. The number of the broad pulses in the He/MMA DBD jet increases with rising power. There was always only one broad pulse per half cycle regardless of the applied power in the case using pure He DBD jet. We observed that the higher the applied power the longer the pulse duration. Both He/MMA DBD jet and He DBD jet have two distinct operation modes, namely a diffuse mode and a concentrated mode, though their breakdown occurs differently. Compared to the He DBD jet higher applied voltage was required to induce the discharge breakdown in the He/MMA DBD jet.

The experimental results from the discharge current traces, PMT traces, and ICCD images indicated that each broad current pulse observed at the positive half cycle consists of several short-duration (1–2 μs) small current pulses which overlap. In other words, the “broadened current pulse” in the He and He/MMA DBD jets can be deconvolved into several small pulses. Each short-duration pulse (one breakdown) was

found to result from an ionization wave front and a trailing plasma channel when the wave travels from the anode to cathode. In both He and He/MMA cases, the number of the short-duration pulses increases as the discharge power rises. The generation of more short-duration current pulses (more breakdowns) causes the formation of a single broadened pulse (4–16 μs) in the He DBD jet with longer duration but several (2–3) broadened pulses (2–4 μs) in the He/MMA DBD jet. The separation of the broadened pulses in the He/MMA case is due to the higher breakdown voltage and the faster decay of electron density in each single short-duration pulse, compared to the case using pure helium. The fast current disappearance can be likely attributed to the electron energy loses and attachment to the MMA and formed radicals.

As more short-duration current pulses are generated at a higher power, more plasma channels are formed by the leading ionization waves during each positive half cycle. Note that instead of distinct ionization waves only plasma channel generation was observed during the breakdown at the negative half cycles. The rising power leads to thinner and brighter plasma channels in the both positive and negative half cycles. These thin plasma channels with intense light emission appear to be the elements leading to the visual observation of a concentrated mode. The pre-existence of a plasma channel also determines the observable of the ionization wave propagation using ICCD. When a plasma channel which is created by the preceding ionization wave is still present in the discharge gap, the propagation of the subsequent ionization wave becomes less noticeable.

7. FUNDAMENTAL STUDIES OF DBD JETS: PRECURSOR, TUBE SIZE, AND ELECTRODE EFFECTS ON DISCHARGE UNIFORMITY AND MODE CHANGES

7.1 Introduction

This section continues with the fundamental studies of DBD jets, but mainly focuses on the investigation of discharge uniformity due to the operation mode changes. As reported in the prior results, with the presence of a treated substrate the floating-electrode helium DBD jets (He DBD jets), used as a film depositing tool in this study, exhibit discharge non-uniformity when the plasma switches to the concentrated mode as the applied power is increased. Significant reduction of the discharge uniformity was found to be induced by the creation of the concentrated plasma channels which have relatively high intensity. Compared to the discharge in the diffuse mode, in the concentrated mode the discharge is concentrated in a local area rather than being spread around. Thus the films deposited using the non-uniform discharge in the concentrated mode will also be spatially inhomogeneous in terms of their morphology, compositions and chemical structures. Several of these inhomogeneous results have been shown in the film characteristics in the prior sections. In order to better understand what affects the formation of non-uniform discharges and the mode changes in the DBD jets, in this section we will examine how the discharges are influenced by three experimental parameters – (1) precursor types, (2) tube sizes, and (3) electrode configurations.

7.2 Experimental Setup and Methods

Figure 71 schematically shows the experimental setup used to generate the DBD jet and to characterize the electrical and optical properties. The methods for plasma generation and plasma electrical measurement are briefly reiterated here since they have been presented in detail in Section 3.3.1. The DBD jet consists of a borosilicate glass tube (dielectric barrier) and a cylindrical powered electrode. In most cases in this work the glass tube with an inner diameter 4 mm, an outer diameter of 6.35 mm, and a length of 120 mm was adopted. An AC high voltage (~kV) power supply with sinusoidal waveform at a fixed frequency of 29.5 kHz was employed to drive the plasma via the powered electrode. A microscope slide, which was placed on an aluminum holder, was utilized as the second dielectric barrier as well as the substrate for film deposition. A LeCroy 1000:1 100 MHz high voltage probe was connected to the powered electrode for the measurement of the applied voltage. An 825 ohm resistor, which was placed between the aluminum holder and ground, serves as a shunt for further discharge current estimation. The applied voltage, discharge current and discharge power of the DBD jet were monitored and recorded by a LeCroy 204MXi (2 GHz) oscilloscope. Optical emission spectroscopy (OES) was performed to detect the excited species in the DBD jet by using a USB spectrometer (Edmund Optics 64813, TE cooled USB spectrometer UV-VIS). The measurement range is from 200 nm to 800 nm. To capture the time resolved images in the plasma jet for the study of the ionization wave propagation and plasma channel formation, a high-speed gated intensified charge coupled device (ICCD, Stanford 4Picos ICCD) was employed. Focusing the emission light of the plasma and its

images into the collectors of the spectrometer and the ICCD was accomplished by a UV/Vis lens.

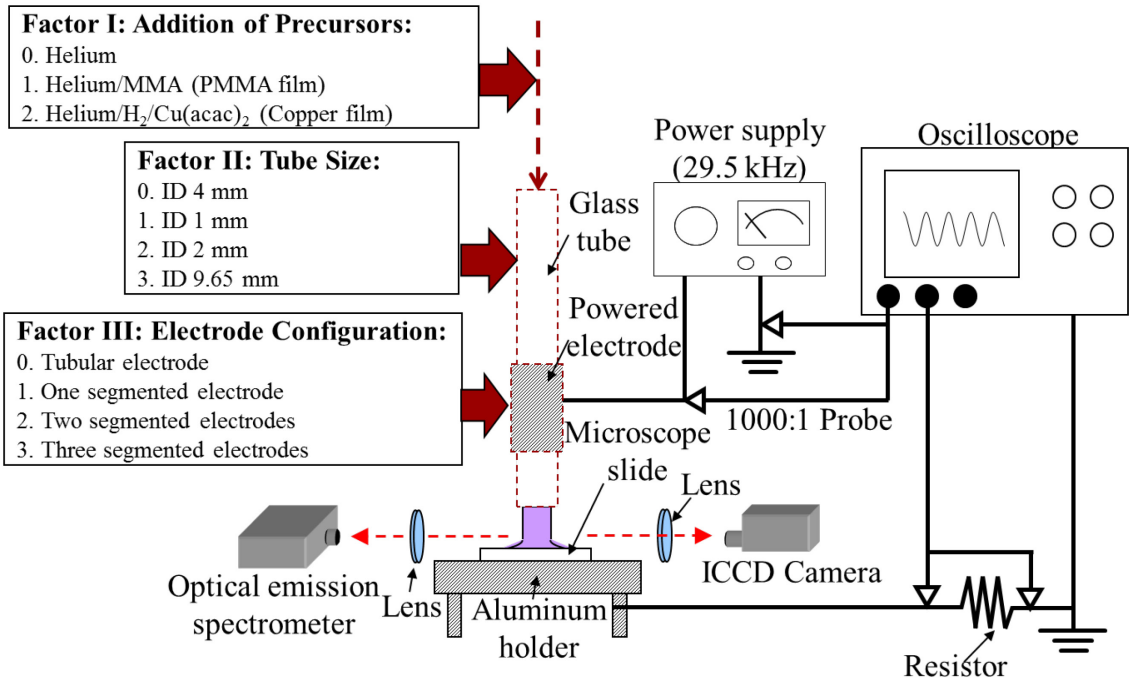

Figure 71. Schematic diagram of the experimental setup for generation and electrical, optical, and imaging measurement of the DBD jet with the illustration of the three factors to be examined.

Figure 71 also illustrates those three factors (precursor types, tube sizes, and electrode configurations) we would like to study. The first factor to be examined is the precursors. This factor is important since the precursors provide additional species in the plasma, which may influence the discharge breakdown processes. The discharge uniformity and the operation modes in the DBD jets fed by the mixture of helium and MMA vapor and the mixture of helium, hydrogen and $Cu(acac)_2$ vapor were investigated and compared with those in the pure helium plasma without any addition of precursors.

The experimental setups for the generation of the He/MMA DBD jet and the $He/H_2/Cu(acac)_2$ DBD jet were given in Figure 16(a) and Figure 19, and they were used for PMMA film deposition and copper film deposition, respectively. The dimension of the glass tube in the DBD jet is the second factor which likely affects the boundary condition of the discharge. In addition to the glass tube with a 4 mm inner diameter (ID) mainly used in our study, smaller tubes (1 mm and 2 mm IDs) and a larger tube (9.65 mm ID) were employed for the DBD jet generation. The last factor, electrode configuration, requires to be researched as it determines the electric field distribution in the DBD jet system. Segmented copper tape, instead of the tubular electrode, was attached to the glass tube to be the powered electrodes. The number of the segmented electrodes on the glass tube and their relative positions were changed to alter the symmetry of the electric field. The DBD jets with one, two, and three segmented electrodes were studied and compared with the commonly used DBD jet with the tubular electrode. Furthermore, the segmented-electrode DBD jets were utilized for clearer observation of the time resolved discharges in the glass tube, especially the portion in the vicinity of the powered electrodes.

7.3 Experimental Results

The experimental results are also divided into three parts based on the three factors mentioned above, and will be given in sequence: the effect of the fed precursors (additional species), the effect of various tube sizes (various boundary conditions), and

the effect of different arrangements of the segmented electrodes (different distribution of electric field).

7.3.1 Effect of Fed Precursors

Figure 72(a), (b), and (c) show the discharge images taken by a digital camera with respect to various powers in He DBD jet, He/MMA DBD jet, and He/H_2/Cu(acac)$_2$ DBD jet, respectively. Note that glass tubes with 4-mm IDs were employed in all these three cases. The DBD jet fed by pure helium gas at a flow rate of 3.0 slm is observed to have two main operation modes – diffuse mode and concentrated mode, as shown in Figure 72(a). At a low discharge power, the plasma exhibits a color with homogeneous distribution in the jet (diffuse mode). An example of the DBD jet in this mode can be seen in the discharge at 0.8 W. An increase in the power leads to the generation of a concentrated discharge at the central axis of the tube, as depicted in the image at 1.5 W. This is the discharge during the transition from the diffuse mode to the concentrated mode. As the discharge power is raised, it is found that visually the diameter of the concentrated discharge (D_c) is increased and its emission light becomes brighter. In addition, the plasma spot diameter (D_s) on the microscope slide expands with the rising power. A sufficient high power causes the DBD jet to switch to a concentrated discharge with a thin, bright appearance located at the central position of the tube (centered concentrated mode, as displayed in the image at 3.0 W). An off-centered concentrated mode, in which the discharge leans against the inner wall of the glass tube, occurs when an even higher applied power is used (e.g., the plasma image at 7.0 W).

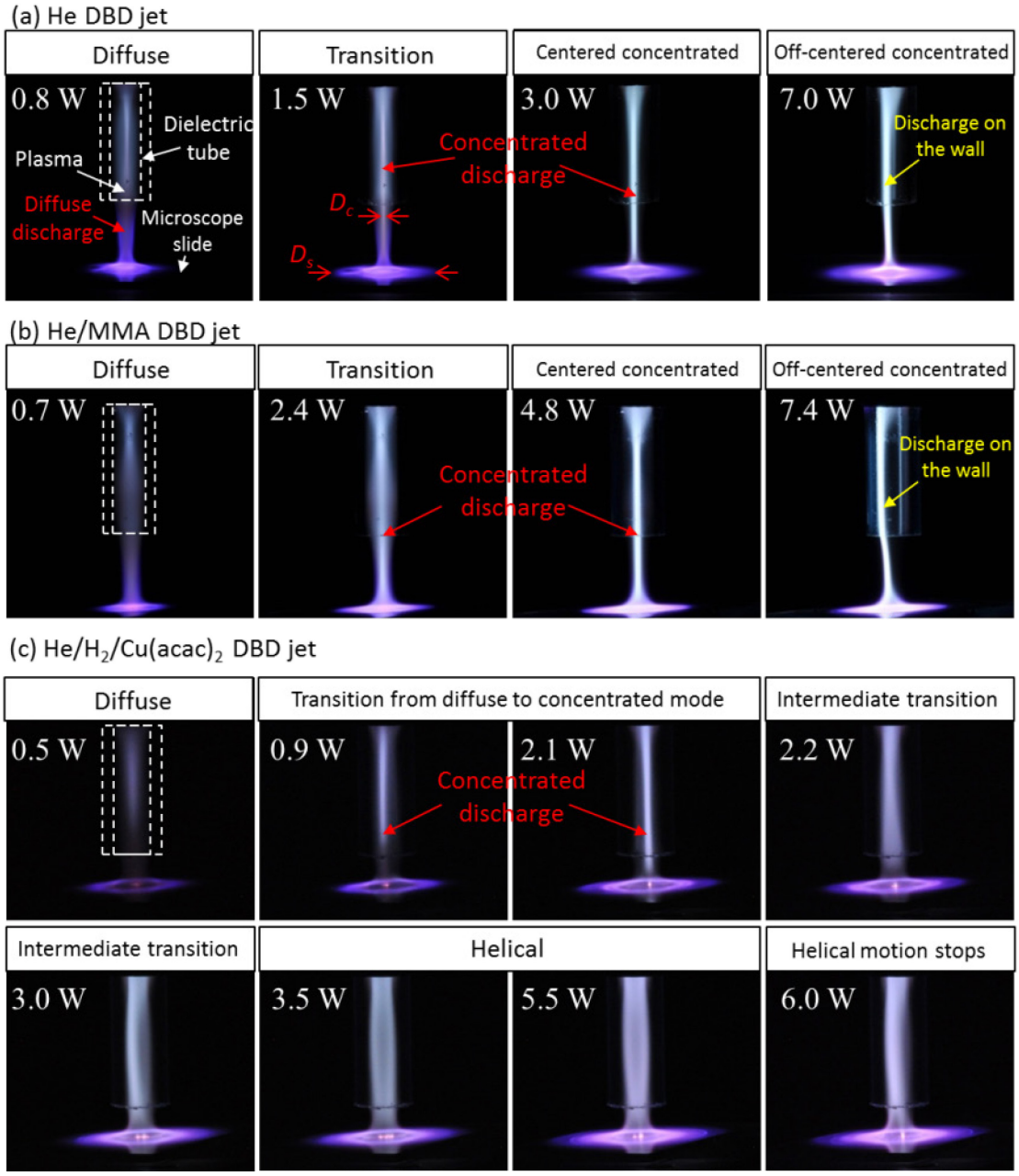

Figure 72. Discharge operation modes in (a) He DBD jet, (b) He/MMA DBD jet, and (c) in He/H_2/Cu(acac)$_2$ DBD jet (the precursor temperature was set to be 100 °C) with a rising power.

After small amounts of the MMA precursors (1800 ppm) are fed into the DBD jet with the helium working gas, similar mode changes but a slightly different color are

observed, as shown in Figure 72(b), compared to the He DBD jet. The plasma appearance of the He/MMA DBD jet changes from a diffuse discharge to a concentrated discharge. Applying a relatively high power to the He/MMA DBD jet also results in an off-centered concentrated discharge. In this case, the helium working gas and the helium carrier gas flowing through the bubbler filled with MMA were set to be 2.9 slm and 0.1 slm, respectively (i.e., the total helium flow rate in this system was maintained at 3 slm). More detailed characterization and comparison of the He DBD jet and the He/MMA DBD jet can be found in Section 6.

The $He/H_2/Cu(acac)_2$ DBD jet shows similar discharge images to those in He and He/MMA DBD jets when the precursor temperature is lower than 90 °C. The flow rates of the helium gas and the hydrogen gas were set to be 2.9 slm and 0.1 slm, respectively. However, as the applied power rises, a precursor temperature higher than 90 °C leads to an unstable concentrated mode, in which the position of the concentrated discharge changes with respect to time instead of remaining at the central axis. When the precursor is heated up to 100 °C, a helical mode rather than a concentrated mode occurs with the rising power. Figure 72(c) displays the discharge images of the $He/H_2/Cu(acac)_2$ DBD jet at a precursor temperature of 100 °C at different powers. Note that the gap distance between the tube exit and the microscope slide was about 2.5 mm in this case, whereas the gap distances in the pure He and He/MMA plasmas were both 10 mm. A 2.5 mm spacing distance was employed in the $He/H_2/Cu(acac)_2$ DBD jet since the copper film growth can be observed in a shorter deposition time (i.e., higher deposition rate) when a

shorter gap distance was utilized, as mentioned in Section 5. Note that the helical mode still occurs in the $He/H_2/Cu(acac)_2$ DBD jet even if a 10-mm gap is employed.

As shown in Figure 72(c), at a power of 0.5 W, similar to the He and He/MMA DBD jets at low powers, the $He/H_2/Cu(acac)_2$ DBD jet appears to be a discharge with a diffuse color (diffuse mode). As the applied voltage is increased, the discharge enters the transition from the diffuse mode to the concentrated mode. A concentrated discharge can thus be seen along the central axis of the glass tube in addition to the diffuse discharge, as shown in the images at 0.9 W and 2.1 W. The concentrated discharge extends from the powered electrode to the vicinity of the microscope slide surface as a higher power is used. If the precursor temperature is lower than 90 °C, a further increase in the discharge power leads to a mode change to the centered concentrated mode. However, in this case with a precursor temperature at 100 °C, an additional transition (intermediate transition state to a helical mode) is observed instead of the occurrence of the concentrated mode as the discharge power is increased from 2.1 W to 2.2 W. As can be seen in the image at 2.2 W, the central concentrated discharge appears to expand in diameter in the glass tube. This is likely due to the fact that the concentrated plasma channels at different voltage cycles are generated at different slightly off-centered positions. Thus the DBD jet exhibits a "diffuse-like" appearance. More experimental results regarding the temporally-resolved discharges in the DBD jets have been presented in Section 6. As a higher applied power is employed during this intermediate transition, the concentrated discharges generated at different voltage cycles begin to bend (instead of being in a straight shape) and occur at a certain position (this position is random) more frequently

than other positions. The image at 3.0 W illustrates that the most of the concentrated discharges are created against the left side of the tube inner wall in this case. A more intense light emission can thus be seen at the place where more concentrated discharges occur. A sufficiently high power (3.5 W) induces the occurrence of a helical mode, in which visually the bent discharge spins in the glass tube around the tube central axis. When the power is kept increasing, the discharge intensity becomes stronger and the plasma spot on the microscope slide surface expands in diameter, as shown in the discharge image at 5.5 W. The helical motion in the $He/H_2/Cu(acac)_2$ DBD jet can be observed until a power of 6.0 W is applied (helical motion stops). Compared to the discharges in the concentrated mode, the discharges in the helical mode appear to be more uniform in terms of the intensity in the tube, thus may leading to more uniform film deposition.

The temporally resolved images of the discharge in the helical mode (5.0 W) over one whole voltage cycle at different time moments were captured by the high-speed ICCD camera. Figure 73 shows the ICCD images of the discharges at four different time moments. Note that each image was taken from the onset of the positive half voltage cycle until the end of the negative voltage cycle with an exposure time about 35 μs. These images show that the concentrated discharges curve against the inner wall of the glass tube and at different voltage cycles the curved discharges were observed at various positions. Since every 35 μs a new discharge is generated at either a similar spot or a totally different position, visually the discharge appears to move in a helical motion.

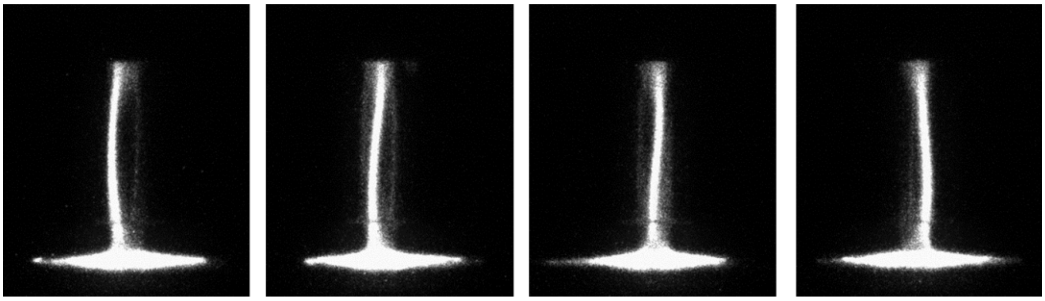

Figure 73. ICCD images of the He/H_2/Cu(acac)$_2$ DBD jet over different voltage cycles (exposure time ~ 35 μs).

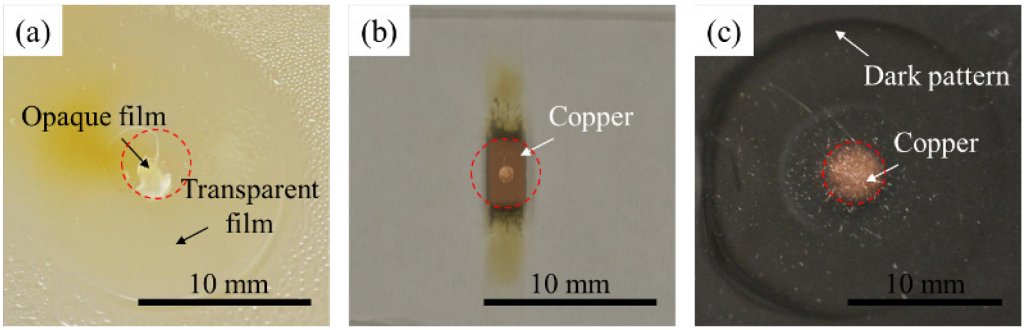

Figure 74. (a) as-deposited PMMA film obtained by the He/MMA DBD jet at 7.7 W in the off-centered concentrated mode after 10-min deposition; as-deposited copper films using the He/H_2/Cu(acac)$_2$ DBD jet (b) at 3.0 W in the concentrated mode with a precursor temperature of 90 °C after 30-min deposition and (c) at 4.0 W in helical mode with a precursor temperature of 100 °C after 15-min deposition.

The uniformity of the deposited films by using the DBD jets was also examined, as shown in Figure 74. Figure 74(a) shows an as-deposited PMMA film obtained on a microscope slide after 10-min deposition using the He/MMA DBD jet at 7.7 W in the off-centered concentrated mode. The nozzle-to-substrate distance in this case was 10 mm. The dashed circles on the images indicate the inner diameter (4 mm) of the tube. The PMMA film shows two different colors. At the film center the film appears white opaque, whereas a transparent film is observed at the outer region. The formation of a white opaque PMMA film is due to the buckling effect in the film induced by a

relatively high deposition rate in the high-intensity concentrated plasma region (See Section 4.3.4 for more details) [151]. The off-centered opaque film is attributed to the off-centered discharge. This result implies that the non-uniform discharge causes the growth of a non-uniform film, in which the relatively spatially inhomogeneous chemical structures, chemical compositions, and morphology were observed. Copper films were also deposited on microscope slides using the $He/H_2/Cu(acac)_2$ DBD jet under different conditions for the investigation of film uniformity. A precursor temperature of 90 °C, a power of 3.0 W, and a gap distance of 5 mm were used to generate a centered concentrated discharge for copper film deposition [Figure 74(b)]. The left and right edges of the film obtained using 30-min deposition time were created by tape masks during deposition for further film thickness measurement. The center of the film exhibits a different color from that in the outer area. In Section 5 we have shown that the lighter color at the film center is likely due to its thicker film with a rougher surface. Thus, again, the non-uniformity in the discharge when it operates in the concentrated mode leads to the inhomogeneous film growth. When a 100 °C precursor temperature was employed to deliver the precursor gas and a 4.0 W discharge power was applied to the DBD jet, a helical discharge was generated to deposit copper film on the microscope slide (the gap distance was 2.5 mm). Figure 74(c) displays the deposition result after 15 min. The copper film obtained by the helical discharge shows relatively homogeneous color distribution in the area downstream of the glass tube. This uniform film appearance is likely due to the relatively uniform treatment by the helical mode. A dark pattern at the outer region shown in Figure 74(c) may be attributed to the formation of the film

with high carbon and oxygen concentrations deposited in the vicinity of edge of the plasma spot (low-power discharge) on the microscope slide.

The fed precursors not only change the operation modes in the plasma jets, but also influence the discharge breakdown phenomena. The discharge current waveforms in the He/MMA DBD jet show significant difference from those in the He DBD jet though they have similar mode changes with the rising power. The difference between their current waveforms can be seen in Figure 75(a) and (b). As the applied power rises, in the He DBD jet only one current pulse with longer duration is observed at each half cycle, whereas the number of the current pulses is increased in the He/MMA plasma. After the MMA is added to the He plasma, the current pulses vanish faster than those in He DBD jet likely due to the electron energy loss and electron attachment to the MMA and formed radicals, as discussed in Section 6.3.4. This result indicates that the MMA precursor change the discharge breakdown in the plasma. More results regarding the comparison between the He DBD jet and the He/MMA DBD jet can be seen in the prior section (Section 6). In contrast, the helium plasma containing the mixture of hydrogen and $Cu(acac)_2$ with a precursor temperature of 100 °C results in similar current waveforms [Figure 75(c)] to those in the He DBD jet though a different operation mode (helical mode) occurs in the $He/H_2/Cu(acac)_2$ plasma. In other words, only one broad current pulse occurs during each half cycle regardless of the applied power.

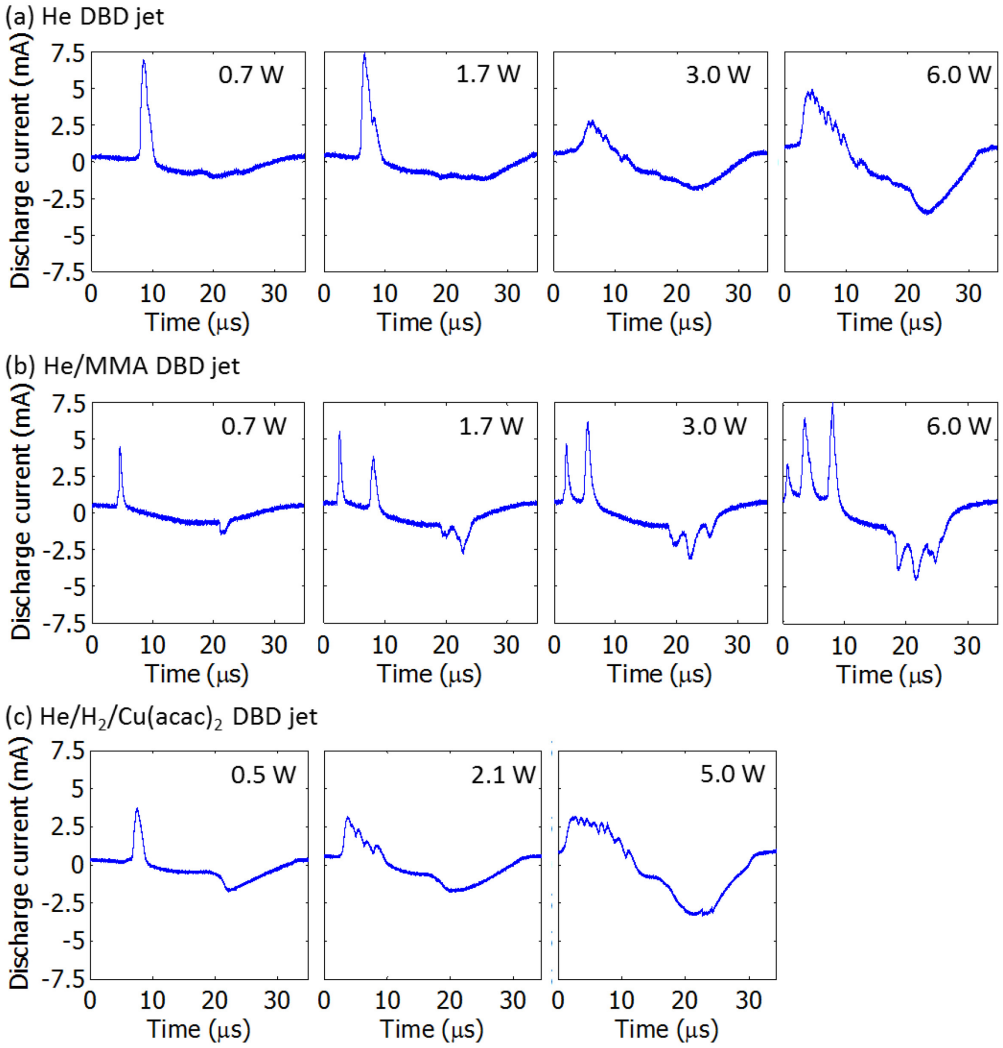

Figure 75. Discharge Current waveforms of (a) He DBD jet, (b) He/MMA DBD jet, and (c) $He/H_2/Cu(acac)_2$ DBD jet with various powers.

7.3.2 Effect of Dielectric Tube Sizes

In the most parts of this dissertation, the dielectric tube used in the experiments has an inner dimension (ID) of 4 mm. In this subsection, borosilicate glass tubes with smaller (1 mm and 2 mm) and larger (9.65 mm) dimensions were employed to study the

effect of the tube size (i.e., the boundary condition) on the discharge uniformity and the mode change in the DBD jets. To operate the DBD jets at the same conditions as those in the case using a 4 mm ID, pure helium flow with identical Reynolds number was used in all the three cases (tubes with IDs of 1, 2, and 9.65 mm). Copper tape with a width of 10 mm was used to cover around the dielectric tube to serve as the powered electrode. The distance between the downstream end of the powered electrode and the tube end was set to be 15 mm, which is the same as that in the case using the 4 mm ID tube.

Figure 76 shows the images of the discharges with various powers when the tube with an ID of 1 mm was utilized. It can be seen that the plasma spot shown on the microscope slide is increased in diameter when a higher power is applied. The images shown at the lower panel in Figure 76 correspond to those in the dashed box at the upper panel. At a low power (0.5 W), the plasma appears to be a diffuse discharge with homogeneous color distribution. As the applied power rises, the intensity of the discharge light emission is also increased, whereas the discharge appearance remains uniform in color without the observation of the concentrated discharge which was seen in the results using 4 mm ID tubes. It is suggested that the concentrated discharge still occurs when a higher power is applied. However, since the dimension of the concentrated discharge is similar to the tube ID in this case, the mode change becomes less observable.

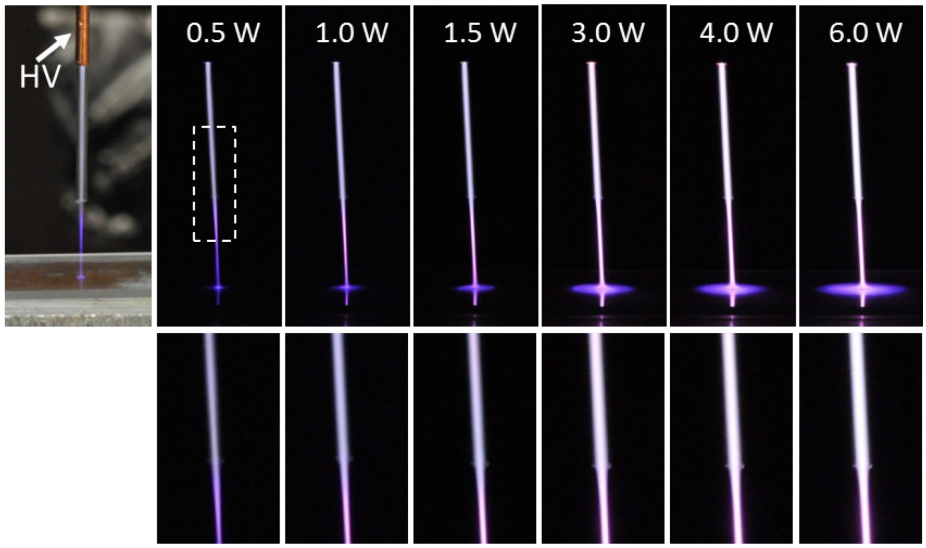

Figure 76. Discharge images of He DBD jet using a dielectric tube with an inner dimension of 1 mm at various powers. The upper panel shows the entire discharge and the lower panel shows the magnified image of the discharge in the dashed box.

When the tube with a 2 mm ID was employed in the experiment, discharge non-uniformity was observed with the rising power, as shown in Figure 77. At the discharge powers of 0.2 and 0.5 W, similar to the case using the tube with an ID of 1mm, the plasma jet outside of the tube appears to be homogenous in color. When the power was increased to 1.5 W, a concentrated discharge (plasma channel) with relatively intensity emission light was formed at the left inner side of the tube, as indicated by an arrow in the figure. Higher discharge power resulted in a more non-uniform discharge. As can be seen in the discharge images at 3.0, 4.0, and 6.0 W, an off-centered concentrated discharge with a diameter smaller than the ID of the glass tube occurred. This result is similar to the previous one using 4 mm ID tube, with which a mode change from the diffuse mode to the concentrated mode was observed. However, the size of the plasma spot on the microscope slide was still greater as a higher power was used.

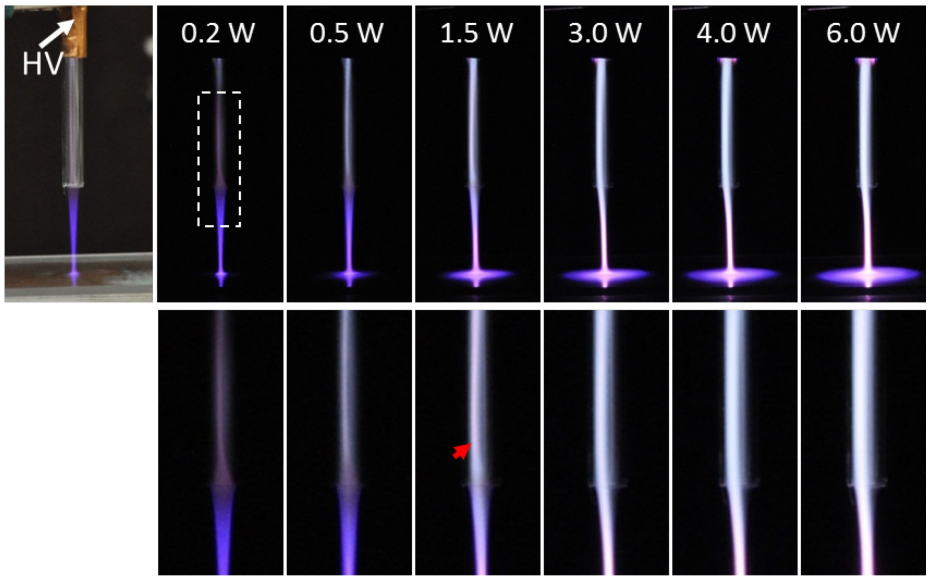

Figure 77. Discharge images of He DBD jet using a dielectric tube with an inner dimension of 2 mm at various powers. The upper panel shows the entire discharge and the lower panel shows the magnified image of the discharge in the dashed box.

The dielectric tube with an ID of 9.65 mm was used to generate the DBD jet and the discharge also exhibited different operation modes with the rising power. Figure 78 displays the discharge images when various powers were applied to the DBD jet with a 9.65 mm ID. Similar to prior cases using smaller tubes, at low power (e.g., 0.2 and 0.5 W) visually the plasma discharge was in the diffuse mode. When a 1.0 W power was utilized, the formation of a concentrated discharge (plasma channel) occurred. Additionally, the plasma spot on the microscope slide was reduced in diameter with the presence of the plasma channel, compared with the plasma spot generated at the lower power in the diffuse mode. The reason of the plasma spot reduction is yet unclear. The plasma spot and plasma channel were then observed to gradually expand in diameter as the applied power was increased (see the images from 1.0 W to 2.0 W in Figure 78).

Eventually the plasma channel in the He DBD jet at 3.0 W formed a cone-shaped structure with a contracted lower end (i.e., the end near the slide) located at the central axis. Further increase in the discharge power led to the enlargement in diameter of lower end of the plasma channel, as shown in the images from 3.0 W to 6.0 W. The lower end of concentrated discharge eventually touched the inner wall of the glass tube as the discharge power kept rising, and the discharge began to be unstable, as shown in the image at 8.0 W. The plasma channel at this power was not a cone-shaped structure anymore. Instead, the plasma channel split in several spatially separated discharges. And visually these discharges randomly changed their radial positions during operation.

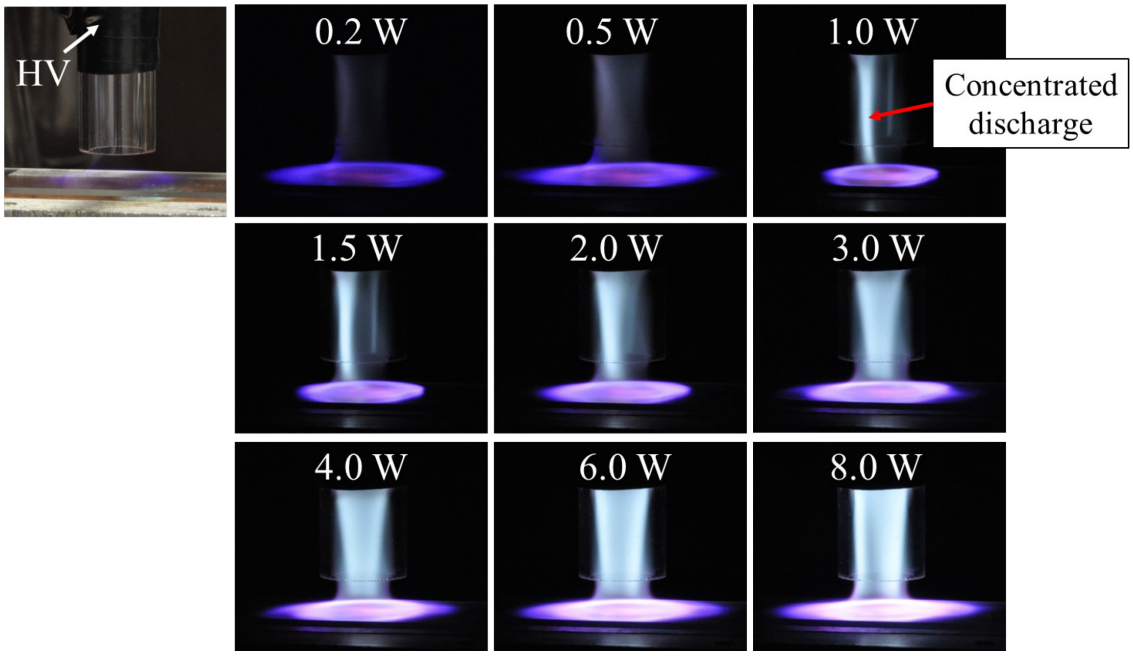

Figure 78. Discharge images of He DBD jet using a dielectric tube with an inner dimension of 9.65 mm at various powers.

The photographs of the He DBD jets with IDs of 1, 2, 4, and 9.65 mm presented in Figure 76, Figure 77, Figure 72(a), and Figure 78 showed that as a smaller tube was utilized to generate the plasma, the mode change was less observable. It was also found that at the relatively high discharge power the size (diameter) of the concentrated discharge shows dependence on the tube size of the plasma jet. If a larger tube ID is employed, a plasma channel with a greater diameter can be obtained (e.g., ~0.73 mm in the case using the 1 mm ID tube, whereas ~3.51 mm in the case using the 9.65 mm ID tube at 3.0 W). The summarized diameters of the plasma channels formed in these four jets can be seen in Table 9.

Table 9. Diameters of the plasma channels and power densities in the DBD jets with the IDs of 1, 2, 4, and 9.65 mm.

ID of Dielectric Tube	**1 mm**	**2 mm**	**4 mm**	**9.65 mm**
Discharge Power (W)	3	3	3	3
Plasma Channel Diameter (mm)	0.73	0.87	1.13	3.51
Power Density (W/mm^2)	7.11	5.08	2.98	0.31

Excited species generated from the DBD jets with IDs of 1, 2, and 4 mm were measured by OES to investigate the influence of the boundary condition on the species generation. The $He/H_2/Cu(acac)_2$ DBD jet was employed in this study as it contains more abundant species, compared to the He DBD jet. The light emission from the plasma jet at 3.0 W at the point downstream of the tube end at a distance of 2.5 mm was measured. Figure 79(a) and Figure 79(b) show the emission spectra of the three DBD

jets with a wavelength range of 300–410 nm and a range of 650–730 nm, respectively, for comparison. Note that the spectra were all normalized with respect to the copper peak at 324 nm. These two figures display that the excited species observed in these plasma jets are atomic copper, N_2 second positive systems, N_2^+ first negative systems, atomic hydrogen, and atomic helium transitions. It can be seen that the greater the tube dimension the stronger the N_2 and He emission peaks. This difference can be attributed to the various plasma densities generated by the DBD jets with different dimensions though an identical discharge power (3.0 W) was applied to all these three devices. The plasma densities of the DBD jets with IDs of 1, 2, and 4 mm are listed in Table 9. The diameters of the concentrated discharges instead of the tube IDs were used to calculate the plasma densities as at 3.0 W the concentrated mode occurred. Since the concentrated discharge was larger in diameter when a greater tube was employed, the power density in the greater tube was decreased. The peak ratios of Cu(324 nm)/N_2(337 nm), Cu(324 nm)/He(667 nm), H_α(656 nm)/ He(667 nm), and N_2^+ (391 nm)/N_2(337 nm) at various power densities (various tube sizes) are plotted in Figure 79(c). The result shows that as the plasma density is augmented (smaller tube is used), Cu/N_2, Cu/He, and H_α/ He are enhanced whereas N_2^+/N_2 drops. This may indicate that more atomic hydrogen and atomic copper can be generated using a smaller tube, whereas the use of a smaller tube leads to the formation of less amount of nitrogen ions. However, this may be also due to the fact that the electronic excitation temperature (T_{elex}) is increased when a smaller tube is used.

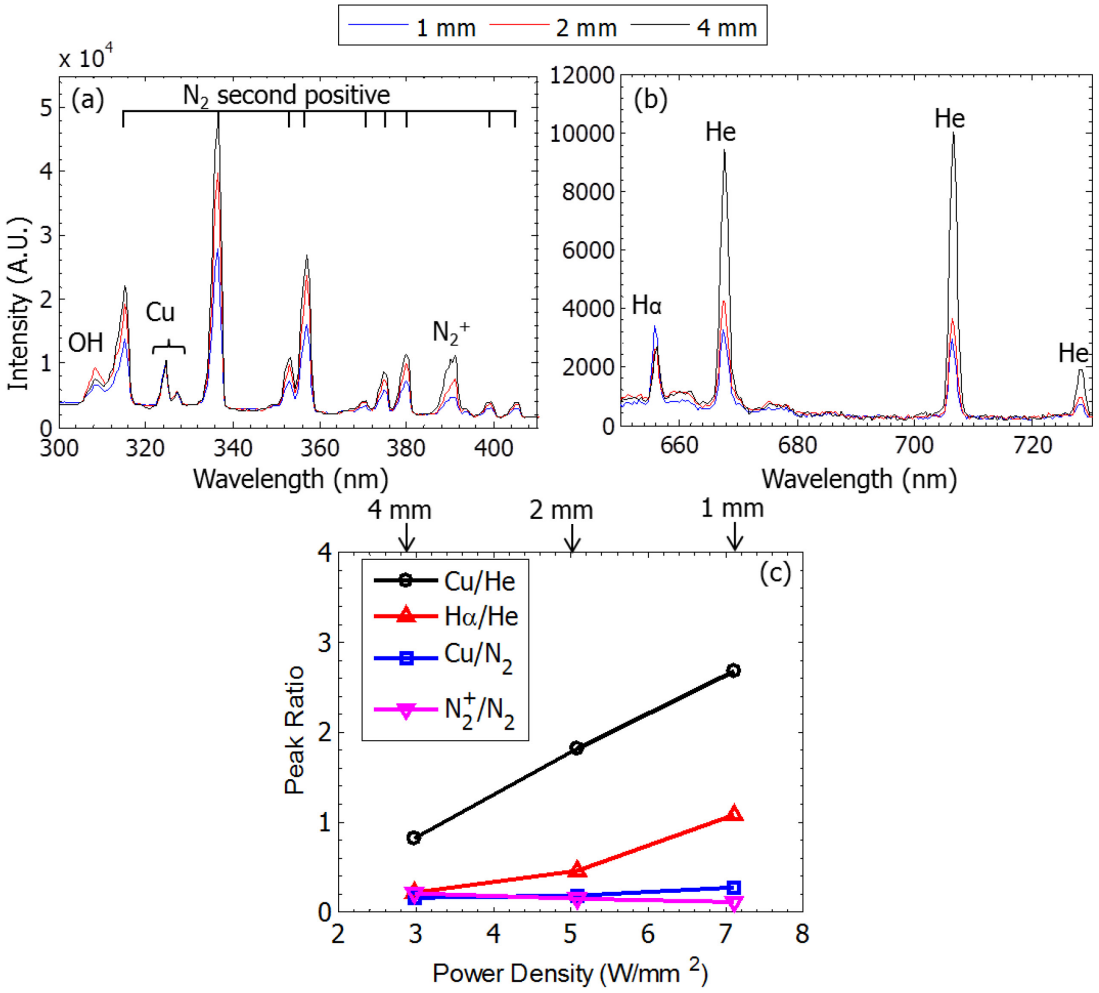

Figure 79. Optical emission spectra of the He/H_2/Cu(acac)$_2$ DBD jets with IDs of 1, 2, and 4 mm in the wavelength ranges (a) between 300 and 410 nm and (b) between 650 and 730 nm. (c) Plot of the ratios of different peaks versus various power densities, which correspond to different tube sizes.

The atomic transitions, including atomic helium lines and atomic hydrogen Balmer lines, were employed to estimate the electronic excitation temperature (T_{elex}) in the He/H_2/Cu(acac)$_2$ DBD jets with different tube sizes. The method to obtain T_{elex} is by comparison of the line intensities of different transitions at upper energy states on a

Boltzmann plot [65, 158]. The relationship between the line intensity and the electronic excitation temperature can be written as [157, 158]:

$$\frac{1}{T_{elex}} \approx -\frac{\ln(I\lambda / A_{ki}g_k)}{E_k} \qquad \textbf{(Equation 4)}$$

where I is the intensity of atomic line, λ is the line wavelength (nm), A_{ki} is the transition frequency (s^{-1}), g_k is the degeneracy of the upper state of the transition, and E_k is the upper state energy. These parameters can be readily found in the spectra database provides on NIST website [159]. Atomic helium lines at 492.19, 501.57, 587.56, 667.81, 706.52, and 728.13 nm were used to determine the T_{elex} for all the three cases with different tube IDs on the Boltzmann plot, as shown in Figure 80(a). Fit lines were obtained by a least squares method in Matlab. The electronic excitation temperatures can be further calculated from the slops of the fit lines on the Boltzmann plot. As shown in Figure 80(a), these three fit lines for DBD jets with the 4, 2, and 1 mm IDs exhibit similar slopes, and their resulting T_{elex} are about 2200 K. Note that in this case only the high energy tail (22.5–24 eV) of the electron distribution function is taken into consideration. The Boltzmann plot of the hydrogen Balmer lines can be seen in Figure 80(b). Since only the intensities of the α and β transitions of the hydrogen Balmer series are strong enough to be measured, only H_α (656.28 nm) and H_β (468.13 nm) lines are employed for the T_{elex} estimation. In the cases using the dielectric tubes with IDs of 4 and 2 mm, similar electronic excitation temperatures (~16000 K) are obtained. The smaller tube (1 mm ID) results in a lower T_{elex} (~7900 K). However, the T_{elex} values in this range (12–13 eV) may exhibit great uncertainty as only two points (e.g., two

hydrogen Balmer lines: H_α and H_β) were utilized to generate the fit line. Additional transitions, such as H_γ (434.04 nm) and H_δ (410.17 nm), are required for more accurate estimation of T_{elex} but in our case these two lines are too weak to be detected. An increase in the acquisition time of the OES system may enhance the intensities of these two lines.

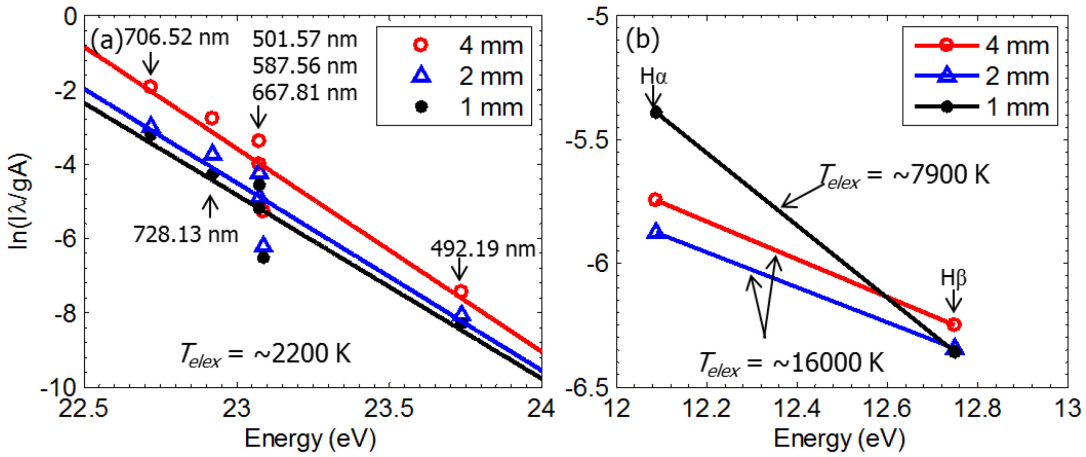

Figure 80. Boltzmann plots of (a) atomic helium lines and (b) atomic hydrogen Balmer lines used to measure the electron excitation temperature (T_{elex}) in the He/H_2/Cu(acac)$_2$ DBD jets with different tube sizes.

When a small amount of air existed in the helium feed line, the He DBD jet with a 9.65-mm ID exhibited different modes with the rising power. It was observed that multiple plasma channels (concentrated discharges) with reduced diameters were formed instead of one broad plasma channel which was displayed in Figure 78. Initially at a medium power, one contracted plasma channel occurred along the inner wall of the glass tube, similar to the case in Figure 78 at 1.0 W. However, as the power rose an additional plasma channel was created at the opposite inner wall, as shown in Figure 81(a). Further

increase of the applied power led to the observation of a third concentrated discharge [Figure 81(b)]. The observation of multiple concentrated plasma channels in this case again shows that mode changes in the DBD jet are sensitive to the additional impurities in the plasma. These results were found to be similar to the self-organized discharges in the He DBD jets reported by Nie *et al.* and Feng *et al.* [95, 110]. In their experiments the number of the plasma channels was also increased with the rising power though rectangular cross-sectional quartz tubes were employed to generate the plasma jets.

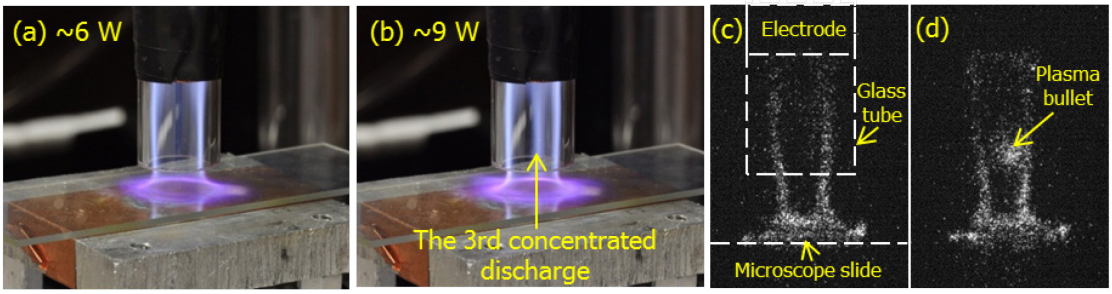

Figure 81. Formation of (a) two plasma channels at ~6 W and (b) three plasma channels at ~9 W when a slightly amount of air exists in the DBD jet. ICCD images with 10 ns exposure time showing (c) the co-existence of two concentrated plasma channels and (d) the plasma bullet generation with the presence of concentrated plasma channels at a discharge power of ~6 W.

To demonstrate if the plasma channels occur simultaneously or consecutively, the high-speed ICCD camera with 10-ns exposure time was utilized to capture the temporally resolved discharge images. Figure 81(c) shows the ICCD image of the 6-W discharge at the onset of the positive discharge current pulse. Two distinct plasma channels can be seen in the image, showing the co-existence of the plasma channels. The presence of the plasma bullet (ionization wave) in addition to the plasma channels was also observed, as can be seen in Figure 81(d). This implies that the ionization wave

propagation still occurs in this large ID DBD jet even though the plasma channels exist. More experiments are required in the future to investigate the spatial and temporal evolution of these self-organized discharges.

7.3.3 Effect of Electrode Configurations

Different numbers of segmented electrodes instead of the tubular electrode were used to study the effect of the electrode configurations on the position of the concentrated discharge (concentrated plasma channel). A piece of copper tape with a dimension of 3.5 mm×10 mm was used as the segmented electrode. Figure 82(a), (b), and (c) show the photographed images of the He DBD jets in the concentrated mode with one, two, and three segmented electrodes (dashed rectangles), respectively. The He DBD jet with the regular tubular electrode is also presented in Figure 82(d) for comparison. Note that in these cases all the electrodes were placed over the glass tube with their downstream ends at a distance of 15 mm from the tube end. The nozzle-to-substrate distance was set to be 10 mm. All these cases employed pure helium at a flow rate of 3 slm as the working gas. The upper panel of Figure 82(a) displays the front view of the He DBD jet with only one segment electrode attached at the left side of the dielectric tube. It can be seen that a concentrated discharge against the left side of the inner tube wall is generated (i.e., off-centered concentrated discharge). A schematic cross-sectional diagram of this case is also drawn at the lower panel of Figure 82(a) to depict the relative position of the plasma channel in the tube. When two segmented electrodes were attached to symmetric positions, the concentrated discharge formed

along the central axis of the glass tube (i.e., centered concentrated discharge), as can be seen in Figure 82(b). Figure 82(c) shows the DBD jet with a third segmented electrode mounted 90 degree relative to the other two electrodes. The presence of the third electrode "pulled" the contracted plasma channel toward it to form, again, an off-centered concentrated discharge. These results indicate that the symmetry of the net electric field created by the electrodes plays an important role determining the position where the plasma channel forms. For example, the cases with one electrode [Figure 82(a)] and three electrodes [Figure 82(c)] both induce relatively intense electric fields close to the left side of the tube (asymmetric electric field with respect to central axis of the dielectric tube). Thus the electrons in the vicinity of the left sidewall can be readily energized, leading to the formation of an intense plasma region. In contrast, the use of two electrodes at symmetric positions [Figure 82(b)] provides a relatively symmetric electric field with the strongest electric field located along the tube central axis. Therefore, the centered concentrated discharge can be obtained in this case. The same reason can be applied to the DBD jet with the most common tubular electrode, as shown in Figure 82(d). The symmetric geometry of the tubular electrode also creates a relatively symmetric electric field, further resulting in the observation of the centered concentrated discharge. As mentioned before, the off-centered concentrated discharge occurs when an ever higher applied power is used in the DBD jet with the tubular electrode (see Figure 72). It is likely due to the fact that the tubular electrode is not perfectly symmetric (nothing is perfectly symmetric). A relatively high power may cause

the net electric field to be asymmetric, rather than relatively symmetric, with respect to the tube central axis.

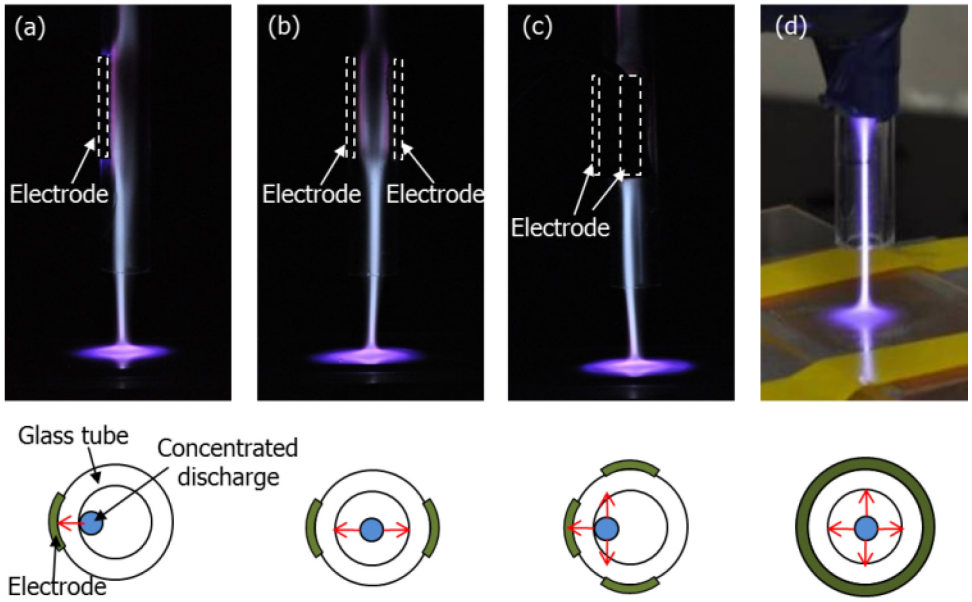

Figure 82. Photographs of He DBD jets with (a) one segmented electrode, (b) two segmented electrodes, (c) three segmented electrodes (one is behind the tube), and (d) a tubular electrode in the concentrated modes.

The He DBD jets with one segmented electrode and two segmented electrodes at various powers are shown in Figure 83(a) and Figure 83(b). Similar to the case using a tubular electrode given in Figure 72(a), the mode change from a diffuse mode to concentrated mode can be observed. At the powers of 0.2 and 0.5 W in Figure 83(a), the plasma jet blown out of the tube exhibits a diffuse color (diffuse mode) with a similar dimension to the inner dimension of the dielectric tube though only a segmented electrode is used. It will be demonstrated later that the diffuse plasma observed downstream of the tube mainly results from the generation of ionization waves. A 1.0 W

discharge power leads to the formation of a concentrated discharge, as indicated in the figure. This plasma state is during transition to the concentrated mode. It can be seen that the upstream of the concentrated plasma channel is connected to (or very close to) the portion of the glass tube in vicinity of the powered electrode. As the discharge power rises from 1.0 to 6.0 W, visually the diffuse discharge (ionization wave) becomes less noticeable whereas the concentrated discharge (plasma channel) becomes more distinct and appears greater in diameter, brighter in color, and closer to the left inner wall of the dielectric tube. In this case, the concentrated mode occurs at about 2–3 W.

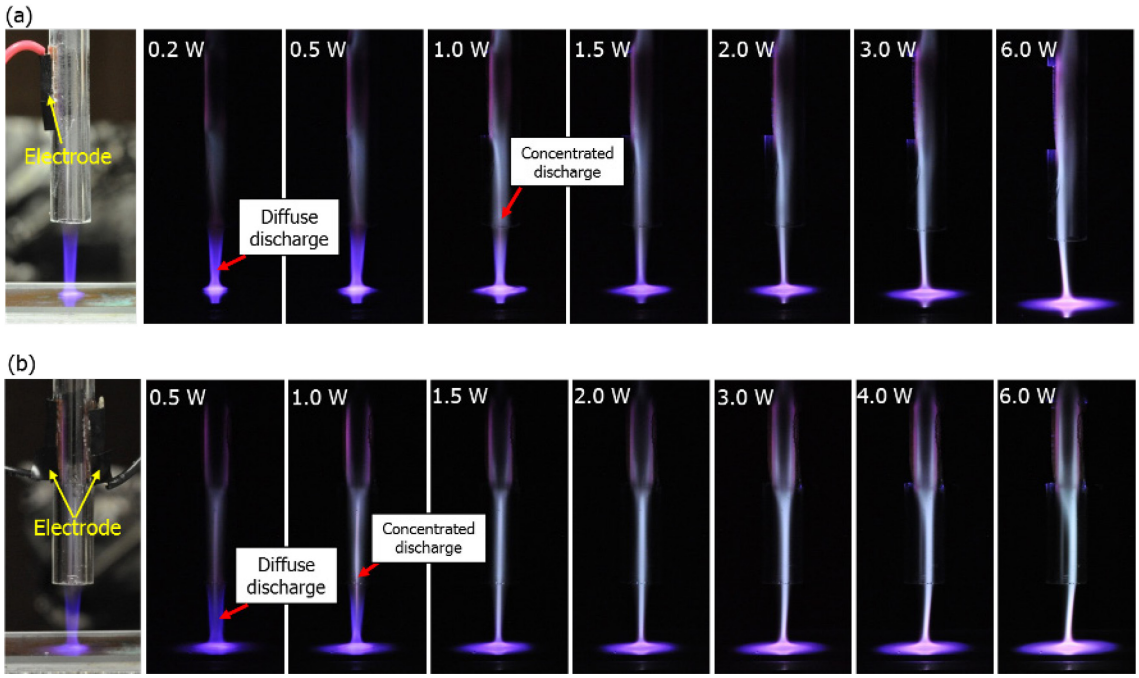

Figure 83. Photographed images of the He DBD jet with (a) one segmented electrode and (b) two segmented electrodes at various powers.

Similar plasma variations are seen in the case with two segmented electrodes [Figure 83(b)]. Diffuse plasma is also observed at the low power and followed by the formation of a spatially thin, visually bright concentrated discharge when the power is increased. Again, the diffuse plasma gradually disappears but the concentrated discharge shows more intense light with the rising power. Note that the concentrated discharge occurs along the tube centerline at the beginning of the concentrated mode (~2 W). Further increase of the discharge power causes the movement of the discharge. Finally the concentrated discharge is observed to lean against the inner wall of the tube (off-centered concentrated mode). This phenomenon (i.e., diffuse discharge → centered concentrated discharge → off-centered concentrated discharge) is similar to that observed in the case using the tubular electrode [Figure 72(a)].

It is worthy to study the temporal resolved behavior of the plasmas with segmented electrodes using the high-speed ICCD camera since more information in the vicinity of the powered electrodes can be obtained. Figure 84 shows the voltage and current waveforms (upper left panel) and several corresponding ICCD images of the He DBD jet with one segmented electrode at 0.3 W (diffuse mode). The gap distance between the tube end and the substrate was set to be 5 mm. The upper right panel displays the ICCD images of the DBD jet over one complete cycle (~ 34 μs), positive half cycle, and negative half cycle. It can be seen that in this case the plasma jet downstream of the dielectric tube in ambient air mainly results from the plasma generated in the positive half cycle. During the negative half cycle, the light emission is only observed from those portions inside the glass tube, in the vicinity of the powered

electrode, and near the surface of the microscope slide. It can be noticed that the plasma in the vicinity of the electrode has more intense light emission when the electrode serves as a cathode than as an anode. For example, during the positive half cycle the discharge near the microscope slide (cathode) appears brighter than that near the slide (anode) during the negative cycle. Similarly, more distinct light was observed from the discharge on the surface near the powered electrode (cathode) during the negative half cycle, compared to the light seen at the same place (anode) during the positive cycle.

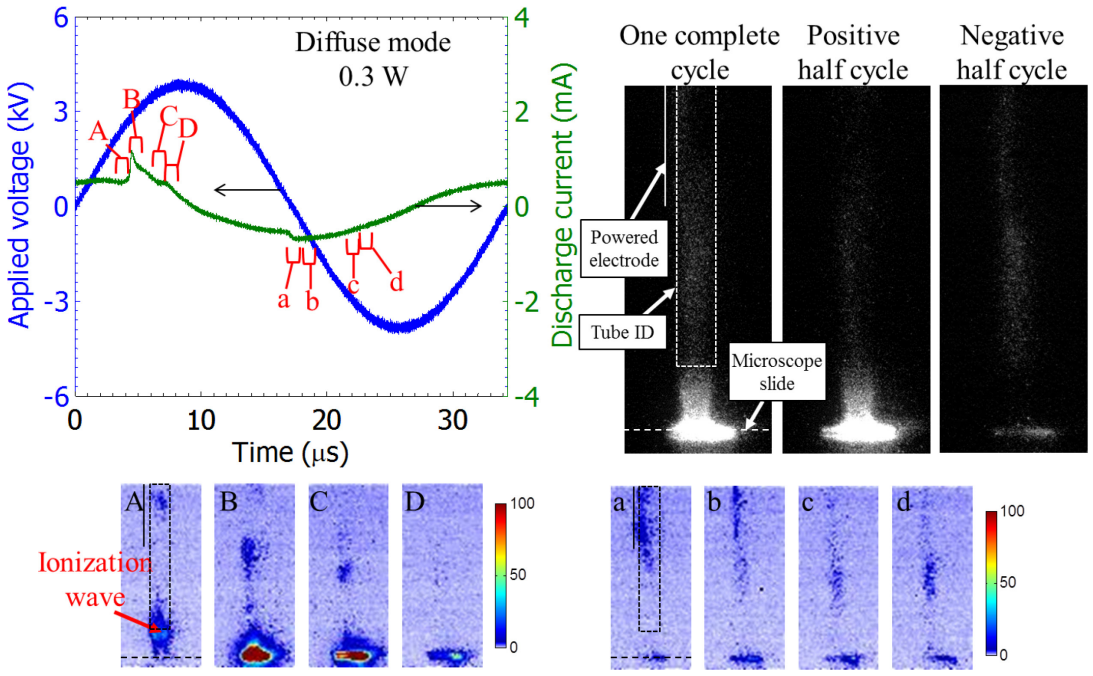

Figure 84. Voltage and current waveforms (upper left panel) of the He DBD jet with one segmented electrode at 0.3 W (diffuse mode). The upper right panel shows the ICCD images over one complete cycle, positive half cycle, and negative half cycle, respectively. The lower panel shows the false-color ICCD images (1-μs exposure time) which correspond to different temporal points as labeled on the current waveform.

The temporally resolved ICCD images with the exposure time of 1 μs can be used to better understand the plasma evolution during the occurrence of the positive and negative current pulses. Note that conversion of the ICCD images with 1 μs exposure time into false-color images with an intensity range from 0 to 100 was performed to more clearly show the discharge features. The mapping can be seen in the intensity color bar as shown at the lower panel in Figure 84. The ICCD images with capital letters correspond to those capital letters labeled on the positive current trace, whereas during the negative current pulse lowercase letters are utilized. Image (A) shows the image during the onset of the positive current pulse. The propagation of an ionization wave (plasma bullet) can be observed. After the wave arrives at the microscope slide surface, a portion of the plasma channel created by the wave front becomes visible in the glass tube [image (B)]. Image (C) displays that an additional ionization wave reaches the substrate surface. Finally as the current pulse vanishes, the intensity of light emitted from the plasma is reduced, as shown in image (D). A detailed study about the multiple ionization waves can be seen in Section 6. The light emission during positive half cycle can thus be attributed to the generation of ionization waves followed by the formation of plasma channel.

Different plasma variations occur during the negative current pulse. At the onset of the negative pulse [label (a)], light emission from the vicinity of the powered electrode was acquired first without the observation of any wave propagation. At label (b) the discharge appears to elongate toward the substrate. Similar discharge structures are observed in images (c) and (d) but with a brighter downstream portion, compared to

that in image (b). These results show that the observation of the diffuse plasma at a relatively low power is mainly due to the ionization wave propagation. Additionally, it should be mentioned that the discharge during the negative half cycle gradually extends to the substrate with rising power. Further increase of the discharge power leads to the reduction in the diameters of the visible discharges in both the positive and negative half cycles. Eventually relatively thin, bright discharges can be observed during both the half cycles (i.e., concentrated mode) when a sufficiently high power is applied.

The voltage and current waveforms (upper left panel) and the corresponding ICCD images (upper right and lower panels) of the He DBD jet with one segmented electrode at 3.0 W (concentrated mode) are given in Figure 85. Similarly, the ICCD images over one complete voltage cycle, positive half cycle, and negative half cycle were acquired and presented at the upper right panel of this figure. Note that in this case the positive current pulse occurs when the applied voltage is still negative. Thus the ICCD image over the positive half cycle was taken from the time before the breakdown was observed (about -5 μs on the waveform plot) to the time when the current waveform complete half the cycle (about 12 μs on the plot). A similar adjustment is also applied to the ICCD image during negative half cycle; that is, the discharge image from 12 μs to 29 μs on the waveform plot was acquired by the ICCD camera. As can be seen in these three images, they all exhibit a thin, bright concentrated discharge against the left side of the inner wall of the dielectric tube. No significant difference between the images during the positive half cycle and the negative half cycle is observed.

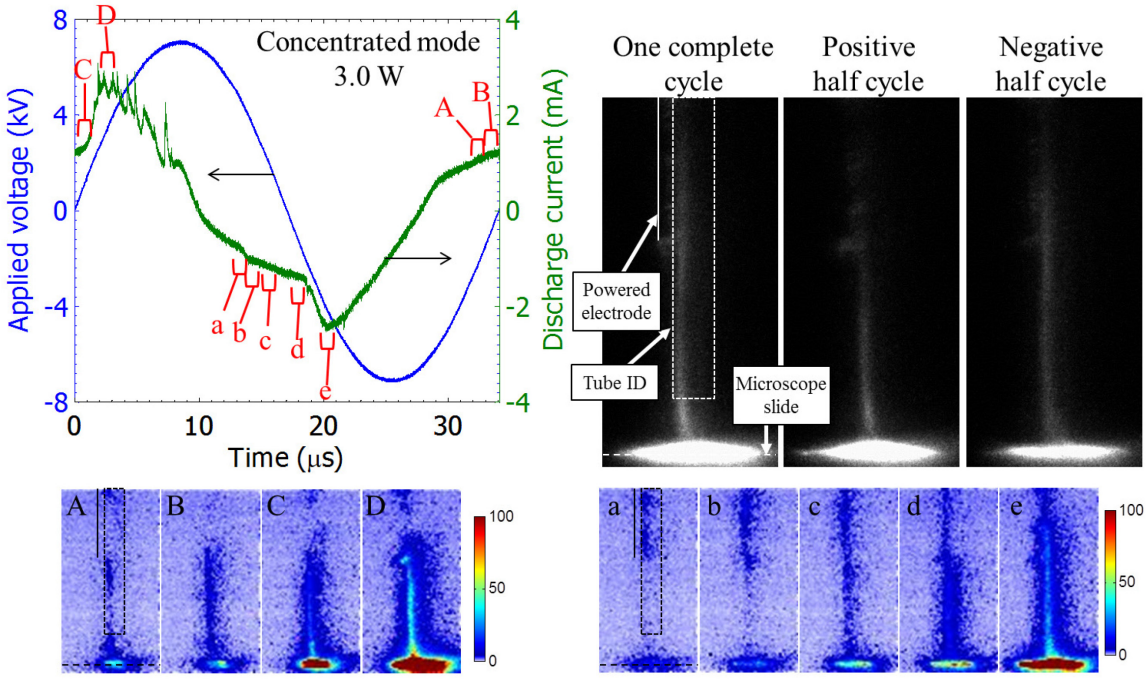

Figure 85. Voltage and current waveforms (upper left panel) of the He DBD jet with one segmented electrode at 3.0 W (concentrated mode). The upper right panel shows the ICCD images over one complete cycle, positive half cycle, and negative half cycle, respectively. The lower panel shows the false-color ICCD images which correspond to different temporal points as labeled on the current waveform.

The detailed difference between the discharges over the positive and negative half cycles can be examined by the false-color ICCD images with 1-μs exposure time, as displayed at the lower panel in Figure 85. Since the current waveform is periodic, label (A) to denote the onset of the current pulse is placed at the tail of the current trace. Image (A) shows that a visible plasma channel is already present in the discharge gap as well as at the left inner wall of the tube, whereas no distinct discharge occurs on the tube inner surface near the powered electrode. As the discharge current rises, the discharge has a more continuous structure with brighter emission light and extends more to the vicinity of the powered electrode [images (B)–(D)]. The plasma during the negative half

cycle evolves in a different way. The discharge is first observed on the surface where the powered electrode is nearby, as shown in image (a). The discharge reaches the surface of the microscope slide and then becomes more intense in its brightness as the absolute current magnitude is increased [images (b)–(e)].

Figure 86 displays the voltage and current traces of the He DBD jet with two segmented electrodes at 0.3 W (diffuse mode) and the corresponding ICCD images to show the temporal and spatial evolution of the plasma. The discharge images (upper right panel) over one complete cycle, positive half cycle, and negative half cycle show similar results to those in the case using one segmented electrode; that is, the plasma jet outside of the tube can be mainly attributed to the ionization waves generated during the positive half cycle. All these three discharge images exhibits a Y-shaped structure as the two segmented electrodes provide similar potential drops for the electric charges to flow to. From the false-color ICCD images with 1-μs exposure time, it is observed again in the diffuse mode that an ionization wave travels toward and arrives at the microscope slide surface during the onset of the positive current pulse [images (A) and (B)]. It is then followed by the formation of a distinct Y-shaped plasma channel as the current reaches its peak value [image (C)]. Note that the relatively dim light emission observed at the upper right end of the Y-shaped plasma channel is due to the glue used to attach the electrode to the tube surface, which slightly influences the brightness of the emission light as can be seen in Figure 83(b). Eventually the current begins to drop due to the insufficiently strong external electric field to generate breakdown, leading to the disappearance of the visible plasma channel, as shown in image (D).

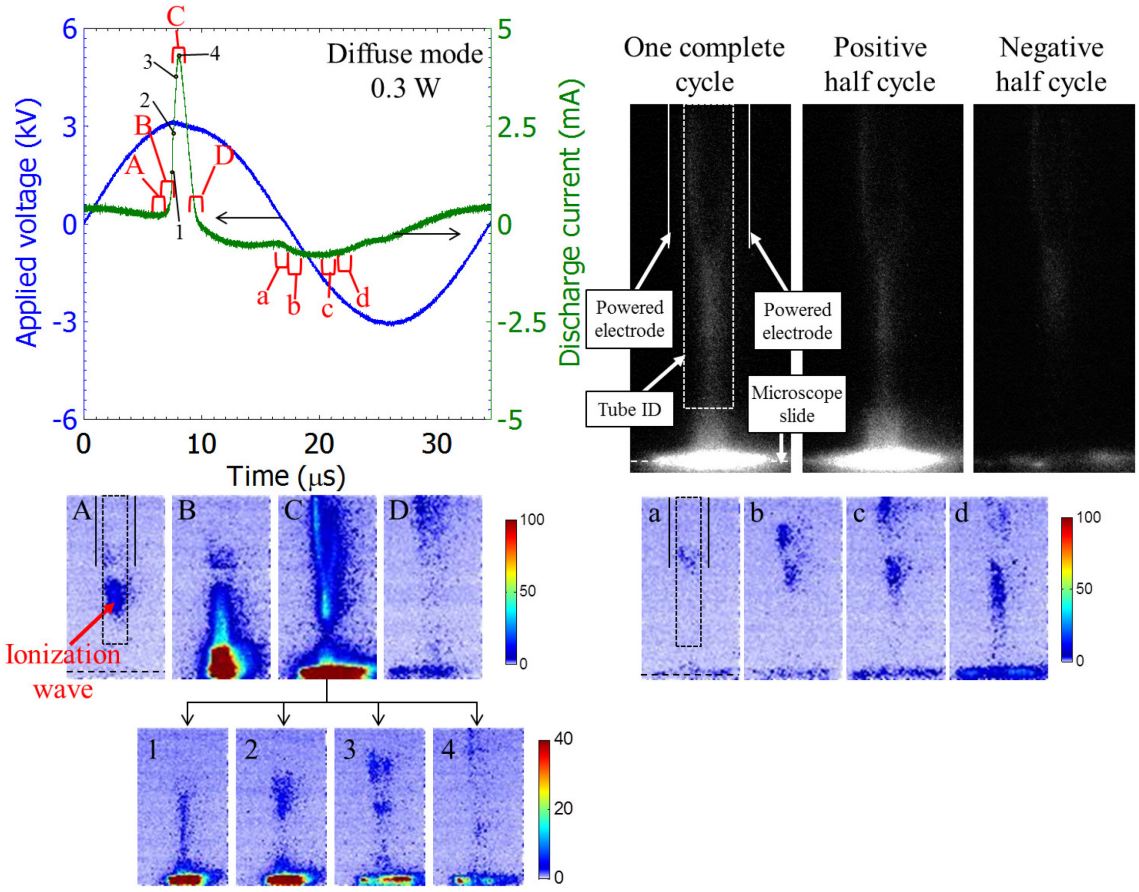

Figure 86. Voltage and current waveforms (upper left panel) of the He DBD jet with two segmented electrodes at 0.3 W (diffuse mode). The upper right panel shows the ICCD images over one complete cycle, positive half cycle, and negative half cycle, respectively. The bottom panel shows the false-color ICCD images which correspond to different temporal points as labeled on the current waveform.

The Y-shaped plasma channel shown in image (C) is found to be formed gradually rather than suddenly. The ICCD camera with an exposure time of 50 ns was employed to capture this evolution, as shown in the false-color ICCD images with labels (1)–(4) in Figure 86. Since the raw images are relatively dim, these images are converted to the false-color ones with an intensity mapping range from 0 to 40. As can be seen in image (1), immediately after the ionization wave reaches the cathode, a visible plasma channel is first observed between the downstream ends of the powered electrodes and

the glass tube. This plasma channel provides a conductive path for electrical current to flow through, resulting in the increase in the current amplitude. As the current rises, the propagation of the light-emitting region toward the upstream ends of the powered electrodes (anodes) can be observed [images (1)–(3)]. Finally, as shown in image (4), the plasma channel becomes less observable at the current peak.

During the negative half cycle, no observable propagation of the ionization wave was acquired. A discharge with faint emission light was first observed in the vicinity of the powered electrodes [image (a)]. Then, the light emission occurs on the surface near the segmented electrodes as well as slightly extends downstream toward the anode (microscope slide), as can be seen in images (a)–(c). Similar to the case with one segmented electrode, as a visible discharge with a longer, brighter downstream portion was observed [image (d)], the discharge in the vicinity of the powered electrodes becomes relatively dimmer.

The ICCD results and the voltage and current waveforms of the He DBD jet with two segmented electrodes at 3.0 W (concentrated mode) are given in Figure 87. Similar to the case with one segmented electrode at 3.0 W, the early breakdown was observed (i.e., the positive current pulse occurs when the applied voltage is still negative). Thus an adjustment to the time used to take the ICCD images was made; that is, the image during the positive half cycle was captured from -3 μs to 14 μs on the waveform plot in Figure 87 and that during the negative half cycle was taken from 14 μs to 31 μs. The ICCD images (upper right panel) over one complete cycle, positive half cycle, and negative

half cycle show that the discharges in these three images exhibit similar Y-shaped structures.

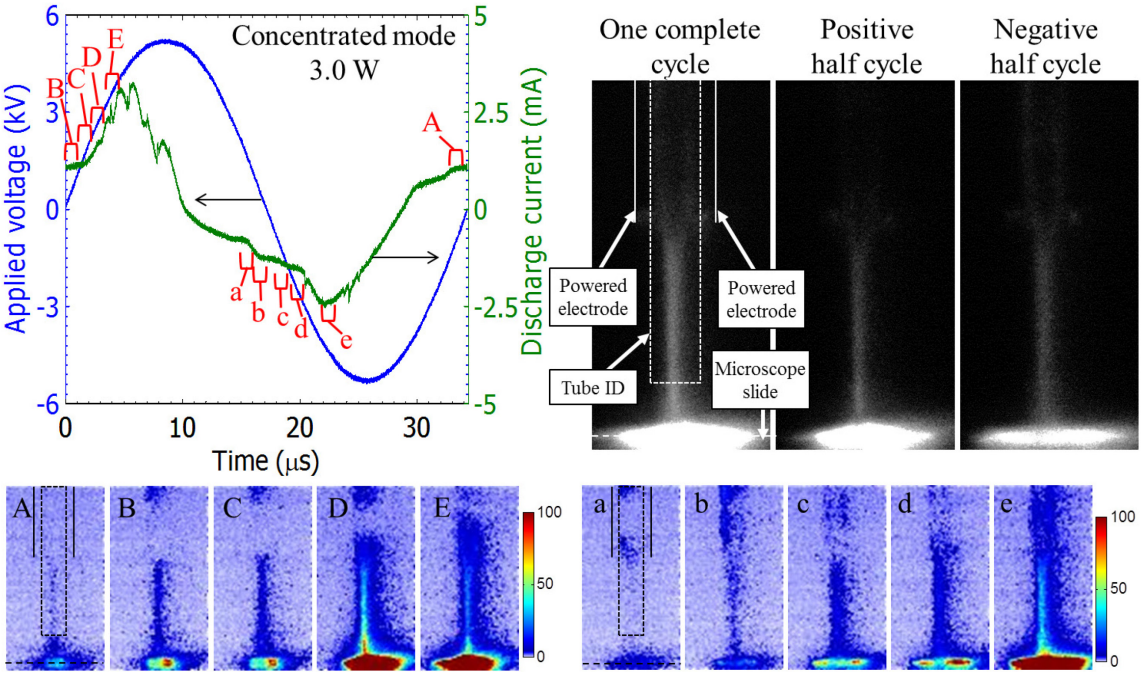

Figure 87. Voltage and current waveforms (upper left panel) of the He DBD jet with two segmented electrodes at 3.0 W (concentrated mode). The upper right panel shows the ICCD images over one complete cycle, positive half cycle, and negative half cycle, respectively. The bottom panel shows the false-color ICCD images which correspond to different temporal points as labeled on the current waveform.

The false-color ICCD images with 1-μs exposure time during the positive half cycle in Figure 87 display that a visible thin plasma channel, which is located along the tube centerline, is present already at the onset of the positive current pulse [image (A)]. This plasma channel, which extends from the downstream ends of the powered electrodes to the microscope slide surface, appears to have a relatively bright downstream portion in ambient air. Again, in this case in the concentrated mode, no

ionization wave propagation was observed. As a higher voltage is applied, the discharge current rises and the plasma channel becomes brighter, as shown in images (A)–(E). Additionally, it can be seen that the plasma splits in two and arrives the dielectric surfaces where the two segmented electrodes are attached to the other sides and gradually elongates to the upstream with the rising current.

The results during the negative half cycle are similar to the previous results using one segmented electrode at 3.0 W. At the beginning of the negative current pulse, the discharge was observed to be generated in the tube near the powered electrodes [image (a)]. It then forms a thin, continuous discharge along the tube centerline, as shown in image (b). An increase in the absolute voltage value leads to a rise in the absolute current magnitude and the generation of more intense discharges, as can be seen in images (c)–(e).

7.4 Section Conclusions

This section investigated the effects of the fed precursors, tube dimensions, and electrode configurations on the discharge non-uniformity in He DBD jets with the presence of a treated dielectric substrate (microscope slide) at various powers. It was found that the increase in the discharge power induces the occurrence of an operation mode change from a diffuse discharge to a concentrated discharge, further leading to the discharge non-uniformity. The dynamics of the concentrated discharge can be adjusted by the precursor addition. For example, using $Cu(acac)_2$ at 100 ºC as the fed precursor results in the occurrence of helical motion of the concentrated discharge. The dielectric

tube size employed to generate the He DBD jet significantly influences the discharge uniformity. It was found that the smaller the tube diameter the more uniform the DBD jet at a relatively high power. The diameter of the concentrated discharge was increased when a dielectric tube with a larger dimension was utilized. A concentrated discharge with a diameter of about 3.51 mm can be obtained using a He DBD jet with an ID of 9.65 mm at 3.0 W. In this case (9.65-mm ID) the addition of a small amount of air leads to the formation of self-organized multiple concentrated discharges. By using segmented electrodes, it was demonstrated that the net external electric field determines the position of the concentrated discharge. An off-centered concentrated discharge was formed due to the relative asymmetry in the net electric field.

The experimental results indicated that it is difficult to achieve large-area, uniform surface processing (e.g., film deposition or etching) using a He DBD jet with a large tube (> 2 mm) since the concentrated discharge, which significantly reduces the discharge uniformity, would occur when the DBD jet operates at high power, particularly with the addition of precursors. Thus for large-area, uniform surface processing an array of DBD jets with smaller tubes (e.g., 1 mm) may be a better choice as the discharge uniformity can be maintained regardless of the applied power.

8. BIOLOGICAL APPLICATION OF AP-PECVD USING DBD JET*

8.1 Introduction

As mentioned in Section 1, the biological application this project "PECVD on biological substrates" would like to achieve first is the sterile bandage deposition on wound. Using the helium DBD jet to deposit a coating on wound can not only sterilize the wound but also offer protection against bacterial infection due to the presence of the protective film blocking the bacteria from reaching the wound (Figure 8). Films with the addition of bacterial indicators, cell adhesion promoters, and/or cell growth promoters may be further achieved to facilitate wound healing processes. To demonstrate the protective ability of the deposited film against bacterial infection (e.g., inhibition of bacterial growth by the deposited film), in this study the attempt of AP-PECVD on top of agar using the helium DBD jet was first made. The agar was employed since it was considered as a simplified, temperature-sensitive, moist, nutrient rich surrogate for an actual wound. By plating bacteria media on agar and observing the bacterial growth, we would like 1) to know how the addition of precursors to the helium DBD jet influences the sterilization ability of the plasma and 2) to investigate whether the deposited film on agar is able to serve as a protective barrier to inhibit the growth of the bacteria from the external environment. The investigation of the bacterial growth on agar with and without the presence of the protective coating was performed and the methods and results will be

*Part of this section is reprinted with permission from "Polymer Film Deposition on Agar Using a Dielectric Barrier Discharge Jet and its Bacterial Growth Inhibition" by T.-C. Tsai, J. Cho, K. McIntyre, Y.-K. Jo, and D. Staack, 2012. *Applied Physics Letters,* vol. 101, pp. 074107-4, Copyright [2012] American Institute of Physics.

shown in the following subsections. In the last part of this section, some results of PMMA film as well as copper film deposition on pork skin will be also presented. The results in this section mainly follow a recent published paper [47].

8.2 Experimental Setup and Methods

Figure 88(a) shows the schematic diagram of the experimental setup for AP-PECVD on agar. The setup was similar to those used in the previous sections except that the petri dish filled with agar was used as the treated substrate in this case. MMA liquid monomer (Sigma-Aldrich, 99%) was employed as the precursor since we mainly focused on the study of PMMA film deposition on agar and its protective ability against the bacterial infection. The working gas flow rate was set to 2.9 slm (standard liter per minute), while the flow rate of the MMA carrier gas was 0.1 slm. It results in a MMA concentration of about 1800 ppm in the helium gas stream. The mixture was then directed through the DBD jet generator. The petri dish filled with agar was placed on the aluminum holder downstream of the jet for plasma treatment and PMMA film deposition. A high voltage (5–6 kV) with sinusoidal waveform at 28.5 kHz was applied to the powered electrode. The image of the DBD jet in the diffuse mode treating the agar surface is shown in Figure 88(b). It can be seen that the plasma spot size on the agar surface is relatively smaller than that in Figure 22(a) in which the microscope slide was used. This is because the agar, which is similar to the living tissues, is more electrically conductive than the microscope slide. Similar phenomenon (i.e., relatively small plasma spot on the treated surface) has been observed when the silicon wafer, whose electric

conductivity is higher than that of the microscope slide, was employed as the substrate for deposition. The electric current thus flows through the agar medium rather than passes along the surface. Besides the DBD jet fed by helium and MMA precursors (He/MMA DBD jet), a helium-only DBD jet (He DBD jet) was used for comparison. Both DBD jets operated at a discharge power of about 1.5 W for film deposition on agar in this study. For pork skin treatment, a piece of the pork skin (purchased from the grocery store), containing the epidermis layer, dermis layer, and fat layer, was directly placed downstream of the DBD jet on the aluminum holder for the preliminary study of the plasma-tissue interaction. The surface coverage of the deposited films on the pork skin and the influence of the discharge on the tissue were observed and photographed.

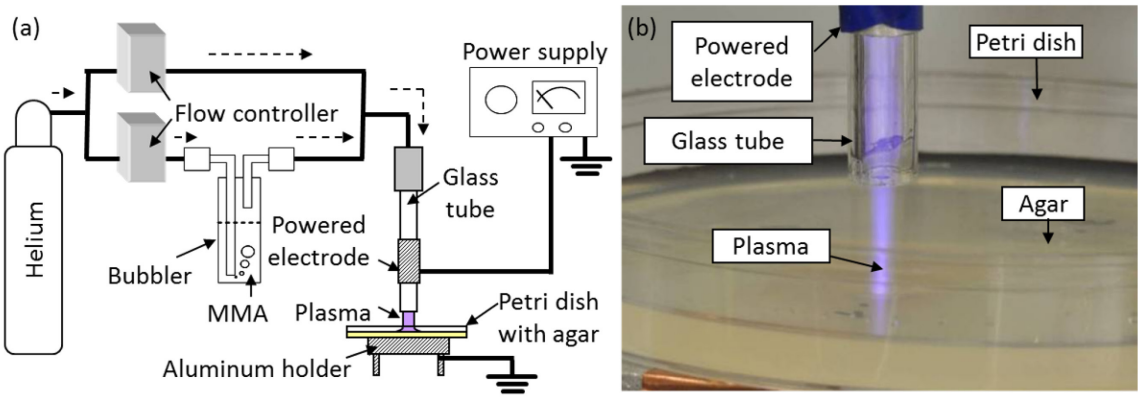

Figure 88. (a) Experimental setup for polymer deposition on agar in ambient air and (b) photograph of the DBD jet on agar.

Sterilization by the DBD jets and bacterial growth inhibition by the deposited films were studied via the observation of the bacterial colony growth on agar. Note that the term sterilization here is used to refer to the lack of reproduction and colony growth

by the bacteria. Two bacterial strains, *Escherichia coli* (*E. coli*) and *Burkholderia glumae* (*B. glumae*, a seedborne pathogen to cause bacterial panicle blight on rice), were prepared in liquid media with a concentration of about 10^9 colony-forming units per mL (CFU/mL). Figure 89 shows the designed experimental processes and the expected results for the sterilization and bacterial growth inhibition studies using the He DBD jet [Figure 89(a)] and the He/MMA DBD jet [Figure 89(b)]. The processes contain two inoculations before incubation. Agar plates for the growth of *E. coli* and *B. glumae* were prepared and stored in the refrigerator, as illustrated in insets (a-1) and (b-1) of Figure 89. After the bacteria media were plated over the entire agar plates [insets (a-2) and (b-2), the 1st inoculation], the petri dishes were air-dried in a laminar flow hood for about 10 min. The 1st inoculation was employed to examine the sterilization ability of the DBD jets. The DBD jets were then used to treat the agar plates and create sterilized areas on agar, as shown in insets (a-3) and (b-3). Besides the sterilized area, the He/MMA DBD jet led to the PMMA film formation on top of the agar [inset (b-3)]. For observation of prevention of bacterial invasion and inhibition of bacterial growth by the deposited PMMA film, additional bacterium suspensions were dropped onto the treated areas [insets (a-4) and (b-4), the 2nd inoculation]. Finally, the dishes were placed in an incubator at 37 °C for one day and the growth of bacteria colonies in untreated areas can be observed. It was expected that, as illustrated in inset (a-5), the bacteria from the 2nd inoculation should still grow and form colonies in the region treated by the He DBD jet (without the deposition of protective film on agar) after incubation. In contrast, the polymer film barrier produced by the He/MMA plasma should lead to no observation of

bacteria colonies on the area owing to the fact that the film would prevent the bacteria access to the nutrient agar [inset (b-5)].

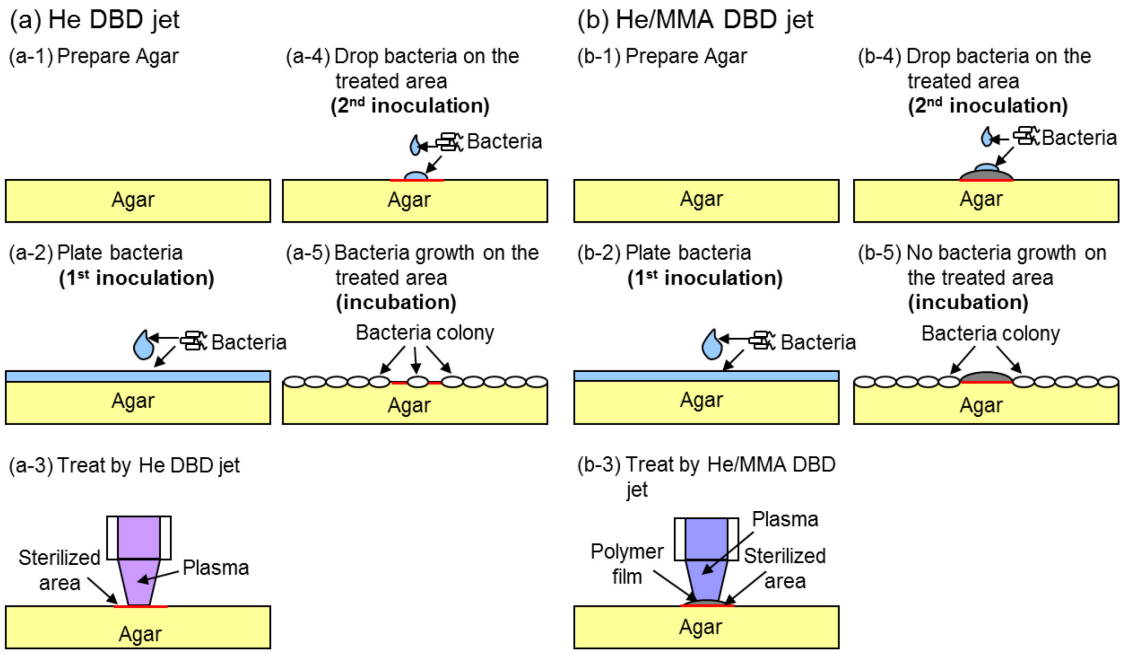

Figure 89. Comparison of experimental processes using (a) He DBD jet and (b) He/MMA DBD jet for the studies of the plasma sterilization ability and the bacterial growth inhibition capability of the deposited films.

8.3 Experimental Results

This subsection gives the results of thin film deposition on agar first. The results include the images of as-deposited PMMA films and copper films on agar surface and the analysis of the PMMA films for the characterization of the film size and the chemical compositions. The comparison of the sterilization results by using pure He stream, He/MMA stream, He DBD jet, and He/MMA DBD jet is presented in Section 8.3.2. Also, the bacterial growth inhibition ability by the deposited film is shown in the same

subsection. Section 8.3.3 will further report some preliminary results of PMMA and copper film deposition on pork skin using our DBD jets.

8.3.1 Film Deposition on Agar

Figure 90(a) shows the image of the PMMA film on the agar plate after 10-min deposition. An opaque film, deposited at the region directly under the plasma jet, was observed on the agar at the center of a cavity created by long treatment duration due to gas pressure and slight heating effect of the DBD jet. A deposition rate of 25 nm/s was estimated through optical microscopy by measuring the thickness of the opaque film, which was removed from the agar surface. The opaque feature becomes less noticeable when shorter treatment time or lower power is applied. The opaque film was formed due to 'buckling effect' caused by a relatively high deposition rate and its detailed explanation can be seen in Section 4.3.4. The deposition result is actually similar to that on the silicon wafer shown in Figure 38(d). There also exists a thinner transparent film surrounding the opaque film outside the region of direct plasma treatment though the outer film is less-noticeable. A cross-sectional illustration of the way the PMMA film grows on agar using He/MMA DBD jet is given in Figure 90(b). A thick opaque film is formed at the region with the direct plasma treatment. A thin, transparent film grows outside of the direct plasma region (afterglow region). The polymerization of the transparent film occurs likely due to those longer-lived species in the plasma afterglow. The existence of the transparent film will be shown in the later results using attenuated total reflection Fourier-transform infrared (ATR-FTIR, Bruker Optics ALPHA-P 10098-4)

spectroscopy. Figure 90(c) shows an image of an opaque PMMA line created by moving the agar plate in a specific direction after 10-min operation. This demonstrates the ability of large area thin film deposition using this DBD-jet-based depositing tool. The deposition of a copper film on agar was also achieved [Figure 90(d)] to present the feasibility of manufacturing electronic circuits on biological surfaces using this technique in the future.

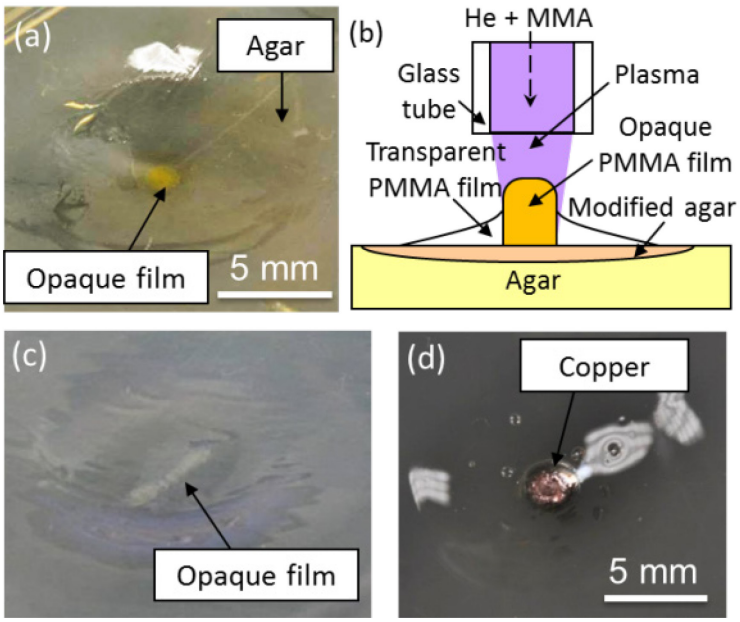

Figure 90. (a) Cross-sectional illustration of PMMA deposition on agar by He/MMA DBD jet; (b) as-deposited PMMA film on agar after 10-min deposition; (c) image of an opaque PMMA line on agar created by moving the agar plate; (d) as-deposited copper film on agar after 3-min deposition.

The plasma also induces a property change in the agar surface, forming a modified agar layer as indicated in Figure 90(b). The modified agar is insoluble in near-boiling water. For clear visualization of the insoluble PMMA film and the underlying modified agar layer a modified lift-off technique was used wherein a 25-mm square of the agar

was cut from the treated region and placed in 90–100 ºC water. It resulted in the dissolution of the agar, leaving behind the insoluble PMMA/agar film, as shown in Figure 91(a). An aluminum mesh sheet was then used to take the insoluble film out of the water [Figure 91(b)]. The insoluble film was dried in ambient air for one day and analyzed. Figure 91(c) shows a dried insoluble film with 10-min PMMA deposition time. The opaque film and the whole insoluble film were around 2.3 mm and 14 mm in diameter, respectively. It should be mentioned that a longer deposition time lead to a larger insoluble region.

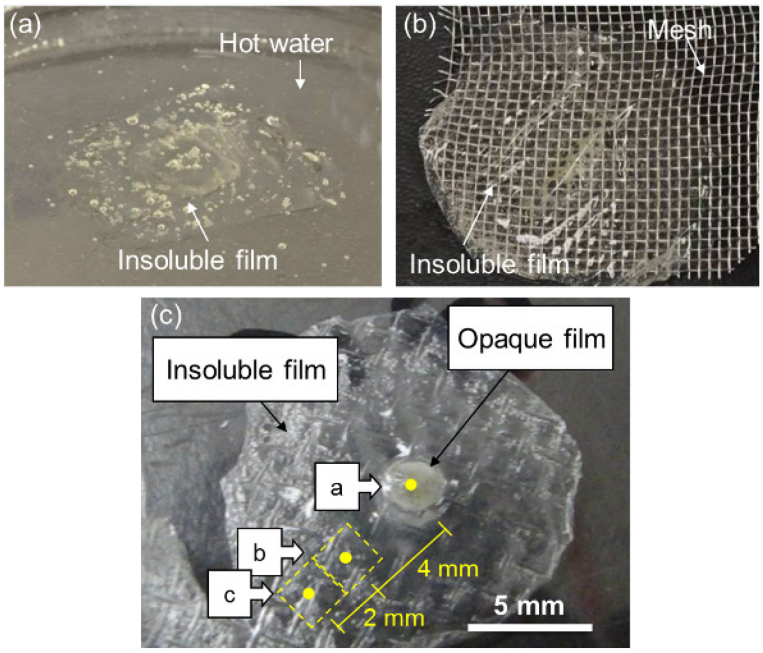

Figure 91. Images of (a) an insoluble film in near-boiling water, (b) the insoluble film taken out of the water by an aluminum mesh sheet, and (c) an insoluble PMMA/agar film after the lift-off method.

ATR-FTIR was used to characterize the chemical compositions of the insoluble films. Three insoluble films (one PMMA/agar film and two pure agar films) obtained

using different methods, as listed in Table 10, were measured by the ATR-FTIR. Three different points (points a, b, and c) in the insoluble PMMA/agar film (Sample 1), as depicted in Figure 91(c), were analyzed to show the existence of the PMMA film on agar and to estimate the PMMA film dimension. The dashed diamond illustrates the dimension of the ATR crystal. The FTIR spectrum of point "a" [Figure 92(a)] shows several functional groups of PMMA, including C–H stretching of methyl (PMMA b1, 3000–2850 cm^{-1}), C=O stretching in ester (PMMA b2, 1730 cm^{-1}), and C–H deformation of CH_2 and CH_3 (PMMA b3, 1480–1420 cm^{-1}). Agar bands, such as C–O/C–C stretching (Agar b4, 1030–1010 cm^{-1}) and 3,6-anhydro-galactose bridges (Agar b5, 930 cm^{-1}), can be also observed [177, 178], showing the existence of the modified agar under the PMMA film. Besides, it contains distinct hydroxyl groups likely due to the water present in the modified agar. At point "b" (4 mm away from the center), the PMMA bands are reduced in intensity while Agar b2 (1640 cm^{-1}) and Agar b3 [1370 cm^{-1}, depicted in Figure 92(b) for clear presentation] become comparable. Agar b2 is associated with the coupling of H–O–H bending in water and stretching of the conjugated peptide. Agar b3 is attributed to the ester sulfate group (S=O) in agar. When point "c" (6 mm away from the center) of the PMMA/agar film was measured, only agar bands were obtained. A broad band at 2850–2820 cm^{-1} (Agar b1) due to the methoxyl groups in agar was observed instead of the sharp band of PMMA (i.e., PMMA b1). These results indicate that the PMMA film covers an area with a diameter of at least 8 mm and is thinner toward edges.

Table 10. Three insoluble films prepared using different methods for ATR-FTIR analysis.

Sample name	Type of insoluble film	Preparation methods	Treatment time
Sample 1	PMMA with agar	He/MMA DBD jet	10 min
Sample 2	Agar	Heat gun	10 min
Sample 3	Agar	He DBD jet	10 min

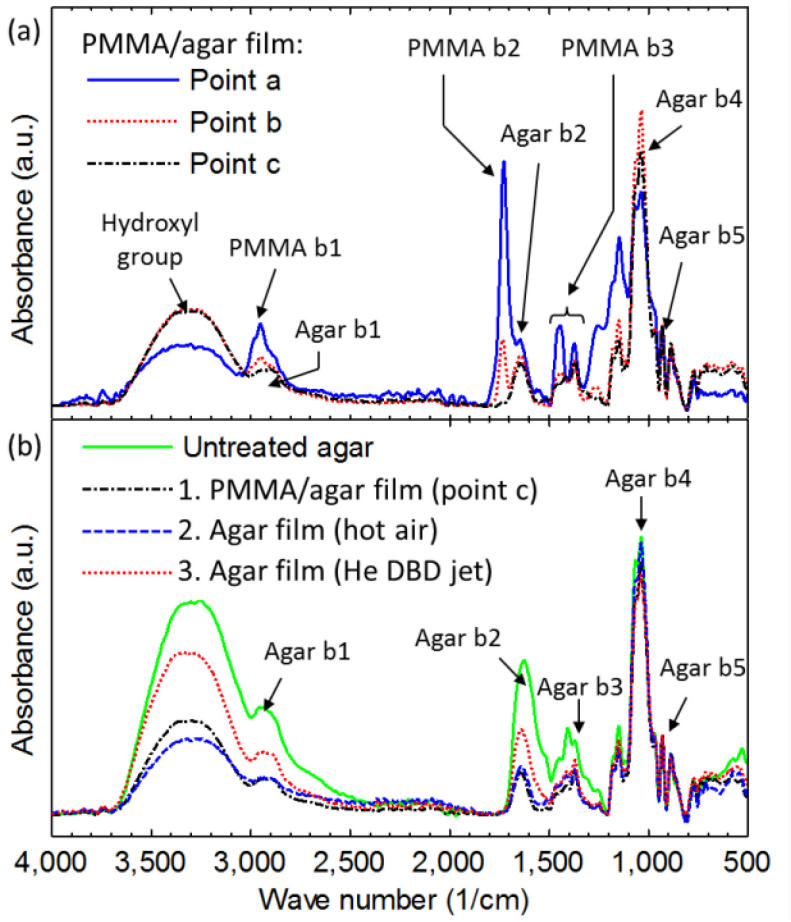

Figure 92. FTIR spectra of (a) three different points of the PMMA/agar film and (b) untreated agar compared with three insoluble modified agars obtained by different methods.

To investigate the factors causing the property change in agar, agar treated by a 85 °C air flow from a heat gun (Sample 2) and agar treated by He DBD jet (Sample 3) for 10-min treatment were also prepared (see Table 10). Similarly, insoluble agar layers (not shown) were obtained after the modified lift-off method. Note that the insoluble agar film formed by He DBD jet is always smaller in size than that obtained by He/MMA DBD jet. Thus the additional radicals (e.g., CH•) from He/MMA DBD jet may also play an important role for the modified agar formation. Figure 92(b) shows the FTIR spectra of Sample 1–3, compared with an untreated agar, which was also left to dry for one day to eliminate the intense water signals in the spectrum. In this result the centers of Sample 2 and 3 and point "c" of Sample 1 were analyzed for the comparison of the agar bands only. Besides the reduction of hydroxyl groups and Agar b2 indicating water loss, a significant decrease in the methoxyl (Agar b1) and sulfate groups (Agar b3) can be observed in Sample 1–3. Similar results, such as elevated melting temperature and reduced functional groups in agar, have been reported during agar degradation by natural weathering exposure (i.e., UV/heat/drying) [177]. It was attributed to the fact that UV/heat/drying may induce crosslinking in the agar, further increasing the melting temperature. Thus in this study it is suggested that crosslinking occurs when the UV/heat/drying and radicals from the DBD jets react with the agar. The agar becomes insoluble due to its elevated melting temperature. It should be mentioned that all the spectra were normalized with respect to the characteristics agar band at 930 cm^{-1}.

8.3.2 Plasma Sterilization and Polymer Film Barriers

As illustrated in Figure 89, the He/MMA DBD jet is able to not only sterilize the treated surface but also deposit a protective barrier for prevention of bacterial infection. To investigate the sterilization efficacy of the He DBD jet with the addition of MMA precursors, incubation was performed right after 1-min treatment of the He/MMA DBD jet on agar plated with bacterium suspensions (without the 2^{nd} inoculation). He gas, He/MMA gas and He DBD jet were also used in the experiment for comparison. Figure 93 shows the images of the treated petri dishes after one-day incubation. In this case, *E. coli* was employed as the tested bacteria. No sterilization was observed at the areas treated by the He gas and the He/MMA gas, as shown in Figure 93(a) and Figure 93(b), respectively. This infers that the vaporized MMA gas does not affect the bacterial growth. The dashed circles on the images indicate the inner dimension of the tube (4 mm in the inner diameter). Using He DBD jet, the sterilized area with a solid circular shape was seen to have a diameter of about 12 mm [Figure 93(c)]. A longer treatment time can lead to a larger sterilized spot. Figure 93(d) shows the sterilization result using He/MMA DBD jet with the same treatment duration (1 min). With the addition of MMA the plasma created a greater (around 18 mm in the diameter) bacterial growth inactivation zone than that by the He DBD jet. The relatively large sterilized area represents the relatively efficient sterilization effect using He/MMA DBD jet, compared to that by pure He plasma. This is likely due to the fact that either 1) active species generated from MMA in the DBD aid in the sterilization, which implies that in addition to reactive oxygen species, reducing species generated in the plasma may also be important [131],

or 2) deposition may result in a film with a diameter of at least 18 mm and this film inhibits the growth of bacteria under the film.

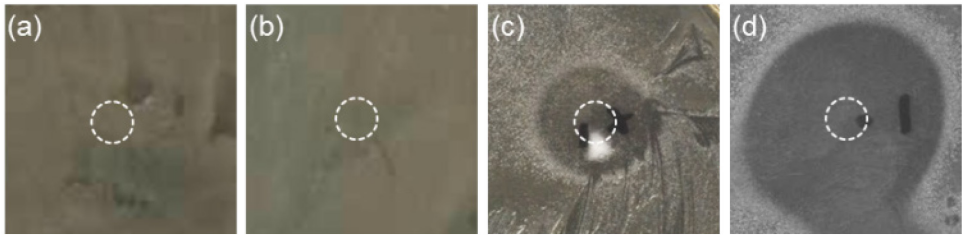

Figure 93. Bacterial growth on agar plates (1st incubation) after the treatment of (a) He gas, (b) He/MMA gas, (c) He DBD jet, and (d) He/MMA DBD jet.

To examine whether the deposited polymer films on agar can serve as barriers against the bacterial invasion and bacterial growth, additional drops of the bacterium suspensions were added onto the treated areas, as referred to as the "2nd inoculation" in Figure 89. The right three columns in Figure 94 show the incubation results after respectively 1, 5, and 10-min plasma treatment followed by the addition of bacterium drops, while the leftmost column displays the sterilized areas (1-min treatment) without the additional drops of the bacterium suspensions for comparison. In this case, both *E. coli* [Figure 94(a) and (b)] and *B. glumae* [Figure 94(c) and (d)] were used to investigate the effect of the plasma and deposited films on different bacterial strains. Again, the dashed circles on the images indicate the inner dimension of the tube (4 mm in the inner diameter). Using He/MMA DBD jet [Figure 94(b) and (d)] created significantly larger sterilized areas (around 18 mm in the diameter) than those treated by He DBD jet [Figure 94(a) and (c)] after 1-min treatment regardless of the types of bacteria. The

sterilized area using He DBD jet has similar dimension to that using He/MMA DBD jet when 5-min treatment duration was applied. These results again demonstrate the relatively efficient (larger area in shorter time) sterilization ability of the He/MMA DBD jet. The capability and efficacy of the deposited polymer films to prevent bacterial invasion and to inhibit the growth of the bacteria from external environment can be observed from the right three columns. Figure 94(a) and (b) show that the *E. coli* colonies still grew on the areas treated by the He DBD jet and the area treated with 1-min He/MMA DBD jet. When the PMMA deposition time was extended to 5 min or longer the *E. coli* growth was inhibited at the treated areas. In the case of *B. glumae* treated by the He DBD jet [Figure 94(c)], the densely grown *B. glumae* colonies still formed on the agar, while slightly reduced *B. glumae* colonies were found in the case of 10-min treatment. This is likely because the modified agar by the He DBD jet slows the *B. glumae* growth. No *B. glumae* colonies were observed at the area treated by the He/MMA DBD jet for deposition time of 1 min and greater [Figure 94(d)]. These results show that the polymer film deposited by He/MMA DBD jet can prevent the bacteria from reaching the agar as well as inhibit the bacterial growth. It should be mentioned that in the cases after 5 and 10-min plasma treatment (the right two columns in Figure 94) we spread the bacterium suspensions on a portion of the sterilized region in order to examine whether the bacterial growth can be inhibited in the whole area. It thus resulted in irregular patterns of the bacterial colonies observed in the images instead of circular patterns. At the outer parts of the sterilized areas treated by the He/MMA DBD jet, bacterial growth can be still observed in the images [the right two columns in Figure

94(b) and (d)]. These results show that the efficacy of the bacterial growth inhibition depends on the film thickness as a short deposition time (e.g., *E. coli* after 1-min treatment using He/MMA DBD jet) as well as the outer parts of the He/MMA plasma sterilized zones still lead to bacterial growth. Different bacterial strains show varying sensitivity to the environment they grow on (*B. glumae* is more sensitive than *E. coli* in this case).

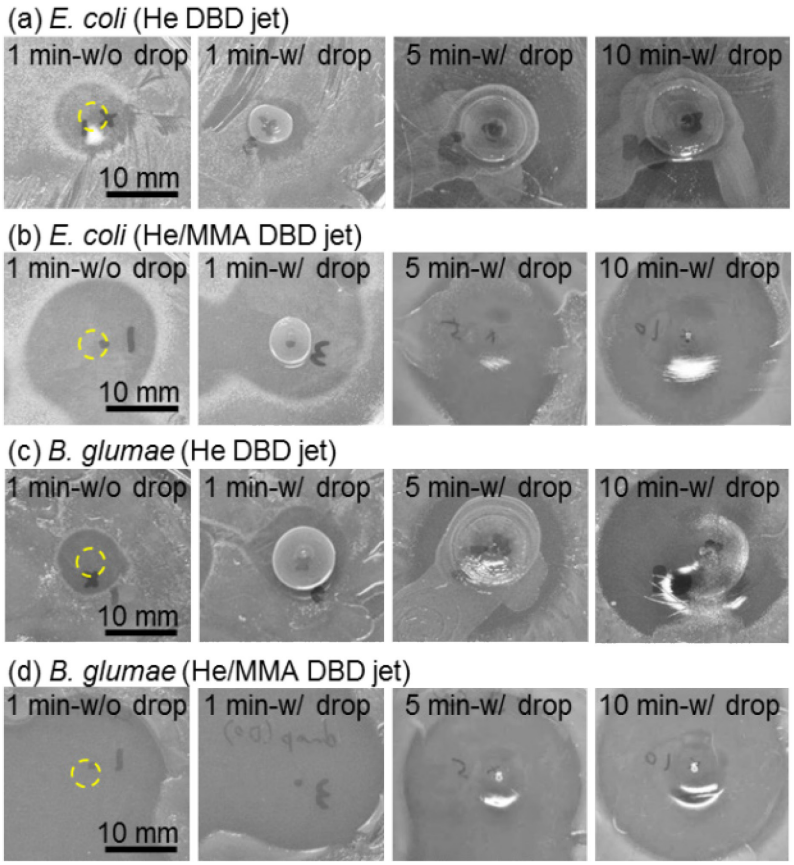

Figure 94. Comparison between the treated areas without (leftmost) and with additional drops of bacterium suspensions at various treatment durations in different cases: (a) *E. coli* treated by He DBD jet; (b) *E. coli* treated by He/MMA DBD jet; (c) *B. glumae* treated by He DBD jet; (d) *B. glumae* treated by He/MMA DBD jet.

8.3.3 Film Deposition on Pork Skin

After the investigation of the film deposition on agar and the efficacy of the bacterial growth inhibition by plasma as well as the deposited coatings, this subsection employs pork skin as the substrate for film growth. The deposited films on the pork skin may provide some preliminary features for the coatings on living tissue in the future study.

Pork skin was purchased from the grocery store for preliminary investigation of plasma polymerized films on tissues. Figure 95(a) shows the photograph of a piece of the pork skin taken during thin film deposition using our DBD jet. The pork skin used in this study contains the epidermis layer, dermis layer, and hypodermis (fat) layer. As can be seen in the figure, the pork skin served as the 2nd electrode in this system. PMMA film deposition on the pork skin was performed using the helium working gas with a flow rate of 2.9 slm, the helium carrier gas with a flow rate of 0.1 slm for MMA vapor transport, and a discharge power of 3.0 W. The deposition time was 30 min and the separation distance between the tube end and the skin surface was around 6 mm. The deposition result can be seen in Figure 95(b). A transparent film with a diameter of about 16 mm can be seen on top of the skin (the noticeable film edge was indicated by a dashed arc). Several dark burn spots were also observed near the treated area due to the excess heat produced by the He/MMA DBD jet at the relatively high discharge power (3.0 W) used for deposition. The burns on the skin can be prevented using a lower discharge power.

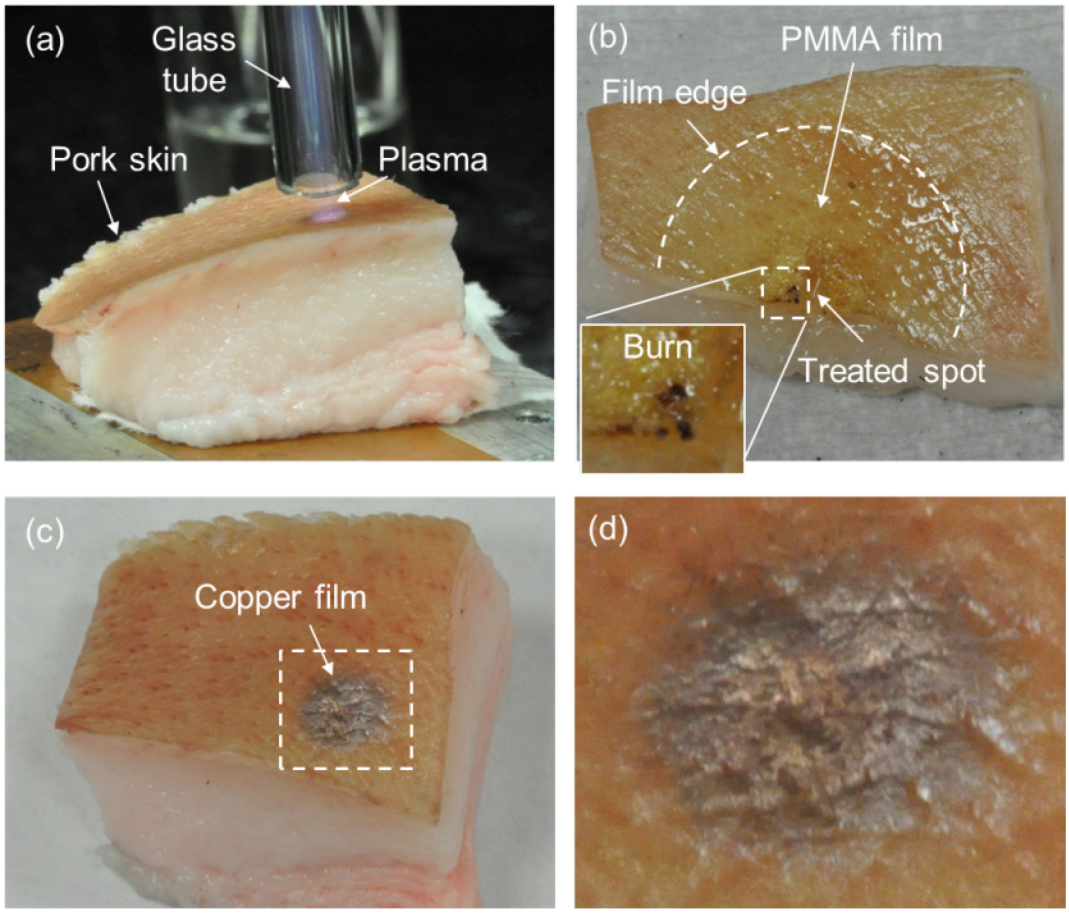

Figure 95. (a) Image of AP-PECVD on pork skin using DBD jet, (b) PMMA film on pork skin after 30-min deposition, (c) copper film on skin after 20-min deposition, (d) magnified copper film image of the insect in (c).

Deposition of more readily observable copper films was also achieved on a piece of the pork skin using the $He/H_2/Cu(acac)_2$ DBD jet at 1.5 W using 20-min deposition time, as displayed in Figure 95(c). The helium flow rate and the hydrogen flow rate were set to be 2.9 slm and 0.1 slm, respectively. The container filled with the precursor $Cu(acac)_2$ powder was heated to 100 °C and the nozzle-to-surface distance was 2.5 mm. A magnified image of the copper film [dashed box in Figure 95(c)] is given in Figure 95(d). The deposited copper film was around 4 mm in diameter, which was similar to the

inner diameter of the glass tube. Similar to the results obtained on the microscope slides, the size of the observable copper film was much smaller than that of PMMA film. Reddish brown copper color can be seen at the center of the film, indicating the existence of the copper coating as well as showing the film is thicker at the center and thinner toward edges. Non-uniform color distribution of the film is owing to the uneven nature of the animal skin. No burns were shown in this case as a relatively low discharge power (1.5 W) was utilized for plasma deposition. These results further demonstrate that applying this technique to the medical treatment, such as wound protection and in-vivo material synthesis, is highly attainable in the future.

8.4 Section Conclusions

In this section, the feasibility of using the DBD-jet-based atmospheric pressure film depositing device in biological applications was examined through three stages of investigation.

First, agar was used as a simplified surrogate for an actual wound for PMMA film deposition using He/MMA DBD jet. Besides, the structures and the chemical compositions of the deposited PMMA films on agar were studied. The as-deposited PMMA film consists of a central thick opaque film surrounded by a relatively thin transparent film. The opaque film was formed at the region treated directly by the plasma, which accelerates the PMMA deposition rate and further leads to buckling in the film. The formation of the outer transparent film was likely due to the polymerization induced by the long-lived reactive species in plasma afterglow. It was found that the

plasma also creates crosslinking in the agar surface, causing the formation of a modified agar layer, which is insoluble in near-boiling water. The deposited PMMA coating along with the underlying insoluble agar film, peeled off by a modified lift-off method, were analyzed by ATR-FTIR. The results confirmed the existence of the less-noticeable thin transparent film and also demonstrated the occurrence of crosslinking in the agar surface treated by plasma. The ATR-FTIR analysis showed that the plasma polymerized PMMA film on agar still exhibits similar chemical compositions to those in pure PMMA.

After the capability to grow film on agar using DBD jet was confirmed, at the second stage we investigated the interaction of the plasma and the deposited coating with two bacterial strains, *E. coli* and *B. glumae*, on agar. MMA addition to the He DBD jet enhanced the sterilization efficiency (i.e., faster sterilization using He/MMA DBD jet was observed, compared to that by pure He plasma). The deposited PMMA barriers significantly inhibited the growth of the bacteria from the 2^{nd} inoculation in which the bacterium suspensions were directly added on top of the deposited film. The results with various plasma treatment times showed that the bacterial inhibition efficacy was influenced by the film thickness and the type of bacterial strains. The modified agar layer created by the DBD jets may also decelerate the growth of some bacterial strains. With this new DBD-jet application, wounds can be not only sterilized but also protected by the deposited coatings (like bandage) from bacterial invasion and growth.

Finally, the attempt of AP-PECVD on pork skin using both the He/MMA DBD jet and the $He/H_2/Cu(acac)_2$ DBD jet was made for preliminary study of the plasma-tissue interaction and the features of the coatings grown on tissue. PMMA films were

successfully deposited on the pork skin and they exhibited a greater diameter than that of the glass tube, similar to the results on the microscope slides and agar. The deposition of reddish brown copper films with a size (~4 mm) close to the inner dimension of the glass tube on pork skin was also achieved. A proper discharge power was required to prevent tissue damage and charring due to the excess heat from plasma.

9. CONCLUSIONS AND FUTURE WORKS

9.1 Conclusions

This dissertation is the first study to propose the idea of directly chemically synthesizing materials onto living substrates using plasma. Through extensive experiments we demonstrated that the PECVD technique can be applied to biological surface for several promising biomedical applications. The knowledge and techniques necessary to perform "PECVD on living substrates" were also established in this dissertation. This study stated that 1) the chemistry in LP-PECVD can be achieved using the DBD-jet-based AP-PECVD with similar operation temperature (low-temperature), but the film quality and deposition rate depend on the plasma operating condition, as shown in Sections 3–5; 2) the discharge characteristics in the DBD jet are determined by the input electrical energy, precursor type and concentration, reactor geometry, and substrate (Sections 6 and 7); 3) the helium DBD jet can be used in thin film deposition on temperature-sensitive (< 50 ºC) biological substrates in open air for sterilization and bacterial growth inhibition, as presented in Section 8. Based on the results shown in this study, the conclusions can be drawn in four main aspects: system development, material characterization, plasma characterization, and biological applications. Several achievements are summarized as follows:

A) System Development

- The floating-electrode DBD jet, which is a direct plasma method instead of just an afterglow one, was first employed to achieve PECVD which can operate in ambient air and at low temperature.
- Instead of the deposition of those inorganic films (SiO_2, SiO_x, TiO_2, or diamond) using APPJs which have been reported frequently in prior studies, we demonstrated that polymeric, metallic, and micro/nanostructure composite films can be grown in ambient air conditions using DBD jets.

B) PMMA Film Deposition

- Open air PECVD of PMMA films was successfully accomplished using the He DBD jet with MMA vapor addition (i.e., He/MMA DBD jet).
- A high PMMA deposition rate up to 22 nm/s, which is three to ten times higher than those in many prior works, was attained with the substrate temperature merely rising to 39 ºC.
- The PMMA film morphology (transparent and opaque films) can be tailored by adjusting the plasma conditions.
- The as-deposited plasma polymerized PMMA films retain similar functional groups, compared with those in pure PMMA.
- The floating-electrode DBD jet enabled rapid PMMA film growth on various types of temperature-sensitive substrates in ambient air conditions.

C) Copper Film Deposition

- Open air PECVD of copper films was successfully achieved using the He DBD jet with the addition of $Cu(acac)_2$ vapor and hydrogen [i.e., $He/H_2/Cu(acac)_2$ DBD jet].
- Even though the copper films were deposited in open air, their main regions (reddish brown regions) were still electrically conductive. The electrical resistivity of the as-deposited copper films was measured to be lower than 1×10^{-7} ohm-m, which is close to that of bulk iron.
- The conductive regions of the copper films were mainly composed of metallic copper, rather than copper oxide, whereas about 20–40 at.% carbon and oxygen impurities existed in the films. However, the impurities can be reduced by applying a higher power.
- The copper films deposited by the DBD jet exhibit higher stability than those films obtained using the traditional PVD method (thermal evaporation).
- The floating-electrode DBD jet enabled conductive copper film growth on various types of temperature-sensitive substrates in ambient air conditions.

D) Characterization of Precursor-Dependent Multiple Breakdowns

- Several previously unknown discharge breakdown processes were revealed in this study. These findings (the knowledge of discharge characteristics) facilitate the development of DBD-jet operation strategies to improve the thin film deposition efficacy.

- The operation mode change from a diffuse mode to a concentrated mode with a rising power in the floating-electrode He DBD jet with the presence of a dielectric substrate was first observed and characterized.
- We found the use of a dielectric substrate induces multiple breakdowns at each half cycle in the DBD jet.
- We showed that the broad discharge current pulse observed at each half voltage cycle in the He DBD jet actually consists of several short-duration (1–2 μs) current pulses. And each short-duration current pulse is induced by a leading ionization wave followed by the formation of a plasma channel.
- With MMA addition, a similar mode change (diffuse to concentrated mode) was observed but multiple broad current pulses occur as the applied power rose.
- The diffuse color of the discharge observed in the diffuse mode is due to the relatively spatially homogeneous light emission from the ionization waves. The occurrence of the concentrated mode was shown to be attributed to the formation of the relatively intense, contracted plasma channels at each half cycle. With the presence of a preceding concentrated plasma channel, the propagation of the subsequent ionization wave became less observable.
- When the time between ionization waves is small enough, the propagation of the second ionization wave is also less observable.

E) Characterization of Discharge Uniformity and Mode Change

- We demonstrated that the precursor addition, dielectric tube size, and electrode configuration determine the discharge uniformity and the mode change in the He DBD jet.
- It was found that the addition of different precursors to the He DBD jet led to different operation modes or breakdown phenomena: With MMA addition, a similar mode change (diffuse to concentrated mode) was observed but multiple broad current pulses occur as the applied power rose; with $Cu(acac)_2$ at 100 ºC, a helical mode, instead of the concentrated discharge with a fixed position, occurred while still only one broadened current pulse was seen.
- The smaller the size of the dielectric tube the less observable the mode change and the more uniform the discharge appearance in the DBD jet.
- The net external electric field created by the electrodes determines where the concentrated discharges are located.

F) Biological Applications

- Polymeric and metallic thin films were first deposited on agar and pork skins in open air conditions.
- It was demonstrated that the addition of precursors can enhance the sterilization efficiency using a He DBD jet.
- The idea of "sterile bandage deposition" was proved using the He/MMA DBD jet. And the polymer films deposited by the DBD jet showed the barrier property which was able to protect the underneath substrate from the bacterial infection.

- The feasibility of using the DBD-jet-based AP-PECVD device in biological applications was first examined.

In summary, this study bridged the gap between the thin film deposition technology and the biological and living substrates. The feasibility of directly applying thin films onto biological and living substrates was demonstrated so that several potential applications may be achieved in the future. These applications include *in vivo* repair of implant, *in vivo* manufacture of electronic circuits, deposition of sterile bandage or adhesive sutures, wound coatings, and scaffolds for the relief of wound mechanical stresses and decreased scaring, and deposition of functional films incorporating cell growth promoters, antibiotics, pharmaceuticals, chemically sensitive dyes, or fluorescent indicators. Although several improvements and modifications in the deposition system are needed and more experiments and tests are required before this technique can actually be applied to living bodies, we believe that the results obtained from this dissertation provide a new, promising path for biological and medical treatment.

9.2 Future Works

Many advances are required to achieve our ultimate goal "PECVD on living substrates". These include four main aspects: 1) system implementation from laboratory to commercialization, 2) system performance improvement, 3) process control, and 4) plasma-biological and material-biological interactions. Detailed descriptions regarding these four future tasks are given as follows.

To implement a system which is able to be commercialized, the reliability and the cost of the system are important. It was found that deposition inside the tube occurred during the operation of our DBD jets since the current system configuration only employed one dielectric tube fed with the mixture of helium and the precursor gases. This significantly reduced the reliability of the DBD jet. We observed that discharge conditions were influenced by the coatings formed on the inner wall of the dielectric tube since those films affected the inner dimension of the dielectric tube, further leading to the change in the boundary conditions of the plasma system. In addition, the films changed the dielectric constant of the system. Especially in copper film deposition, the copper coatings inside the tube caused the dielectric barrier to lose its ability to limit current (i.e., the system is not a DBD anymore). Thus regular replacement of the dielectric tube was necessary. To improve the reliability of the deposition system, the precursor gas can be delivered by an additional tube instead of in the same route as the main helium stream to prevent the deposition in the tube. This can be achieved by simply inserting a capillary, which is specifically used to deliver the precursor gas, into the main dielectric tube, which allows only the helium working gas to flow through. An example of the plasma jet with separate gas and precursor feed tubes can be seen in ref [72]. Regarding the cost of the system, the use of helium is usually the main issue which prevents the APPJs from being commercialized since helium is expensive. Employing argon as the working gas may solve this problem as argon is more cost effective, compared to helium. However, the breakdown voltage of an argon plasma jet is higher than that of a helium plasma jet due to the smaller mean free path of argon

[179]. The argon plasma jet also tends to be unstable (i.e., tends to transition to arc) and its downstream plume is much shorter than that of the helium plasma jet [180, 181]. It has been shown that a submicrosecond high-voltage pulsed DC power supply with kHz frequencies can be employed to sustain a stable, low-temperature argon DBD jet [182].

The DBD jet performance, such as its deposition rate, can be possibly improved by using a pulsed DC power supply without increasing the deposition temperature. Using the present He DBD jet device driven by the AC sinusoidal voltage, typically the gas temperature was increased with the rising power. However, it was found that a sufficiently high discharge power was required to achieve a high deposition rate. This indicates that to attain a relatively high film growth rate the gas temperature would be increased. If the gas temperature becomes too high, this technique will be not suitable anymore to be applied to the biological or living substrate. It has been shown that pulsed DC-excited APPJs are able to generate more species but its gas temperature still can remain very close to room temperature, compared to the APPJs driven by sinusoidal voltage at the same power [25, 31]. Thus in the future using the pulse DC power supply to drive our DBD jets is likely an ideal choice to achieve low-temperature, high-rate film deposition.

Process control is also important in order to improve the cost effectiveness of the deposition process as well as the quality of deposited films. It was shown that the discharge in the DBD jet is not ignited all the time. Instead, the discharge during each half voltage cycle only occurs when a current pulse, induced by the propagation of an ionization wave followed by the plasma channel formation, is observed (see Section 6).

During the plasma-off time, the precursors in the helium stream may not be effectively used since no discharge is present to activate the polymerization processes. To reduce the significant waste of the precursors, the precursor delivery can be controlled to be synchronous with the occurrence of the current pule; that is, "pulsed precursor delivery" can be further employed in the deposition processes. In other words, the precursors are only delivered to the helium stream when the current pulses are generated (plasma-on time), whereas only helium flows through the DBD jet reactor during the plasma-off time. This pulsed precursor delivery method may improve the precursor utilization efficiency. In addition, reduction of the impurities (carbon and oxygen) in the copper films deposited by the $He/H_2/Cu(acac)_2$ DBD jet can be achieved by a similar method. It has been shown that hydrogen plasma is able to reduce the impurity concentrations [148, 161, 163]. If the $He/H_2/Cu(acac)_2$ DBD jet and the He/H_2 DBD jet are employed in the copper deposition in turn, the carbon and oxygen impurities in every deposited copper layer [using $He/H_2/Cu(acac)_2$ DBD] can be further removed by the subsequent treatment using the He/H_2 plasma, further improving the film quality. Thus advanced control of the precursor delivery is necessary for the future commercialization.

To introduce this technique into clinical practice, several steps, from *in vitro* tests to *in vivo* tests, to characterize the biological effects of the plasma sources as well as the deposited films are required. These include the investigations of 1) plasma-liquid interactions, 2) microbiological tests, 3) cell-culture-based tests, 4) tests based on isolated tissues and organs, and 5) clinical trials [183]. Different from the tests with only the plasma sources in all the prior studies, in our cases the biological effects of the fed

precursors and plasma polymerized films on the biological and living substrates are also very important to examine. With the precursor addition, more diverse species are generated, compared with the DBD jet with pure helium, in which common species, such as OH, ozone, N_2, N_2^+, O, O_2^-, and He*, are observed. For example, in our He/MMA DBD jet, the additional radicals (e.g., CH•) from He/MMA DBD jet may play an important role on the sterilization ability. Atomic hydrogen and radicals from the precursor ligands in the $He/H_2/Cu(acac)_2$ DBD jet may also result in additional biological effects. Additionally, whether the deposited films would cause tissue irritation and/or toxic reactions needs further investigation; that is, the biocompatibility tests of the deposited films are required.

In summary, many works remain to be done to improve the reliability of the DBD jet system and to actually introduce PECVD on living substrates. However, the feasibility of this idea has been demonstrated in this dissertation. This idea is expected to have a marked impact on the future of biomedical treatment.

REFERENCES

[1] L. Tonks and I. Langmuir, "Oscillations in ionized gases," *Physical Review,* vol. 33, p. 195, 1929.

[2] J. J. Lowke and D. K. Davies, "Properties of electric discharges sustained by a uniform source of ionization," *Journal of Applied Physics,* vol. 48, pp. 4991-5000, 1977.

[3] N. W. Harris, F. O'Neill, and W. T. Whitney, "Operation of a 15-atm electron-beam-controlled CO_2 laser," *Applied Physics Letters,* vol. 25, pp. 148-151, 1974.

[4] Y. P. Raizer, *Gas Discharge Physics*. New York, NY: Springer-Verlag, 1997.

[5] U. Kogelschatz, "Atmospheric-pressure plasma technology," *Plasma Physics and Controlled Fusion,* vol. 46, p. B63, 2004.

[6] A. Fridman, A. Chirokov, and A. Gutsol, "Non-thermal atmospheric pressure discharges," *Journal of Physics D: Applied Physics,* vol. 38, p. R1, 2005.

[7] U. Kogelschatz, "Dielectric-barrier discharges: Their history, discharge physics, and industrial applications," *Plasma Chemistry and Plasma Processing,* vol. 23, pp. 1-46, 2003.

[8] H.-H. Kim, "Nonthermal plasma processing for air-pollution control: A historical review, current issues, and future prospects," *Plasma Processes and Polymers,* vol. 1, pp. 91-110, 2004.

[9] M. Laroussi and T. Akan, "Arc-free atmospheric pressure cold plasma jets: A review," *Plasma Processes and Polymers,* vol. 4, pp. 777-788, 2007.

[10] U. Kogelschatz, "Filamentary, patterned, and diffuse barrier discharges," *Plasma Science, IEEE Transactions on,* vol. 30, pp. 1400-1408, 2002.

[11] G. Fridman, A. D. Brooks, M. Balasubramanian, A. Fridman, A. Gutsol, V. N. Vasilets, H. Ayan, and G. Friedman, "Comparison of direct and indirect effects of non-thermal atmospheric-pressure plasma on bacteria," *Plasma Processes and Polymers,* vol. 4, pp. 370-375, 2007.

[12] G. Fridman, A. Shereshevsky, M. Jost, A. Brooks, A. Fridman, A. Gutsol, V. Vasilets, and G. Friedman, "Floating electrode dielectric barrier discharge plasma in air promoting apoptotic behavior in melanoma skin cancer cell lines," *Plasma Chemistry and Plasma Processing,* vol. 27, pp. 163-176, 2007.

[13] G. Fridman, G. Friedman, A. Gutsol, A. B. Shekhter, V. N. Vasilets, and A. Fridman, "Applied plasma medicine," *Plasma Processes and Polymers,* vol. 5, pp. 503-533, 2008.

[14] R. Bartnikas, "Note on discharges in helium under a.c. conditions," *Journal of Physics D: Applied Physics,* vol. 1, p. 659, 1968.

[15] S. Okazaki, M. Kogoma, M. Uehara, and Y. Kimura, "Appearance of stable glow discharge in air, argon, oxygen and nitrogen at atmospheric pressure using a 50 Hz source," *Journal of Physics D: Applied Physics,* vol. 26, p. 889, 1993.

[16] M. Kogoma and S. Okazaki, "Raising of ozone formation efficiency in a homogeneous glow discharge plasma at atmospheric pressure," *Journal of Physics D: Applied Physics,* vol. 27, p. 1985, 1994.

[17] I. Radu, R. Bartnikas, G. Czeremuszkin, and M. R. Wertheimer, "Diagnostics of dielectric barrier discharges in noble gases: atmospheric pressure glow and pseudoglow discharges and spatio-temporal patterns," *Plasma Science, IEEE Transactions on,* vol. 31, pp. 411-421, 2003.

[18] I. Radu, R. Bartnikas, and M. R. Wertheimer, "Frequency and voltage dependence of glow and pseudoglow discharges in helium under atmospheric pressure," *Plasma Science, IEEE Transactions on,* vol. 31, pp. 1363-1378, 2003.

[19] I. Radu, R. Bartnikas, and M. R. Wertheimer, "Diagnostics and modelling of noble gas atmospheric pressure dielectric barrier discharges in homogeneous or diverging electric fields," *Journal of Physics D: Applied Physics,* vol. 38, p. 539, 2005.

[20] M. Laroussi, "Low temperature plasma-based sterilization: Overview and state-of-the-art," *Plasma Processes and Polymers,* vol. 2, pp. 391-400, 2005.

[21] Z. Fang, Y. Qiu, and Y. Luo, "Surface modification of polytetrafluoroethylene film using the atmospheric pressure glow discharge in air," *Journal of Physics D: Applied Physics,* vol. 36, p. 2980, 2003.

[22] N. De Geyter, R. Morent, S. Van Vlierberghe, P. Dubruel, C. Leys, L. Gengembre, E. Schacht, and E. Payen, "Deposition of polymethyl methacrylate on polypropylene substrates using an atmospheric pressure dielectric barrier discharge," *Progress in Organic Coatings,* vol. 64, pp. 230-237, 2009.

[23] H. Koinuma, H. Ohkubo, T. Hashimoto, K. Inomata, T. Shiraishi, A. Miyanaga, and S. Hayashi, "Development and application of a microbeam plasma generator," *Applied Physics Letters,* vol. 60, pp. 816-817, 1992.

[24] X. Lu and M. Laroussi, "Dynamics of an atmospheric pressure plasma plume generated by submicrosecond voltage pulses," *Journal of Applied Physics,* vol. 100, pp. 063302-6, 2006.

[25] J. L. Walsh, J. J. Shi, and M. G. Kong, "Contrasting characteristics of pulsed and sinusoidal cold atmospheric plasma jets," *Applied Physics Letters,* vol. 88, pp. 171501-3, 2006.

[26] R. Foest, E. Kindel, A. Ohl, M. Stieber, and K.-D. Weltmann, "Non-thermal atmospheric pressure discharges for surface modification," *Plasma Physics and Controlled Fusion,* vol. 47, p. B525, 2005.

[27] J. Schäfer, R. Foest, A. Quade, A. Ohl, and K.-D. Weltmann, "Chemical composition of SiOx films deposited by an atmospheric pressure plasma jet (APPJ)," *Plasma Processes and Polymers,* vol. 6, pp. S519-S524, 2009.

[28] M. Laroussi, C. Tendero, X. Lu, S. Alla, and W. L. Hynes, "Inactivation of bacteria by the plasma pencil," *Plasma Processes and Polymers,* vol. 3, pp. 470-473, 2006.

[29] M. Laroussi and X. Lu, "Room-temperature atmospheric pressure plasma plume for biomedical applications," *Applied Physics Letters,* vol. 87, pp. 113902-3, 2005.

[30] S. J. Kim, T. H. Chung, and S. H. Bae, "Striation and plasma bullet propagation in an atmospheric pressure plasma jet," *Physics of Plasmas,* vol. 17, pp. 053504-5, 2010.

[31] Q. Xiong, X. P. Lu, K. Ostrikov, Y. Xian, C. Zou, Z. Xiong, and Y. Pan, "Pulsed dc- and sine-wave-excited cold atmospheric plasma plumes: A comparative analysis," *Physics of Plasmas,* vol. 17, pp. 043506-8, 2010.

[32] G. Fridman, M. Peddinghaus, M. Balasubramanian, H. Ayan, A. Fridman, A. Gutsol, and A. Brooks, "Blood coagulation and living tissue sterilization by floating-electrode dielectric barrier discharge in air," *Plasma Chemistry and Plasma Processing,* vol. 26, pp. 425-442-442, 2006.

[33] S. E. Babayan, J. Y. Jeong, V. J. Tu, J. Park, G. S. Selwyn, and R. F. Hicks, "Deposition of silicon dioxide films with an atmospheric-pressure plasma jet," *Plasma Sources Science and Technology,* vol. 7, p. 286, 1998.

[34] D. L. Smith, *Thin-Film Deposition: Principles and Practice*. New York, NY: McGraw-Hill Professional, 1995.

[35] M. Ohring, *Materials science of thin films: deposition and structure*. San Diego, CA: Academic Press, 2002.

[36] J. Friedrich, "Mechanisms of plasma polymerization – Reviewed from a chemical point of view," *Plasma Processes and Polymers,* vol. 8, pp. 783-802, 2011.

[37] R. d'Agostino, P. Favia, C. Oehr, and M. R. Wertheimer, "Low-temperature plasma processing of materials: Past, present, and future," *Plasma Processes and Polymers,* vol. 2, pp. 7-15, 2005.

[38] J. L. West and J. A. Hubbell, "Photopolymerized hydrogel materials for drug delivery applications," *Reactive Polymers,* vol. 25, pp. 139-147, 1995.

[39] J. A. Hubbell, "Hydrogel systems for barriers and local drug delivery in the control of wound healing," *Journal of Controlled Release,* vol. 39, pp. 305-313, 1996.

[40] D.-H. Kim, N. Lu, R. Ma, Y.-S. Kim, R.-H. Kim, S. Wang, J. Wu, S. M. Won, H. Tao, A. Islam, K. J. Yu, T.-i. Kim, R. Chowdhury, M. Ying, L. Xu, M. Li, H.-J. Chung, H. Keum, M. McCormick, P. Liu, Y.-W. Zhang, F. G. Omenetto, Y. Huang, T. Coleman, and J. A. Rogers, "Epidermal electronics," *Science,* vol. 333, pp. 838-843, August 12, 2011 2011.

[41] S. E. Alexandrov and M. L. Hitchman, "Chemical vapor deposition enhanced by atmospheric pressure non-thermal non-equilibrium plasmas," *Chemical Vapor Deposition,* vol. 11, pp. 457-468, 2005.

[42] S. P. Bugaev, A. D. Korotaev, K. V. Oskomov, and N. S. Sochugov, "a-C:H films deposited in the plasma of barrier and surface discharges at atmospheric pressure," *Surface and Coatings Technology,* vol. 96, pp. 123-128, 1997.

[43] O. Goossens, E. Dekempeneer, D. Vangeneugden, R. Van de Leest, and C. Leys, "Application of atmospheric pressure dielectric barrier discharges in deposition,

cleaning and activation," *Surface and Coatings Technology,* vol. 142–144, pp. 474-481, 2001.

[44] T. Opalinska, B. Ulejczyk, and K. Schmidt-Szalowski, "Applications of pulsed discharge to thin-film deposition," *Plasma Science, IEEE Transactions on,* vol. 37, pp. 934-940, 2009.

[45] T.-C. Tsai and D. Staack, "Low-temperature polymer deposition in ambient air using a floating-electrode dielectric barrier discharge jet," *Plasma Processes and Polymers,* vol. 8, pp. 523-534, 2011.

[46] T.-C. Tsai and D. Staack, "Characteristics of precursor-dependent breakdown in helium dielectric barrier discharge jet," *Plasma Science, IEEE Transactions on,* vol. 40, pp. 2931-2945, 2012.

[47] T.-C. Tsai, J. Cho, K. McIntyre, Y.-K. Jo, and D. Staack, "Polymer film deposition on agar using a dielectric barrier discharge jet and its bacterial growth inhibition," *Applied Physics Letters,* vol. 101, pp. 074107-4, 2012.

[48] D. Staack, "Characterization and stabilization of atmospheric pressure DC microplasmas and their application to thin film deposition," Ph.D. dissertation, Mechanical Engineering, Drexel University, Philadelphia, PA, 2008.

[49] *KLA-Tencor P-6 profilometer* [Online]. Available: http://www.kla-tencor.com/surface-profiling/general-purpose-p-6.html [Accessed: September 28, 2012].

[50] S. Swapp, *Scanning Electron Microscopy (SEM)*. Available: http://serc.carleton.edu/research_education/geochemsheets/techniques/SEM.html [Accessed: October 10, 2012].

[51] *JEOL JSM-7500F FE-SEM* [Online]. Available: http://mcf.tamu.edu/instruments/fe-sem [Accessed: September 28, 2012].

[52] *Atomic Force Microscopy*. Available: http://www.nanoscience.com/education/afm.html [Accessed: October 10, 2012].

[53] *Atomic Force Microscopy: General Concept and Defining Characteristics*. Available: http://www.nrl.navy.mil/chemistry/6170/6177/afm_concept.php [Accessed: October 10, 2012].

[54] *Digital Instruments Nanoscope AFM/STM* [Online]. Available: http://mcf.tamu.edu/instruments/afm [Accessed: September 28, 2012].

[55] R. M. Nix, *Photoelectron Spectroscopy*. Available: http://www.chem.qmul.ac.uk/surfaces/scc/scat5_3.htm [Accessed: October 10, 2012].

[56] *Kratos Axis Ultra Imaging X-ray photoelectron spectrometer* [Online]. Available: http://mcf.tamu.edu/instruments/xps [Accessed: September 28, 2012].

[57] *Guide to Surface Analysis Software Tools* [Online]. Available: www.uksaf.org/software.html [Accessed: September 28, 2012].

[58] *What is FT-IR?* Available: http://mmrc.caltech.edu/FTIR/FTIRintro.pdf [Accessed: October 10, 2012].

[59] *ALPHA FTIR Spectrometer* [Online]. Available: http://www.brukeroptics.com/alpha.html [Accessed: September 28, 2012].

[60] *Picosecond High Speed ICCD Camera* [Online]. Available: http://www.stanfordcomputeroptics.com/p-picosecond-iccd.html [Accessed: September 28, 2012].

[61] M. Teschke, J. Kedzierski, E. G. Finantu-Dinu, D. Korzec, and J. Engemann, "High-speed photographs of a dielectric barrier atmospheric pressure plasma jet," *Plasma Science, IEEE Transactions on,* vol. 33, pp. 310-311, 2005.

[62] *Hamamatsu Photomultiplier Tube R928* [Online]. Available: http://sales.hamamatsu.com/en/products/electron-tube-division/detectors/photomultiplier-tubes/part-r928.php [Accessed: September 28, 2012].

[63] *PMT Handbook*. Available: http://sales.hamamatsu.com/assets/pdf/catsandguides/PMT_handbook_v3aE.pdf [Accessed: October 10, 2012].

[64] J. M. Hollas, *Modern Spectroscopy*, 4th ed. Chichester, UK: John Wiley & Sons, Ltd, 2004.

[65] D. Staack, B. Farouk, A. Gutsol, and A. Fridman, "DC normal glow discharges in atmospheric pressure atomic and molecular gases," *Plasma Sources Science and Technology,* vol. 17, p. 025013, 2008.

[66] *UV-VIS TE Cooled CCD Spectrometer* [Online]. Available: http://www.edmundoptics.com/testing-targets/spectrometers/te-cooled-ccd-based-spectrometers/3156 [Accessed: September 28, 2012].

[67] K. Inomata, N. Aoki, and H. Koinuma, "Production of fullerenes by low temperature plasma chemical vaper deposition under atmospheric pressure," *Japanese Journal of Applied Physics,* vol. 33, p. L197, 1994.

[68] K. Inomata, H. Ha, K. A. Chaudhary, and H. Koinuma, "Open air deposition of SiO_2 film from a cold plasma torch of tetramethoxysilane-H_2-Ar system," *Applied Physics Letters,* vol. 64, pp. 46-48, 1994.

[69] H.-K. Ha, M. Yoshimoto, H. Koinuma, B.-K. Moon, and H. Ishiwara, "Open air plasma chemical vapor deposition of highly dielectric amorphous TiO_2 films," *Applied Physics Letters,* vol. 68, pp. 2965-2967, 1996.

[70] R. Foest, E. Kindel, H. Lange, A. Ohl, M. Stieber, and K. D. Weltmann, "RF capillary jet - a tool for localized surface treatment," *Contributions to Plasma Physics,* vol. 47, pp. 119-128, 2007.

[71] J. Schäfer, R. Foest, A. Quade, A. Ohl, and K. D. Weltmann, "Local deposition of SiO_x plasma polymer films by a miniaturized atmospheric pressure plasma jet (APPJ)," *Journal of Physics D: Applied Physics,* vol. 41, p. 194010, 2008.

[72] J. Benedikt, K. Focke, A. Yanguas-Gil, and A. von Keudell, "Atmospheric pressure microplasma jet as a depositing tool," *Applied Physics Letters,* vol. 89, pp. 251504-3, 2006.

[73] J. Benedikt, V. Raballand, A. Yanguas-Gil, K. Focke, and A. v. Keudell, "Thin film deposition by means of atmospheric pressure microplasma jet," *Plasma Physics and Controlled Fusion,* vol. 49, p. B419, 2007.

[74] V. Raballand, J. Benedikt, and A. von Keudell, "Deposition of carbon-free silicon dioxide from pure hexamethyldisiloxane using an atmospheric microplasma jet," *Applied Physics Letters,* vol. 92, pp. 091502-3, 2008.

[75] V. Raballand, J. Benedikt, S. Hoffmann, M. Zimmermann, and A. von Keudell, "Deposition of silicon dioxide films using an atmospheric pressure microplasma jet," *Journal of Applied Physics,* vol. 105, pp. 083304-6, 2009.

[76] A. Yanguas-Gil, K. Focke, J. Benedikt, and A. von Keudell, "Optical and electrical characterization of an atmospheric pressure microplasma jet for Ar/CH_4 and Ar/C_2H_2 mixtures," *Journal of Applied Physics,* vol. 101, pp. 103307-8, 2007.

[77] C. Huang, W.-T. Hsu, C.-H. Liu, S.-Y. Wu, S.-H. Yang, T.-H. Chen, and T.-C. Wei, "Low-temperature atmospheric-pressure-plasma jet for thin-film deposition," *Plasma Science, IEEE Transactions on,* vol. 37, pp. 1127-1128, 2009.

[78] S.-H. Yang, C.-H. Liu, C.-H. Su, and H. Chen, "Atmospheric-pressure plasma deposition of SiOx films for super-hydrophobic application," *Thin Solid Films,* vol. 517, pp. 5284-5287, 2009.

[79] M. Leduc, S. Coulombe, and R. L. Leask, "Atmospheric pressure plasma jet deposition of patterned polymer films for cell culture applications," *Plasma Science, IEEE Transactions on,* vol. 37, pp. 927-933, 2009.

[80] Y. Shimizu, T. Sasaki, T. Ito, K. Terashima, and N. Koshizaki, "Fabrication of spherical carbon via UHF inductively coupled microplasma CVD," *Journal of Physics D: Applied Physics,* vol. 36, p. 2940, 2003.

[81] S. Stauss, Y. Imanishi, H. Miyazoe, and K. Terashima, "High rate deposition of ZnO thin films by a small-scale inductively coupled argon plasma generated in open air," *Journal of Physics D: Applied Physics,* vol. 43, p. 155203, 2010.

[82] G. Nutsch, S. Nolin, T. H. Heider, and W. Rother, "Application of the dielectric barrier discharge jet in surface treatment and film deposition," *Annals of the New York Academy of Sciences,* vol. 891, pp. 216-222, 1999.

[83] Q. Chen, Y. Zhang, E. Han, and Y. Ge, "SiO_2-like film deposition by dielectric barrier discharge plasma gun at ambient temperature under an atmospheric pressure," *Journal of Vacuum Science & Technology A: Vacuum, Surfaces, and Films,* vol. 24, pp. 2082-2086, 2006.

[84] Y. Ito, K. Urabe, N. Takano, and K. Tachibana, "High speed deposition of SiO_2 films with plasma jet based on capillary dielectric barrier discharge at atmospheric pressure," *Applied Physics Express,* vol. 1, p. 067009, 2008.

[85] W.-J. Liu, X.-J. Guo, C.-L. Chang, and J.-H. Lu, "Diamond-like carbon thin films synthesis by low temperature atmospheric pressure plasma method," *Thin Solid Films,* vol. 517, pp. 4229-4232, 2009.

[86] R. M. Sankaran and K. P. Giapis, "Hollow cathode sustained plasma microjets: Characterization and application to diamond deposition," *Journal of Applied Physics,* vol. 92, pp. 2406-2411, 2002.

[87] T. P. Kasih, S.-i. Kuroda, and H. Kubota, "Poly(methyl methacrylate) films deposited via non-equilibrium atmospheric pressure plasma polymerization using argon as working gas," *Plasma Processes and Polymers,* vol. 4, pp. 648-653, 2007.

[88] M. H. Han, J. H. Noh, T. I. Lee, J. H. Choi, K. W. Park, H. S. Hwang, K. M. Song, and H. K. Baik, "High-rate SiO_2 deposition by oxygen cold arc plasma jet at atmospheric pressure," *Plasma Processes and Polymers,* vol. 5, pp. 861-866, 2008.

[89] U. Lommatzsch and J. Ihde, "Plasma polymerization of HMDSO with an atmospheric pressure plasma jet for corrosion protection of aluminum and low-adhesion surfaces," *Plasma Processes and Polymers,* vol. 6, pp. 642-648, 2009.

[90] D. B. Kim, J. K. Rhee, B. Gweon, S. Y. Moon, and W. Choe, "Comparative study of atmospheric pressure low and radio frequency microjet plasmas produced in a single electrode configuration," *Applied Physics Letters,* vol. 91, pp. 151502-3, 2007.

[91] J. L. Walsh and M. G. Kong, "Frequency effects of plasma bullets in atmospheric glow discharges," *Plasma Science, IEEE Transactions on,* vol. 36, pp. 954-955, 2008.

[92] H. S. Park, S. J. Kim, H. M. Joh, T. H. Chung, S. H. Bae, and S. H. Leem, "Optical and electrical characterization of an atmospheric pressure microplasma jet with a capillary electrode," *Physics of Plasmas,* vol. 17, pp. 033502-10, 2010.

[93] J. Kędzierski, J. Engemann, M. Teschke, and D. Korzec, "Atmospheric pressure plasma jets for 2D and 3D materials processing," *Solid State Phenomena,* vol. 107, pp. 119-124, 2005.

[94] D. B. Kim, J. K. Rhee, S. Y. Moon, and W. Choe, "Study of geometrical and operational parameters controlling the low frequency microjet atmospheric pressure plasma characteristics," *Applied Physics Letters,* vol. 89, pp. 061502-3, 2006.

[95] Q.-Y. Nie, C.-S. Ren, D.-Z. Wang, S.-Z. Li, J.-L. Zhang, and M. G. Kong, "Self-organized pattern formation of an atmospheric pressure plasma jet in a dielectric barrier discharge configuration," *Applied Physics Letters,* vol. 90, pp. 221504-3, 2007.

[96] X. Lu, Z. Jiang, Q. Xiong, Z. Tang, and Y. Pan, "A single electrode room-temperature plasma jet device for biomedical applications," *Applied Physics Letters,* vol. 92, pp. 151504-3, 2008.

[97] J. Shi, F. Zhong, J. Zhang, D. W. Liu, and M. G. Kong, "A hypersonic plasma bullet train traveling in an atmospheric dielectric-barrier discharge jet," *Physics of Plasmas,* vol. 15, pp. 013504-5, 2008.

[98] Z. Cao, J. L. Walsh, and M. G. Kong, "Atmospheric plasma jet array in parallel electric and gas flow fields for three-dimensional surface treatment," *Applied Physics Letters,* vol. 94, pp. 021501-3, 2009.

[99] N. Jiang, A. Ji, and Z. Cao, "Atmospheric pressure plasma jet: Effect of electrode configuration, discharge behavior, and its formation mechanism," *Journal of Applied Physics,* vol. 106, pp. 013308-7, 2009.

[100] H. Kim, A. Brockhaus, and J. Engemann, "Atmospheric pressure argon plasma jet using a cylindrical piezoelectric transformer," *Applied Physics Letters,* vol. 95, pp. 211501-3, 2009.

[101] X. Lu, Q. Xiong, Z. Xiong, J. Hu, F. Zhou, W. Gong, Y. Xian, C. Zou, Z. Tang, Z. Jiang, and Y. Pan, "Propagation of an atmospheric pressure plasma plume," *Journal of Applied Physics,* vol. 105, pp. 043304-4, 2009.

[102] N. Mericam-Bourdet, M. Laroussi, A. Begum, and E. Karakas, "Experimental investigations of plasma bullets," *Journal of Physics D: Applied Physics,* vol. 42, p. 055207, 2009.

[103] S. B. Olenici-Craciunescu, A. Michels, C. Meyer, R. Heming, S. Tombrink, W. Vautz, and J. Franzke, "Characterization of a capillary dielectric barrier plasma jet for use as a soft ionization source by optical emission and ion mobility spectrometry," *Spectrochimica Acta Part B: Atomic Spectroscopy,* vol. 64, pp. 1253-1258, 2009.

[104] A. Shashurin, M. N. Shneider, A. Dogariu, R. B. Miles, and M. Keidar, "Temporal behavior of cold atmospheric plasma jet," *Applied Physics Letters,* vol. 94, pp. 231504-3, 2009.

[105] J. Jarrige, M. Laroussi, and E. Karakas, "Formation and dynamics of plasma bullets in a non-thermal plasma jet: influence of the high-voltage parameters on the plume characteristics," *Plasma Sources Science and Technology,* vol. 19, p. 065005, 2010.

[106] E. Karakas, M. Koklu, and M. Laroussi, "Correlation between helium mole fraction and plasma bullet propagation in low temperature plasma jets," *Journal of Physics D: Applied Physics,* vol. 43, p. 155202, 2010.

[107] E. Karakas and M. Laroussi, "Experimental studies on the plasma bullet propagation and its inhibition," *Journal of Applied Physics,* vol. 108, pp. 063305-6, 2010.

[108] J. L. Walsh, F. Iza, N. B. Janson, V. J. Law, and M. G. Kong, "Three distinct modes in a cold atmospheric pressure plasma jet," *Journal of Physics D: Applied Physics,* vol. 43, p. 075201, 2010.

[109] Z. Xiong, X. Lu, Q. Xiong, Y. Xian, C. Zou, J. Hu, W. Gong, J. Liu, F. Zou, Z. Jiang, and Y. Pan, "Measurements of the propagation velocity of an atmospheric-pressure plasma plume by various methods," *Plasma Science, IEEE Transactions on,* vol. 38, pp. 1001-1007, 2010.

[110] Y. Feng, C.-S. Ren, Q.-Y. Nie, and D.-Z. Wang, "Study on the self-organized pattern in an atmospheric pressure dielectric barrier discharge plasma jet," *Plasma Science, IEEE Transactions on,* vol. 38, pp. 1061-1065, 2010.

[111] H. Akamatsu and K. Ichikawa, "Characteristics of atmospheric pressure plasma jet generated by compact and inexpensive high voltage modulator," *Surface and Coatings Technology,* vol. 206, pp. 920-924, 2011.

[112] K. Urabe, T. Morita, K. Tachibana, and B. N. Ganguly, "Investigation of discharge mechanisms in helium plasma jet at atmospheric pressure by laser spectroscopic measurements," *Journal of Physics D: Applied Physics,* vol. 43, p. 095201, 2010.

[113] L. Mangolini, K. Orlov, U. Kortshagen, J. Heberlein, and U. Kogelschatz, "Radial structure of a low-frequency atmospheric-pressure glow discharge in helium," *Applied Physics Letters,* vol. 80, pp. 1722-1724, 2002.

[114] Y. B. Golubovskii, V. A. Maiorov, J. Behnke, and J. F. Behnke, "Modelling of the homogeneous barrier discharge in helium at atmospheric pressure," *Journal of Physics D: Applied Physics,* vol. 36, p. 39, 2003.

[115] T. Nozaki, Y. Miyazaki, Y. Unno, and K. Okazaki, "Energy distribution and heat transfer mechanisms in atmospheric pressure non-equilibrium plasmas," *Journal of Physics D: Applied Physics,* vol. 34, p. 3383, 2001.

[116] F. Fanelli, F. Fracassi, and R. d'Agostino, "Deposition of hydrocarbon films by means of helium-ethylene fed glow dielectric barrier discharges," *Plasma Processes and Polymers,* vol. 2, pp. 688-694, 2005.

[117] J. Raiser and M. Zenker, "Argon plasma coagulation for open surgical and endoscopic applications: state of the art," *Journal of Physics D: Applied Physics,* vol. 39, p. 3520, 2006.

[118] M. Leduc, D. Guay, R. L. Leask, and S. Coulombe, "Cell permeabilization using a non-thermal plasma," *New Journal of Physics,* vol. 11, p. 115021, 2009.

[119] M. Leduc, D. Guay, S. Coulombe, and R. L. Leask, "Effects of non-thermal plasmas on DNA and mammalian cells," *Plasma Processes and Polymers,* vol. 7, pp. 899-909, 2010.

[120] X. T. Deng, J. J. Shi, H. L. Chen, and M. G. Kong, "Protein destruction by atmospheric pressure glow discharges," *Applied Physics Letters,* vol. 90, pp. 013903-3, 2007.

[121] A. Shashurin, M. Keidar, S. Bronnikov, R. A. Jurjus, and M. A. Stepp, "Living tissue under treatment of cold plasma atmospheric jet," *Applied Physics Letters,* vol. 93, pp. 181501-3, 2008.

[122] I. E. Kieft, D. Darios, A. J. M. Roks, and E. Stoffels, "Plasma treatment of mammalian vascular cells: a quantitative description," *Plasma Science, IEEE Transactions on,* vol. 33, pp. 771-775, 2005.

[123] S. Coulombe, V. Léveillé, S. Yonson, and R. L. Leask, "Miniature atmospheric pressure glow discharge torch (APGD-t) for local biomedical applications," *Pure and Applied Chemistry,* vol. 78, pp. 1147-1156, 2006.

[124] E. Stoffels, I. E. Kieft, R. E. J. Sladek, L. J. M. v. d. Bedem, E. P. v. d. Laan, and M. Steinbuch, "Plasma needle for in vivo medical treatment: recent

developments and perspectives," *Plasma Sources Science and Technology,* vol. 15, p. S169, 2006.

[125] I. E. Kieft, M. Kurdi, and E. Stoffels, "Reattachment and apoptosis after plasma-needle treatment of cultured cells," *Plasma Science, IEEE Transactions on,* vol. 34, pp. 1331-1336, 2006.

[126] G. J. Kim, W. Kim, K. T. Kim, and J. K. Lee, "DNA damage and mitochondria dysfunction in cell apoptosis induced by nonthermal air plasma," *Applied Physics Letters,* vol. 96, pp. 021502-3, 2010.

[127] S. J. Kim, T. H. Chung, S. H. Bae, and S. H. Leem, "Induction of apoptosis in human breast cancer cells by a pulsed atmospheric pressure plasma jet," *Applied Physics Letters,* vol. 97, pp. 023702-3, 2010.

[128] A. B. Shekhter, V. A. Serezhenkov, T. G. Rudenko, A. V. Pekshev, and A. F. Vanin, "Beneficial effect of gaseous nitric oxide on the healing of skin wounds," *Nitric Oxide,* vol. 12, pp. 210-219, 2005.

[129] D. Dobrynin, G. Fridman, G. Friedman, and A. Fridman, "Physical and biological mechanisms of direct plasma interaction with living tissue," *New Journal of Physics,* vol. 11, p. 115020, 2009.

[130] X. Lu, T. Ye, Y. Cao, Z. Sun, Q. Xiong, Z. Tang, Z. Xiong, J. Hu, Z. Jiang, and Y. Pan, "The roles of the various plasma agents in the inactivation of bacteria," *Journal of Applied Physics,* vol. 104, pp. 053309-5, 2008.

[131] D. B. Graves, "The emerging role of reactive oxygen and nitrogen species in redox biology and some implications for plasma applications to medicine and biology," *Journal of Physics D: Applied Physics,* vol. 45, p. 263001, 2012.

[132] E. Stoffels, Y. Sakiyama, and D. B. Graves, "Cold atmospheric plasma: charged species and their interactions with cells and tissues," *Plasma Science, IEEE Transactions on,* vol. 36, pp. 1441-1457, 2008.

[133] M. G. Kong, G. Kroesen, G. Morfill, T. Nosenko, T. Shimizu, J. v. Dijk, and J. L. Zimmermann, "Plasma medicine: An introductory review," *New Journal of Physics,* vol. 11, p. 115012, 2009.

[134] S. J. Kim, T. H. Chung, S. H. Bae, and S. H. Leem, "Bacterial inactivation using atmospheric pressure single pin electrode microplasma jet with a ground ring," *Applied Physics Letters,* vol. 94, pp. 141502-3, 2009.

[135] K. D. Weltmann, E. Kindel, R. Brandenburg, C. Meyer, R. Bussiahn, C. Wilke, and T. von Woedtke, "Atmospheric pressure plasma jet for medical therapy: Plasma parameters and risk estimation," *Contributions to Plasma Physics,* vol. 49, pp. 631-640, 2009.

[136] S. K. Kang, M. Y. Choi, I. G. Koo, P. Y. Kim, Y. Kim, G. J. Kim, A.-A. H. Mohamed, G. J. Collins, and J. K. Lee, "Reactive hydroxyl radical-driven oral bacterial inactivation by radio frequency atmospheric plasma," *Applied Physics Letters,* vol. 98, pp. 143702-3, 2011.

[137] X. T. Deng, J. J. Shi, G. Shama, and M. G. Kong, "Effects of microbial loading and sporulation temperature on atmospheric plasma inactivation of Bacillus subtilis spores," *Applied Physics Letters,* vol. 87, pp. 153901-3, 2005.

[138] H. S. Uhm, J. P. Lim, and S. Z. Li, "Sterilization of bacterial endospores by an atmospheric-pressure argon plasma jet," *Applied Physics Letters,* vol. 90, pp. 261501-3, 2007.

[139] P. Sun, Y. Sun, H. Wu, W. Zhu, J. L. Lopez, W. Liu, J. Zhang, R. Li, and J. Fang, "Atmospheric pressure cold plasma as an antifungal therapy," *Applied Physics Letters,* vol. 98, pp. 021501-3, 2011.

[140] K. Kim, J. D. Choi, Y. C. Hong, G. Kim, E. J. Noh, J.-S. Lee, and S. S. Yang, "Atmospheric-pressure plasma-jet from micronozzle array and its biological effects on living cells for cancer therapy," *Applied Physics Letters,* vol. 98, pp. 073701-3, 2011.

[141] C.-H. Kim, S. Kwon, J. H. Bahn, K. Lee, S. I. Jun, P. D. Rack, and S. J. Baek, "Effects of atmospheric nonthermal plasma on invasion of colorectal cancer cells," *Applied Physics Letters,* vol. 96, pp. 243701-3, 2010.

[142] D. O'Connell, L. J. Cox, W. B. Hyland, S. J. McMahon, S. Reuter, W. G. Graham, T. Gans, and F. J. Currell, "Cold atmospheric pressure plasma jet interactions with plasmid DNA," *Applied Physics Letters,* vol. 98, pp. 043701-3, 2011.

[143] A. V. Nastuta, I. Topala, C. Grigoras, V. Pohoata, and G. Popa, "Stimulation of wound healing by helium atmospheric pressure plasma treatment," *Journal of Physics D: Applied Physics,* vol. 44, p. 105204, 2011.

[144] S. Chaisitsak, J. Nukeaw, and A. Tuantranont, "Parametric study of atmospheric-pressure single-walled carbon nanotubes growth by ferrocene–ethanol mist CVD," *Diamond and Related Materials,* vol. 16, pp. 1958-1966, 2007.

[145] M. J. Hampden-Smith and T. T. Kodas, "Chemical vapor deposition of metals: Part 1. An overview of CVD processes," *Chemical Vapor Deposition,* vol. 1, pp. 8-23, 1995.

[146] N. Awaya and Y. Arita, "Plasma-enhanced chemical vapor deposition of copper," *Japanese Journal of Applied Physics,* vol. 30, pp. 1813-1817, 1991.

[147] J. Pelletier, R. Pantel, J. C. Oberlin, Y. Pauleau, and P. Gouy-Pailler, "Preparation of copper thin films at ambient temperature by microwave plasma-enhanced chemical vapor deposition from the copper (II) acetylacetonate-argon-hydrogen system," *Journal of Applied Physics,* vol. 70, pp. 3862-3866, 1991.

[148] T. Maruyama and T. Shirai, "Copper thin films prepared by chemical vapour deposition from copper (II) acetylacetonate," *Journal of Materials Science,* vol. 30, pp. 5551-5553, 1995.

[149] C. T. Black, K. W. Guarini, K. R. Milkove, S. M. Baker, T. P. Russell, and M. T. Tuominen, "Integration of self-assembled diblock copolymers for semiconductor capacitor fabrication," *Applied Physics Letters,* vol. 79, pp. 409-411, 2001.

[150] K. W. Guarini, C. T. Black, K. R. Milkove, and R. L. Sandstrom, "Nanoscale patterning using self-assembled polymers for semiconductor applications," Washington, DC (USA), 2001, pp. 2784-2788.

[151] M. Takahashi, T. Maeda, K. Uemura, J. Yao, Y. Tokuda, T. Yoko, H. Kaji, A. Marcelli, and P. Innocenzi, "Photoinduced formation of wrinkled microstructures with long-range order in thin oxide films," *Advanced Materials,* vol. 19, pp. 4343-4346, 2007.

[152] P. Gröning, O. M. Küttel, M. Collaud-Coen, G. Dietler, and L. Schlapbach, "Interaction of low-energy ions (< 10 eV) with polymethylmethacrylate during plasma treatment," *Applied Surface Science,* vol. 89, pp. 83-91, 1995.

[153] T. B. Casserly and K. K. Gleason, "Effect of substrate temperature on the plasma polymerization of poly(methyl methacrylate)," *Chemical Vapor Deposition,* vol. 12, pp. 59-66, 2006.

[154] G. P. López, D. G. Castner, and B. D. Ratner, "XPS O 1s binding energies for polymers containing hydroxyl, ether, ketone and ester groups," *Surface and Interface Analysis,* vol. 17, pp. 267-272, 1991.

[155] F. Z. Tighilt, N. Gabouze, S. Sam, S. Belhousse, and K. Beldjilali, "Morphology and specific interaction of PMMA coating with the surface of porous silicon," *Surface Science,* vol. 601, pp. 4217-4221, 2007.

[156] E. Gonzalez and R. F. Hicks, "Surface analysis of polymers treated by remote atmospheric pressure plasma," *Langmuir,* vol. 26, pp. 3710-3719, 2010/03/02 2009.

[157] D. Staack, B. Farouk, A. F. Gutsol, and A. A. Fridman, "Spectroscopic studies and rotational and vibrational temperature measurements of atmospheric pressure normal glow plasma discharges in air," *Plasma Sources Science and Technology,* vol. 15, p. 818, 2006.

[158] S. Darwiche, M. Nikravech, S. Awamat, D. Morvan, and J. Amouroux, "Optical emission spectroscopic investigation of hydrogen plasma used for modification of electrical properties of multi-crystalline silicon," *Journal of Physics D: Applied Physics,* vol. 40, p. 1030, 2007.

[159] A. Kramida, Y. Ralchenko, and J. Reader, and NIST ASD Team, *NIST Atomic Spectra Database (ver. 5.0)* [Online]. Available: http://physics.nist.gov/asd [Accessed: September 28, 2012].

[160] *Characterization of Conductors for Printed Electronics* [Online]. Available: http://www.nanopchem.com/pdf/understanding.pdf [Accessed: October 2, 2012].

[161] T. Maruyama and Y. Ikuta, "Copper thin films prepared by chemical vapour deposition from copper dipivalylmethanate," *Journal of Materials Science,* vol. 28, pp. 5540-5542, 1993.

[162] V. V. Bakovets, T. M. Levashova, I. P. Dolgovesova, and V. S. Danilovich, "Chemical vapor deposition of copper films from copper dipivaloylmethanate in hydrogen atmosphere," *Inorganic Materials,* vol. 38, pp. 457-463, 2002.

[163] Y. Sawada, H. Tamaru, M. Kogoma, M. Kawase, and K. Hashimoto, "The reduction of copper oxide thin films with hydrogen plasma generated by an

atmospheric-pressure glow discharge," *Journal of Physics D: Applied Physics,* vol. 29, p. 2539, 1996.

[164] N. S. McIntyre and M. G. Cook, "X-ray photoelectron studies on some oxides and hydroxides of cobalt, nickel, and copper," *Analytical Chemistry,* vol. 47, pp. 2208-2213, 1975.

[165] T. H. Fleisch and G. J. Mains, "Reduction of copper oxides by UV radiation and atomic hydrogen studied by XPS," *Applications of Surface Science,* vol. 10, pp. 51-62, 1982.

[166] S. Poulston, P. M. Parlett, P. Stone, and M. Bowker, "Surface oxidation and reduction of CuO and Cu_2O studied using XPS and XAES," *Surface and Interface Analysis,* vol. 24, pp. 811-820, 1996.

[167] D. Barreca, A. Gasparotto, C. Maccato, E. Tondello, O. I. Lebedev, and G. Van Tendeloo, "CVD of copper oxides from a β-diketonate diamine precursor: Tailoring the nano-organization," *Crystal Growth & Design,* vol. 9, pp. 2470-2480, 2009.

[168] T. Robert, M. Bartel, and G. Offergeld, "Characterization of oxygen species adsorbed on copper and nickel oxides by X-ray photoelectron spectroscopy," *Surface Science,* vol. 33, pp. 123-130, 1972.

[169] X. Deng, A. Verdaguer, T. Herranz, C. Weis, H. Bluhm, and M. Salmeron, "Surface chemistry of Cu in the presence of CO_2 and H_2O," *Langmuir,* vol. 24, pp. 9474-9478, 2008.

[170] D. A. Svintsitskiy, A. I. Stadnichenko, D. V. Demidov, S. V. Koscheev, and A. I. Boronin, "Investigation of oxygen states and reactivities on a nanostructured cupric oxide surface," *Applied Surface Science,* vol. 257, pp. 8542-8549, 2011.

[171] B. Pelissier, A. Beaurain, H. Fontaine, A. Danel, and O. Joubert, "Investigations on HCl contaminated Cu 200 mm wafers using Parallel Angle Resolved XPS," *Microelectronic Engineering,* vol. 86, pp. 1013-1016, 2009.

[172] A. S. W. Wong, R. G. Krishnan, and G. Sarkar, "X-ray photoelectron spectroscopy and Auger electron spectroscopy investigation on the oxidation resistance of plasma-treated copper leadframes," *Journal of Vacuum Science & Technology A,* vol. 18, pp. 1619-1631, 2000.

[173] H. Inui, K. Takeda, H. Kondo, K. Ishikawa, M. Sekine, H. Kano, N. Yoshida, and M. Hori, "Measurement of hydrogen radical density and Its impact on reduction of copper oxide in atmospheric-pressure remote plasma using H_2 and Ar mixture gases," *Applied Physics Express,* vol. 3, p. 126101, 2010.

[174] M. R. Baklanov, D. G. Shamiryan, Z. Tokei, G. P. Beyer, T. Conard, S. Vanhaelemeersch, and K. Maex, "Characterization of Cu surface cleaning by hydrogen plasma," *Journal of Vacuum Science & Technology B: Microelectronics and Nanometer Structures,* vol. 19, pp. 1201-1211, 2001.

[175] K. Okada, J. Kawai, and A. Kotani, "Triple-peak feature of Cu 2p x-ray-photoemission spectrum in copper acetylacetonate," *Physical Review B,* vol. 48, pp. 10733-10738, 1993.

[176] M. E. Alnes, E. Monakhov, H. Fjellvåg, and O. Nilsen, "Atomic layer deposition of copper oxide using copper(II) acetylacetonate and ozone," *Chemical Vapor Deposition,* vol. 18, pp. 173-178, 2012.

[177] Y. Freile-Pelegrín, T. Madera-Santana, D. Robledo, L. Veleva, P. Quintana, and J. A. Azamar, "Degradation of agar films in a humid tropical climate: Thermal, mechanical, morphological and structural changes," *Polymer Degradation and Stability,* vol. 92, pp. 244-252, 2007.

[178] E. Gómez-Ordóñez and P. Rupérez, "FTIR-ATR spectroscopy as a tool for polysaccharide identification in edible brown and red seaweeds," *Food Hydrocolloids,* vol. 25, pp. 1514-1520, 2011.

[179] J.-P. Lim, H. S. Uhm, and S.-Z. Li, "Atmospheric-pressure argon/oxygen plasma-discharge source with a stepped electrode," *Applied Physics Letters,* vol. 90, pp. 051504-3, 2007.

[180] Q. Li, J.-T. Li, W.-C. Zhu, X.-M. Zhu, and Y.-K. Pu, "Effects of gas flow rate on the length of atmospheric pressure nonequilibrium plasma jets," *Applied Physics Letters,* vol. 95, pp. 141502-3, 2009.

[181] Q. Li, H. Takana, Y.-K. Pu, and H. Nishiyama, "A nonequilibrium argon-oxygen planar plasma jet using a half-confined dielectric barrier duct in ambient air," *Applied Physics Letters,* vol. 100, pp. 133501-4, 2012.

[182] J. L. Walsh and M. G. Kong, "Room-temperature atmospheric argon plasma jet sustained with submicrosecond high-voltage pulses," *Applied Physics Letters,* vol. 91, pp. 221502-3, 2007.

[183] K. D. Weltmann and T. von Woedtke, "Campus PlasmaMed—from basic research to clinical proof," *Plasma Science, IEEE Transactions on,* vol. 39, pp. 1015-1025, 2011.